EXPERIMENTAL QUANTUM CHEMISTRY BY BINARY (e,2e) SPECTROSCOPY

by

KAM TONG LEUNG

B.Sc., University Of British Columbia, 1980

A THESIS SUBMITTED IN PARTIAL FULFILMENT OF

THE REQUIREMENTS FOR THE DEGREE OF

DOCTOR OF PHILOSOPHY

in

THE FACULTY OF GRADUATE STUDIES

Chemistry Department

We accept this thesis as conforming

to the required standard

THE UNIVERSITY OF BRITISH COLUMBIA

August 1984

In presenting this thesis in partial fulfilment of the requirements for an advanced degree at the University of British Columbia, I agree that the Library shall make it freely available for reference and study. I further agree that permission for extensive copying of this thesis for scholarly purposes may be granted by the Head of my Department or by his or her representatives. It is understood that copying or publication of this thesis for financial gain shall not be allowed without my written permission.

Department of Chemistry

The University of British Columbia
2075 Wesbrook Place
Vancouver, Canada
V6T 1W5

Date: August 1984

Abstract

The notion that chemists might benefit by looking at molecular orbitals and chemical bonding phenomena from the complementary momentum-space perspective was first suggested by Coulson and Duncanson some forty years ago. With the development of binary (e,2e) spectroscopy in the last decade, experimental momentum densities of individual orbitals can now be measured directly and this has provided the first "real" look at molecular bonding in the laboratory. Binary (e,2e) spectroscopy measures the binding energy spectrum and the spherically averaged momentum distribution using high energy electron impact ionization and coincidence detection techniques. The experimental orbital momentum distributions not only have helped to identify the symmetry (s-type or p-type), order and nature of the characteristic orbital involved in the ionization process, but also have made it possible to stringently evaluate the quality of *ab-initio* self-consistent-field wavefunctions.

The valence-shell binding energy spectra and momentum distributions of the noble gases and a number of small molecules including H_2, CO_2, CS_2, OCS and CF_4 have been measured using a state-of-the-art binary (e,2e) spectrometer. An existing spectrometer has been modified to provide high momentum and timing resolutions as well as sufficient energy resolution for resolving most of the structures of the species reported. New and definitive results on the valence-

shell electronic structure and orbital bonding pattern of these species have been obtained. Possible chemical trends in the electronic structure and orbital densities in the noble gas group and in the valence isoelectronic linear triatomic group: CO_2, CS_2 and OCS have been investigated. Computer generated density contour maps and three-dimensional orbital density visualization of theoretical wavefunctions in both position and momentum space are used to facilitate interpretation of the experimental momentum distributions. This density topographical approach is instrumental in extending the present understanding of momentum-space chemical properties. In particular, such an approach has provided a new and complementary picture of the covalent bond in molecular hydrogen in momentum-space. The first experimental estimation of the spherically averaged bond density in momentum-space by binary (e,2e) spectroscopy is also attained.

Table of Contents

List of Tables

List of Figures

Acknowledgement

I would like to thank my research supervisor, Professor Christopher E. Brion, for the many things that I have learned from him both consciously and unconsciously. It has indeed been my privilege and honor not only to be guided by his academic insights but also perhaps more importantly to be influenced by his approach to human relations. I am most grateful for his continual support throughout the course of this work and especially for his encouragement and advice at critical moments.

I owe a special gratitude to Dr. John P.D. Cook for his invaluable assistance during the initial phase of this work. I wish also to thank Professors D.C. Chong, J.A.R. Coope, R.F. Snider and L.S. Weiler of the Chemistry Department and Professor P.W. Langhoff of Chemistry Department at Indiana University for many illuminating interactions, discussions and personal advice. Many thanks are also due to Professor M.J. van der Wiel and his co-workers of the FOM Institute for their assistance in the lens trajectory program and their very kind hospitality during my two week visit to Amsterdam. I wish also to thank Dr. W. Lewis-Bevan for his interest and careful proof-reading of this thesis.

I would like to gratefully acknowledge the staff members of the Chemistry Department for their technical, secretarial

and graphic support. In particular, I wish to thank chief engineerers B. Powell (Mechanical Shop) and J. Sallos (Electronic Shop) not only for their interest and efficiency in job coordination but also for their incredible tolerance to my persistence in getting every job done spontaneously. For the many excellent and instantaneous repair and construction jobs of the many potential technical nightmares, I wish to express my deepest gratitude to E. Gomm, J. Edwards and C. McCafferty of the Mechanical Shop and to B. Greene, P. Carpendale and H. Chow of the Electronic Shop. For without the technical assistance and enthusiasm of these people, the work reported in this thesis would not be possible. I wish also to thank A. Rees and B. Gray of the Main Office for their secretarial advice and special assistance, and to P. Parsons and E. Jensen for their graphic assistance. The technical staff of the Computer Centre should also be acknowledged for their helpful consultations and suggestions.

Finally, I gratefully acknowledge the financial assistance of the Natural Sciences and Engineering Research Council of Canada (in the form of a postgraduate scholarship). Last but by no means the least I wish to thank my parents for their understanding and everlasting support in making all of this possible.

Chapter I

INTRODUCTION

1.1 MOMENTUM DISTRIBUTIONS, ORBITALS AND QUANTUM CHEMISTRY

One of the major challenges in quantum chemistry [PCR73, LCG77, C82, LP83] is the search for the exact solution to the equation of motion for electrons in atoms and molecules. The complex motion of the electrons in any atomic or molecular system (in a stationary state) is conveniently described by the (time-independent) Schrodinger equation [P68, S72, A83, RC83]:

$$[1.1] \qquad H\Psi = E\Psi,$$

where H is the Hamiltonian. Since this equation cannot be solved exactly for systems with more than one electron, iterative numerical procedures [PB70, S72, W76, LP83, RC83] are used to obtain the best approximate solution. The (normalized) eigen-solution Ψ is commonly obtained by the variational method [PW35, S72, RC83], which varies the wavefunction parameters striving to obtain the lowest total energy. Once Ψ has been determined, the expectation value of any measurable physical observable can be calculated by:

[1.2] $$\langle O \rangle = \int \Psi^*(w)\, O\, \Psi(w) dw,$$

where w can either be the position **r** or the momentum **p**. The quantum-mechanical operator O of the physical observable is chosen according to physical or chemical intuition and often involves approximation. The many-electron wavefunction, Ψ, for atoms or molecules is usually written as antisymmetrized products of one-electron atomic or molecular orbitals. i.e.

[1.3] $$\Psi = A| \psi_1\psi_2\psi_3\cdots\psi_i\cdots\psi_N |,$$

where A represents the antisymmetrizer and ψ_i is the ith orbital in the many-electron wavefunction. The many-electron wavefunction is commonly obtained using the self-consistent-field LCAO-MO method[1] [R51, D69, PB70, SB72, RC83]. Although the orbital (or independent particle) description [H28, M28, PW35, LP64, JS73, SO73, VA75] of the many-electron wavefunction is only an approximation, it has become one of the most important concepts in modern quantum chemistry and has been found to be extremely useful in interpreting a variety of chemical data [WM77]. Using qualitative information on the orbital energies and electron densities, general methods have been developed to provide an understanding of molecular structures and shapes [B80],

---

[1] LCAO stands for Linear Combination of Atomic Orbitals and MO stands for Molecular Orbital.

chemical reactivities and bonding phenomena [K74] as well as other physical and chemical properties [S72, L72a, SM72].

There are two general approaches to the experimental evaluation of the quality of the approximate wavefunctions. The first involves comparison of the expectation values of physical observables (equation 1.2) such as dipole moment, polarizability, transition energy and probability, and binding energies, etc. [S72, L72a, SM72] between those calculated using the approximate wavefunction and those measured by experiments. In the important case where the operator is the Hamiltonian, the physical observable is the energy of the system. Traditional methods used to obtain the energy information associated with various electronic states include photoabsorption and photoionization spectroscopies [B79] as well as high energy electron impact spectroscopies which simulate photon impact experiments [HS&76, BH81, B82]. The energies of these electronic states, especially in the outer valence region, are related to the orbital energies in the Koopmans' approximation [K33]. Photoabsorption spectroscopy [S67, B79] measures the differences between (orbital) energy eigenvalues, and through selection rules, some relations between the quantum numbers of the involved pairs of states. Photoelectron spectroscopy [S&69, TB&70, R77, B79, KK&81, E82], on the other hand, measures the binding energies of photoelectrons and hence the energies of the ionic states. In addition the intensities of the states

observed in the photoabsorption and photoelectron spectra are related to the photoabsorption oscillator strengths and partial ionization oscillator strengths respectively [B79]. The oscillator strengths are the probabilities of the involved transitions and depend upon the photon energy (or effectively the photon momentum =h/λ) [I71, B79]. This dependence of the partial oscillator strength of a particular state on the photon energy can be used to identify that ionic state. Because of the limited availability of continuous tunable photon sources until the recent development of synchrotron radiation facilities [K79, WD80] for photon-impact experiments, these measurements have been made possible by high energy electron impact simulation [HS&76, BH81, B82] of photoabsorption and photoelectron studies. It should be noted also that the angular asymmetry parameters measured by angular resolved photoelectron spectroscopy [CA71, B79] can also be used to indicate the signature of a particular state.

A more direct approach to the evaluation of *ab-initio* wavefunctions involves the comparison of the calculated and measured position (or charge) density $\Psi^*(\mathbf{r})\Psi(\mathbf{r})$ and momentum density $\Psi^*(\mathbf{p})\Psi(\mathbf{p})$. The density function[2] provides an inherently more direct quantity for the evaluation of

---

[2] The quantity $\psi_i^*(\mathbf{r})\psi_i(\mathbf{r})d\mathbf{r}$ is the probability of observing the *ith* electron between position $\mathbf{r}$ and $\mathbf{r}+d\mathbf{r}$. Similarly the quantity $\psi_i^*(\mathbf{p})\psi_i(\mathbf{p})d\mathbf{p}$ represents the probability of observing the *ith* electron moving with momentum between $\mathbf{p}$ and $\mathbf{p}+d\mathbf{p}$.

wavefunctions since there is no operator involved. In the former approach, approximation to the mathematical form of the operator representing a particular observable is often necessary. Moreover, the comparison between experimental and calculated wavefunction properties usually depends upon which part of the wavefunction is emphasized in the optimization procedure. For instance it has been found that the theoretical wavefunction which gives lower total energy does not necessarily model the outer valence electrons correctly. The total position-space wavefunction $\Psi(\mathbf{r})$ and the total momentum-space wavefunction $\Psi(\mathbf{p})$ are equivalent solutions written in different representations. They are related to each other by the Fourier transform, i.e.

$$[1.4] \qquad \Psi(\mathbf{p}) = (2\pi)^{-3/2}\int\Psi(\mathbf{r})\exp(-i\mathbf{p}.\mathbf{r})d\mathbf{r}.$$

Total position densities [B75] can be measured using X-ray and electron diffraction methods [BF80] which are mainly limited to the study of crystals and surfaces. Total momentum densities [E75, W77a] can be derived from the experimentally determined Compton profiles obtained using X-ray and γ-ray Compton scattering [C71, W77b], high energy electron impact ionization [BF74] and positron annihilation [S75] techniques. Details of each of the individual methods are referred to in the corresponding review articles. It is important to note that all of these conventional methods

measure the electron density (either in position or momentum space) due to all the electrons in the target system, and cannot routinely partition the total electron density into individual orbital components. The recently introduced technique of binary (e,2e) spectroscopy [MW76a] measures both the energy and momentum information associated with the ejection of a single electron using high energy electron impact ionization and coincidence detection technique. The binary (e,2e) method can in principle provide a fairly complete "anatomy" of the total momentum density into its individual orbital components. It represents one of the most powerful methods for the study of electronic structure and in the investigation of the molecular orbital bonding pattern. To date, the technique has been used to provide the most comprehensive studies of orbital momentum densities for both atoms and molecules and has provided the possibility of critical evaluation of the *ab-initio* wavefunction especially in the chemically interesting valence region. This has enhanced the understanding of molecular orbital concepts and has provided a unique vantage point for observing chemical bonding phenomena in the laboratory.

1.2 BINARY (e,2e) SPECTROSCOPY AND CONVENTIONAL METHODS

Binary (e,2e) spectroscopy [MW76a] (see also appendix A) is based on the following electron impact ionization reaction:

$$[1.5] \qquad \underset{(E_0,p_0)}{e} + \underset{(E,p)}{(ion\text{-}e)} \longrightarrow \underset{(E_1,p_1)}{e} + ion + \underset{(E_2,p_2)}{e}$$

Making use of the energy and momentum conservations, it is possible to sample the binding energy E and momentum **p** of the bound electron before the knockout reaction by controlling the kinetic energies and momenta of the incident electron (labelled by subscript 0) and the two outgoing electrons (labelled by subscripts 1 and 2 for the scattered and ejected electrons respectively). i.e.

$$[1.6a] \qquad E = (E_0 - E_1) - E_2; \quad E_1 = E_2.$$

$$[1.6b] \qquad \mathbf{p} = \mathbf{p}_2 - (\mathbf{p}_0 - \mathbf{p}_1); \quad \mathbf{p}_0 - \mathbf{p}_1 \gg 0.$$

Here the recoil momentum of the ion is ignored (see chapter 2). The experiment involves complete determination of the scattering kinematics of the incident and outgoing electrons and coincident counting of the outgoing electrons (i.e. of (e,2e) events) under kinematic conditions in which the momentum transfer ($\mathbf{p}_0$-$\mathbf{p}_1$) is maximized and the energies of the incident and outgoing electrons are made sufficiently

high. The resulting histogram of coincidences yields the binding energy spectrum or the orbital momentum distribution depending upon the sampling parameter (i.e. either E or **p**, see also chapter 2).

It is important to compare the information obtained by the new technique with those obtained using conventional methods. Information on ionization energies can be obtained by photoelectron [S&69, TB&70, R77, B79, KK&81, E82] and dipole (e,2e) [HS&76, BH81, B82] spectroscopies. In the case of photoelectron and dipole (e,2e) spectroscopies the kinematics can be written as

$$[1.7]\quad \begin{matrix}\text{Photoelectron:}\\ \text{Dipole (e,2e):}\end{matrix}\ \left.\begin{matrix}\gamma\\ e\end{matrix}\right\} + (\text{ion-e}) \longrightarrow \left.\begin{matrix}\\ e\end{matrix}\right\} + \text{ion} + e$$

$$(E_0,\mathbf{p}_0)\quad (E,\mathbf{p})\quad (E_1,\mathbf{p}_1)\quad (E_2,\mathbf{p}_2)$$

In the dipole limit where the momentum transfer is minimized, i.e. $\mathbf{p}_0-\mathbf{p}_1\to 0$, the corresponding energy and momentum conservation equations are:

$$[1.8a]\qquad E = (E_0 - E_1) - E_2;$$

$$[1.8b]\qquad \mathbf{p} \simeq \mathbf{p}_2.$$

The quantity E_0-E_1 is the effective photon energy (i.e. = $h\nu$) in the case of photoelectron spectroscopy [B79] or is the energy loss in dipole (e,2e) spectroscopy [B82]. By

combining equations 1.8a and 1.8b, one gets that the magnitude of the electron momentum becomes simply (in atomic units):

[1.8c] $$p \simeq \{2[(E_0-E_1) - E]\}^{1/2}.$$

Since the normal energy range in (X-ray) photoelectron spectroscopy is 100eV-1000eV [B79], the corresponding electron momentum is therefore in the range $1a_0^{-1}$-$10a_0^{-1}$. It is important to note, however, that a variable photon energy is necessary in order to vary the momentum. The availability of tunable photon sources is limited only to synchrotron radiation [WD80] and photon simulation techniques such as dipole (e,2e) spectroscopy [B82]. A peak in the binding energy spectrum (i.e. a histogram of (e,2e) events as a function of E at an essentially constant momentum) measured by binary (e,2e) spectroscopy corresponds to an ion state in the same way as that obtained by photoelectron or dipole (e,2e) measurements [MUP78]. The enormous advantage in the new technique is the extra kinematic flexibility which allows the electron momentum to be varied independently. For each ion state, the momentum distribution (i.e. a histogram of (e,2e) events as a function of p) is, to a close approximation, the square of the momentum-space orbital of the struck electron (see chapter 2). Such a momentum profile affords an instant identification of the characteristic hole

associated with the ion state. Moreover, the binary (e,2e) reaction samples the low momentum part ($0a_0^{-1}$-$3a_0^{-1}$) of the orbital, which corresponds to the large (position) spatial part (the bonding region), in contrast to photoelectron spectroscopy which probes only the large momentum region corresponding to the small spatial part of the orbital (i.e. the region very close to the nuclei).

Of paramount importance is that binary (e,2e) spectroscopy is sufficiently sensitive to provide experimental definitions for the orbitals best suited to form the basis expansion of the many-electron wavefunction. The truely unique momentum distribution associated with a particular single particle state (i.e. the orbital momentum distribution) provides direct experimental evaluation of the theoretical *ab-initio* SCF LCAO-MO wavefunction in the chemically sensitive outer regions of valence orbitals. Other conventional methods such as Compton scattering type experiments[3] [W77b] can only sample total momentum distributions. The reaction equation for Compton scattering (i.e. a (γ,γ') reaction) can be represented as:

---

[3] Compton scattering type experiments include X-ray and γ-ray Compton scattering [C71, W77b] and high energy electron impact spectroscopy (HEEIS) [BF74].

$$\text{[1.9]}\qquad \left.\begin{matrix}\text{Compton:}\ \gamma \\ \text{HEEIS:}\ e\end{matrix}\right\} + (\text{ion-e}) \longrightarrow \left.\begin{matrix}\gamma' \\ e'\end{matrix}\right\} + (\text{ion-e})$$

$$(E_0,p_0) \qquad (E,p) \qquad (E_1,p_1) \qquad (E',p')$$

where the conservation laws dictate:

$$\text{[1.10a]}\qquad E_0 - E_1 = E' - E;$$

$$\text{[1.10b]}\qquad \mathbf{p}_0 - \mathbf{p}_1 = \mathbf{p}' - \mathbf{p}.$$

Essentially Compton scattering type experiments can be considered as inelastic scattering of a high energy photon or electron. The (relativistic Doppler) broadening [W77b] of the scattered radiation is related to the electron momentum distribution. Because Compton scattering type experiments essentially involve a single-particle measurement (i.e. the detection of the photon or electron that suffers the inelastic collision), it is not possible to partition the measured Compton profile based upon orbital energy selection. Consequently only the Compton profile due to all of the electrons is measurable. Even in the special case where double-particle measurements (such as using fluorescence coincidence techniques [FH72]) are possible, the measured Compton profile must be differentiated (often using numerical techniques with varying degrees of accuracy) in order to derive the momentum distribution. This is in marked contrast to binary (e,2e) spectroscopy which allows direct

measurements of momentum distributions of individual orbitals. Binary (e,2e) spectroscopy is therefore truely unique in its capability of evaluating the electronic wavefunction on an orbital-by-orbital basis in modern experimental quantum chemistry.

1.3 BRIEF HISTORICAL REMARKS

The origin of binary (e,2e) spectroscopy can be traced back to two Nobel prize winning experiments in atomic physics; namely, the 1914 electron scattering experiment of Franck and Hertz [FH14] and the 1922 X-ray scattering experiment of Compton [C22]. The Franck and Hertz experiment established the similarity between electron-atom interactions and photon-atom interactions. This experiment subsequently gave rise to the later vast development of electron spectroscopy [MB52, TRK70, BH81]. The Compton experiment demonstrated not only the particle nature of a high energy photon (in the wave-particle duality of matter) but also the inelastic scattering of light. It triggered the emergence of an array of Compton scattering experiments and demonstrated the importance of momentum distributions in the understanding of electronic structure. After the initial thrust of the development in 1922-1936, during which many important discoveries concerning the Compton effect were made, the field lay essentially "dormant" for forty years, despite

encouragement from the theoretical community. In particular, Coulson and Duncanson [CD41] had published a series of papers in the early 1940s, stressing the importance of interpreting chemistry from the momentum-space perspective.

The development of (e,2e) experiments was, however, really inspired by the important development of the (p,2p) (and also the $(\gamma,2\gamma)$) reaction in nuclear physics. The feasibility of using the (e,2e) reaction to study electronic structure was first noted by McCarthy *et al*. in 1959 [MJK59] in their theoretical study of applying the (p,2p) reaction to investigate nucleon structure. This, together with the work by Mathies and Neudatchin in 1963 [MN63], laid the foundation of the (e,2e) reaction theory. Indeed, a vast volume of jargon used nowadays by (e,2e) spectroscopists has come from nuclear physics terminology. The use of the term "(e,2e)" itself to indicate electron impact ionization reaction and terms such as "separation energy" to mean binding energy are just two of many notable examples of the nuclear physics heritage.

The very first (e,2e) measurement was reported by Ehrhardt *et al*. (in West Germany) in 1969 for He [ES&69]. This and subsequent works by Ehrhardt *et al*. were directed to investigate the scattering reaction mechanism at low energies using asymmetric scattering geometry. The second experimental work on (e,2e), reported by Amaldi *et al*. (in Italy) also in 1969 [AE&69], gave the first (e,2e) binding

energy spectrum for the carbon K-shell of a thin film at high energies. Following this preliminary study, Camilloni *et al.* (in Italy) in 1972 [CG&72] reported the first (e,2e) angular correlation (or momentum distribution) for the carbon K and L shells of a thin film. Both of these experiments [AE&69, CG&72] made use of the high energy coplanar symmetric geometry and clearly demonstrated the sensitivity of the momentum distribution to the shape of the orbital wavefunction. In 1973, Weigold *et al.* (in Australia) [WHT73] reported the first (e,2e) momentum distributions for separate Ar 3p and 3s orbitals using the high energy noncoplanar symmetric geometry. This experiment also gave the first evidence of intense electron-electron correlation in the inner valence region for the ionization of the Ar 3s electrons. The follow-up works by the Australian group in the first molecular (e,2e) experiments for hydrogen [WH&73] and methane [HW&73] also indicated the importance of electron correlation effects in molecular ionization phenomena. The 1973 work on Ar [WHT73] has established the high energy noncoplanar symmetric kinematics as the most appropriate scattering geometry in structural determination. These pioneering works of the atomic physicists were later followed by two chemistry groups: C.E. Brion (in Canada) (this group) in 1976 and M.A. Coplan and J.H. Moore (in the United States) in 1978. During the infancy of the (e,2e) technique much effort was directed towards the firm establishment of the

various reaction approximations [UWM75, CG&78, FM&78, DM&78] using noble gases as targets. It was the input from the chemists which led to systematic studies of orbital momentum distributions which in turn allowed the study of chemical trends and group related properties. To date, over forty atoms and small molecules have been investigated by binary (e,2e) spectroscopy. These include a number of important series of atoms and small molecules.

(i) **Atoms**

1) Carbon film;
2) Group VIII: He, Ne, Ar, Kr and Xe;
3) One electron atom: H;
4) Open-shell atoms: Na, K and Cd.

(ii) **Molecules**

1) First-row hydrides: HF, H_2O, NH_3 and CH_4;
2) Second-row hydrides: HCl, H_2S and PH_3
3) Hydrogen and hydrogen halides: H_2, HF, HCl, HBr and HI;
4) Methane, methyl halides and other methyl-substituted compounds:

   CH_4, CH_3F, CH_3Cl, CH_3Br, CH_3I,

   CH_3OH, CH_3NH_3 and CH_3CN;
5) Ethylene and halogen-substituted ethylenes:

   C_2H_4, C_2H_3F, C_2H_3Cl and C_2H_3Br;
6) Fluoro-substituted methane:

CH_4, CH_3F, CHF_3 and CF_4;

7) The isoelectronic series: CO, N_2 and C_2H_2;

8) The valence-isoelectronic series: N_2O, CO_2, OCS and CS_2;

9) Open-shell molecules: NO and O_2;

10) Other small organic molecules.

A bibliograhy of all the (e,2e) works published to date is given in appendix A. Details of each of the individual studies are referred to in the corresponding papers (see appendix A). Of all these studies, the work of Lohmann and Weigold [LW81] on the H atom should be particularly noted since it provides the first direct experimental measurement of the momentum density where an exact solution to the Schrodinger equation is available. Of fundamental chemical interest is the recent work of Leung and Brion [LB84a] (see also chapter 6) on molecular hydrogen which provides the first experimental estimation of the bond density in molecular hydrogen. The relevance of the (e,2e) reactions as a unique powerful tool not only for testing different scattering theories but also for the extraction of energy and momentum information of individual orbitals of atoms and molecules has been amply demonstrated.

1.4 MAJOR APPLICATIONS

Two general types of electronic structural information can be obtained by binary (e,2e) spectroscopy, namely, the binding energy spectrum (measured at an essentially fixed momentum) and the electron momentum distribution (measured at a fixed binding energy corresponding to a particular ion state). In principle, the technique is capable of studying the full ionization electronic spectrum including both the core and valence regions. Because of the very high energies required to satisfy the kinematic approximations (see chapter 2) involved in the (e,2e) binary encounter, knockout reaction, almost all of the (e,2e) works published to date are concerned only with the valence region. It should be noted also that because of the random orientations of the gaseous targets, the measured momentum distribution corresponds to momentum density averaged over all the orientations (i.e. spherical averaging occurs). Despite these limitations, important and informative results can be obtained from these spectra. An overview of the more important applications is given below. These applications will be further illustrated in greater detail in individual studies reported in the later chapters.

1.4.1 Valence-Shell Binding Energies

Binary (e,2e) spectroscopy measures the complete valence-shell binding energy spectrum of atoms and molecules. This is especially important in the inner valence region which is inaccessible to (UV) photoelectron spectroscopy. Evidence of many-body states in the inner regions of many atoms and molecules, such as for instance Ar [WHT73], CH_4 [HW&73] and more recently methyl halides [MC&84], have been uncovered using the binary (e,2e) method. These have provided direct experimental confirmation of the breakdown of the Koopmans' approximation [K33] and indicated the importance of electron correlation effects in ionization phenomena. Furthermore, the spectroscopic factor (which is defined to be the probability that an eigenstate having a principal configuration of a hole in the characteristic orbital, see chapter 2) can be derived from the intensities in the binding energy spectra. These provide a direct indication of the extent of an orbital contribution in a particular configuration interaction process as well as further details of electron correlation effects.

1.4.2 Orbital Symmetry

In general, two types of momentum distributions can be distinguished according to where the maximum occurs. The totally symmetric "s-type" distribution has its maximum at p=0 while the nonsymmetric "p-type" distribution has its maximum at nonzero p value. The symmetry of the orbital can be identified from its characteristic momentum distribution. For instance, atomic s and diatomic σ_g orbitals have totally symmetric components in their wavefunctions and therefore the corresponding momentum distributions follow the s-type behaviour. Atomic p or diatomic σ_u and π orbitals, on the other hands, have p-type momentum distributions. Notable examples are the momentum distributions of the outer valence ns and np orbitals in the noble gases (chapter 4) and those of π and σ orbitals of linear diatomics and triatomics (chapters 5-9). The symmetry of orbitals of polyatomic systems can be similarly identified. Moreover, in the case of a mixed "s-p type" orbital, the relative intensities between the maxima (due to s and p components) of the experimental momentum distribution can be used to probe the extent of s-p hybridization. One example of a s-p type orbital is the outermost sigma bonding orbital of the valence-isoelectronic triatomic series CO_2, CS_2 and OCS (chapters 7-9 respectively).

1.4.3 Orbital Ordering

In essence, the momentum distribution represents the fingerprint of an orbital. Although the energy resolution in binary (e,2e) spectroscopy is still not comparable to that of photoelectron spectroscopy, orbital ordering can be easily identified by the corresponding momentum profiles measured at carefully chosen binding energies. By comparing the shapes of the observed momentum distributions with those of the theoretical distributions of individual orbitals, one can unambiguously identify the proper orbital ordering. An example can be found in OCS where an unambiguous identification between 2π and 9σ is made using the corresponding experimental orbital momentum distributions (see chapter 9). In formaldehyde the proper ordering of the $5a_1$ and $1b_2$ orbitals was earlier identified by the angular variation of the binary (e,2e) binding energy spectrum [HHB76b].

1.4.4 Assignment Of The Many-body States

According to Koopmans' theorem [K33], ionization of an orbital can only result in one transition or observed peak in the binding energy spectrum. This independent particle ionization (or one peak per orbital) picture generally applies quite well to the outer valence orbitals. However, in the case of inner valence orbitals, many-body (or

satellite) states arising from the ionization of a single orbital have been commonly observed. Numerous examples can be found, for instance, in the isoelectronic CO [DD&77b, TM&82], N_2 [CS&76, WD&77] and C_2H_2 [DM&77, CMT78, CM&79] series, the valence isoelectronic CO_2, CS_2 and OCS series (see chapters 7-9 respectively) and other methyl substituted compounds [CC&81, MBW81, MC&84]. This breakdown of the independent particle picture is generally attributed to electron correlation effects in both the initial states and/or final states [MW76a]. The major orbital contribution of a many-body state can be obtained from the momentum profile sampled at the energy corresponding to the many-body state. A good example of this advantage is demonstrated in the heavier members of the noble gases: Ar, Kr and Xe; where the characteristic momentum distributions of the satellite states in the inner valence region are found to follow those of the corresponding ns orbitals (see chapter 4). These satellites can therefore be identified as arising from the ionization of the respective ns electrons. In fact, it has been consistently observed that significant population splittings occur usually only in the inner valence orbitals. The correct prediction of these many-body states has been the central object of theoretical methods such as the many-body Green's function method [CTY71, CD77] and the symmetry adapted cluster expansion method [NH78]. The momentum distributions and the associated pole-strengths of these

many-body states are instrumental in the evaluation of the quality of these calculations.

1.4.5 Stringent Test Of Ab-initio Wavefunctions

A theoretical *ab-initio* wavefunction is normally obtained using the so-called self-consistent-field (SCF) procedure to minimize the total energy (the variational method) [P68, S72, A83, RC83]. Such a procedure of energy minimization often underestimates the chemically significant outer (large r) part of valence orbitals since these regions do not contribute significantly to the total energy. The experimental binary (e,2e) momentum distributions of the valence orbitals can thus be used as a stringent extra test for the quality of the theoretical wavefunction since the method is particularly sensitive to the low momentum (large r) part of the orbital wavefunction. The measurements made by binary (e,2e) spectroscopy have shown that the widely used double-zeta quality wavefunctions have been unsuccessful to provide a satisfactory agreement with the (e,2e) data especially for the lone pair electrons in a number of small molecules. Notable examples are the first-row hydrides: HF [BH&80], H_2O [HHB77, DD&77a] and NH_3 [HHB76a, CS&76, TL&84]. The inclusion of polarization functions in the theoretical wavefunction (although helping to lower the energy) does not necessarily lead to a better agreement with the momentum

distributions. Comparison of the theoretical momentum distributions with the (e,2e) data can therefore reveal inadequacies in the theoretical wavefunction, especially in the variationally less sensitive outer valence part. These experimental results can then be used as feedback for further improvement of the theoretical wavefunctions.

1.5 SCOPE OF THE THESIS

The above introductory discussions of binary (e,2e) spectroscopy are intended to provide a general overview of the field in its brief fifteen years of development. Excellent reviews [MW76a, GF&81, MW83] of the field can be found in the literature (see Appendix A). In the following chapters, the author's contributions to the field will be reported. More specifically, brief outlines of the basic kinematic and scattering equations used in noncoplanar symmetric binary (e,2e) reactions as well as summaries of the major momentum-space concepts are discussed in chapter 2. In chapter 3, detailed discussions of the construction of a second generation binary (e,2e) spectrometer and its operation are given. This high momentum resolution binary (e,2e) spectrometer has been used for investigating the electronic structure of atoms as well as the bonding phenomena of a variety of small molecules. In particular, results for the noble gases are reported in chapter 4. The

momentum-space chemistry of the two electron systems: He and H_2 are investigated in chapter 5. Chapter 6 provides an experimental estimation of the spherically averaged bond density in molecular hydrogen. Results for the valence isoelectronic linear triatomic series: CO_2, CS_2 and OCS are given in chapters 7, 8 and 9 respectively. Finally, the study of a truely three-dimensional molecule: CF_4 by binary (e,2e) spectroscopy is reported in chapter 10. In all of the experimental works, two-dimensional density contour maps and three-dimensional constant density surface plots calculated using theoretical wavefunctions are used to assist interpretation of the observed features in the measured momentum distributions and to provide general discussions of various momentum-space properties. These experimental works (chapters 4-10) have provided new definitive results for the respective orbital momentum distributions and have further illustrated the practicality of binary (e,2e) spectroscopy as a probe for bonding and electronic structural investigations. A summary of this thesis and an outlook on the field are given in chapter 11.

Unless otherwise stated, atomic units ($\hbar=m_e=e=1$) are used in this thesis. The graphic convention for the density visualization is given in chapter 5. As with the references quoted in this chapter, references in the remaining of this thesis are enclosed by square brackets in the text and are indicated using a five (or six) character code composing of

the first characters of the last names of the contributing authors and the year of the publication. (Details of the convention are given in the References.)

Chapter II

THEORETICAL BACKGROUND

2.1 REACTION THEORY

The validity of a particular scattering theory [MM65, MB69, M79] depends critically on the scattering kinematics. There are basically four distinct kinematic regimes for the (e,2e) reaction; these are normally classified according to the momentum transfer and energy involved. The asymmetric (e,2e) reaction involves low momentum transfer while the symmetric (e,2e) reaction involves high momentum transfer. The low energy asymmetric (e,2e) geometry was used in the first (e,2e) experiment by Ehrhardt *et al*. [ES&69] for the investigation of the interaction mechanism [EJS80]. The high energy asymmetric (e,2e) kinematics, also known as dipole (e,2e) spectroscopy, was used by van der Wiel and Brion [VB74] for an effective simulation of photoelectron measurements of dipole oscillator strengths with the tunable virtual photon field of a fast electron [HS&76, BH81, B82]. The symmetric coplanar arrangement (both high and low energy) provides a stringent evaluation of various reaction approximations (such as the optical potential model, distorted wave approximation, averaged eikonal wave approximation and factorization approximation) [UWM75, MW76a,

CG&78, FM&78, SCG78]. Finally, the high energy symmetric noncoplanar kinematics is the most suitable geometry for the investigation of electronic structure and is the scattering geometry used in the studies reported in this thesis. The fundamental binary (e,2e) theory has been reviewed extensively in the literature [FM73, M73, M75, MW76a, MW76b, MS80, M80]. Only a summary of the most relevant equations used in this thesis will therefore be given. The following discussions should be applied strictly to the high energy symmetric noncoplanar collisions.

2.1.1 Scattering Kinematics

In an (e,2e) experiment [MW76a, M80], the scattering kinematics are completely determined. A target (atom or molecule) is ionized by high energy electron impact using a fast incident electron with kinetic energy E_0 and momentum $\mathbf{p}_0$. An ejected electron[1] with kinetic energy E_2 and momentum $\mathbf{p}_2$ emerges, along with the scattered electron with kinetic energy E_1 and momentum $\mathbf{p}_1$ as well as the ion with ion recoil energy E_{recoil} and ion recoil momentum $\mathbf{q}$.

---

[1] In effect it is not possible to distinguish the "ejected" electron from the "scattered" one. For convenience, one often associates the "faster" electron to be the "scattered" one in scattering theory.

$$[2.1] \qquad M + e^- \longrightarrow M^+ + e^- + e^-.$$
$$(\mathbf{p}_0, E_0) \quad (\mathbf{q}, E_{recoil}) \quad (\mathbf{p}_1, E_1) \quad (\mathbf{p}_2, E_2)$$

Neglecting the very small ion recoil energy, conservation of energy requires that:

$$[2.2] \qquad E = E_0 - (E_1 + E_2),$$

where E is the binding (or separation) energy of the ejected electron. Clearly, if the kinetic energies of the outgoing electrons (i.e. E_1 and E_2) are kept constant, the binding energy can be sampled by varying E_0. Also (neglecting the very small thermal motions of the target before the impact) conservation of momentum requires that:

$$[2.3a] \qquad \mathbf{q} = \mathbf{p}_0 - (\mathbf{p}_1 + \mathbf{p}_2),$$

where the momentum transfer (of the incident electron to the ionized electron) is defined as $\mathbf{K} = \mathbf{p}_0 - \mathbf{p}_1$. If one considers that the scattering takes place in a close, binary encounter [MW76a, M80] situation (a condition which can be realized by maximizing the momentum transfer), then the ion can be virtually regarded as a spectator. Clearly, under these conditions the momentum **p** of the bound electron to be ionized in the (e,2e) reaction is equal in magnitude but opposite in sign to the ion recoil momentum **q**.

[2.3b] $\mathbf{p} = \mathbf{p}_2 - (\mathbf{p}_0 - \mathbf{p}_1)$,

[2.3c] $p = \{[2p_1\cos\theta_1 - p_0]^2 + [2p_1\sin\theta_1\sin(\phi/2)]^2\}^{1/2}$,

where $\phi = \pi-(\phi_1-\phi_2)$. The symmetric noncoplanar scattering kinematics ($p_1=p_2$, $\theta_1=\theta_2=45°$ and ϕ variable) [MW76a, M80] used in the present work and the definitions of the solid angles used in equation 2.3c are given in figure 2.1. Under the symmetric noncoplanar scattering kinematic conditions, the magnitude of the momentum p can be effectively sampled by varying the relative azimuthal angle ϕ.

2.1.2 Differential Cross Section

Consider an (e,2e) reaction on a system with N electrons in its electronic ground state (whose wavefunction is denoted by Ψ_O^N) which leaves a final ion in an electronic eigenstate (denoted by Ψ_F^{N-1}). The (e,2e) differential cross section[2] $\sigma_F(\mathbf{p}_0,\mathbf{p}_1,\mathbf{p}_2)$ is proportional to the absolute square of the reaction amplitude $M_F(\mathbf{p}_0,\mathbf{p}_1,\mathbf{p}_2)$. In atomic units ($\hbar=m_e=e=1$) the (e,2e) differential cross section can be written as [MW76a, M80]:

---

[2] The (e,2e) differential cross section used here is also referred to as the triple differential cross section $d^3\sigma/d\Omega_1 d\Omega_2 dE_1$ [ES&69] or as the five fold differential cross section $d^5\sigma/d\Omega_1 d\Omega_2 dE_1$ [MW76a] in the literature. In this thesis the term triple differential cross section is preferred.

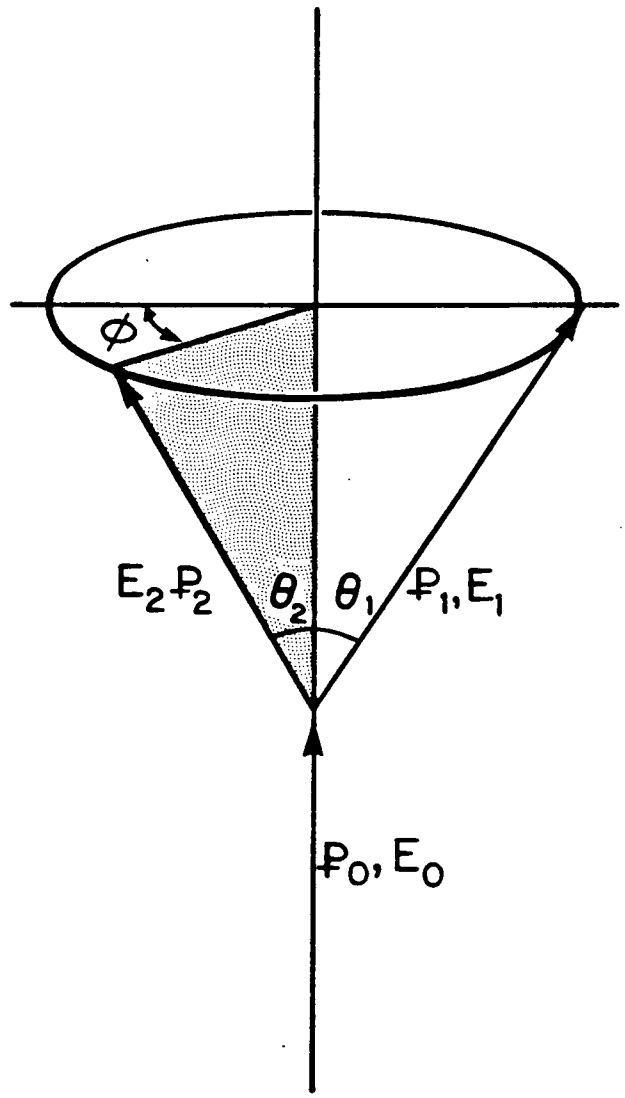

Figure 2.1 - Scattering kinematics of symmetric non-coplanar binary (e,2e) reaction.

$$[2.4] \qquad \sigma_F(p_0,p_1,p_2) = (2\pi)^4 \, \Sigma_{av}(p_1p_2/p_0)|M_F(p_0,p_1,p_2)\,|^2,$$

where Σ_{av} represents an average over the initial degenerate states and a sum over the unresolved final states. The square of the scattering amplitude describes the transition probability of the initial two-body system (the incident electron and the target) to the final three-body system (the scattered electron, the ejected electron and the residual ion).

$$[2.5] \qquad M_F(p_0,p_1,p_2) = \langle \chi_1 \; \chi_2 \; \Psi_F^{N-1} |\; T(E) \; |\Psi_O^N \; \chi_0 \rangle,$$

where the χ's represent the wavefunctions of the incident and outgoing electrons and T(E) represents the transition operator. Antisymmetrization is assumed implicitly.

2.1.3 Plane Wave Impulse Approximation

Under the high energy and maximized momentum transfer kinematic conditions, the incident electron knocks out a target electron in an essentially clean manner. The incident, ejected and scattered electrons interact only very weakly with the residual ion. The (e,2e) collision may then be considered as a close, binary encounter, direct knockout reaction. At sufficiently high energies, the incident and the outgoing electron wavefunctions can then be represented

by plane waves. (The plane wave wavefunction $|\mathbf{p}\rangle$ of an electron of momentum $\mathbf{p}$ is $(2\pi)^{-3/2}\exp(i\mathbf{p}.\mathbf{r})$.) The transition operator T(E) becomes a three-body operator, depending only on the coordinates of the two colliding electrons and the centre of mass of the residual ion, and can be further approximated by the electron-electron scattering operator t(E) [MM65, MW76a, M80]. Under these conditions, the scattering amplitude becomes a product of the anti-symmetrized electron-electron collision amplitude and the overlap amplitude of the target and ion states (in the momentum-space representation). i.e.

$$[2.6] \qquad M_F(\mathbf{p}_0,\mathbf{p}_1,\mathbf{p}_2) = \langle \mathbf{k}'| \; t(E) \; |\mathbf{k}\rangle \; \langle \mathbf{p}\Psi_F^{N-1}|\Psi_O^N\rangle,$$

where $\mathbf{k}'=(\mathbf{p}_1-\mathbf{p}_2)/2$; $\mathbf{k}=(\mathbf{p}_0-\mathbf{p})/2$; and $\mathbf{p}=\mathbf{p}_1+\mathbf{p}_2-\mathbf{p}_0$. The differential cross section, in the plane wave impulse approximation, is therefore given by:

$$[2.7] \qquad \sigma_F(\mathbf{p}_0,\mathbf{p}_1,\mathbf{p}_2) = (2\pi)^4(p_1p_2/p_0)\sigma_{Mott}\Sigma_{av}|\langle \mathbf{p}\Psi_F^{N-1}|\Psi_O^N\rangle \; |^2.$$

The half-off-shell Mott scattering cross section, σ_{Mott}, is given [MW76a] by:

$$[2.8a] \qquad \sigma_{Mott} = |\langle \mathbf{k}'| \; t(E) \; |\mathbf{k}\rangle|^2,$$
$$= (2\pi^2)^{-2}[2\pi a/(\exp(2\pi a)-1)]$$
$$\{1/K^4+1/K'^4-[1/(K^2K'^2)]\cos[a\ln(K^2/K'^2)]\},$$

where $K=|\mathbf{p}_0-\mathbf{p}_1|$; $K'=|\mathbf{p}_0-\mathbf{p}_2|$ and $a=|\mathbf{p}_1-\mathbf{p}_2|^{-1}$. The Mott cross-section varies rapidly with θ and this must be taken into account in the interpretation of the symmetric coplanar measurements [MW76a]. In the noncoplanar symmetric geometry, σ_{Mott} reduces to:

[2.8b] $$\sigma_{Mott} = (2\pi^2)^{-2}\{2\pi A/[\exp(2\pi A)-1]\}(1/K^4),$$

where $A=1/\{2p_1\sin\theta_1\sin[(\pi-\phi)/2]\}$ and $K^2=p_0^2+p_1^2-2p_0p_1\cos\theta_2$. A plot of σ_{Mott} as a function of ϕ corresponding to $E_0=1215.6$eV and $E_1=E_2=600$eV is given in figure 2.2. Clearly for the range of ϕ accessible in the experiment, the Mott cross section is virtually constant (variation over the effective experimental range $\phi=0°$ to $35°$ is less than 2%). Since absolute cross sections are not measured in the present symmetric non-coplanar experiment, the Mott term as well as the constant kinematic factors in equation 2.7 can be ignored.

2.1.4 Target Hartree-Fock Approximation

The only important term in equation 2.7 is the modulus square of the overlap amplitude $\langle \mathbf{p}\Psi_F^{N-1}|\Psi_O^N\rangle$. Here again antisymmetrization is understood implicitly. The ground state of the target wavefunction Ψ_O^N and the fth eigenstate of the ion wavefunction Ψ_F^{N-1} can each be expanded into a set of

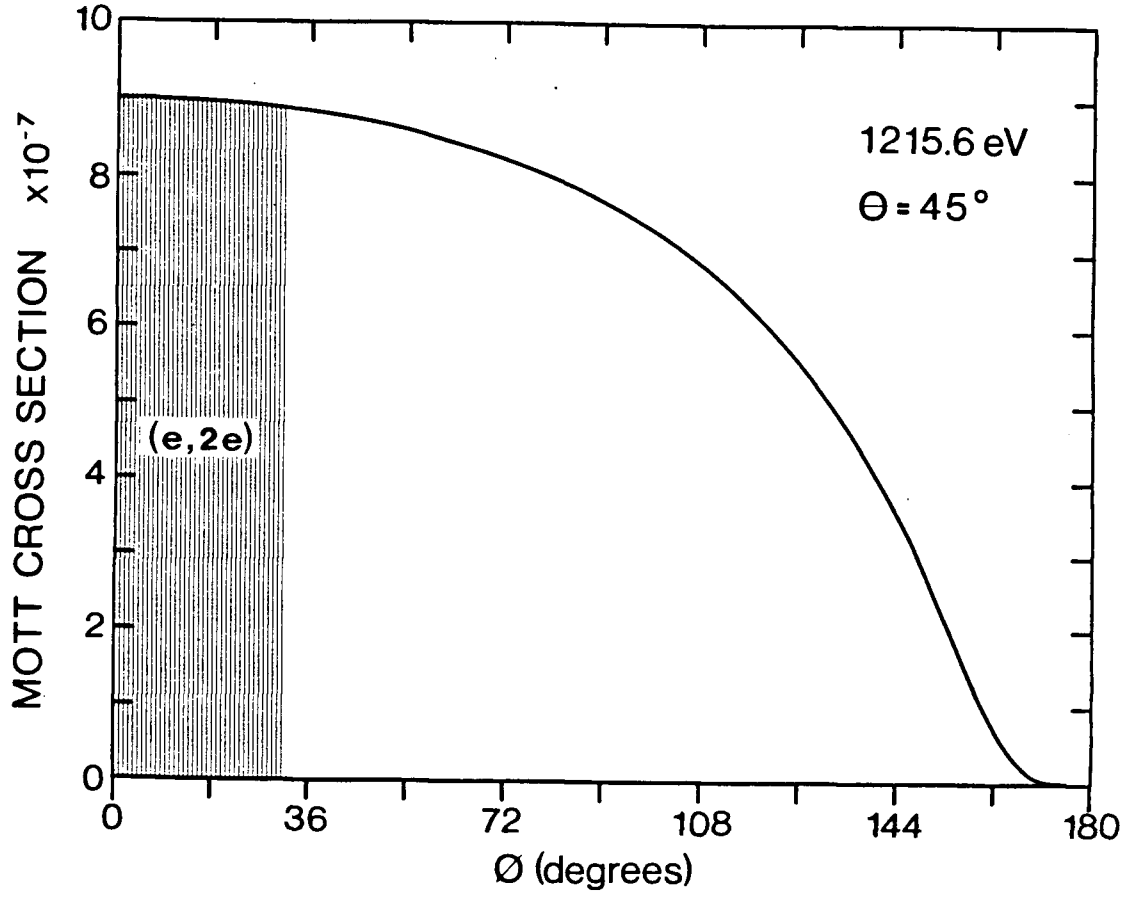

Figure 2.2 - Mott scattering cross section for the symmetric non-coplanar kinematics with E_0=1215.6eV, E_1=E_2=600eV and θ=45°. The normal range of ϕ in the experiment is shown by the shaded area.

configurations, Φ_A.

[2.9] $$|\Psi_O^N> = \Sigma_A\ a_A|\Phi_A>.$$

[2.10] $$|\Psi_F^{N-1}> = \Sigma_B\ t^F_{jB}C_{jsB}\psi_j\dagger|\Phi_B>.$$

The ion wavefunction is regarded as an expansion of a hole orbital, $\psi_j\dagger$, coupled by the Clebsch-Gordon coefficients, C_{jsB}, with a target configuration, Φ_B, to give an ion state of symmetry s. The overlap amplitude then becomes:

[2.11] $$<\mathbf{p}\Psi_F^{N-1}|\Psi_O^N> = \Sigma_{ABj}\ a_A t^F_{jB}C_{jsB}\ <\mathbf{p}|\psi_j><\Phi_B|\Phi_A>.$$

If the same one electron potential is used for the ion as for the target then orthonormality of the configurations gives:

[2.12] $$<\mathbf{p}\Psi_F^{N-1}|\Psi_O^N> = n_s\Sigma_{Aj}\ a_A t^F_{jA}C_{jsA}\ \psi_j(\mathbf{p}),$$

where n_s is the number of equivalent electrons (or the dimension of the symmetry group s). The momentum-space orbital $\psi_j(\mathbf{p})$ is given by the Fourier transform of the position-space orbital $\psi_j(\mathbf{r})$. i.e.

[2.13] $$\psi_j(\mathbf{p}) = (2\pi)^{-3/2}\int d\mathbf{r}\ \exp(-i\mathbf{p}.\mathbf{r})\psi_j(\mathbf{r}).$$

In the special case when the Hartree-Fock ground state Φ_O is a good description of the target state Ψ_O^N, i.e. $a_A \simeq 0$

for A≠0, the overlap amplitude becomes [MW76a]:

$$[2.14a] \qquad \langle p\Psi_F^{N-1}|\Psi_O^N\rangle = n_s^{1/2}\Sigma_j\, a_O t_{jO}^F C_{jsO}\psi_j(p);$$

and for a close-shell target,

$$[2.14b] \qquad \langle p\Psi_F^{N-1}|\Psi_O^N\rangle = n_s^{1/2} a_O \Sigma_j\, t_{jO}^F \psi_j(p).$$

Normally, any set of independent particle orbitals, ψ_j, can be redefined so that for a given ion state $|\Psi_F^{N-1}\rangle$ only one term is sufficient in the sum (equation 2.14b). The associated orbital is called the characteristic orbital, ψ_c, so that:

$$[2.15] \qquad \langle p\Psi_F^{N-1}|\Psi_O^N\rangle = n_s^{1/2} a_O t_{cO}^F \psi_c(p).$$

The final expression in the plane wave impulse and target Hartree-Fock approximations for the differential cross section is given by:

$$[2.16] \qquad \sigma_F(p_0,p_1,p_2) = (2\pi)^4(p_1p_2/p_0)\sigma_{Mott} \{[n_s(a_O)^2 S_{cO}^F]\ \Sigma_{av}|\psi_j(p)|^2\}.$$

The spectroscopic factor $S_{cO}^F=(t_{cO}^F)^2$ can be regarded as the probability that the f^{th} ion state contains the configuration with a hole orbital $\psi_c\dagger$ in the target. The differential

cross section is therefore simply proportional to $\Sigma_{av}|\psi_c(\mathbf{p})|^2$. In the Born-Oppenheimer approximation, a molecular wavefunction is a product of separate electronic, vibrational and rotational functions. In cases where the final rotational and vibrational states cannot be resolved, the wavefunction must be integrated over the rotational and the vibrational states. The differential cross section is given by:

$$[2.17] \qquad \sigma_F(\mathbf{p}_0,\mathbf{p}_1,\mathbf{p}_2) \propto \int d\Omega \int d\nu |\psi_c(\mathbf{p})|^2.$$

The vibrational integral $\int d\nu$ has been shown to be accurately approximated by assuming the nuclei are fixed in their equilibrium positions [DM&75, MW76a].

The differential cross section, in the plane wave impulse and target Hartree-Fock approximations, is therefore proportional to the spherically averaged modulus square of the characteristic orbital in the momentum-space representation. i.e.

$$[2.18] \qquad \sigma_F(\mathbf{p}_0,\mathbf{p}_1,\mathbf{p}_2) \propto \int d\Omega |\psi_c(\mathbf{p})|^2.$$

2.1.5 Validities Of The Approximations

The final expression of the (e,2e) (or triple) differential cross section (equation 2.16) depends on the validities of the plane wave impulse approximation (PWIA) and the target Hartree-Fock approximation (THFA). The PWIA requires scattering kinematics with high momentum transfer and high energy. The noncoplanar symmetric scattering kinematics ensures maximized momentum transfer. Earlier works [HM&73, HM&74, WHM75] on the PWIA have demonstrated its essential validity for incident energies $E_0 \geq$ 400eV. Although the use of the more sophisticated scattering approximations such as the distorted wave impulse approximation (DWIA) [UWM75, CG&78, FM&78, GF&80] and the averaged eikonal approximation (EA) [FM&78, SCG79, CG&80, GF&80] has provided significant improvement in the prediction of the shape of the angular correlation in coplanar (e,2e) studies, no obvious differences can be found in noncoplanar experiments, except in the high p region ($p \geq 1.5 a_0^{-1}$) [DM&78, BH&80, BM&82]. It has, however, been suggested [MW76a, MW83] that in order for the PWIA to predict the correct s-to-p intensity ratio (when all the correlation satellite states are considered), an incident energy $E_0 \geq$1200eV is necessary. The use of higher incident energy also imposes more demanding requirements on the performance of the binary (e,2e) spectrometer. At higher incident energies the (e,2e) cross-section decreases but the smaller range of ϕ (for a given range of p) results in

improvement in statistics due to a lower relative accidental coincidence rate. The smaller ϕ range, however, also necessitates a smaller acceptance angle as well as better designed optics for the angular selection (see chapter 3) in order to maintain sufficient angular (or momentum) resolution. A smaller acceptance angle will undoubtedly cut down the count rate. All (e,2e) works reported in this thesis are carried out with E_0 equal to 1200eV plus the binding energy. The presently used incident energy appears to be a good compromise.

The target Hartree-Fock approximation (THFA) defines a unique set of orbitals (the canonical ones) apart from a unitary transformation. The Hartree-Fock orbitals for the ion ground state are in general not exactly the same as for the ion excited states or for the target (i.e. neutral) ground state. The overlap amplitude has been calculated in some cases [BS&74] and is found to be over 90% for valence orbitals. This orthogonality problem is "eliminated" in the THFA by defining all single-particle orbitals to be those of the target ground state (see equation 2.12). Such a treatment has been found to be essentially adequate (for the outer valence orbitals) in most of the (e,2e) studies to date. In the case where electron correlation effects are important [MU&74, DHW78], the more general expression (equation 2.11) must be used. Moreover, the ion wavefunction (equation 2.10) must be expanded to include 2-particle-1-

hole, 3-particle-2-hole, etc. processes. In this case, the interpretation of the cross section will be complex [MW76a]. The resulting momentum distribution contains an admixture of orbital momentum densities and is not characteristic of any single orbital. The weighting coefficients will depend upon whether initial or final state configurational interactions (or both) are important.

2.2 MOMENTUM-SPACE LCAO-MO WAVEFUNCTIONS

Theoretical quantum chemistry [PCR73, LCG77, C82, LP83] has almost totally relied upon the position representation to formulate problems in atomic and molecular structure. The momentum representation, although being an equivalent representation in atomic and molecular problems, is generally believed to lead to greater mathematical difficulties. Although there have been some attempts [PP29, F35, L50, L82] to use momentum-space wavefunctions directly, these works have been limited to some simple atomic systems mainly because of the complexities involved in solving the integral equation of motion in momentum-space, which corresponds to the (differential) Schrodinger equation in position-space. A more practical way of obtaining the momentum-space wavefunction is therefore to first solve the quantum mechanical problem in the more usual position-space and then apply the Fourier transform to the solution to obtain the

momentum-space wavefunction [PP29].

In table 2.1, a summary of the basic equations of a molecular wavefunction in the LCAO-MO formalism written in position and momentum representations is given. The momentum-space wavefunction is obtained by Fourier transformation as mentioned above. (See equation 2.13.) Detailed derivations of these equations can be found in refs. [E71, L72b, LN&75, KT76, MW76a, KS77, CB82a]. It is obvious from table 2.1 that the Fourier transform preserves the general LCAO-MO formalism; i.e. a position-space LCAO molecular wavefunction can be expressed in momentum-space again as a linear combination of momentum-space atomic wavefunctions. The major difference is the introduction of a phase factor (which depends on the nuclear positions $\mathbf{R}_a$) into the complex molecular orbital (MO) coefficients.

There are many interesting relations between the position-space density and the corresponding momentum-space density. These relations are useful in unravelling the origins of many structures in the experimental momentum distributions and in the theoretical molecular momentum density topography, namely, density [CS&79, CB82b] and density difference [HC68] maps. Many of the momentum-space notions first discussed by Coulson and Duncanson [CD41] in the early 40's and later extended by Epstein *et al.* [E73, E75, ET77] are indeed centred upon Fourier transform (FT) properties. Recently the momentum-space properties of atoms

Table 2.1
Summary of LCAO MO wavefunction and density equations in position and momentum space.

Wavefunction		Position space[a]	Momemtum space[a]	Comment
(I)	molecular orbital	$\psi_m(\underline{r})=\sum_a C_{ma}\phi_a(\underline{r})$	$\psi_m(\underline{p})=\sum_a C_{ma}\exp(-i\underline{p}\cdot\underline{R}_a)\phi_a(\underline{p})$	LCAO MO formalism ψ_m-MO ϕ_a-AO
(II)	atomic function	$\phi_a(\underline{r})=\sum_{i=1}^{n_a} b_i\chi_{ai}(\underline{r}-\underline{R}_a)$	$\phi_a(\underline{p})=\sum_{i=1}^{n_a} b_i\chi_{ai}(\underline{p})$	AO is again a linear combination of basis function with correct symmetry
(III)	basis function	$\chi_{ai}(\underline{r}_a)=N_{n_i l_i m_i}R_{n_i l_i}(r_a)Y_{l_i m_i}(\Omega)$ where $\underline{r}_a=\underline{r}-\underline{R}_a$; $r_a=\lvert\underline{r}-\underline{R}_a\rvert$	$\chi_{ai}(\underline{p})=N_{n_i l_i m_i}P_{n_i l_i}(p)Y_{l_i m_i}(\Omega)$	angular part of the basis function is the same in both r-space and p-space
(IV)	radial part	$R_{n_i l_i}(r_a)$: STF,GTF,etc.	$P_{n_i l_i}(p)=(2/\pi)^{1/2}(-i)^{l_i}$ $\int r_a^2 dr_a j_{l_i}(pr_a)R_{n_i l_i}(r_a)$	for $P_{n_i l_i}(p)$ see ref. [KS77]. Note that j_{l_i} is the spherical Bessel function
(V)	density	$\rho_m(\underline{r})=\phi_m^*(\underline{r})\phi_m(\underline{r})$ $=\rho_m^{QC}(\underline{r})+\rho_m^{I}(\underline{r})$	$\rho_m(\underline{p})=\phi_m^*(\underline{p})\phi_m(\underline{p})$ $=\rho_m^{QC}(\underline{p})+\rho_m^{I}(\underline{p})$	orbital density decomposition
(VI)	quasi-classical part	$\rho_m^{QC}(\underline{r})=\sum_a\lvert C_{ma}\rvert^2\lvert\phi_a(\underline{r}-\underline{R}_a)\rvert^2$	$\rho_m^{QC}(\underline{p})=\sum_a\lvert C_{ma}\rvert^2\lvert\phi_a(\underline{p})\rvert^2$	one-centre part
(VII)	interaction	$\rho_m^{I}(r)=\sum_{a\neq b} C_{ma}^*C_{mb}\phi_a^*(\underline{r}-\underline{R}_a)\phi_b(\underline{r}-\underline{R}_b)$	$\rho_m^{I}(p)=\sum_{a\neq b} C_{ma}^*C_{mb}\exp[-i\underline{p}\cdot(\underline{R}_b-\underline{R}_a)]$ $\phi_a^*(\underline{p})\phi_b(\underline{p})$	two-centre part

[a] $\underline{r}$ and $\underline{p}$ correspond to the position and momentum of the electron respectively. $\underline{R}_i$ refers to the equilibrium position of the atomic centre i.

have also been examined by Smith and co-workers [HS&83, SWS84]. Briefly, there are four major FT momentum-space concepts: (i) symmetry invariance with an automatic inversion centre at the p-space origin; (ii) inverse spatial reversal; (iii) p-space molecular density directional reversal; and (iv) p-space molecular density oscillation. Extensive discussions of these have been given in the literature [CD41, ET77, CB82a, CB82b, MB&83, LB83b]; only a brief summary will therefore be given here. In addition, another important property (first discussed by Epstein and Tanner [ET77]), which is a direct consequence of the Virial theorem, will also be mentioned. This Virial property is found to be useful in discussing features in density difference (or bond density) maps [HC68, LB83b] of the two electron systems (see chapters 5 and 6).

2.2.1 Fourier Transform Properties

The momentum-space wavefunction is obtained by the Fourier transform of the position-space wavefunction (equation 2.13). Before discussing the individual Fourier transform properties, it is important to have a closer look at the Fourier transform itself. By writing $\exp(-i\mathbf{p}.\mathbf{r})$ in a power series expansion and replacing $\mathbf{p}$ with its corresponding (position-space) operator form ∇_r, the following relation is obtained,

$$[2.19] \qquad \psi_j(\mathbf{p}) = (2\pi)^{-3/2} \int d\mathbf{r} \left(1 - i(\nabla_r . \mathbf{r}) - \tfrac{1}{2}(\nabla_r . \mathbf{r})^2 + \ldots\right) \psi_j(\mathbf{r}).$$

The momentum-space (p-space) wavefunction involves an integral of the sum of powers of the gradient of the position-space (r-space) wavefunction over all space. In the case of atomic orbitals where large changes in the r-space wavefunction occur only near the nucleus, the small r part of the r-space wavefunction contributes most significantly to the large p part of the p-space wavefunction (the inverse spatial reversal). In the case of molecular orbitals, however, the spatial reversal relation, although still qualitatively correct, must be applied with caution since any region where there is a rapid change in the r-space wavefunction will contribute significantly to the high p part of the p-space wavefunction. Such rapid change can occur between atomic centres, for instance across a nodal plane. A notable example of this is the CO_2 ($1\pi_g$) orbital [CB82b, LB84b] (chapter 7). It should be noted that this physical association of the gradient of the r-space wavefunction with the p-space wavefunction is also helpful in rationalizing the p-space molecular density directional reversal property. The longitudinal change across any r-space density lobe is obviously less rapid (small p part) than changes in the other perpendicular direction (large p part). The corresponding directional properties of the p-space density lobe will be reversed.

(i) Symmetry, P-space Origin, And P-space Virtual Boundary.

All symmetry properties of the position-space wavefunctions are preserved under the Fourier transform. This is evident from equation (III) in table 2.1 which indicates that the spherical harmonics (which determine the angular dependence of the atomic orbitals) are invariant under the transformation. In addition the momentum-space wavefunction has inversion symmetry (i.e. the electron has no net translational motion in the centre-of-mass frame). This inversion symmetry is again obvious from table 2.1 and is the result of the phase shift in the MO coefficients. One important difference between the r-space and p-space LCAO-MO formalisms is in the different ways of expressing the localities of the density function. In r-space these localities are expressed by referencing electrons to their own atomic centres, i.e., $\mathbf{r}_a$. In p-space, however, these direct references are lost (i.e. there are no nuclear positions in p-space) and the nuclear position vectors ($\mathbf{R}_a$) introduce an extra phase into the MO coefficients (equation (I), table 2.1). The resulting momentum density function has inversion symmetry in p-space because of the linear combination of the symmetric (with respect to inversion) p-space atomic orbital density functions. However, the nuclear geometry information is not lost but is retained in the interference term. The inversion symmetry in p-space can also be regarded as a direct manifestation of the invariance

of the SCF wavefunction under time reversal operation.

Since electrons experience sharp attractive potentials near the nuclear centres (thus increasing their momenta) the nuclear centres in r-space act, by cosmological analogy, like "black holes", i.e. increasing the momentum as the electrons fall towards them and causing the corresponding p-space density to inflate outward towards the p-space virtual boundary at $\mathbf{p}=\infty$ (which corresponds to the electron momenta at the nuclei). The p-space origin, on the other hand, can be thought of as being like a cosmological "white hole" since the electrons with zero momentum (i.e. free electrons) are being pushed out into the more attractive high momentum region near the nuclear centres. The low momentum regime corresponds in r-space to the chemically important valence region. One can therefore picture the effect of the Fourier transform as "turning the wavefunction inside out", without changing the symmetry properties, by inflating the chemically less interesting core (inner r-space) region (around each nuclear centre) towards the p-space virtual boundary and collapsing the chemically significant valence (outer r-space) region towards the p-space origin, where the binary (e,2e) technique is most sensitive. The binary (e,2e) method therefore provides a new and unique vantage point from which to view the most chemically significant part of the molecular wavefunction in chemical bonding phenomena.

(ii) Inverse Spatial Reversal.

In addition to the inversion symmetry in momentum-space orbitals, there is also amplitude inversion, namely, contraction of the r-space wavefunction corresponds to expansion of the p-space wavefunction and vice versa. This inverse spatial reversal arises from the pr_a dependence of the spherical Bessel function in equation (IV), table 2.1. This property has been demonstrated in many earlier works [CD41, ET77, CB82a, CB82b, LB83b] and is well illustrated in the study of noble gases using binary (e,2e) spectroscopy [LB83a] (chapter 4). The property can be readily explained using the Heisenberg uncertainty principle, namely, a more localized r-space wavefunction with a small spatial uncertainty Δr will result in a large p-space uncertainty Δp, i.e. a more diffuse p-space wavefunction.

(iii) Molecular Density Directional Reversal.

The relative longitudinal and transverse spatial extensions of lobes in an orbital in r-space are interchanged in p-space and vice versa [CD41, ET77, BC&82, CB82a, CB82b, MB&83, LB83b]. For instance, in the sigma bonding orbital of a diatomic molecule, the bonding density is directed along the internuclear axis in r-space (the longitudinal direction) whereas the momentum density of such a bonding orbital is oriented in the transverse direction, i.e. perpendicular to the internuclear direction. Similar concepts can be used to

draft out the directions of lobes in an antibonding orbital. In essence, the density directional reversal property is a combined effect of the symmetry property and the inverse spatial reversal property applied specifically to molecular orbitals.

(iv) Molecular Density Oscillations.

The molecular momentum density of a bonding (antibonding) orbital exhibits cosinusoidal (sinusoidal) modulations with spatial p periodicity of $2\pi/|\mathbf{R}_b-\mathbf{R}_a|$ in the bond-parallel direction [CD41, ET77, CB82a, CB82b, LB83b]. This is a direct consequence of the phase factor introduced by the Fourier transform in the p-space LCAO-MO formalism. The modulation effects come from the complex coefficient product term, $C^*_{ma}C_{mb}\exp(-i\mathbf{p}.(\mathbf{R}_b-\mathbf{R}_a))$, in the interference density $\rho^I_m(\mathbf{p})$ in equation (VII), table 2.1. The periodicity is determined by the $\mathbf{p}.(\mathbf{R}_b-\mathbf{R}_a)$ term and the relative sign of the product of MO coefficients $C^*_{ma}C_{mb}$. (Note that C_{ma} and C_{mb} for an antibonding sigma orbital are opposite in sign, which introduces an extra 90° phase shift.) The significance of the oscillations is that in principle the relative nuclear separations can be inferred from the p-space periodicities.

2.2.2 Virial Property

The formation of a chemical bond is accompanied by an increase in the average momentum <p> [CD41, ET77] by transferring momentum density at the p-space origin into the high momentum region in the transverse direction. This is a direct result of the Virial theorem (for diatomic molecules in the Born-Oppenheimer approximation):

[2.20] $2\langle T\rangle + \langle V\rangle + R\,dE/dR = 0$

where E, T and V are respectively the total, kinetic and potential energies and R is the internuclear separation. For a system in its equilibrium nuclear geometry, one has the special case where the average potential energy is the negative of twice the kinetic energy, i.e. $\langle V\rangle=-2\langle T\rangle$. Hence any process which lowers the total energy (noting that $\langle E\rangle=-\langle T\rangle$) will raise the average momentum <p> since $\langle T\rangle=\frac{1}{2}\langle p^2\rangle$. This therefore produces a general redistribution of the momentum density into the high momentum region. The direction of such density redistribution is of course governed by the Fourier transform properties mentioned above. Interestingly, this property leads to a redrawing of the binding and antibinding boundaries in p-space and also a somewhat different bonding concept in momentum-space. This property will be discussed further using density difference maps (chapters 5 and 6).

Chapter III

EXPERIMENTAL METHOD

3.1 INTRODUCTION

The first generation version of the U.B.C. binary (e,2e) spectrometer has been described by Hood *et al*. [HHB77] and in further detail by Cook [C80]. The present (second generation) version of the binary (e,2e) spectrometer is modified from the original [HHB77, C80] to provide major improvements in momentum and timing resolutions as well as in significantly better signal-to-noise ratio. It operates at a significantly higher incident electron energy (>1200eV) than that used in the first generation spectrometer (>400eV) so as to ensure the validity of the reaction approximation (i.e. plane wave impulse approximation) [MW76a]. It is also under the control of a dedicated computer system, which allows sequential data collection and automatic data normalization. The present instrumentation represents a state-of-the-art binary (e,2e) spectrometer, which operates routinely with high momentum and timing resolutions, for the investigation of orbital momentum densities and the electronic structure of atoms and molecules. It is only potentially inferior in terms of data collection efficiency to the multichannel plate version that is presently under

development by Weigold and coworkers [CM&84] at Flinders University.

The binary (e,2e) spectro-system can be divided into three major integrated sub-systems, namely the spectrometer itself, the associated control electronics and an executive microcomputer. A simplified block diagram outlining the basic components of the sub-systems is shown in figure 3.1. The spectrometer consists of one primary electron optical system (PEOS) and two identical secondary electron optical systems (SEOSs). The PEOS provides a finely focussed incident electron beam for the high energy electron impact ionization of the gaseous targets. The SEOSs then momentum analyse the outgoing electrons after the (e,2e) reaction under the symmetric noncoplanar scattering conditions. The control electronics supply the power to the various optical components in the spectrometer and provide the actual scan voltages for the experimental parameters: E_0 and ϕ. The coincidence circuitry registers any coincident occurrence of pulses arising from the two SEOSs. The microcomputer system performs executive functions such as time-averaging the collected data and controlling the scan sequence for the real-time data acquisition. Once various voltages of individual electron optical elements have been optimized both in terms of resolution and count rate, the operator only needs to input the gaseous targets of interest into the spectrometer, set up the necessary scan sequences for the

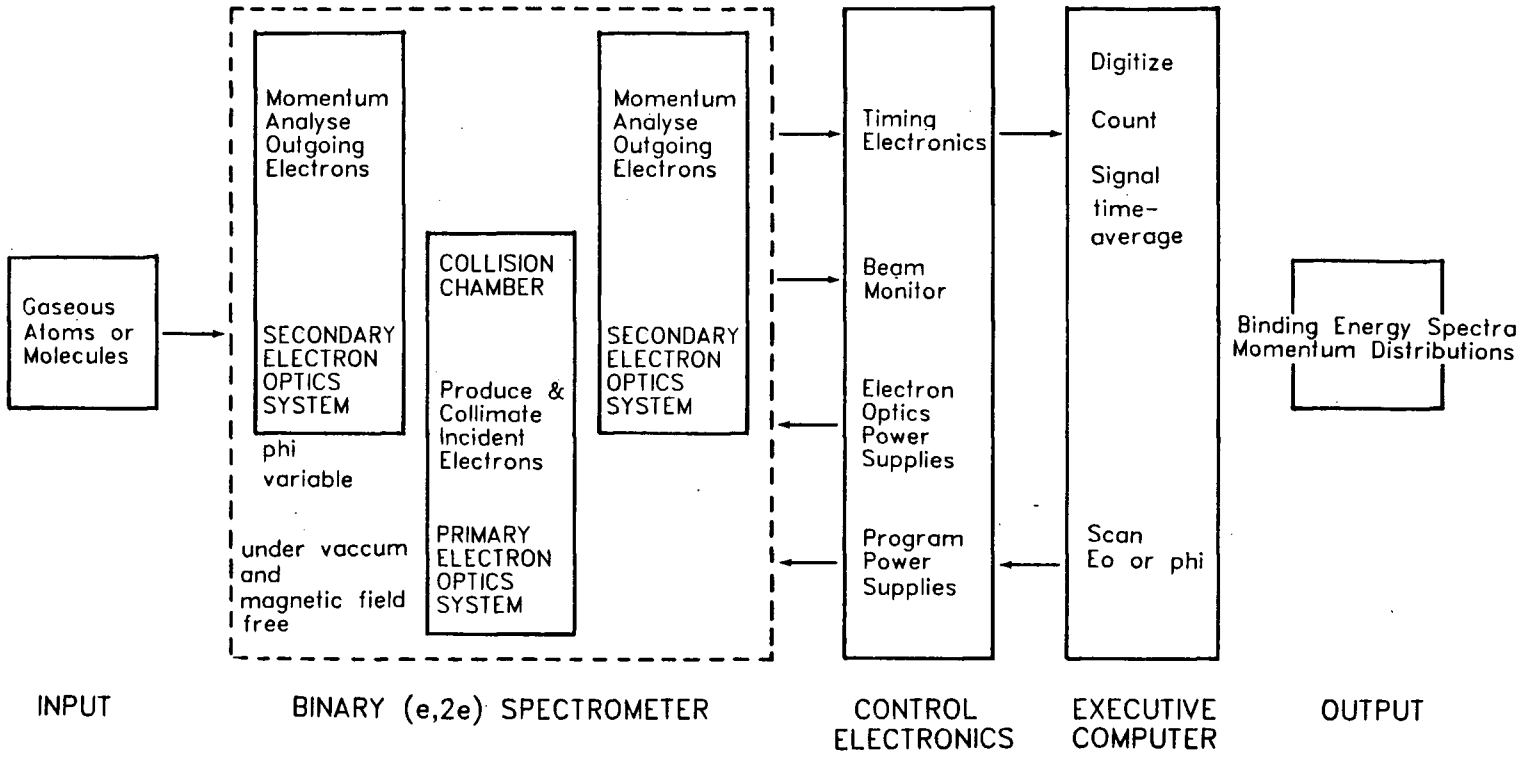

Figure 3.1 - Block diagram of the binary (e,2e) spectrosystem.

microcomputer and allow sufficient time for the spectra to accumulate. The present instrumentation requires a minimal amount of attention and servicing from the operator for the often time consuming data collection process. Detailed discussions of each of the major components in the binary (e,2e) spectro-system are given in the following sections.

3.2 BINARY (e,2e) SPECTROMETER

A schematic diagram of the binary (e,2e) spectrometer is given in figure 3.2. The spectrometer is composed of a primary electron optical system (PEOS) and two identical secondary electron optical systems (SEOSs), controlling the kinematics of the incident electron beam and the outgoing electron beams respectively. The PEOS consists of an electron gun (EG), a gas cell (GC) and an electron beam collimator. The SEOS each consists of a three-element asymmetric immersion lens (AIL), a 135° sector cylindrical mirror analyser (CMA) and a single channel electron multiplier (CEM). One of the SEOSs is stationary while the other is mounted on a rotatable turntable (RT) driven by a servo-motor (SM) outside the vacuum chamber, which allows the relative azimuthal angle ϕ to be varied.

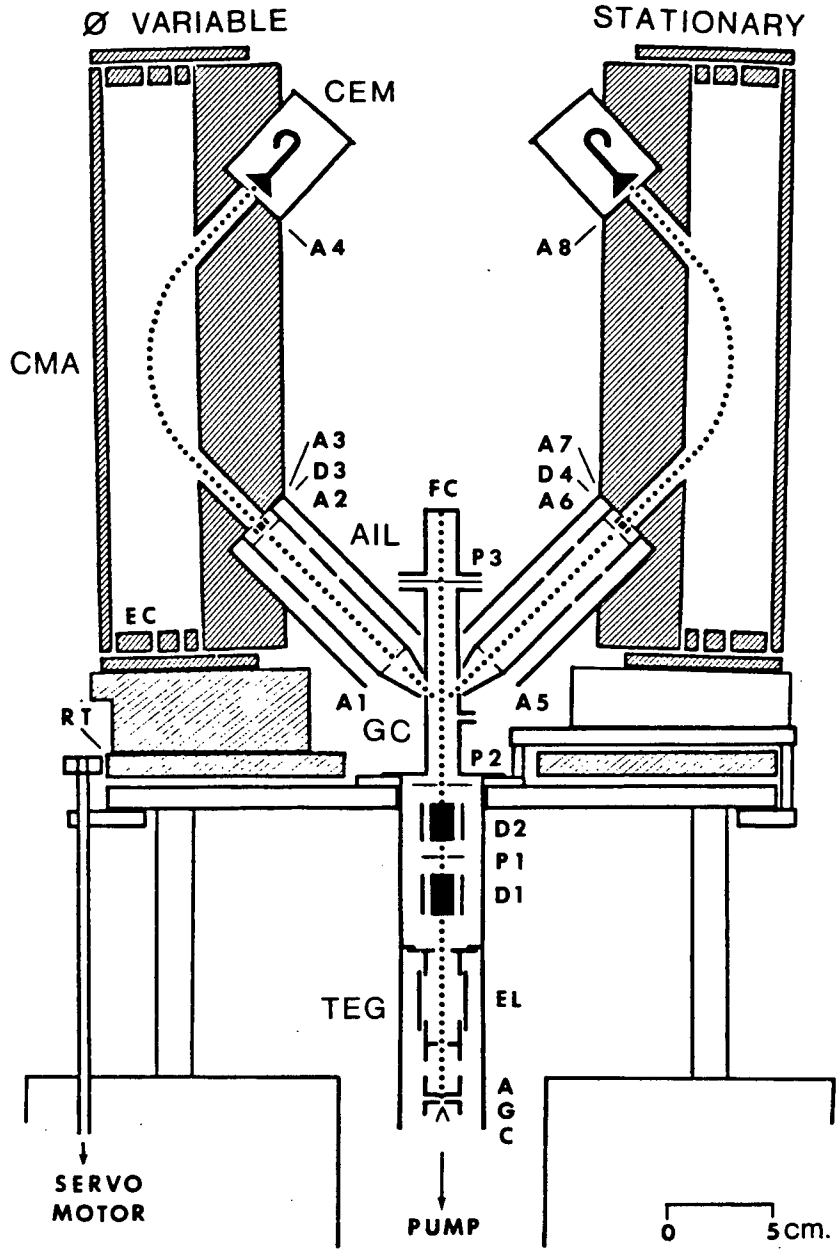

Figure 3.2 - Schematic of binary (e,2e) spectrometer. Legend: CEM - Channel Electron Multiplier, CMA - Cylinder Mirror Analyser, AIL - Asymmetric Immersion Lens, GC - Gas Cell, EG - Electron Gun; EL - Einzel Lens, A - Anode, G - Grid, C - Cathode, FC - Faraday Cup, EC - End Corrector, RT - Rotatable Turntable; A1 to A8 - Apertures, P1 to P3 - Spray Plates, D1 to D4 - Deflectors.

3.2.1 Electron Gun

The incident electrons are produced by thermionic emission using a commercial intermediate energy (100-2000eV) electron gun (Cliftronics CE5AH). It consists of a three-element cathode lens and a three-element einzel lens. The three-element cathode lens [D55, M67, G72] represents the simplest version of a thermionic source and consists of an emissive cathode (C), a focussing control grid (G) and an accelerating anode (A). In the present arrangement, the cathode is made of a thoriated tungsten filament (Goodfellow metal, W/Th 0.6%, 0.125mm dia.) and is bent into a V-shaped hairpin. The filament is electrically heated by a DC current of 2.2-2.6Amps. with a nominal operating filament temperature of 1700-1900K. When the electrons are released from the metal, they are almost stationary with an energy spread of 0.2-0.8eV. The nominal life-time of a filament operating under this condition and a 10^{-3} Torr pressure of inert gases is 50-80 days. These electrons can be extracted by an accelerating potential (usually a few hundred eV) between the filament and the anode. Focussing of the electrons is achieved by applying a small potential to the grid of opposite polarity with respect to that of the accelerating (anode) potential. Because the grid is so close to the filament where the electrons are moving slowly, a slight variation in the grid potential can significantly alter both the shape and the gradient of the local potential

distribution near the cathode. This critically affects both the intensity and the focus of the produced electron beam. Such a local potential distribution is determined primarily by three parameters: the cathode-grid separation, the aperture size of the grid and the grid potential. The optimized cathode-grid separation (obtained by trial-and-error) for the V-shaped filament is 0.25-0.40mm.

The quality of an electron gun is usually rated by the brightness[1] and the divergence of the produced electron beam. The brightness R can be written [G72] as:

$$[3.1] \qquad R \propto (jV)/T,$$

where j is the current density at the filament, V is the accelerating potential in electron volts and T is the filament temperature. It is clear that the brightness can be increased by applying either a higher accelerating potential or a larger current through the filament. It should be noted, however, that a larger applied current will have the adverse effect of increasing the operating temperature, which will not only decrease the brightness but also cause a faster burn-out rate (i.e. a shorter life-time). Beam divergence can be minimized by physically limiting the emitting surface area so that the emitted electrons all travel closely

---

[1] Brightness is defined as the beam current per unit area per unit solid angle.

parallel to the mean beam direction. The use of a V-shaped filament to give a fine point has proven to produce an electron beam with a smaller divergence [M67]. Beam divergence can be further controlled by using a supplemental three-element einzel lens (EL) [AR72a]. The two outer elements of the lens are at the same potential (ground). Only the potential of the central element is varied to produce the focussing action. As the electron passes through the lens, it is first decelerated (or accelerated) from the outer potential to the central potential and then accelerated (or decelerated) back to the outer potential. The kinetic energy of an electron exiting the anode is therefore unaffected by the einzel lens (i.e. no retardation or acceleration). Only focussing of the electron beam is obtained with the einzel lens.

3.2.2 Gas Cell

The electron beam produced by the electron gun (EG) must be aligned with the axis of the gas cell (GC) using an electron beam collimator to correct for any small physical misalignment between the electron gun and the gas cell as well as to compensate for any beam distortion caused by residual magnetic field (see section 3.2.8). The gas cell is a brass cylinder (15.9mm o.d.) enclosed at the bottom and the top by two spray plates: P2 and P3 respectively. Annular

slots in the gas cell allow the passage of the outgoing electrons into the secondary electron optical systems. Sliding brass shims are attached to the sides of the movable lens cone (see later) to blind off any open areas not covered by the lens cones. Gas is admitted into the gas cell through a small hole (1mm dia.) in the gas cell. The present semi-enclosed arrangement allows the "local" dynamic gas pressure inside the gas cell to be at least two orders of magnitude higher than the ambient vacuum chamber pressure. The direction of the incident electron beam is defined by the aperture sizes of the spray plates P2 (2.5mm dia.) and P3 (1.5mm dia.). These defining apertures are mechanically aligned to unambiguously define the axis of the gas cell. The maximum geometrical entrance half-angle (with respect to the axis of the gas cell) for an electron to pass through both P2 and P3 is approximately ±1.3°.

3.2.3 Beam Collimator

The beam collimator consists of two sets of quadrupole deflectors (D1, D2), a set of three spray plates (P1, P2, P3) and a Faraday cup (FC). The spray plates as well as the Faraday cup are joined to separate micro-ammeters to monitor the collected current at each point of the incident beam path independently. Beam collimation is achieved by manipulating the voltages of the deflector elements of the quadrupole

deflectors to minimize the current collected by the spray plates (P1, P2 and P3) and to simultaneously maximize the current collected by the Faraday cup (FC). In practice both the grid voltage and the focus voltage (central voltage of the three-element einzel lens) of the electron gun are also adjusted during the beam collimation process. Typically a current of 50μA is collected at the Faraday cup for a 1200eV incident beam energy. The nominal current (in μA) ratio for FC:P3:P2:P1 in this case is 50:1:1:0.1. It should be noted that it is extremely important to have a well aligned incident electron beam since the polar angles of the outgoing electron beams are dependent on the incident beam direction. Moreover, an off-axis incident beam will cause variation of the singles count rate with the relative azimuthal angle ϕ because of the change in volume of the effective collision space. This will result in spurious variations in the intensity of the measured momentum distribution.

3.2.4 Three-element Asymmetric Immersion Lens

The scattered and ejected electrons (after the (e,2e) reaction) emerge from the gas cell each with a kinetic energy of $\frac{1}{2}$(E_0-binding energy), where E_0 is the incident electron energy. In the present case, these outgoing electrons have kinetic energies of 600eV for an incident electron energy of E_0>1200eV. A three-element asymmetric immersion lens (AIL)

is used to retard the outgoing electrons so that a lower pass energy[2] of the electron energy analyser can be used in order to improve the energy resolution. A second function of the AIL is to transport and focus the emerging electrons from the collision centre (in the gas cell) to the entrance aperture of the energy analyser. In the present application, the three-element AIL focusses and retards the outgoing electrons from 600eV to 100eV, which is the normal pass energy of the analyser.

A simple three-element asymmetric immersion lens (AIL) [H69, HK70, AR72b, HR76, R78] requires seven geometrical specifications, i.e. 3 wall-thicknesses, 2 element spacings and 2 aperture sizes, each with respect to the third aperture size. The relevant geometrical parameters of the three-element electrostatic cylindrical lens are given in figure 3.2 (see also figure 3.4). All the focal properties of the three-element AIL are determined by two voltage ratio parameters: V3/V1 and V2/V1, where V1, V2 and V3 are the applied voltages of the entrance, central and exit elements of the AIL respectively. Using the voltage ratio V2/V1 to control the focussing properties and the other V3/V1 to change the energy of the image, it is possible to keep the image distance fixed for a chosen object distance even when

---

[2] The pass energy of an electron analyser is commonly used to refer to the mean entrance kinetic energy of an electron beam being transported from the entrance to the exit of the electron energy analyser.

the energy of the image is varied. This "zooming" property is important in the present application if a different retardation ratio (i.e. V1/V3) is desired because the object to image separation is physically fixed in the spectrometer. The relations between the object to image distances for a particular lens system are shown by the corresponding P-Q curves [HR76] for various voltage ratios V2/V1 and magnifications.

The three-element AIL used in the present application has been constructed using a unique design. The cylinders used for the lens stacks are made of brass and are accurately aligned using hidden teflon tube spacers. Teflon rings are used for providing the important spacings between lens elements. Two angular selection plates with defining apertures A1 (A5) and A2 (A6) are used to physically limit the geometrical acceptance angle of the lens. In the present arrangement, the defining apertures A1 (A5) and A2 (A6) are 2.0mm dia. and 1.0mm dia. respectively. The maximum geometrical acceptance half-angle of the lens is therefore ±0.8° with respect to the axis of the lens. A set of X-Y parallel plates electrostatic deflectors D3 (D4) [G72] are used to make minor correction to the entrance angle of the energy analyser *after* the angular selection. The aperture A3 (A7) corresponds to the ideal image plane of the lens and is at the co-axis of the cylindrical mirror analyser (section 3.2.5). The complete lens assembly is carefully mounted on

the inner element of the 135°-sector cylindrical mirror analyser (CMA) at an inclination angle of 42.3°. The 42.3° inclination angle is used to take advantage of the second order axis-to-axis focussing effect of the CMA [R72] (section 3.2.5). The polar angle θ is defined mechanically to be the angle between the axis of the gas cell and the axis of the AIL. This angle (45°) is accurately achieved by mounting the complete CMA and lens assembly on to a 2.7° sloping slab. The thickness of the slab is precisely constructed so that the axes of the two lenses intercept with the axis of the gas cell. The CMA assembly and the slab are then positioned accurately onto the supporting plate using dowell pins.

3.2.5 Sector Cylindrical Mirror Analyser

Any pair of electrodes which create an electrostatic field acting transversely to the electron instantaneous velocity give the effect of an electrostatic prism [EE70, G72]. If the deflection field is weak, the primary lens action on a quasi-chromatic electron beam is to steer it into a new direction, without much degradation in the convergence of the beam. Such weak electrostatic deflection is the main function of the quadrupole and parallel plate deflectors [EE70, G72] discussed in the earlier sections. If, on the other hand, a strong electrostatic deflection field is used to obtain a large angular deflection, a high energy

dispersion can be effected for the purpose of energy (or momentum) analysis of electrons from a quasi-chromatic beam. More common electrostatic energy analysers in electron impact and related studies include (segments of) cylindrical, spherical or even toroidal condensers [EE70, G72, S73].

In the present application, a 135° sector cylindrical mirror analyser (CMA) [ZKK66, A71, A72, R72, DL77, AY78] is used to energy analyse the outgoing electrons in each channel. The important geometrical dimensions of the CMA are given in figure 3.2. Because of the finite length and cut-off on the sides of the CMA elements, the imperfect non-infinitely long and incomplete 2π cylindrically symmetric deflection field must be corrected. The effect of geometrical truncation in the sector CMA and the resulting end field effects are compensated for by using logarithmically spaced end correctors (EC) at both the top and the bottom as well as the sides of the CMA. Additional side shields are used to prevent any stray electrons from entering into the analyser. The entrance slit A3 (A7) with an aperture of 2.5mm dia. is mainly used to isolate the field of the lens deflectors D3 from that of the CMA. It is also used to cover any exposed teflon insulator used for mounting the lens deflectors in order to prevent charging of the insulator. The size of the aperture in the exit slit A4 (A8) in the θ direction (2.0mm) determines the maximum possible $\Delta\theta$ acceptance whereas that in the ϕ direction has no marked

effect on the focussing property and is therefore doubled (i.e. 4.0mm) to take advantage of the increase in count rate. The sector CMA is normally operated with a 100eV pass energy.

One inherent advantage of the CMA is the double focussing property.[3] In particular, Zashkvara *et al.* [ZKK66] showed that for axis-to-axis focussing, electrons with energy E and entrance angle θ=42.3° are focussed at z=6.12r with an applied potential V=0.763E(ln(R/r)), where r and R are the radii of the inner and outer cylinders of the CMA respectively. From the Taylor series for Δz one can show [ZKK66, R72, S73] that for other angles $\theta\pm\Delta\theta$ and energy $E\pm\Delta E$, the geometric aberration as represented by Δz is:

$$[3.2] \qquad \Delta z \simeq 5.6r\Delta E/E - 15.4r(\Delta\theta)^3 + 10.3r(\Delta E/E)\Delta\theta.$$

Neglecting the second and higher order terms, one gets that the relative energy resolution, i.e. $\Delta E/E$, for this case is 1.4% for r=25.4mm and a 2mm exit aperture in the theta direction (which defines the maximum possible Δz). Detailed study of the design parameters for the CMA with double focussing was given by Riley [R72]. It is however not possible for the sector CMA employed here to achieve the

---

[3] The n-th order focussing is commonly refered to the case where the n-th derivative of the image distance with respect to the entrance angle of the CMA is zero. In the present case double focussing means both the first and second derivatives are zero.

double focussing effect. The object to image separation in the present design (Hood *et al.* [HHB77]) is larger (i.e. 7.00r) than the optimal separation (i.e. 6.12r) required for axis-to-axis double focussing [R72]. As a result, small voltages applied to the Y-deflectors (D3) between the lens assembly and the CMA are necessary to allow slight alteration of the entrance angle as well as to reoptimize the focussing property. The applied voltage corresponds to a change of approximately 0.4° in the entrance angle. A more detailed discussion of the energy resolution obtained by the present optical system is given in section 3.6.1. It should be noted that the deflectors D3 come after the angular selection apertures A1 and A2 and thus do not affect the mean value of the scattering polar angle θ sampled by the CMA.

3.2.6 Single Channel Electron Multiplier

Electrons with the correct pass energy are transported from the entrance slit to the exit slit by the deflection action of the CMA. A single channel electron multiplier (CEM) (Mullard B318AL) [Mu75, Mu76, W79] is used to amplify any detected electron into a workable current pulse, which is used as input for the timing electronics (section 3.3.2). The CEM consists of a hollow glass tube with the internal resistive surface processed to have a high secondary emission

coefficient [Mu75, Mu76]. When an incident electron enters the input side and collides with the wall, several secondary electrons are produced. These secondary electrons are accelerated down the tube by a high bias potential between the input side and the output side. Such a multiplication process is repeated many times until the output side is reached. Typical electron gain is 10^8 at a bias voltage of 3keV. The CEMs used are manufactured curved in order to eliminate ion feedback [Mu75, Mu76].

The electron pulses are capacitively decoupled using a 0.0022μF capacitor. The resulting current pulse is fed to a preamplifier (outside the vacuum chamber) using a properly ground-shielded coaxial cable with a 50Ω characteristic impedence (RG174U). The length of the coaxial cable used is made as short as possible to prevent unnecessary degradation of the pulse amplitude as well as to eliminate possible signal pick-ups. A matching resistor (47Ω) is used for the proper termination of the coaxial cable at the receiving end (i.e. the input side of the preamplifier). Proper termination of the signal cable is extremely vital in eliminating the problem of ringing [C72, C75]. The CEM as well as the decoupling capacitor are mounted inside a properly shielded brass housing. Care has been taken to completely shield the whole CEM and signal cable arrangement to eliminate any crosstalk [C72, C75] between the two signal cables. A schematic diagram of the signal decoupling system

is shown in figure 3.3. Further details of the timing electronics, which require the generated current pulses after the signal decoupling process as inputs, are described in section 3.3.2.

3.2.7 Computer Simulation Of The Electron Trajectory

In figure 3.4 some typical electron trajectories through the secondary electron optical system are shown. The trajectories are calculated using computer codes [V80] originally developed by H.A. van Hoof at the FOM Institute, Amsterdam. Details and the principle of the charge density method [MW73, HR76] of the trajectory program are given in reference [V80]. In figure 3.4 the kinetic energy of an electron transversing the i^{th} lens element is denoted by T_i while the corresponding applied voltage is denoted by V_i. Under the present scattering conditions, the kinetic energy of the electron entering the three-element AIL (i.e. T_1) is 600eV and that of the electron exiting the AIL (i.e. T_3) is 100eV, which is also the pass energy of the CMA. The corresponding voltages (with respect to ground) applied on the first and third lens elements are therefore (V_1=) 0eV and (V_3=) -500eV respectively. The inner cylinder of the CMA is at the same potential as the third lens element of the AIL (i.e. -500eV). In effect, there are only two control voltages, i.e. that of the central element of AIL (V_2) and of

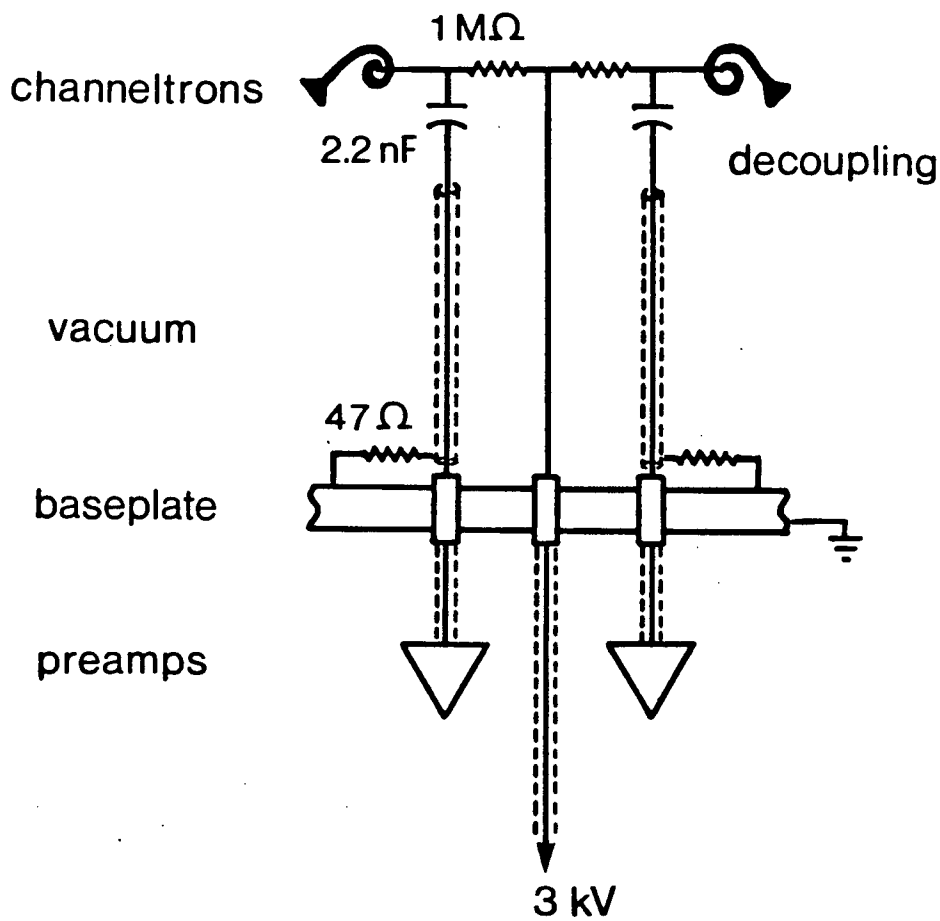

Figure 3.3 - Signal decoupling arrangement for the channeltron.

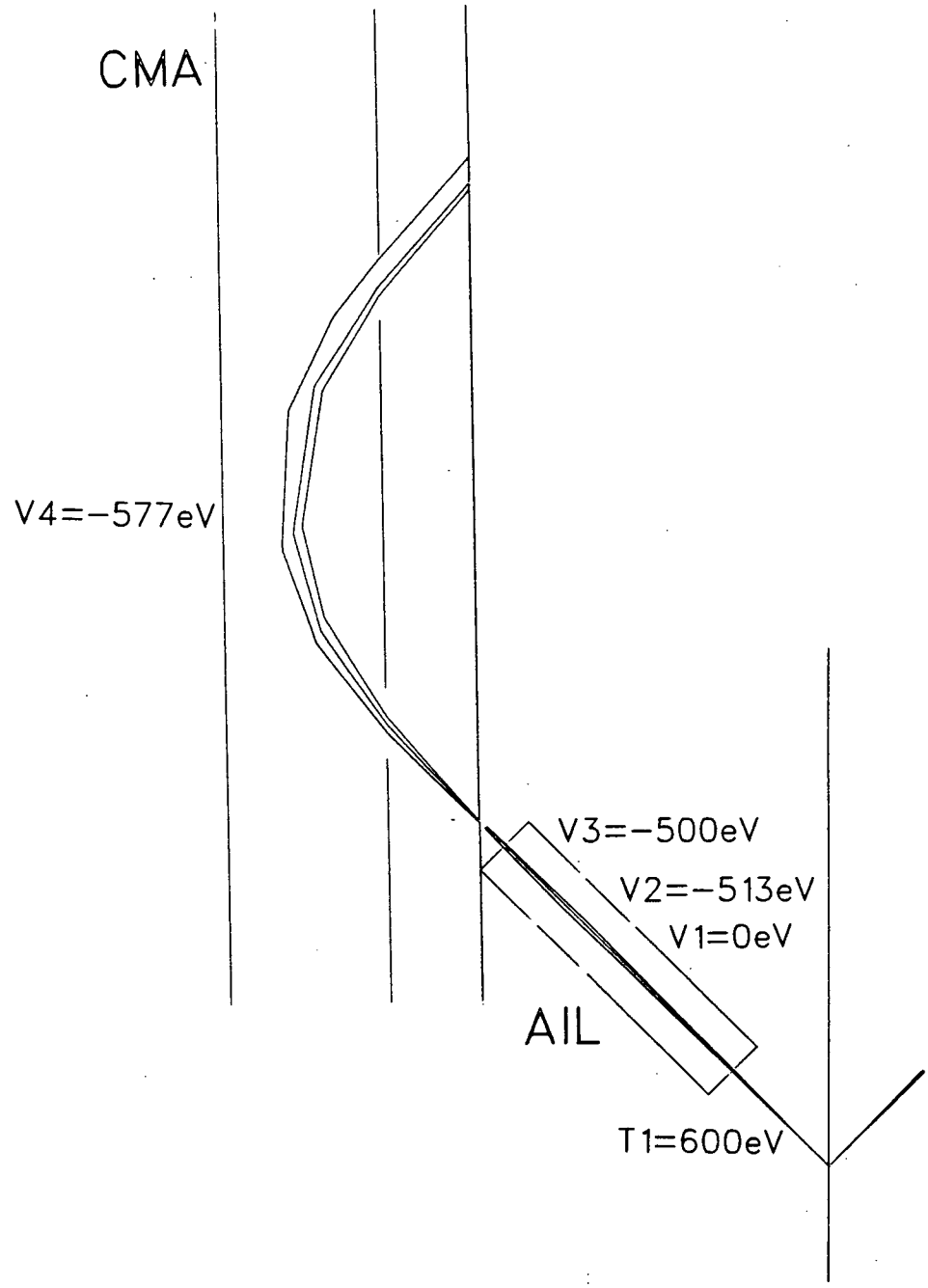

Figure 3.4 - Computer simulation of electron trajectories for electrons passing through the secondary electron optical system with 600eV kinetic energies.

the outer cylinder of the CMA (V_4), which are being used to control the trajectory through the secondary electron optical system (SEOS). The effect of the X-Y deflectors between A2 and the CMA is small and is ignored in the present computer simulation. Two possible trajectories representing the limiting cases[4] of the electron transit paths through the SEOS are shown in figure 3.4. The computed values of V_2 and V_4 for the present case (i.e. for T_3=100eV) correspond very closely to the optimized values used in the experiment. It is evident from figure 3.4 that the three-element AIL is clearly a convergent lens. In addition, for a constant entrance angle and pass energy, electrons with different energies are focussed at a different image position by the CMA.

3.2.8 Vacuum And Material Specifications

The spectrometer is mounted on an aluminum base plate (43cm dia.) and operates under vacuum in a removable aluminum cylindrical vacuum chamber (40cm dia., 40cm height) O-ring sealed at the bottom by the base plate and at the top by a removable lid (43cm dia.). It is evacuated by an alkylated diphenyl ether (Santovac 5) oil diffusion pump (NRC VHS-4), which is fore-pumped by a belt driven rotary pump (Sergeant

[4] In the present case the maximum entrance angle is taken to be half of the maximum possible geometrical acceptance angle.

Welch 1402). Brass flanges are used to house high vacuum octal connectors and high voltage connectors, and are bolted with O-ring seals to the feedthroughs of the base plate to facilitate electrical connections outside the vacuum. Two circular plexi-glass windows bolted with O-ring seals to the top lid and to the side of the vacuum chamber are used for viewing the spectrometer in operation as well as for reading the angular scale on the turntable (without releasing the vacuum) for scale calibration purposes. The base pressure of this chamber is 5×10^{-7} Torr. The normal operating dynamic pressure, as measured by an ionization gauge (Veeco RG75K) mounted on the top lid, is 5×10^{-5} Torr with a long term stability better than 5%. It has been estimated from the relative response of the singles count rate as a function of pressure that the actual dynamic pressure inside the gas cell is at least two orders of magnitude higher than the ambient pressure. No liquid nitrogen cooling trap is necessary to achieve the present vacuum status.

Almost all of the components of the electron optics (both the primary or the secondary electron optical systems) are constructed of brass. In order to minimize the effect of back scattering, all the slits are made of molybdenum. In addition the internal surfaces of the optical components, except those of the AILs and the electron gun, are benzene sooted to further reduce the effect of secondary emission from surfaces. The end correctors in the CMA are

electrically insulated from each other using sapphire balls as well as nylon screws and washers. Components in the lens assembly as well as in the collimator are insulated using teflon spacers. Attempt is made to shadow all the insulator material from the electron beam paths so as to eliminate any charging problem. Electrical connections from the optical elements to the octal connectors in the chambers are made using color coded teflon coated wires and Bundy connectors. Such arrangement allows quick and easy servicing of the optics in the spectrometer. The turntable on which one of the secondary electron optical systems is mounted is supported by nonmagnetic stainless steel balls. No magnetic material is used inside the vacuum chamber. The earth's magnetic field (0.5G) is reduced to 5mG using an external mu-metal shield to enclose the vacuum chamber.

3.3 CONTROL ELECTRONICS

The control electronics mainly consists of various DC power supplies for the optical components in the spectrometer and for the actual scan voltages for the experimental parameters. Part of the electronics (the timing electronics) is used for the coincidence detection of (e,2e) events.

3.3.1 Power Supplies

The stablility of the operating conditions of the electron optics depends upon many factors. The stabilities of the local residual magnetic field and the operating gas pressure as well as the various power supplies of the optical elements can affect critically the scattering dynamics. Measurements should only be made when there is no observable fluctuation in the gas pressure, since a different pressure will not only directly influence the count rate but also cause a different contact potential, which in turn affects the effective potentials applied to various optical elements and consequently the focussing property of the optics. More importantly, the potentials of optical components must be supplied by stable power supplies to avoid any problem caused by voltage drifts.

Figure 3.5 shows a detailed schematic of power supplies used for various electron optical components. Power supplies for only one of the two secondary electron optical system are shown.[5] The available voltage and current ranges of the power supplies are indicated. The incident electron energy, E_o, is scanned by changing a high voltage power supply (Fluke 412B). The variable portion of the output voltage range (0-200eV) of this power supply can be modified by a programmable resistor

[5] A similar arrangement has also been made to the other secondary optical system.

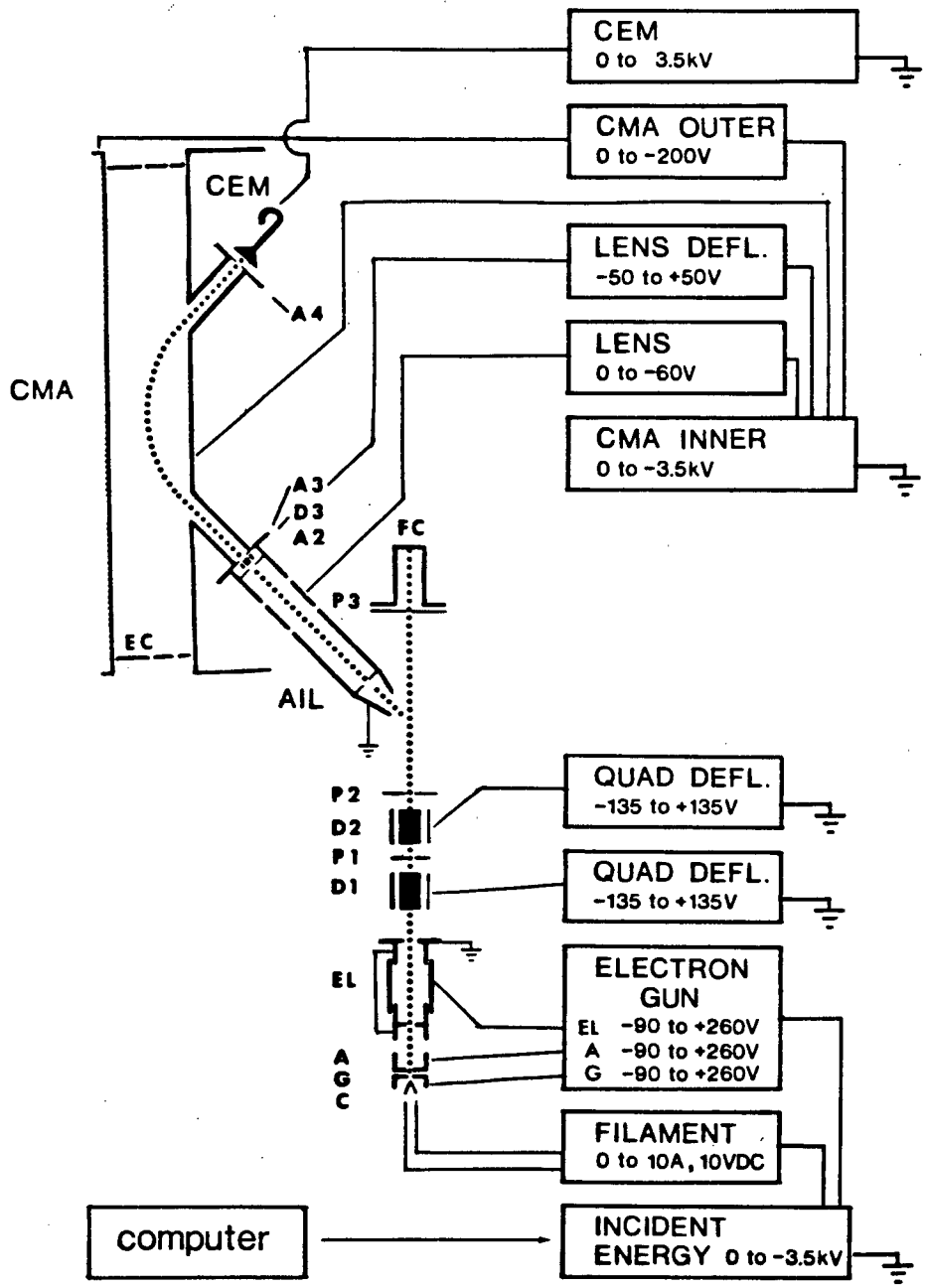

Figure 3.5 - Power supplies for the electron optical elements. The voltage (and current) range of each unit is indicated. Under normal operation conditions the CEM, CMA INNER and INCIDENT ENERGY high voltage power supplies are set at 3.0keV, 500eV and 1200eV respectively. A programmable range of 200eV for the INCIDENT ENERGY power supply is controlled by the computer system.

controlled by the DC voltage level of a digital-to-analogue voltage converter (DAC) inside the computer system (section 3.4). The power supplies for the optical components of the electron gun are floated on top of this incident electron energy power supply. The incident electron undergoes two stages of acceleration, i.e. from the filament to the anode and from the anode to the gas cell. The gas cell is maintained at ground potential. The currents collected by the Faraday cups and the three spray plates are individually monitored by micro-ammeters. The voltage of the inner cylinder of the CMA is supplied by a second high voltage power supply (Fluke 415B). The power supplies of all the other optical components of the secondary electron optical system are floated on top of this power supply. A third high voltage power supply (Hewlett-Packard 6516A), modified to extend its range up to 3500V, is used to provide the bias potential for the channel electron multipliers. The relative azimuthal angle is varied by rotating the turntable using a servo-motor driven by a servo amplifier [C72]. The reference voltages (±24V) of the servo amplifier are provided by a NIM (Nuclear Instrument Module) bin power supply (ORTEC 401A). The variable voltage of the servo amplifier is supplied by a second DAC in the computer system (see section 3.4). Calibration of the dynamic voltage ranges of the incident electron energy as well as that of the angular scale must be performed routinely. External test points are incorporated

in the various power supplies for checking that no voltage drift occurs during the progress of the experiment.

3.3.2 Timing Electronics

Electrons with the correct pass energies are detected and amplified by the CEMs. The current pulses coming from the movable and stationary CEMs must be analysed for coincident occurrence in order to be counted as an (e,2e) event. A single delay timing method is used [MW76a]. Figure 3.6 shows the timing electronics and the computer controlled data acquisition system. In the single delay timing method, the CEM pulses are first amplified and converted into voltage pulses with a fast preamplifier (ORTEC 9301). These voltage pulses are further amplified using a timing filter amplifier (ORTEC 454). Typical pulse shapes of these voltage pulses obtained after the pre-amplification and time shaping amplification under normal operation are shown in figure 3.7. It should be noted that a considerable reduction in the number of secondary reflection peaks has been achieved by appropriate termination of the transmission lines at the receiving ends as discussed in section 3.2.6. In principle termination of transmission lines at both the sending and the receiving ends [C75] should be used for very long cables. In the present case, the coaxial cables used are made as short as possible (less than 0.5m) and consequently only

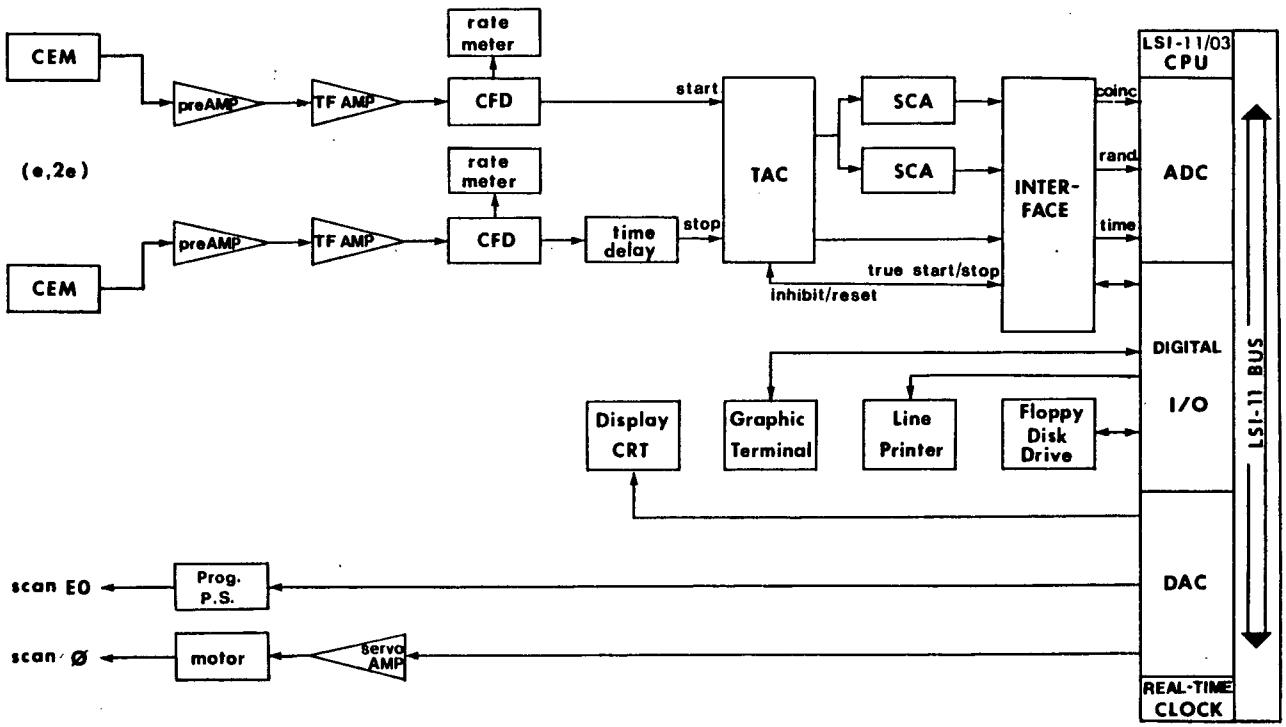

Figure 3.6 - Timing electronics and computer-controlled data acquisition system. Legend: CEM - Channel Electron Multiplier, CFD - Constant Fraction Discriminator, TAC - Time to Amplitude Converter, SCA - Single Channel Analyser; CPU - Central Processing Unit, ADC - Analog to Digital Converter, DAC - Digital to Analog Converter.

termination at the receiving end is necessary.[6] The residual reflections in the preamplifier pulse are probably due to the small impedence mismatch between the available resistor (47Ω) used for termination and the characteristic impedence of the coaxial signal cable (RG174U, 50Ω). The magnitude of the residual reflections can be further reduced by choosing an appropriate RC time filter for the time filter amplifier. As demonstrated in figure 3.7, correct choice of the RC constant in the timing filter amplifier can significantly reduce the magnitude of the secondary reflections without affecting the rise-time of the first peak. Moreover, it can also eliminate spurious noise in the signal cables in the experimental area. Only the first peak of the resulting fast (rise-time <2nsec) voltage pulse is used for timing purposes.

All the secondary reflections are blocked using constant fraction discriminators (ORTEC 463) by setting the voltage discriminator level considerably higher than the maximum voltage magnitude of the strongest secondary reflections. Discrimination using the constant fraction method [Or80] has the advantage that no time jitter is possible even for pulses with variable pulse height distributions. Slow NIM-standard[7] logic pulses are output from the discriminators to the rate-meters (HARSHAW NR-10) for monitoring the count rate. The

---

[6] In fact, termination at both ends of the coaxial cables causes even more reflections than termination at just the receiving end.

[7] NIM stands for Nuclear Instrument Module.

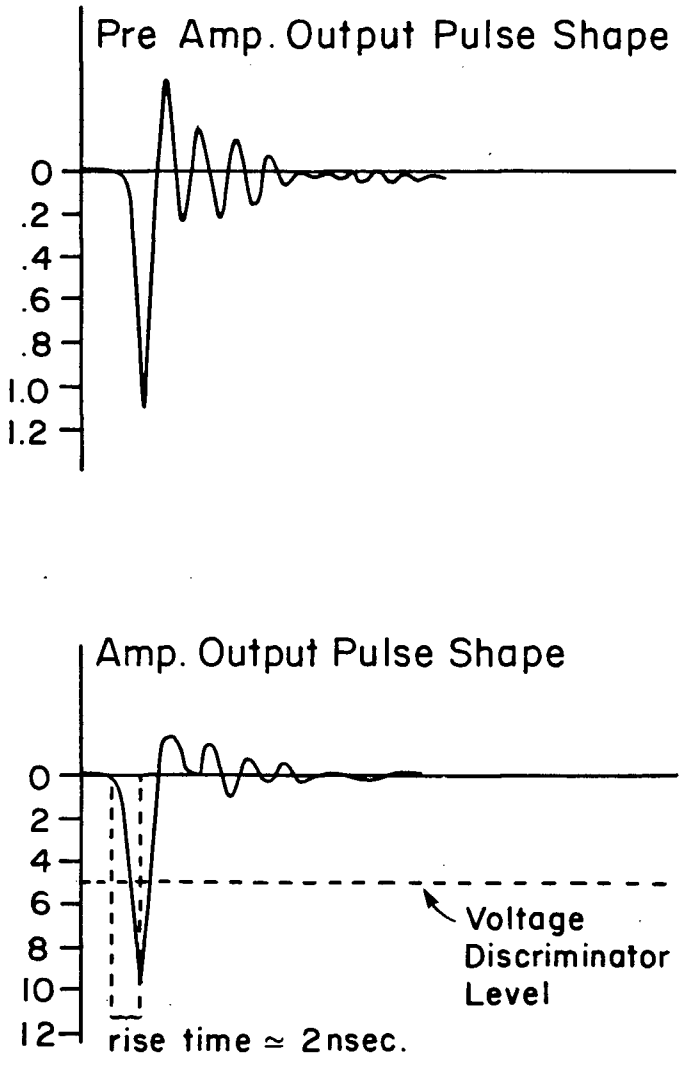

Figure 3.7 - Typical output pulse-shapes for the preamplifier (top) and the time filter amplifier (bottom). Considerable reduction of secondary reflections in the output pulse-shape of the time filter amplifier is achieved by employing an appropriate RC time constant.

fast NIM-standard logic pulse output from one of the discriminators is used as a "start" pulse to a time-to-amplitude converter (TAC-ORTEC 467). The output from the other discriminator is time delayed with a length of coaxial cable to provide the "stop" pulse to the TAC. The TAC produces a voltage pulse with height proportional to the time difference between successive "start" and "stop" pulses. A histogram of the resulting pulse height distribution, which is referred to as the time spectrum, is shown in figure 3.8. The true coincidences can be extracted by using two single channel analysers (SCA-ORTEC 406A and ORTEC 467) to pass pulses with height occurring inside the windows labelled COINC and RAND in figure 3.8. A single channel analyser functions essentially like a "double-level" discriminator as it outputs a logic pulse only when the height of the input pulse falls between the two discriminator (lower and upper) levels. The ratio of the widths of the random to coincidence windows, x, is related to the number of true coincidences N_{TRUE} by the following relation:

$$[3.3] \qquad N_{TRUE} = N_{COINC} - N_{RAND}/x,$$

with the standard deviation:

$$[3.4] \qquad \Delta N_{TRUE} = (N_{COINC} + N_{RAND}/x^2)^{1/2}.$$

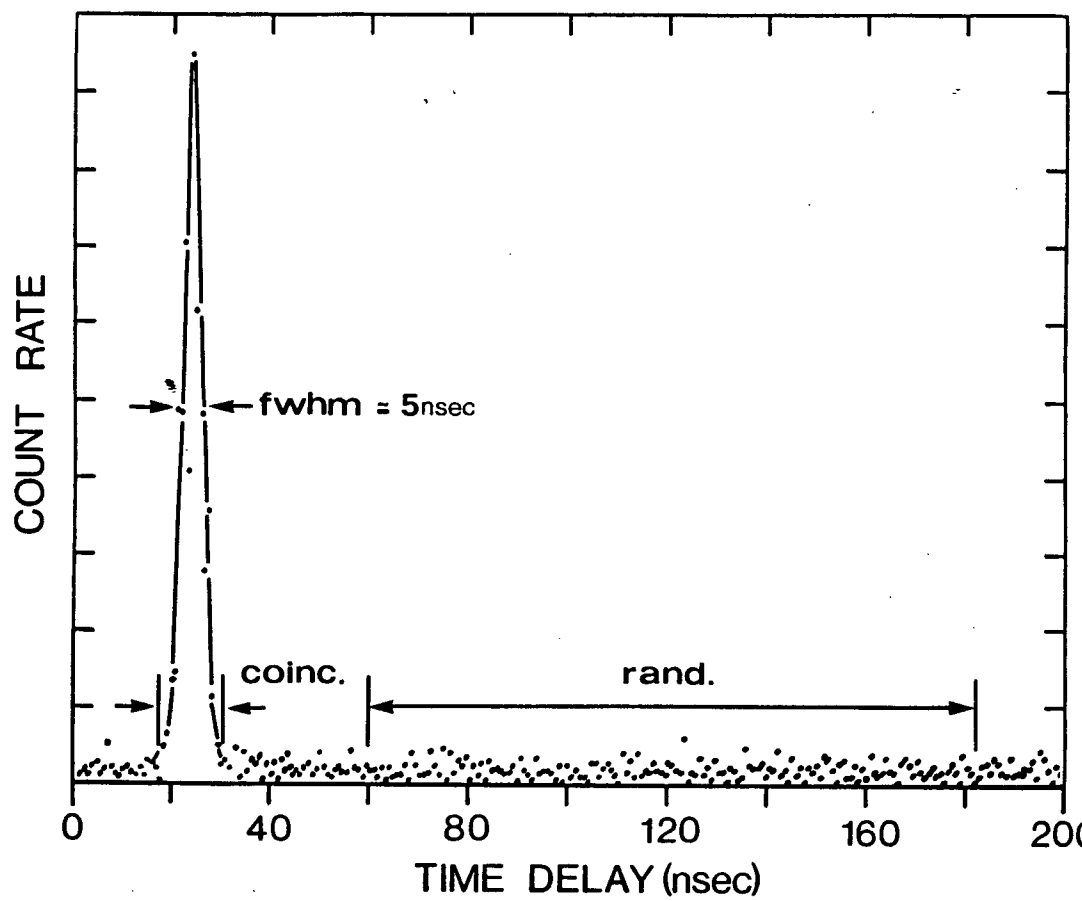

Figure 3.8 - Typical time spectrum for argon 3p ionization. Locations of the COINCidence and RANDom SCA windows in the time spectrum are indicated.

Clearly, a large x will improve the overall statistical accuracy in N_{TRUE}. A window width ratio of (x=) 8 is used in the studies reported in this thesis. The outputs from both SCAs as well as outputs from the TAC are fed into a computer interface unit for further processing.

3.4 COMPUTER CONTROL

The major peripherals [Di78] of the microcomputer system (Digital PDP11/03) are listed in table 3.1. (See also figure 3.8.) A real-time data acquisition software package was developed to retrieve and store counting information. Four one-dimensional arrays are used for separate storage of the scanning experimental parameters (E_0 or ϕ), the coincidence N_{COINC}, the random N_{RAND} and the time histograms. The true coincidence N_{TRUE} histogram (i.e. the experimental cross section) is then obtained from the coincidence and random histograms using equation 3.3. Only one of the two experimental parameters is scanned at a time while the other is kept unchanged. When the scan parameter is the incident electron energy E_0 (=1200eV+binding energy in the present case), the resulting true coincidence spectrum is called the binding energy spectrum (measured at a fixed ϕ). On the other hand, when the scan parameter is the relative azimuthal angle ϕ, the resulting true coincidence spectrum is called the angular correlation (at a fixed E_0 or binding energy). A

Table 3.1
Configuration of the microcomputer system.

Device	Company	Model
LSI 11/03 CPU	Digital	M7270
Memory (32k)	MDB Systems	MSC 4601
Real-time Clock	Data Translation	DT2769
D/A Converter	Data Translation	DT2766-BR
A/D Converter	Data Translation	DT2762-SE-BR
Parallel I/O	MDB Systems	MLSI-DRV11C #40346 Rev A
Serial I/O	MDB Systems	MLSI-DLV11 #40320 Rev B
CPU Enclosure System Monitor	MDB Systems	MLSI-SMU #40341
Video Terminal	Digital	VT100-AA (upgraded to VT125)
Dual 8" Floppy Disk Drive Controller	Data Systems Design	DSD-440 L11-2A A4432 Rev 2
Dot Matrix Printer	Integral Data Systems	IDS-460
Reference Manuals	Digital	

conversion from the azimuthal angle ϕ to the momentum p using equation 2.3c generates the momentum distribution (measured at a fixed binding energy). One major advantage of the separate storage of the coincidence, random and time spectra is to allow more accurate calculation of the statistical errors using equation 3.4. The random spectrum also provides a scale linearity check on the random coincidence (or background noise). The time spectrum is of a fixed time range (200nsec) and the time variable is obtained by digitizing the TAC output. The time spectrum allows a close monitoring of the presence of any spurious noise or crosstalk between signal lines. Two major functions of the microcomputer system and its associated real-time data acquisition software are summarized in the following sections.

3.4.1 Parameters Scanning

The experimental independent variables, i.e. the incident electron energy E_0 and the relative azimuthal angle ϕ, are set using a four channel digital-to-analogue converter (DAC) [Di78]. The DAC converts a digital value into an analogue voltage (0-10V), which is then used as the input for controlling the programmable power supply for E_0 or as a variable voltage level for the servo-amplifier for control of ϕ (figure 3.6). Once the digital-to-analogue conversions are

completed and the experimental parameters (E_0 and ϕ) are set accordingly, a count-until-overflow sequence is initiated in the programmable real-time clock [Di78] with a preset clock-rate and clock-count. The overflow bit of the control status word of the clock board is then checked periodically. This procedure is used for controlling the dwell-time per scan channel. Any event that occurs within this dwell-time is counted and stored in the appropriate array element corresponding to the scanning parameter. A new set of experimental values for E_0 and ϕ are used for the DAC channels on encounter of clock overflow and the whole scan procedure is repeated until the scan sequence is interrupted by the operator or on response to the preset scan count. It is possible to set up a scan procedure which performs sequential angular correlation scans at a set of binding energies interleavingly or vice versa, i.e. binding energy scans at a set of relative azimuthal angles. Such an interleaving scan procedure allows automatic self-normalization between spectra within the set without performing complex corrections due to pressure variation and fluctuations in other experimental conditions.

3.4.2 Event Counting

Once a coincident event (regardless of whether it is a random or true event) has been registered by the TAC, the TAC (voltage) outputs must be digitized to locate the appropriate bin number, corresponding to a specific delay time, for count incrementation. The interface unit (figure 3.6) is used to temporarily "inhibit" the TAC from accepting more inputs and to "hold" the TAC output signal sufficiently long for the analogue-to-digital converter (ADC) [Di78] to complete the digitization, which typically takes 30μsecs. On completion, the interface "resets" the TAC for further signal processing. Outputs from the two SCAs are used for incrementing the number of counts in the coincidence and random array elements, each corresponding to the respective scan parameter. When the chosen channel dwell time expires, the contents of these array elements are stored. The next set of experimental parameters are then used and the whole procedure is repeated as discussed above (section 3.4.1).

The computer also provides other services including periodic data printout, routine update of recorded spectra on floppy diskettes and display of the spectrum on either a graphic terminal (Digital VT125) or an X-Y scope. Periodic data printouts are used to monitor the stability of the spectrometer and to correct for any spurious noise due to power surges during the often lengthy scanning process.

3.5 OPERATION PROCEDURE AND SAMPLE HANDLING

There are three modes of operation: the noncoincident elastic scattering scan, and the coincident binding energy and angular correlation scans. The noncoincident elastic scattering scan is used for initial tuning and optimization of the voltage settings of the secondary electron optical systems (SEOSs) before the coincident (e,2e) experiments (i.e. binding energy or angular correlation scans) are performed. In this elastic mode, the incident energy E_0 is set to be identical to E_1 (i.e. 600eV). The SEOSs are adjusted to momentum and energy analyse only the elastically scattered electrons with kinetic energies of 600eV. Figure 3.9 shows a typical transmission function of the SEOS for an electron entering with 600eV kinetic energy after the elastic collision with a gaseous target. The voltages of the central elements and the X-Y deflectors D3 (D4) following the AIL are manipulated to maximize the amplitude and to minimize the FWHM of the peak without introducing any asymmetry to the overall peak-shape. The voltage of the outer element of the CMA is used to centre the peak at the correct mean kinetic energy (600eV). This procedure must be performed individually for both secondary electron optical systems.

After the elastic scattering scans, the incident energy is reset to its original value (i.e. 1200eV plus the binding energy). The incident electron beam is reoptimized as discussed in section 3.2.3. The binding energy and the

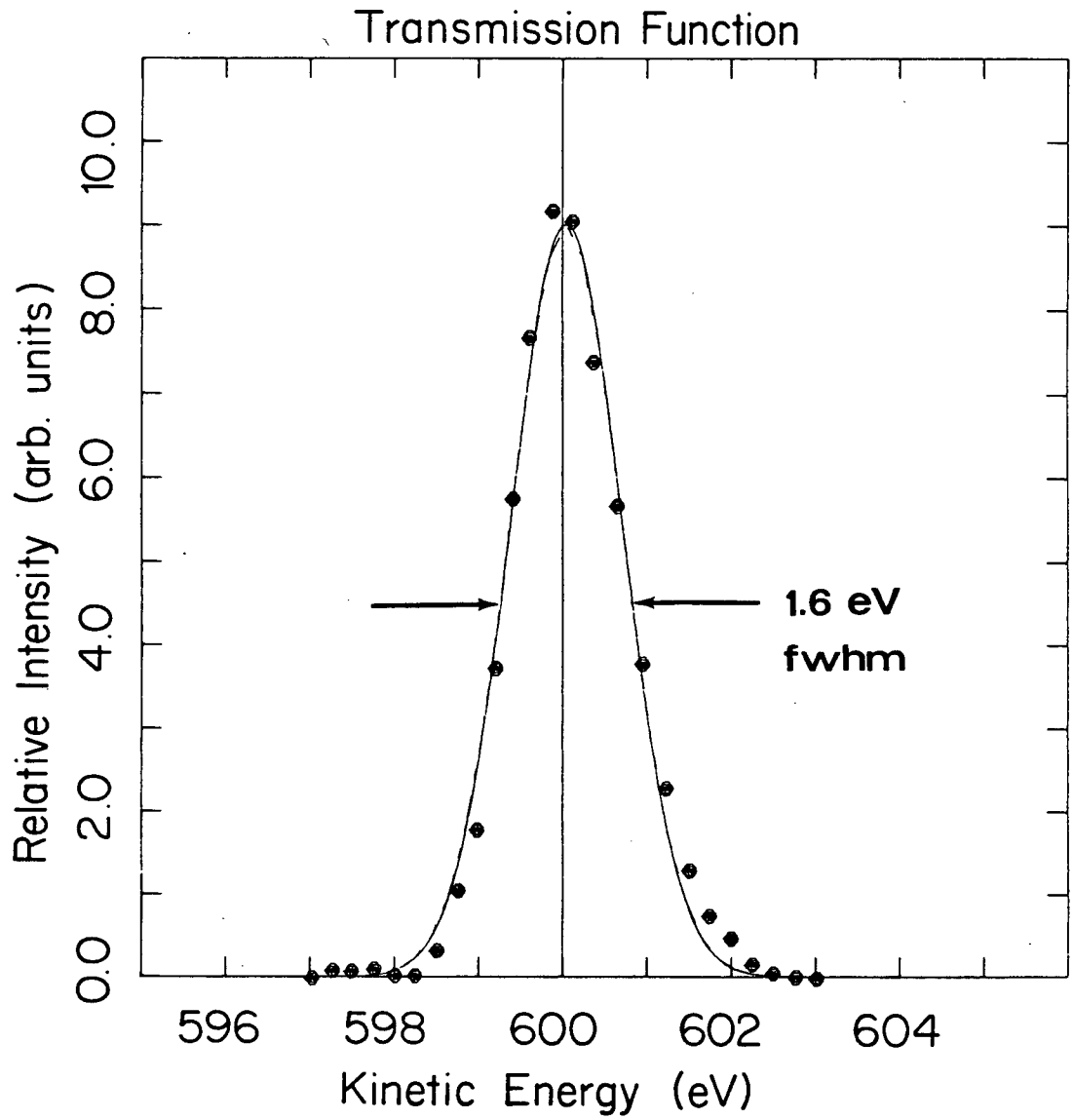

Figure 3.9 - Typical transmission function for the secondary electron optical system operating with a 100eV pass energy for the CMA. A Gaussian function (solid line) with a 1.6eV FWHM gives an excellent fit to the data.

angular correlation scans can then be initiated with the appropriate scan sequences in the computer system. It should be noted that the binding energy scan is obtained by scanning E_0 at a fixed relative azimuthal angle ϕ. The angular correlation scan is obtained by scanning ϕ while keeping E_0 constant. The incident energy is related to the binding energy by equation 2.2 and the momentum p is related to ϕ by equation 2.3c under the present noncoplanar symmetric scattering condition (chapter 2).

All chemicals used in the studies reported in this thesis were of high purity (>99%) and were obtained commercially from Matheson except for CS_2 which was supplied by Matheson-Coleman & Bell. No impurity was detected in the binding energy spectrum. For CS_2, appropriate freeze-thaw cycles were performed to eliminate any absorbed air contained in the liquid sample before introduction into the gas cell. The gas handling system for sample introduction consists of a pressure reduction variable leak valve (Granville-Phillips 203) and various vacuum compatible valves. Heating tape is used to maintain the whole gas handling system at a sufficiently high temperature (40-60°C) to prevent condensation and blocking of the leak valve due to cooling caused by expansion in the leak valve. Each of the gas cylinders is equipped with the proper gas regulator to control the input pressure.

3.6 PERFORMANCE

The performance of an electron spectrometer is usually rated by several factors. The more important ones include resolutions, signal-to-noise ratio, data collection efficiency and flexibility in the range of applications.

3.6.1 Resolutions

A good measure of the energy resolution can be obtained from the binding energy spectrum for He 1s ionization (see figure 3.10). Gaussian and Lorentzian line-shapes are fitted to the experimental He 1s binding energy spectrum. The excellent fit of the Gaussian line-shape to the experimental spectrum indicates that the energy line-shape function is of a Gaussian type with a FWHM of 1.6eV. It also justifies the use of Gaussian functions for the deconvolution procedure used in the data analyses reported in this thesis. The Gaussian line-shape is due to the effect of the transmission functions of the secondary electron optical systems, which dominates any effect of natural line-shape. It is clear from figure 3.9 that the transmission function itself can also be closely represented by a Gaussian function of $\simeq$1.6eV FWHM. Under the present symmetric arrangement, the overall energy resolution is simply the larger of the two single energy resolutions as measured in the elastics experiment. i.e.

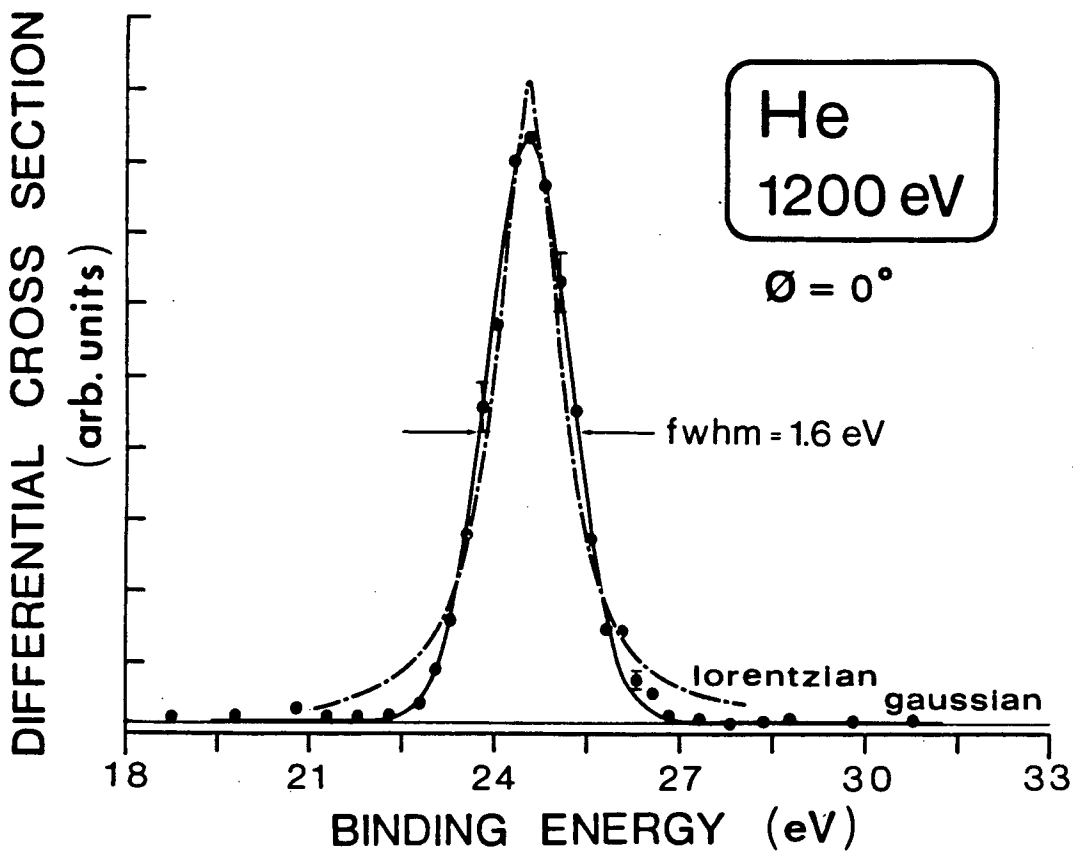

Figure 3.10 - Typical binding energy spectrum for helium 1s ionization at ϕ=0°. The Gaussian function (solid line) with a 1.6eV FWHM gives the best fit to the experimental data.

$$[3.5] \qquad \Delta E = (\Delta E_{PEOS}^{\ 2} + \Delta E_{SEOS}^{\ 2})^{1/2} + \delta e,$$
$$= (\Delta E_{filament}^{\ 2} + \Delta E_{CMA}^{\ 2})^{1/2} + \delta e,$$

where δe is zero if identical line-shapes are obtained by both SEOSs and there is no difference in the energy position between the corresponding Gaussian peaks. The contribution of the PEOS to ΔE is mainly due to the thermal spread of the thermionic source (i.e. the filament), which is estimated to be 0.8eV in the present case. The energy dispersion of the three-element AIL in the SEOS is generally small compared to that of the CMA. The resolution for the CMA is 1.4% of the pass energy and is therefore 1.4eV for a pass energy of 100eV. Clearly lowering the pass energy of the CMA will in general improve the resolution but only at the expense of count rate. Without the use of energy monochromation of the incident electron beam, it is unlikely that the overall energy resolution of the present instrumentation can be improved beyond 1.0eV FWHM.

The angular resolution function is in general complex and depends upon many factors including backlash of the turntable, angular divergence of the incident beam, the entrance and exit apertures and the focal properties of the three-element AILs as well as the exit aperture and the aberration of the CMA. It is impractical, and very difficult, to determine accurately the effects of all the contributing factors. An angular convolution procedure,

first discussed by Hood *et al.* [HHB77] (see also Frost and Weigold [FW82a]) has therefore been employed to include the effects of the angular resolution in the theoretical momentum distributions before comparison with the experimental results. To a first approximation, the primary contributing factors are the entrance and exit apertures of the AILs as these apertures define geometrically the maximum acceptance angles of the lenses. The collision region is defined as the overlap volume between the incident electron beam and the two acceptance cones of the lenses. The size of the acceptance cones are defined by the maximum acceptance angle. (See figure 3.11.) Consequently, the smaller is this overlap volume, the smaller is the angular resolution. (If the width of the incident electron beam or the defining apertures of the lenses are infinitely small, then the overlap volume becomes the ideal collision *point*.) Any (e,2e) event occurring inside this overlap volume would contribute to the signal. If one ignores all the nonsymmetric collisions, then symmetric collisions can only occur from collision centres confined on the largest cross-section of the overlap volume. It is therefore reasonable to average over the momentum distributions with momentum scales corresponding to the set of polar and azimuthal angles defined by points on this area. The size of the area is defined by the *effective* sizes of the apertures: (full-angle) $\Delta\theta$ and $\Delta\phi$. The effects of varying either $\Delta\theta$ or $\Delta\phi$ on typical p-type and s-type momentum

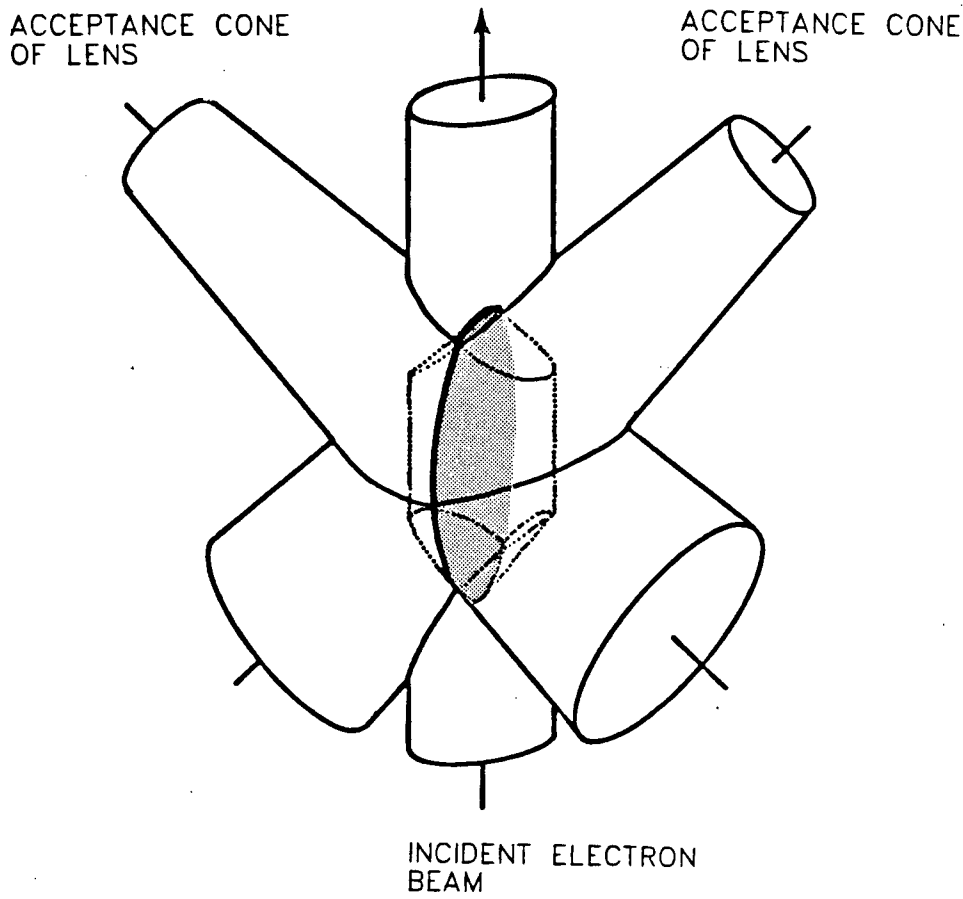

Figure 3.11 - The collision region resulting from the overlap of the incident electron beam and the acceptance cones of the lenses. The shaded area is defined by the "effective" angular spreads (full angle) $\Delta\theta$ and $\Delta\phi$. Adapted from figure 3.7 in reference [C80].

distributions are shown in figure 3.12. Clearly, enlarging these effective aperture dimensions tends to increase the intensity of the p-type distribution in the low momentum region. To determine the effective aperture size, the momentum distribution of Ar 3p calculated using the Hartree-Fock wavefunction [CR74] is convoluted with various combinations of $\Delta\theta$ and $\Delta\phi$ values. The resulting convoluted distributions are then compared with the experimental distribution for Ar 3p. Under the present arrangement, an excellent fit is obtained for (full-angle) $\Delta\theta$=1.2° and (full-angle) $\Delta\phi$=2.0°, which then define the effective aperture dimensions for subsequent (e,2e) studies. The uncertainty in the momentum corresponding to these angular uncertainties is $\simeq 0.1 a_0^{-1}$. It should be noted that varying the mean theta angle of the outgoing electrons (away from θ=45°) would not change the overall shape of the theoretical p-type distribution. However, it has the effect of shifting the experimental momentum distribution toward the origin of the momentum scale. This appears to raise the momentum distribution in the low momentum region. An incorrect θ (i.e. not the optimal value) would therefore produce a similar experimental observation to that which would occur if the momentum resolution is poor (i.e. large $\Delta\theta$ and $\Delta\phi$). It is therefore extremely important to have high precision alignment of the lenses at θ=45° with respect to the axis of the gas cell (section 3.2.4). In the present arrangement,

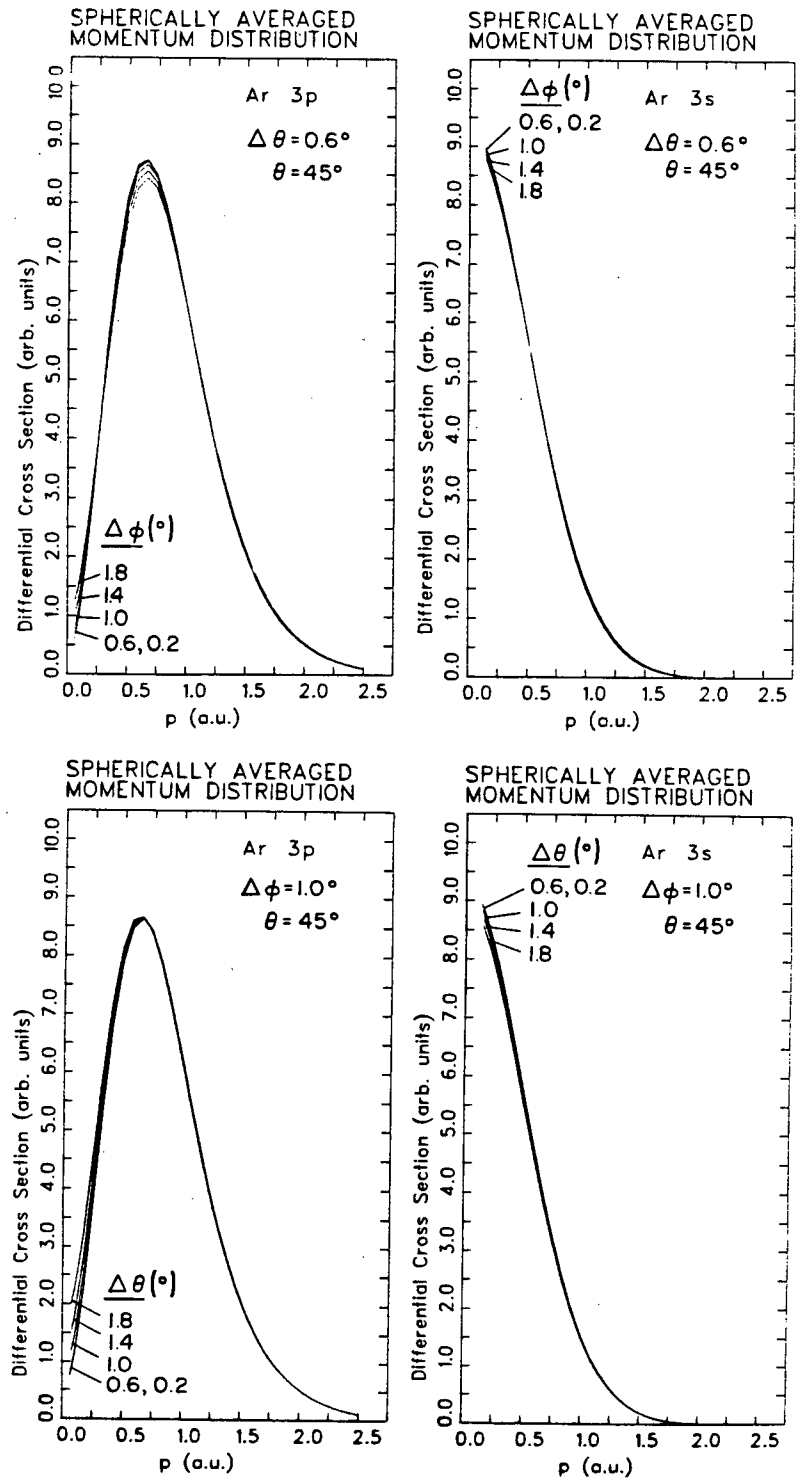

Figure 3.12 - Effects of folding different "effective" angular spreads (full angle) $\Delta\theta$ and $\Delta\phi$ into the Ar 3p and Ar 3s momentum distributions calculated using Hartree-Fock wavefunctions [CR74].

the very low minimum observed at the momentum origin of the experimental Ar 3p momentum distribution (figure 4.6) confirms the high accuracy in the physical alignment of the lenses.

Finally, the timing resolution is shown to be approximately 5nsec FWHM (figure 3.8). The small time spread is due to the small variation in the transit time of an electron passing through the CMAs as well as the difference in amplification time in the CEMs. The latter factor should be much smaller than the former factor because of the much smaller physical dimension of the CEMs.

3.6.2 Signal-To-Noise Ratio

The experimental true coincidence count rate is of course related to the triple differential cross section (chapter 2). i.e.

$$[3.6] \qquad N_{TRUE} = nI(d^3\sigma/d\Omega_1 d\Omega_2 dE_1)\ \Delta\Omega_1 \Delta\Omega_2 \Delta E_1,$$

where n is the number of target species in the collision region and I is the number of incident electrons per second. The experimental random coincidence count rate is given by:

$$[3.7] \qquad N_{RAND} = N_1 N_2 \tau,$$

where τ is the width of the coincidence time window. The singles (elastics) count rates N_1 and N_2 are defined by:

$$[3.8] \qquad N_1 = nI(d^2\sigma/d\Omega_1 dE_1)\ \Delta\Omega_1\Delta E_1 .$$

The signal-to-noise ratio is therefore given by:

$$[3.9] \qquad N_{TRUE}/N_{RAND} = (nI\tau\Delta E)^{-1} (d^3\sigma/d\Omega_1 d\Omega_2 dE_1)/(d^2\sigma/d\Omega_1 dE_1)^2 ,$$

where $\Delta E=\Delta E_1=\Delta E_2$.

It should be noted that the singles count rate increases with the number of target electrons possible to be excited or ejected from the target species. Consequently the signal-to-noise ratio becomes worse for the inner levels of high Z targets. Ignoring the target dependent triple and double cross sections, the signal-to-noise ratio $N_{TRUE}/N_{RAND} \propto 1/(nI\tau\Delta E)$ and the true coincidence count rate $N_{TRUE} \propto (nI)\Delta\Omega_1\Delta\Omega_2\Delta E$. Clearly the best operating condition is a compromise between the signal-to-noise ratio and the true coincidence count rate. Increasing the solid angles will increase the true coincidence count rate at the expense of the angular resolution. It is also obvious that it is advantageous to have a smaller width for the time window because a smaller time width will improve the signal-to-noise ratio without affecting the count rate.

3.6.3 Limitations

The more pertinent limitations of the present binary (e,2e) spectro-system include data collection efficiency and flexibility in studying corrosive or short-lived chemicals. Under normal ambient sample pressure and operating conditions, the (noncoincident) singles count rate of the present spectrometer is 100-1000Hz depending upon the target. The corresponding coincident count rate is of the order of 0.1Hz. A typical spectrum with reasonable statistics normally requires 1-3 days to accumulate. As such, the efficiency of the spectrometer must be improved in order to extend the binary (e,2e) method to the studies of short-lived species such as radicals and negative or positive ions. One approach to improving the efficiency is by means of multichannel and angular sensitive detection techniques presently being investigated in this laboratory (work not reported in this thesis). Such development requires a different electron optical system as well as signal decoupling methods. It should be noted that improving the data rate (using multichannel detection technique) is also a prerequisite in upgrading the energy resolution using electron energy monochromation. In the present arrangement, the spectrometer is also not suitable for studying corrosive and reactive gases. This is because long exposure of the spectrometer to these types of gases will cause instability in the potentials of the optical elements due to continual

metal surface deterioration, which continuously affects the effective contact potentials. This problem can be alleviated by differentially pumping different sections of the spectrometer, in particular the gas cell. During the later stage of this Ph.D. work, a quick modification (not reported in this thesis) has been made so that the section below the gas cell (i.e. the electron gun section) is separately pumped. This has helped to extend the life-time of the filament by operating the filament at a much lower ambient pressure. This arrangement has been used to study water (not reported in this thesis, see [BL&84]) which would be problematic without such arrangement due to the well known strong surface absorption characteristic of water. The present partially differential pumping arrangement is intended for the study of corrosive compound such as fluorine. The next generation binary (e,2e) spectrometer can therefore be envisioned to incorporate multichannel angular sensitive detection and differential pumping technologies.

Chapter IV

NOBLE GASES

4.1 INTRODUCTION

The study of atoms, in particular the noble gases, has played an important role in the "evolution" of binary (e,2e) spectroscopy. Since all the noble gases are gaseous at room temperature and also because of their relative chemical inertness and closed shell electronic structure, they are the ideal test targets for studying the (e,2e) ionization theories. The coplanar angular correlation studies which have been reported for He [CG&78, FM&78], Ne, Ar and Xe [UWM75, FM&78] were mainly intended to test the validity of various approximations (plane wave impulse approximation, distorted wave impulse approximation, etc.) in the scattering process. Absolute triple differential cross sections have also been obtained for He [SCG78, WK&81], Ne [SCG79], Ar [KPH81], and Xe [GFT80]. Most of these works studied the application of the (averaged) eikonal approximation in the (e,2e) process. Other theoretical works on ionization theories include those by Madison *et al.* [MC77, ML81] and Camilloni *et al.* [CG&80]. Of more relevance to the present work are earlier studies of noble gases using the noncoplanar scattering kinematics: He [HM&73, DMW76], Ne [DM&78], Ar

[WHT73, HM&74, MUP78], Kr [WHM75, FG&81], and Xe [WHM75, HHB77, GF&79, FG&81]. In most of these studies a great deal of emphasis was placed on structural determination (i.e. the importance of the wavefunctions in predicting the measured (e,2e) cross section). However, most of these works were often limited by the energy and/or momentum resolutions compared with presently available performance in binary (e,2e) spectrometers. It should be noted that binary (e,2e) studies by Dixon *et al.* [DMW76] and more recently by Cook *et al.* [CM&84] have also investigated the role of ground state correlations in the n=2 [DMW76] and n=2 and 3 [CM&84] states of He^+. Observations of relativistic effects in the Xe $5p_{3/2}$ and $5p_{1/2}$ orbitals have also been made recently by Cook *et al.* [CMW84].

Ionization in the outer valence-shell of the noble gases has also been studied with photoelectron spectroscopy: He [CKM71, KW72, SFC74, WA&80, WS80], Ne [CKM71, WK72, SFC74, WK74], Ar [CKM71, SFC74, AW&78a, SH81], Kr [SFC74] and Xe [G74, SH77, W77c, AW&78b, HP78, SH81]. All of these data show significant satellite[1] structures in the ns binding

[1] The parent and satellite state descriptions are used here to distinguish the most intense ionic state from the others. There is no other intended physical distinction between the various ionic states produced by many-body effects and described in appropriate ionization theories. In some cases, for instance in the ionization of inner valence molecular orbitals [CD77], the ionization spectrum may contain several relatively intense poles, none of which maybe overwhelmingly dominant and thus no clearly defined "parent" exists.

energy spectra of the heavier members of the noble gases. Although the relative intensities of these satellite states are in general different from those found in the (e,2e) study [MW76a, MUP78] due to the differing fundamental nature of the two processes, the energy positions provide useful references for the (e,2e) study because of the somewhat better energy resolution presently attainable in photoelectron spectroscopy.

A number of *ab-initio* calculations have been carried out pertaining to satellite structure and electron correlations [CKM71, MS76, MKS78, DL79, L81, DL82a, DL82b]. Recent multiconfiguration calculations by Dyall and Larkins [DL82a, DL82b] show that although good relative energy agreements can be obtained, such calculations are still inadequate in the prediction of relative intensities between satellite states. Other similar configuration interaction (CI) calculations on Kr [FG&81] show similar discrepancies in intensity prediction.

A systematic study of the binding energy spectra and momentum distributions of all the valence orbitals of the noble gases: He, Ne, Ar, Kr and Xe is given below. The present measurements represent the first comprehensive study of all the noble gases on the same spectrometer under identical instrumental conditions. The significance of literature SCF wavefunctions in predicting the measured momentum distributions using the plane wave impulse

approximation (PWIA) is also investigated. Electron correlation effects and the breakdown of the independent particle picture are discussed and compared with the recent theoretical work of Dyall and Larkins [DL82a, DL82b] as well as with photoelectron spectroscopic data. The measured momentum distributions of the noble gases are compared with calculations using wavefunctions of Hartree-Fock (HF) and lesser quality. The trends down the noble gas group are discussed with the aid of the binding energy spectra as well as the momentum and position density maps calculated using HF quality wavefunctions. The observed behaviour is correlated with the known electronic structure and periodic properties of the noble gases.

4.2 AN OVERVIEW

The binding energy spectra at several azimuthal angles at E_0=1200eV for the noble gases He, Ne, Ar, Kr and Xe are presented in figures 4.1, 4.3, 4.5, 4.7 and 4.9 respectively. For Ar, Kr and Xe binding energy spectra at several ϕ angles are overlayed on an approximate momentum (p) scale to provide a better perspective of the variation of the relative intensity of the satellite structures with respect to p. (The p scale is only approximate since the ϕ to p conversion (equation 2.3c) depends slightly on the scanning binding energy and in the above cases, the indicated scales are only

exact for a binding energy of 30eV.) The energy scales of the binding energy spectra are normalized on the photoelectron data [CKM71, SFC74] for the ionization of the outermost orbitals (i.e. the $(np)^{-1}$ states). The raw data (black dots) are overlayed in the region of ns ionization with individual deconvoluted Gaussian line shapes (dot-dash lines in figures 4.5, 4.7 and 4.9) with a FWHM corresponding to the overall instrumental energy resolution (1.6eV FWHM). The sums of the individual Gaussians are represented by solid lines in figures 4.3, 4.5, 4.7 and 4.9. No deconvolution is attempted for the portion of the data with insufficient statistics (high energy side) although further structures are indicated corresponding to higher excited ion states. Although absolute triple differential cross sections are not measured, relative normalization is maintained in each set of measurements.

Figures 4.2, 4.4, 4.6, 4.8 and 4.10 show the experimentally measured spherically averaged momentum distributions of the noble gases at several selected binding energies. The instrumental momentum resolution ($\Delta p \simeq 0.1 a_0^{-1}$ FWHM) has been convoluted into the calculations of theoretical momentum distributions obtained using Clementi and Roetti wavefunctions of different qualities [CR74]. These are Hartree-Fock (solid line), double-zeta (dot-dashed line) and single-zeta (dot-short dashed line). For the np distribution, the calculations are normalized at the maximum

of the experimental distribution and for the ns distribution, the calculated distributions are area normalized in the range 0 to $1.5a_0^{-1}$. Clearly only shape comparison can be made with the present relative measurement. Note that the "sitting" experimental binding energies (not the theoretical Hartree-Fock I.P.'s) are indicated in the figures. This is of particular importance in the case of ns ionization in Ar, Kr and Xe where multiple final ion states occur due to many-body effects in the ionization process.

4.2.1 Helium

Figure 4.1 shows the binding energy spectrum of He. This spectrum is significant because it not only provides a measure of the experimental instrumental energy resolution, but also justifies the use of a Gaussian (rather than a Lorentzian) line shape for the structure deconvolution procedure, which is particularly important in the interpretation of the heavier members of the group. The Gaussian shape is due to the effect of the electron analyser transmission function (section 3.6.1) which dominates any effect of natural line shape. The zero background confirms the accuracy of the method used for substracting the accidental coincidences (section 3.3.2). The momentum distribution of He 1s electron is shown in figure 4.2. There is excellent agreement between the experiment and the

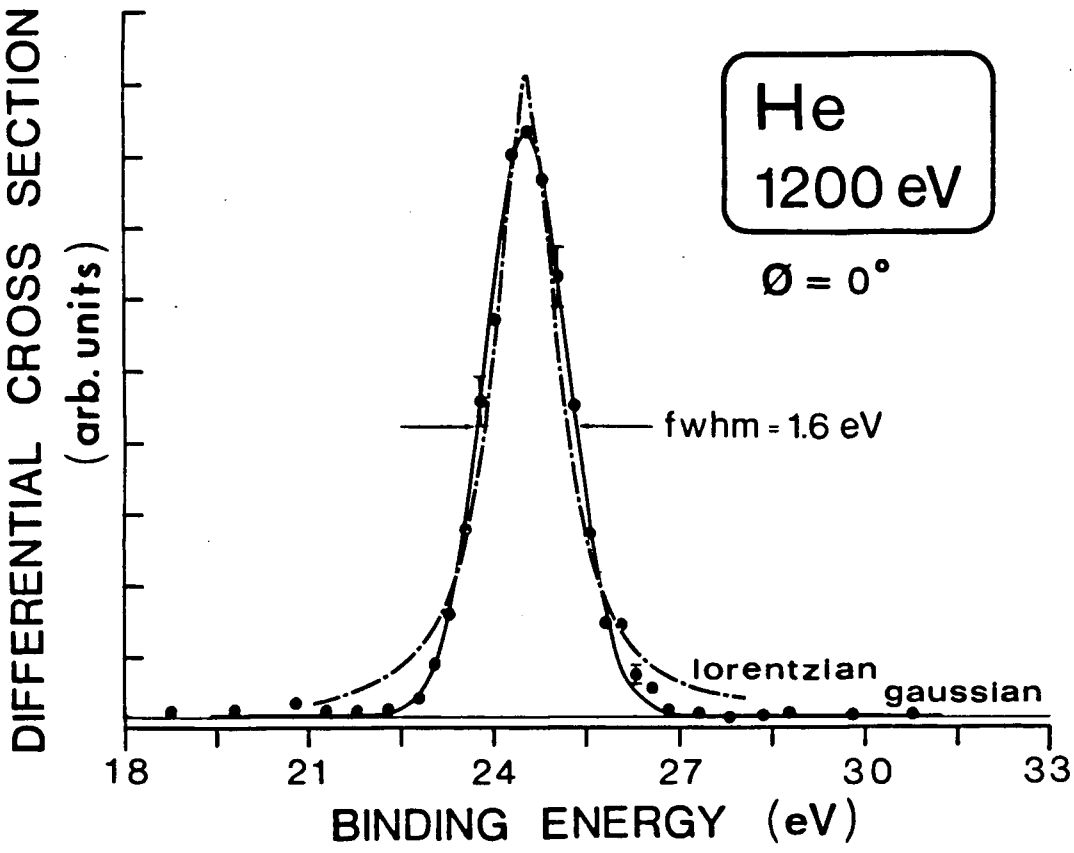

Figure 4.1 - Binding energy spectrum for He 1s ionization at ϕ=0°. The Gaussian and Lorentzian line shapes are indicated by solid and dot-dashed lines respectively.

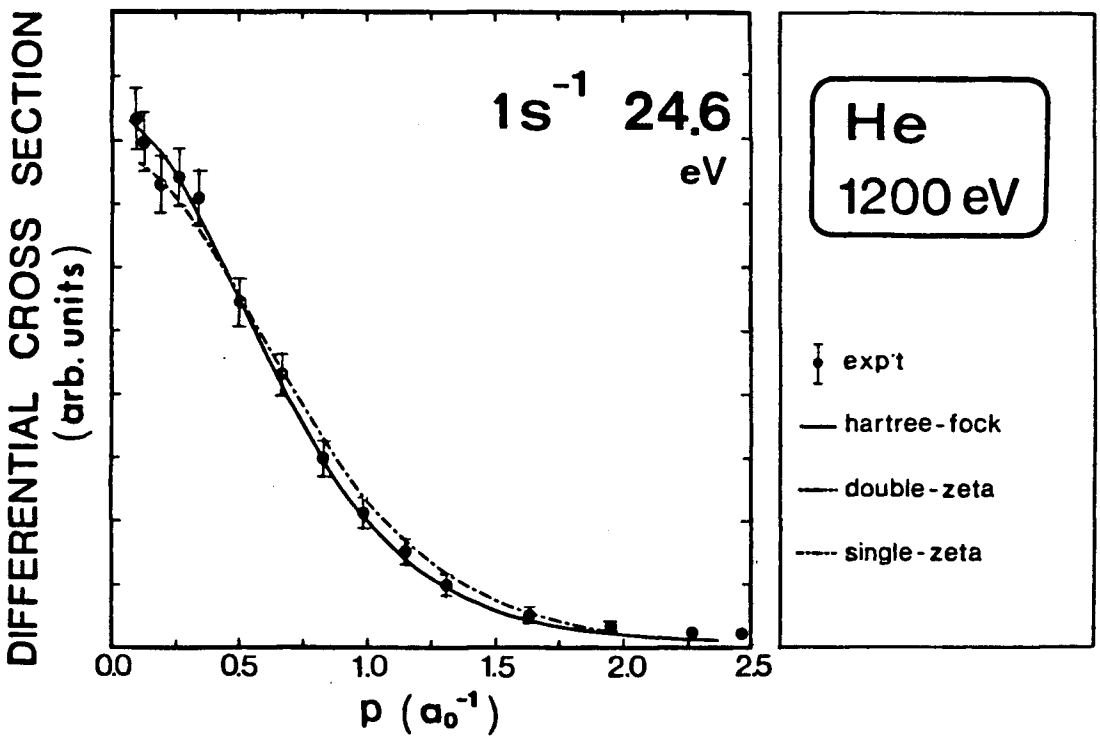

Figure 4.2 - Atomic momentum distribution of He 1s orbital. Theoretical distributions are calculated from Clementi and Roetti wavefunctions [CR74]. The Hartree-Fock and double-zeta theoretical distributions are indistinguishable from each other.

Hartree-Fock calculation as has also been seen in earlier work [HM&73]. This also constitutes an important consistency check of the instrumental function and also the convolution of the momentum resolution into the calculated momentum distribution.

4.2.2 Neon

Figure 4.3 shows the binding energy spectra of Ne at two different azimuthal angles (ϕ=0° and 10°) which correspond approximately to momentum values at the maxima of the 2s and 2p momentum distributions respectively (figure 4.4). The ϕ=0° spectrum emphasizes ionization of an s (l=0) orbital while the ϕ=10° spectrum emphasizes the p (l=1) orbital. In addition to the two main transitions which correspond to the $(2p)^{-1}$ and $(2s)^{-1}$ states, a third peak at 59.5eV is also found at ϕ=0°. In table 4.1 the energy positions and the relative intensities of 2s structure as determined by the present (e,2e) study are compared with other earlier (e,2e) [MW76a, DM&78], XPS [CKM71, SFC74] and optical emission data [P71]. A recent theoretical calculation by Dyall and Larkins [DL82a, DL82b] is also indicated.

Very briefly, the multiconfiguration shake model of Dyall and Larkins [DL82a, DL82b] includes electron correlation effects using a configurational interaction (CI) method where a limited number of relevant configurations are

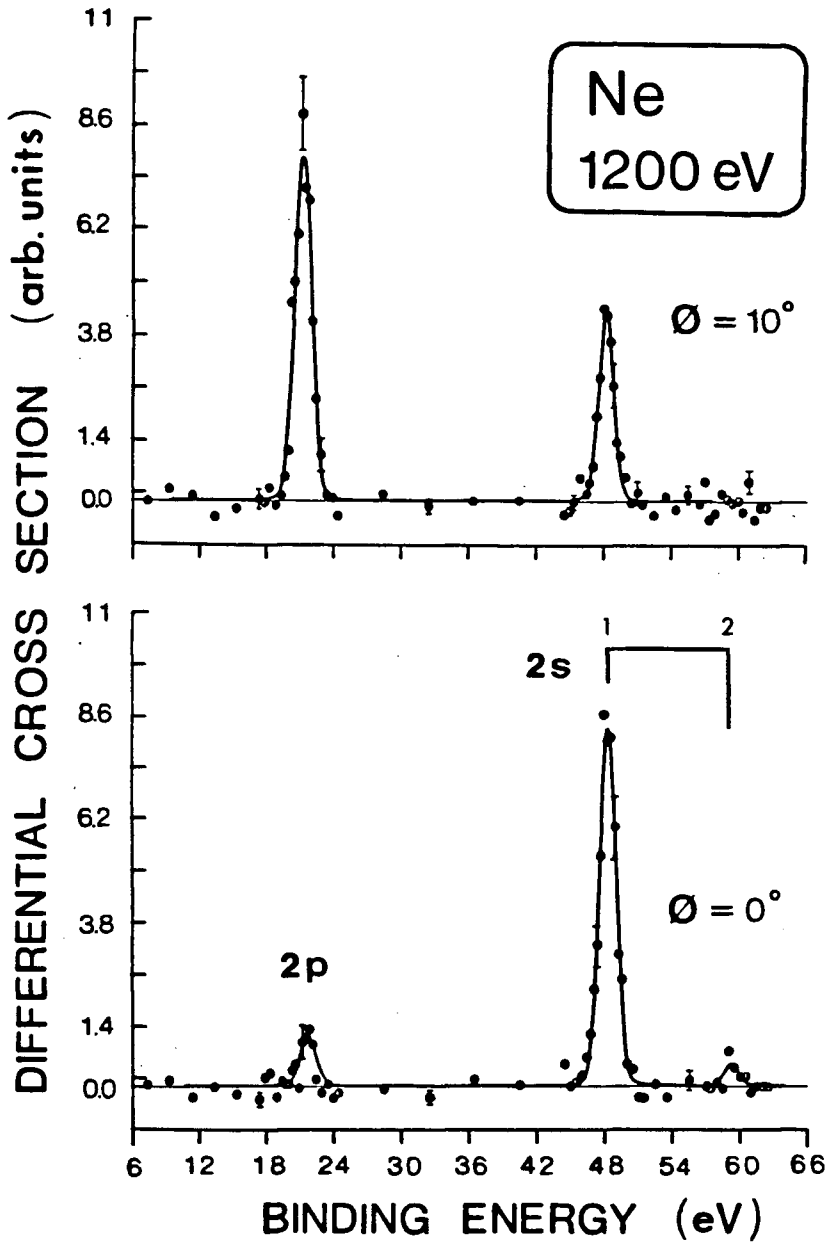

Figure 4.3 - Binding energy spectrum for Ne at ϕ=0° and 10°. Least squared Gaussian deconvolution of the experimental data is indicated by solid line.

Table 4.1
Satellite structure of Ne.

Peak*	Dominant Configuration	Energy (eV)						Relative Intensity				
		Binary (e,2e)		XPS		Optical	Theory	Binary (e,2e)		XPS		Theory
		This work	a	b	c	d	e	This work	a	b	c	f
1	$2s2p^5$	48.5	48.5	48.5	48.5	48.5	48.9	100	100	100	100	100
	$2s^22p^43s$			55.8	55.9	55.9	58.1			2	16	1
2	$2s^22p^43d$	59.5(4)	60	59.8	59.5	59.5	61.1	6(2)	4(1)	1	5	2
	$2s^22p^44d$						63.7					1

* : see figure 4.3;
a : reference [MW76a];
b : reference [SFC74], photon energy 1487eV;
c : reference [CKM71], photon energy 132.2eV;
d : reference [P71];
e : reference [DL82a];
f : reference [DL82b].

included. A single initial configuration is chosen and satellites appearing in the predicted spectrum are obtained by configuration interaction of the final ionic states with the same symmetry. The frozen core approximation is implicit in the calculation and the calculation is intended for high energy photon experiments.

Excellent agreement in the energy of the $(2s)^{-1}$ transition is found between the present and the earlier (e,2e) experiments, as well as with XPS and optical data. The relative intensities in (e,2e) cannot be related directly to those in XPS. Evidently, the theoretical intensities agree better with the XPS data at 1487eV [SFC74] than that at 132.3eV [CKM71] photon energies. Fair agreement is found between the two (e,2e) measurements of the relative satellite intensity for the $2s^22p^43d$ configuration. The satellite with $2s^22p^43s$ configuration at 56eV predicted by theory and found in XPS [CKM71, SFC74] and optical emission [P71] data is not observed in the binary (e,2e) spectrum in the present work nor in that of Dixon *et al*. [DM&78].

The momentum distributions of the 2p and 2s electrons are shown in figure 4.4. It can be seen that for both orbitals the SZ function is grossly inadequate whereas the HF gives an excellent description of the momentum distribution. The DZ function result is indistinguishable from HF in the case of the 2s orbital and is a slightly worse fit for the 2p orbital.

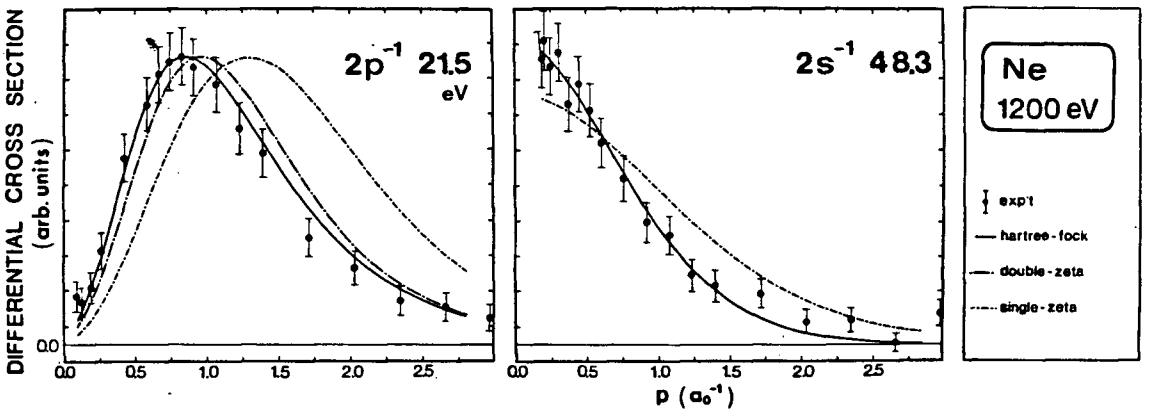

Figure 4.4 - Atomic momentum distributions for Ne 2p and 2s orbitals. The indicated energies are the sitting binding energies. The Hartree-Fock and double-zeta [CR74] distributions for Ne 2s are indistinguishable from each other.

4.2.3 Argon

The angular correlated binding energy spectrum of argon is shown in figure 4.5. The first peak (at 15.6eV) corresponds to ionizations of the 3p electrons. The peak at 29.8eV and the satellite structure at higher energy is due to ionization of the 3s electrons. Gaussian deconvolution is performed to identify the more intense satellite states. The intensities of these states generally decrease from the maximum at ϕ=0° as ϕ increases, indicating an overall s-type angular dependence. Table 4.2 gives the energy positions and the relative intensities of the parent and satellite $(3s)^{-1}$ transitions obtained by the (e,2e) [MW76a, W78], XPS [CKM71, SFC74] and optical [N73] experiments. Excellent agreement in energy positions is obtained between the various different experiments. Also shown are the multiconfiguration shake model calculations of Dyall and Larkins [DL82a, DL82b] as well as a more detailed CI calculation by Mitroy [M83] which includes continuum effects and also initial and final state correlations. There is a discrepancy of approximately 1eV between most of the calculated energies and the experimental results. It is evident that the calculations by Mitroy [M83] gives the best agreement with the relative intensities measured by binary (e,2e) spectroscopy. The calculated relative intensities by Dyall and Larkins [DL82a, DL82b] appear to be in better agreement with the XPS measurements than with the (e,2e) data.

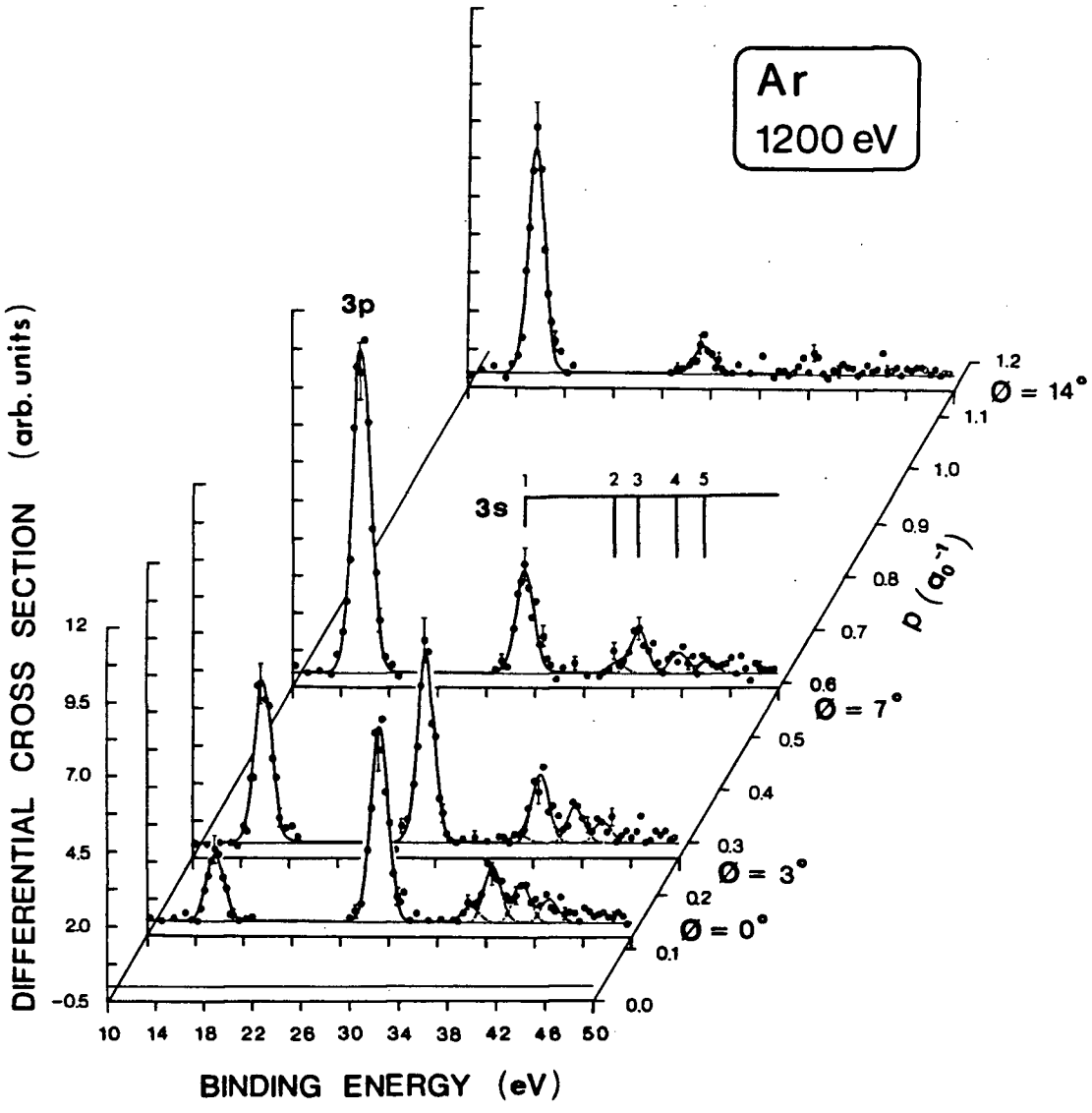

Figure 4.5 - Angular correlated binding energy spectrum for Ar. The momentum, p, scale is approximate. Individual Gaussian line shapes (dot-dashed lines) are least squared fitted to the spectrum. The sum of the Gaussians is represented by the solid line.

Table 4.2
Satellite structure of Ar.

Peak*	Dominant Configuration	Energy (eV)								Relative Intensity						
		Binary (e,2e)			XPS		Optical	Theory		Binary (e,2e)			XPS		Theory	
		This work	a	b	c	d	e	f	h	This work	a	b	c	d	g	h
1	$3s3p^6$	29.3(1)	29.3(1)	29.3	29.3(1)	29.2	29.22	28.78	28.95	100	100	100	100	100	100	100
2	$3s^13p^64s$	36.8(4)		36.7	37.4(2)	36.6	36.48	37.28	37.51	7(3)		5	3(2)	3	2	2
3	$3s^13p^63d$	38.6(1)	38.6(1)	38.6	38.7(1)	38.4	38.56	39.34	39.72	32(3)	40(3)	41	19(2)	19	13	27
4	$3s^13p^64d$	41.2(2)	41.2(2)	41.2	41.2(2)	40.6	41.19	41.77	42.37	20(3)	22(3)	25	6	9	9	12
5	$3s^13p^65s$ $3s^13p^65d$	43.5(2)	43.4(1)	43.4		42.1	42.41	42.90 43.06		12(3)	10(3)	11			2 2	

* : see figure 4.5;
a : reference [MW76a];
b : reference [W78];
c : reference [SFC74], photon energy 1487eV;
d : reference [CKM71], photon energy 132.2eV;
e : reference [N73];
f : reference [DL82a];
g : reference [DL82b];
h : reference [M83].

There are also some small differences in relative intensities between the present noncoplanar (e,2e) data and those of the coplanar (e,2e) data of Williams [W78]. The relative intensities of the first three satellites obtained by Williams are generally higher as compared with those in the present study. In the case of the $3s^2 3p^4 3d$ state[2] the difference is quite large. The present study, however, shows good agreement with the previous (e,2e) measurement of McCarthy and Weigold [MW76a]. With a poorer energy resolution, the weak structure at 36.8eV was not reported by these authors [MW76a] and it is likely that the reported peak at 38.6eV actually corresponded to the first two excited ionic states. The sum of the intensities of the first two states in the present study (38%) is in excellent agreement with the reported [MW76a] intensity (40%). The sum derived from Williams' data is, however, 47%. The third satellite reported by Williams is also more intense compared to both noncoplanar (e,2e) results. These discrepancies may be the result of different scattering conditions, since Williams used the coplanar scattering kinematics with rather low impact energy (E_0>300eV or $E_1=E_2$=150eV) where the variation of the cross section due to the Mott scattering factor is more severe. Under these low energy conditions, it is well

---

[2] The configuration given to a state in the present work implies the dominant configuration in the CI expansion.

known [MW76a] that the impulse approximation is less adequate and it has been found that relative intensities are modified accordingly. In particular it has been found that although correct momentum distributions are given at E_0=400eV [MW76a] the relative intensities of different peaks are not in conformity with PWIA calculations. Even at 1200eV impact energy significant differences have been observed between PWIA calculations and experiment particularly for inner valence molecular orbitals similar to the s orbitals in the noble gases [BH&80, BM&82].

To definitively assign some of the most prominent satellites as arising from the 3s hole state, momentum distributions have been measured at 38.5eV and 41.1eV (figure 4.6). Typical s-type behavior is obtained in each case. As with helium and neon, Hartree-Fock (indistinguishable from DZ) wavefunctions can be used to reproduce the experimental distributions much better than the SZ wavefunctions for both 3p and 3s electrons.

4.2.4 Krypton

Figure 4.7 shows the angular correlated binding energy spectrum of Kr. Similar results for krypton were also determined recently by Fuss *et al*. [FG&81] The angles at which the binding energy scans were taken are slightly different in the present case but nevertheless it is apparent

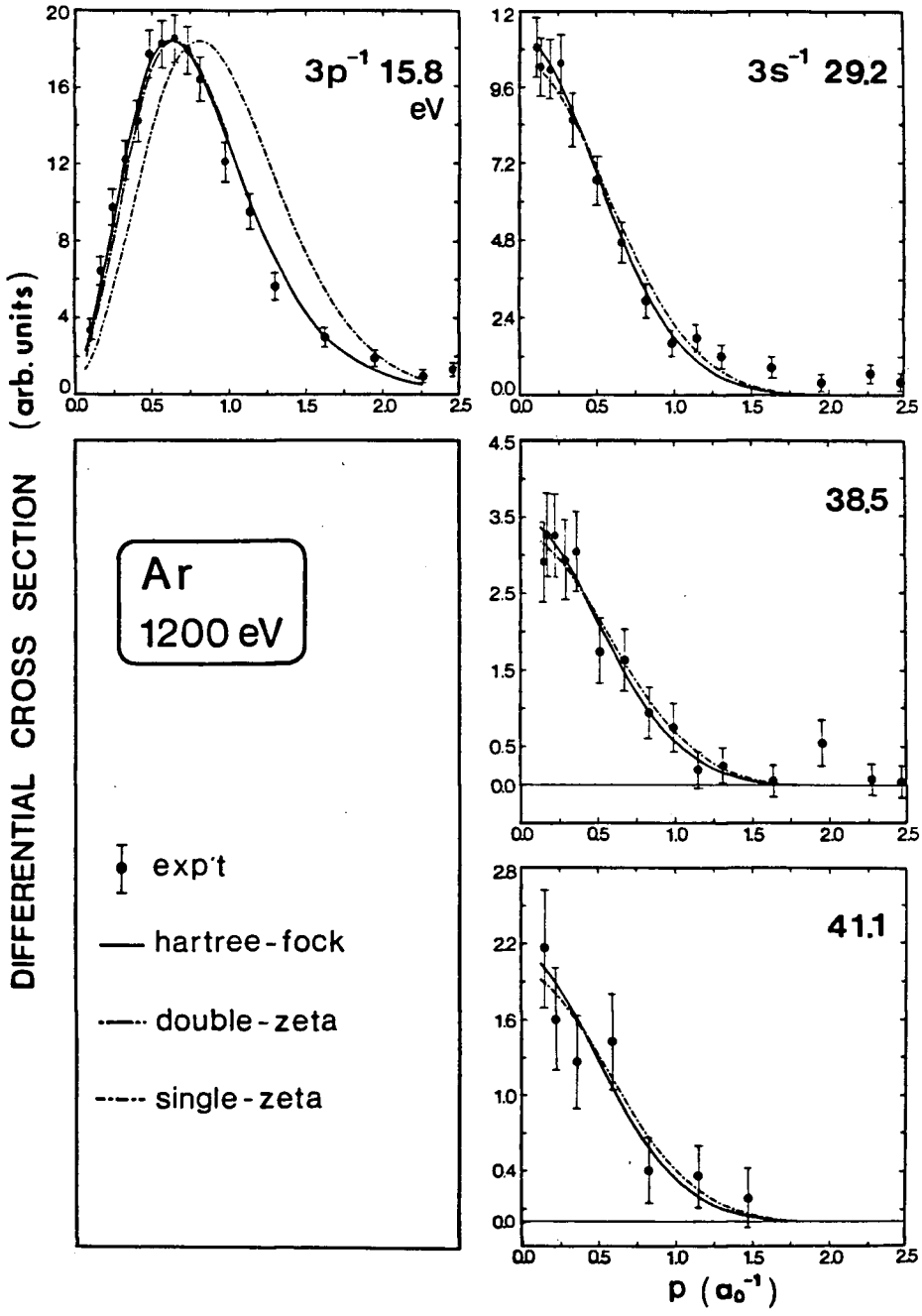

Figure 4.6 - Atomic momentum distributions for Ar. The s-type distributions at 29.2, 38.5 and 41.1eV correspond to ionic states labelled 1, 3 and 4 in fig. 4.5 respectively. The HF and DZ distributions for Ar 3s are indistinguishable from each other.

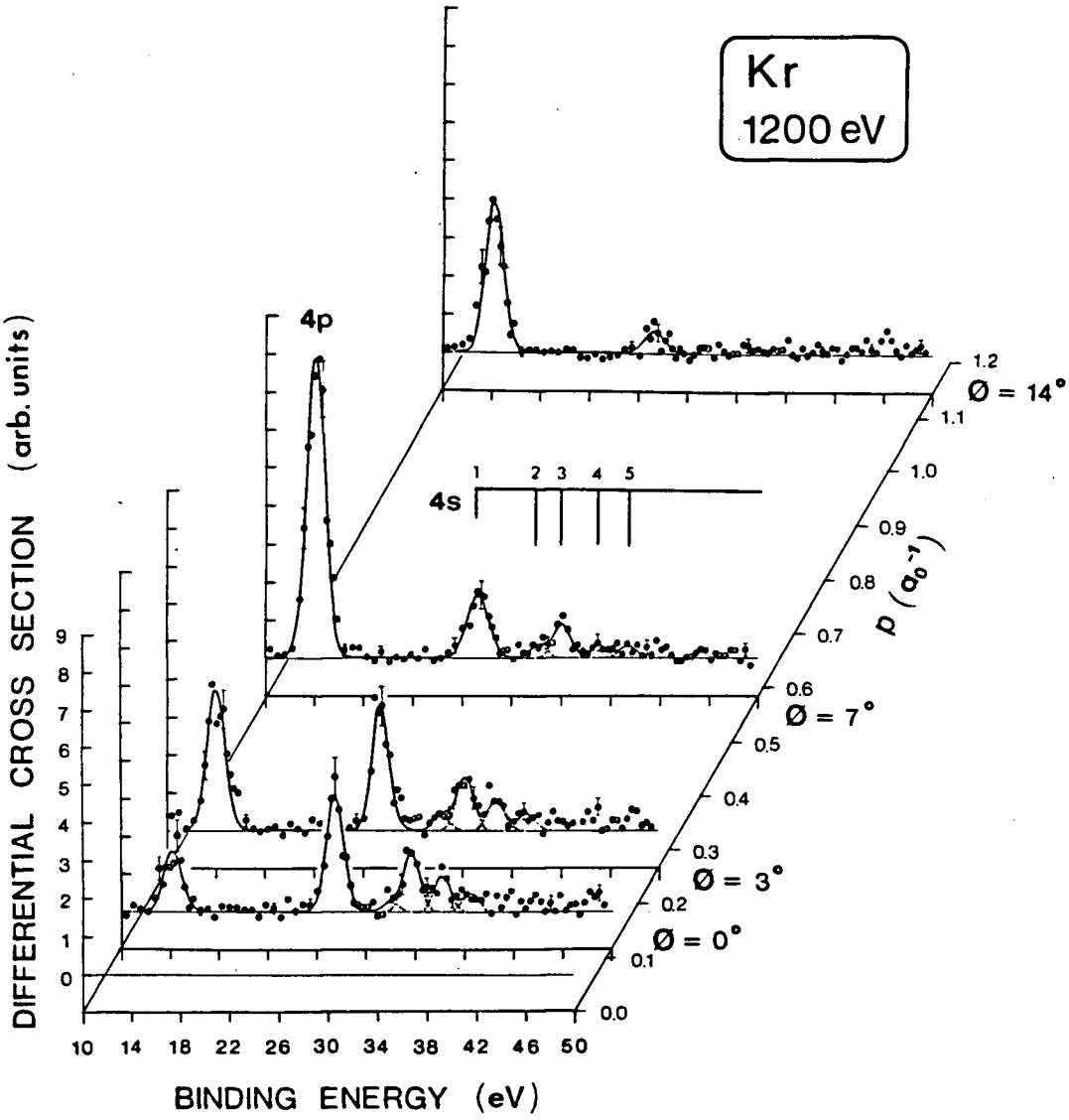

Figure 4.7 - Angular correlated binding energy spectrum for Kr. The momentum, p, scale is approximate. Individual Gaussian line shapes (dot-dashed lines) are least squared fitted to the spectrum. The sum of the Gaussians is represented by the solid line.

that the two sets of spectra are in excellent agreement. As in the case of argon 3s, there are considerable electron correlation effects in the 4s ionization of krypton, resulting in significant population splitting of the s hole among several final ionic states. The energy positions and satellite intensities are summarized in table 4.3. Excellent agreement in energies are found in all experiments. There is good agreement between the spectra obtained in the binary (e,2e) work and those reported by Fuss *et al*. [FG&81]. In addition to the two satellites reported previously [FG&81], the presence of satellite states at 36.7eV and 39.1eV is indicated by the Gaussian deconvolution procedure. With reference to the multiconfiguration calculations of Dyall and Larkins [DL82a, DL82b], these two states are tentatively assigned to the $4s^2 4p^4 5d$ configuration and an admixture of $4s^2 4p^4 6s$ and $4s^2 4p^4 6d$ configurations respectively. Obviously better resolution and improved statistics are required to further define these inner valence satellite structures. It is interesting to note that the calculations by Dyall and Larkins are in no better agreement with the measured (e,2e) satellite intensities than are the results of a large series of ground state and final ionic state CI calculations reported by Fuss *et al*. [FG&81]. The calculations of Fuss *et al*. [FG&81] took into account of the continuum but used only a limited number of configurations. However better agreement with the XPS data is obtained by Dyall and Larkins.

Table 4.3
Satellite structure of Kr.

Peak*	Dominant Configuration	Energy (eV)						Relative Intensity				
		Binary (e,2e)		XPS	Optical	Theory		Binary (e,2e)		XPS	Theory	
		This work	a	b	c	a	d	This work	a	b	a	e
1	$4s4p^6$	27.3(2)	27.5(1)	27.5	27.51	27.5	26.48	100	100	100	100	100
2	$4s^24p^45s$	32.2(5)	32.1(2)	32.4	32.07	32.1	32.29	11(6)	15(4)	9(2)	4	3
3	$4s^24p^44d$	34.0(2)	33.9(1)	34.0	33.93	33.9	34.22	47(6)	43(4)	25(3)	22	20
4	$4s^24p^45d$	36.7(3)	>35.5			>35.5	36.46	27(6)	59(7)		56	13
5	$4s^24p^46s$ $4s^24p^46d$	39.1					37.40 37.64	15(6)				2 5

* : see figure 4.7;
a : reference [FG&81];
b : reference [SFC74], photon energy 1487eV;
c : reference [MSP69];
d : reference [DL82a];
e : reference [DL82b].

Momentum distributions at several "sitting" binding energies are given in figure 4.8. The first and the second peaks in the binding energy spectrum correspond to the ionization of the 4p and the principal hole state for the removal of 4s electrons respectively. The other momentum distributions spectra show that the satellites at 33.8eV and 36.2eV are clearly due to the 4s electron. The Hartree-Fock (indistinguishable from DZ) wavefunction closely predicts the measured momentum distributions.

4.2.5 Xenon

Figure 4.9 shows the angular correlated binding energy spectrum of Xe. Table 4.4 compares the present (e,2e) data with other related experimental data. Two Gaussians are fitted to the first $(5p)^{-1}$ peak to account for the well known (1.3eV) spin-orbit splitting of $^2P_{3/2}$ and $^2P_{1/2}$ states of Xe^+. Gaussian deconvolution was used to decompose the structure above 28eV into four CI states as suggested by Dyall and Larkins' calculations [DL82a, DL82b]. The present binding energy spectrum (figure 4.9) is in general agreement with the low resolution data of the Flinders University group [MW76a] and it is also in accord with the higher resolution (1.0eV FWHM) spectrum obtained by Hood *et al.* [HHB77]. Extra unassigned states in the 24 to 26eV region (which are labelled 1 and 2 by Hood *et al.*) are clearly present in the

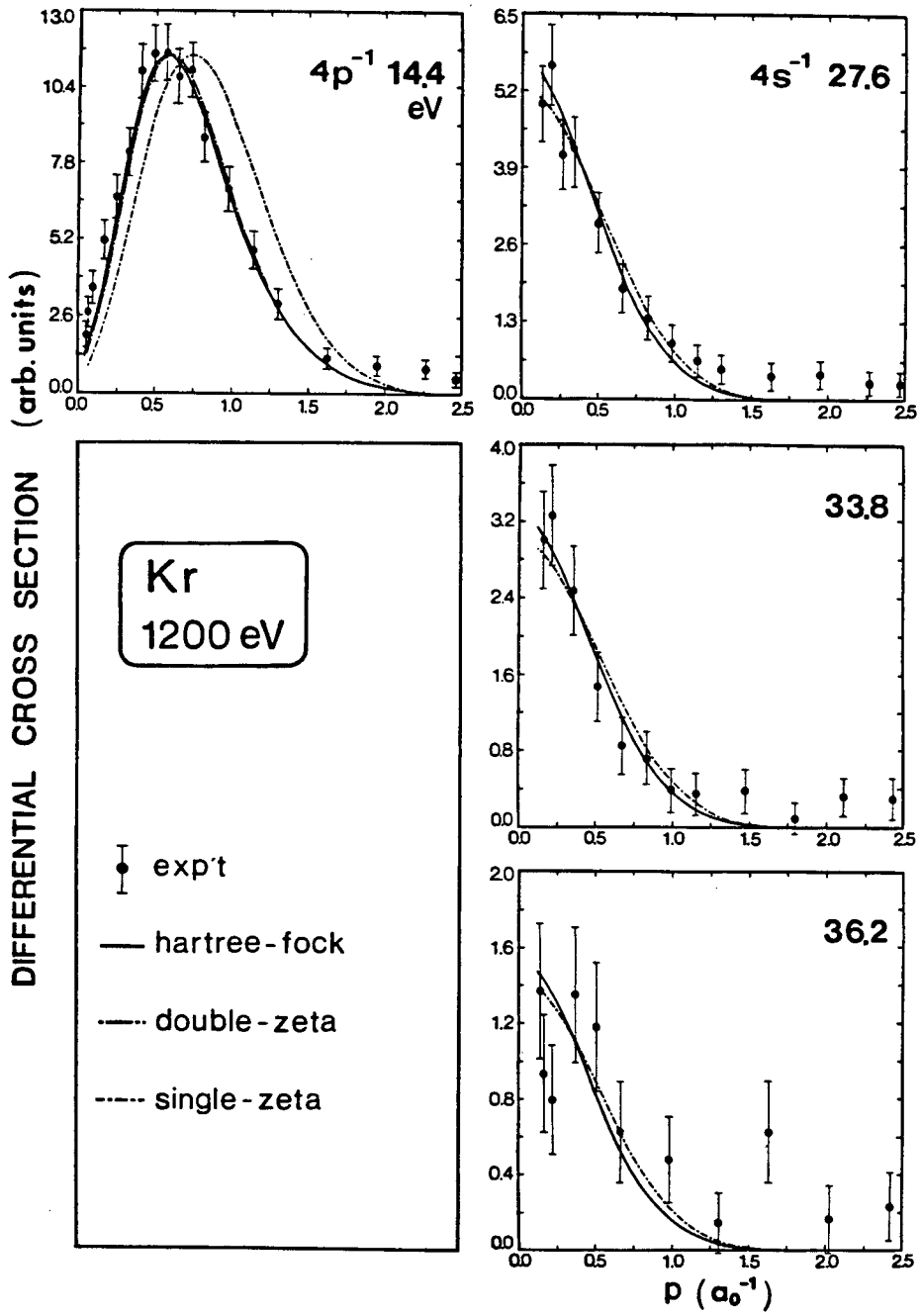

Figure 4.8 - Atomic momentum distributions for Kr. The s-type distributions at 27.6, 33.8 and 36.2eV correspond to ionic states labelled 1, 3 and 4 in fig. 4.7 respectively. The HF and DZ distributions for Kr 4s are indistinguishable from each other.

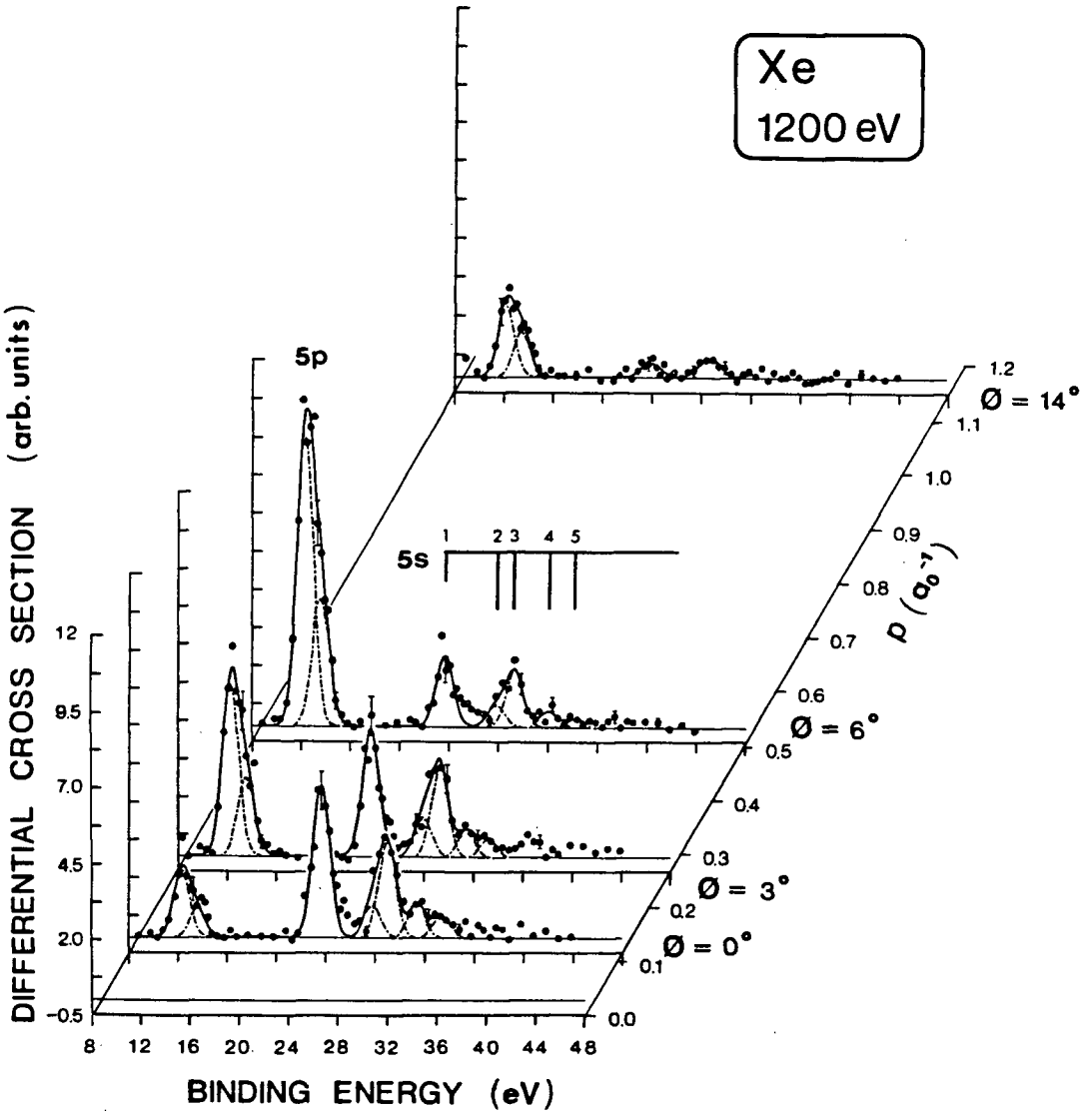

Figure 4.9 - Angular correlated binding energy spectrum for Xe. The momentum, p, scale is approximate. Individual Gaussian line shapes (dot-dashed lines) are least squared fitted to the spectrum. The sum of the Gaussians is represented by the solid line.

Table 4.4
Satellite structure of Xe.

Peak*	Dominant Configuration	Energy (eV)						Relative Intensity				
		Binary (e,2e)		XPS		Optical	Theory	Binary (e,2e)		XPS		Theory
		This work	a	b	c	d	e	This work	a	b	c	f
1	$5s5p^6$	23.2(1)	23.2(1)	23.4	23.4	23.37	21.36	100	100	100	100	100
	?			24.6						6(2)		
	?			25.2						7(2)		
2	$5s^15p^46s$	27.7(3)	>28.1	28.0	27.6	28.13	27.49	26(8)	194(4)	25(4)	11(3)	6
3	$5s^15p^45d$	28.9(1)		29.0	29.0	28.85	28.83	67(8)		52(4)	62(7)	24
4	$5s^15p^46d$	31.2(3)		31.4			30.91	23(5)		20(3)		16
5	$5s^15p^47s$			32.8			31.93			6(2)		3
	$5s^15p^47d$	33.1		33.8			32.12	15(5)		4(2)		6

* : see figure 4.9;
a : reference [MW76a];
b : reference [G74], photon energy 1487eV;
c : reference [SFC74], photon energy 1487eV;
d : reference [HP78];
e : reference [DL82a];
f : reference [DL82b].

form of a shoulder on the high energy side of the main $(5s)^{-1}$ peak. Similar satellites are also reported in the high resolution XPS data of Gelius [G74]. It is possible that these states are the result of initial state configuration interactions.

Momentum distributions are measured at several binding energies (figure 4.10). Excellent agreement between Hartree-Fock (and DZ) momentum distributions and the experimental ones are observed. The s-type momentum distributions at 29.0eV and 33.5eV confirm that the dominant configurations $5s^25p^45d$ and $5s^25p^47s/7d$ are excited ionic states arising from the $5s^{-1}$ hole state. The observation of the deep minimum in the extremely sharp momentum distribution of the 5p electron is in confirmation of the high angular resolving power of the present spectrometer.

4.3 SATELLITE STRUCTURE

To summarize, there is generally good agreement between the present (e,2e) data and other experimental data in the energy positions of satellite states above the main $(ns)^{-1}$ parent transitions. The relative intensities of these transitions in (e,2e) and (γ,e) (or photoelectron) experiments cannot be compared directly because of the different ionization conditions. The intensities of most of these satellites relative to that of the parent $(ns)^{-1}$ hole

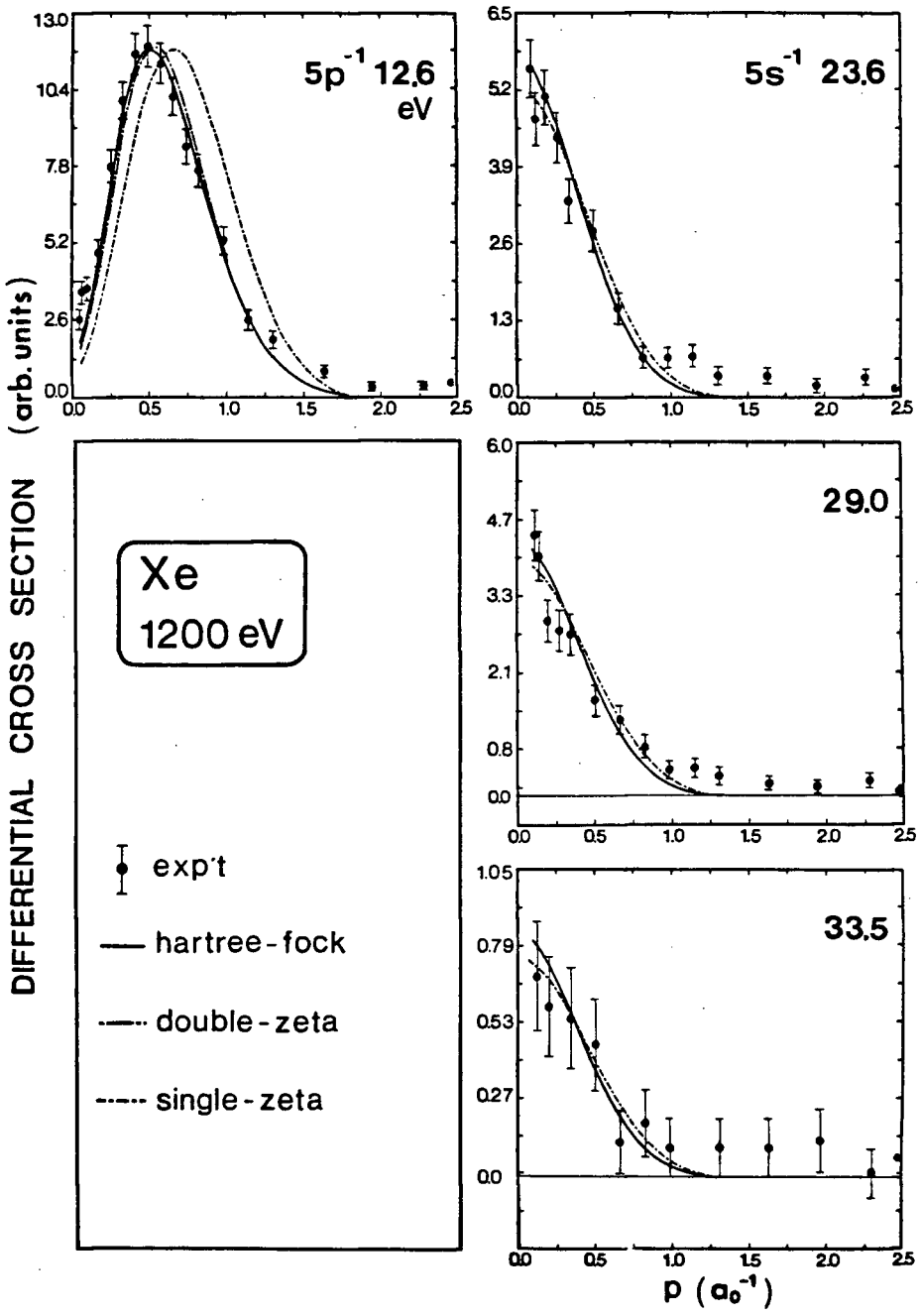

Figure 4.10 - Atomic momentum distributions for Xe. The s-type distributions at 23.6, 29.0 and 33.5eV correspond to ionic states labelled 1, 3 and 4 in fig. 4.9 respectively. The HF and DZ distributions for Xe 5s are indistinguishable from each other.

state obtained by (e,2e) studies are 1 to 3 times larger than those obtained by (γ,e) studies. However, it should be noted that there is closer agreement in the case of xenon between (e,2e) and (γ,e) measurements. It is also interesting to note in tables 4.1 to 4.4 that for ^2S symmetry, the $ns^2np^4n'd$ (n'=n+1,n+2, etc.) satellites are much more intense than the $ns^2np^4n's$ satellites.

There is some confusion in some of the assignments by Spears *et al.* [SFC74]. For instance the assignment of the satellite at 32.2eV of Kr to the "$5p(^2P_0)$ shake-up" configuration [SFC74] does not agree with the measured s-type momentum distribution and should be assigned to a $4s^24p^45s$ dominant configuration as indicated in table 4.3. Also the variation of satellite intensities with momentum in the angular correlation binding energy spectra suggests a "global" s-type angular behaviour, reinforcing the conclusion that the satellite structure is mainly the result of final ionic state configuration interaction associated with the $(ns)^{-1}$ hole.

There are several interesting trends in the binding energy spectra of the noble gases, all of which can be understood within the framework of the quantum chemistry of atoms. Figure 4.11 shows the ϕ=0° binding energy spectra of the noble gases grouped together to emphasize some of these chemical trends. One striking feature is the overall increase in satellite intensities as compared to the parent

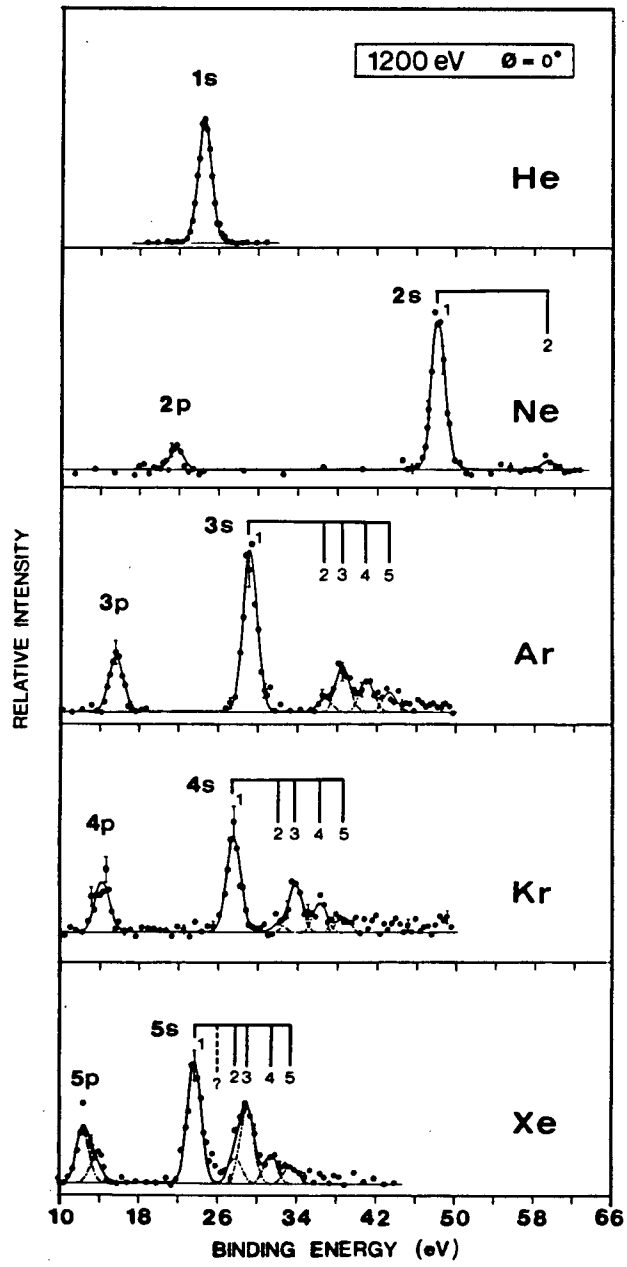

Figure 4.11 - Comparison of valence binding energy spectra of Noble Gaeses. The ionic states identified by Gaussian deconvolution are labelled in each of the spectra. See also tables 4.1-4.4.

intensities as one moves down the group: i.e. from Ne to Xe. Table 4.5 shows the ratio of the total intensity of the deconvoluted satellite states to the intensity of the parent state. This is a lower limit since there will be some further contribution from higher lying excited and continuum states. The increase in satellite intensity proceeding down the group is also observed in XPS data and predicted by Dyall and Larkins' calculation [DL82a, DL82b]. The onset of the increase really begins with Ar and not with Ne. This is consistent with the idea that the $ns^2np^4n'd$ configurations are more important than the $ns^2np^4n's$ series because of the fact that there is no d orbital in the n=2 shell.

The second noticeable trend with increasing atomic number is the decrease in energy separation in the $(ns)^{-1}$ manifold between the first excited ion state and the parent ion $(ns)^{-1}$ state. This is again consistent with the fact that the energy spacings between shells decrease with increasing principal quantum number. The decrease in energy spacings results in more configuration mixing and further enhances the overall satellite intensities.

Table 4.5
Total assigned satellite intensity relative to the parent for the ns ionization of Noble Gases.

Species	Total assigned Sat. Int./Parent Int.*		
	(e,2e) This work	XPS a	Theory b
Ne	0.06	0.03	0.04
Ar	0.70	0.28	0.28**
Kr	1.00	0.34	0.43
Xe	1.31	1.07	0.55

a : reference [SFC74], photon energy 1487eV;
b : reference [DL82b].
* : Only the measured peaks shown in tables 4.1-4.4 are taken into consideration. The contribution from higher excited and continuum states is not included.
**: compare also 0.43 (reference [M83], which does not include intensity from peak 5 - table 4.2) and 0.40 (reference [W79]).

4.4 OUTER VALENCE ORBITAL ELECTRON MOMENTUM DISTRIBUTIONS

In order to further explore the existence of any chemical trend associated with the momentum distribution of the outer valence orbitals of the noble gases, the momentum distributions of np and ns series in the momentum range from 0 to $2.5a_0^{-1}$, are shown along with the corresponding Hartree-Fock directional momentum density and position (or charge) density contour maps in figures 4.12 and 4.13 respectively. The arrows on the momentum distributions indicate p_{max} (i.e. the momentum at which the probability distribution is at its maximum height) for the np series and $p_{1/2max}$ (i.e. the momentum at which the distribution is half of its maximum) for the ns series. All the other notations are identical to those in the previous momentum distribution (figures 4.2, 4.4, 4.6, 4.8 and 4.10). The density maps show the "directional" probability of an orbital in both momentum and position-space. In particular, the present momentum contour maps sample probability momentum density $(\psi_j^*(\mathbf{p})\psi_j(\mathbf{p})$ where $\psi_j(\mathbf{p})$ is the j^{th} orbital of the Hartree-Fock wavefunction in the momentum representation) in the $p_x=0$ plane, and similarly the position density maps sample the corresponding position density in the $r_x=0$ plane. The contour values are logarithmic, namely, at 0.2, 0.4, 0.6, 0.8, 2, 4, 6, 8, 20, 40, 60 and 80% of the maximum density. Note that the range of the position density maps for the ns series (figure 4.13, right hand side) is from -0.5 to 0.5 a_0

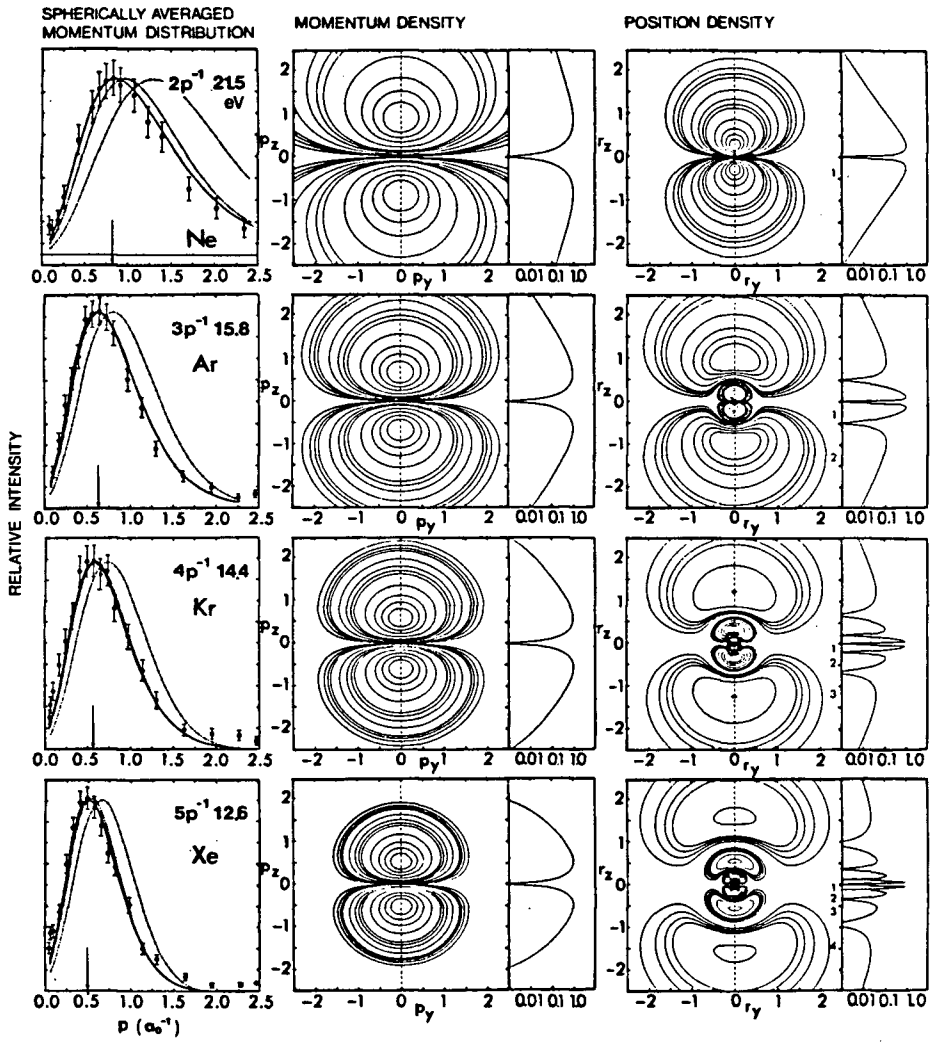

Figure 4.12 - Momentum distributions (left), momentum density (centre) and position density (right) maps for np orbitals of Noble Gases. The arrows in the momentum distributions indicate p_{max}.

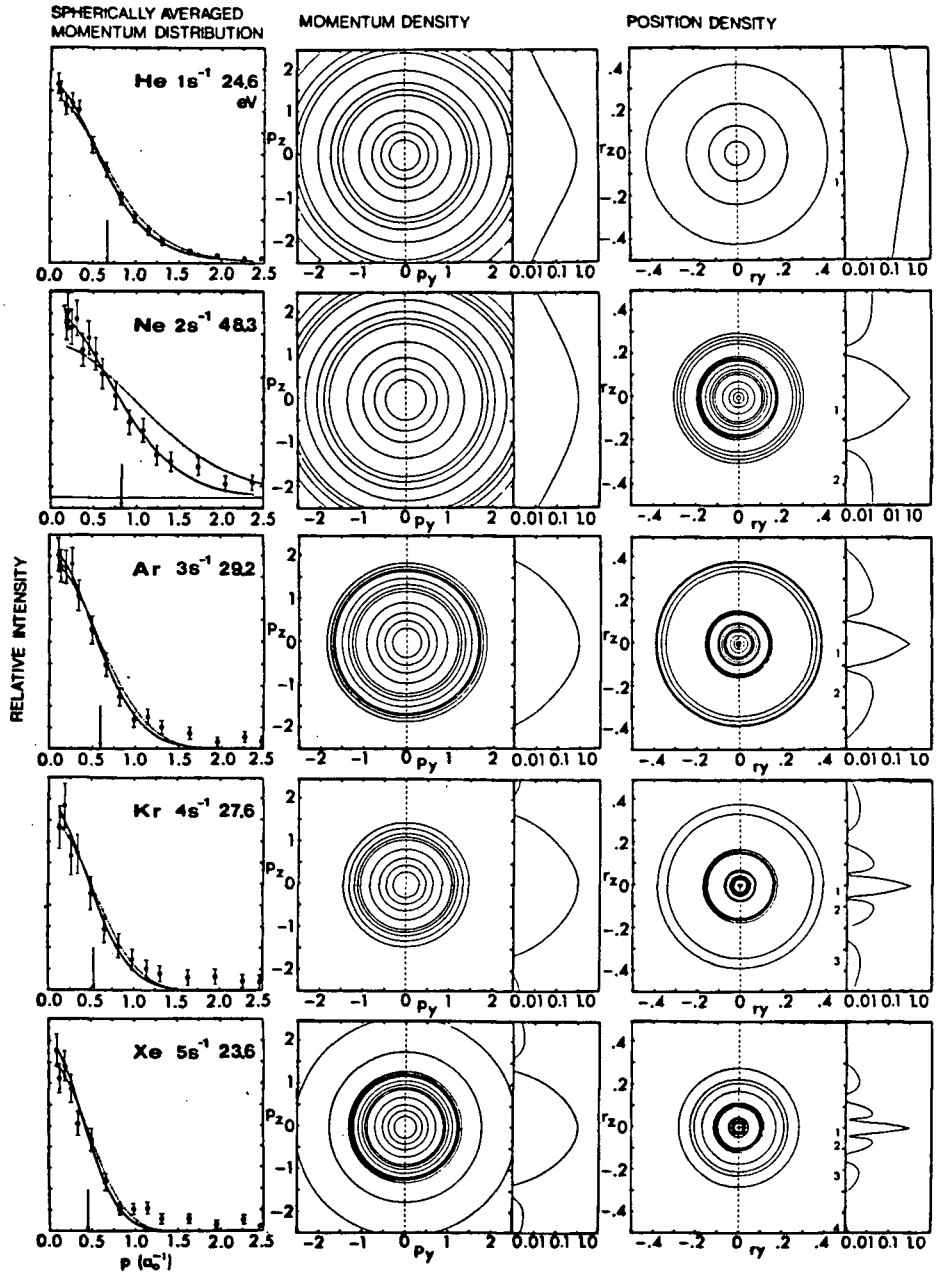

Figure 4.13 - Momentum distributions (left), momentum density (centre) and position density (right) maps for ns orbitals of Noble Gases. The arrows in the momentum distributions indicate $p_{1/2max}$.

while the range for all the other maps in figures 4.12 and 4.13 is from -2.5 to 2.5 a.u. in both position and momentum space. Along with the density maps, line projections (also with logarithmic intensity) of the density surfaces are shown to give some idea of the overall one dimensional density projection along a certain axis. The line projection plots are useful in providing an immediate indication of the relative density magnitude associated with each equidensity contour line in the sampling plane. In the diagrams the z axis (shown by the dash line in the density maps of figures 4.12 and 4.13) is chosen for the projection.

There are several noteworthy features in the two figures. The Hartree-Fock wavefunction, which gives the lowest total energy, is the best of the three wavefunctions for describing the spherically averaged momentum distribution (see left hand sides of figures 4.12 and 4.13). The double-zeta result is almost as good as the Hartree-Fock and is in fact indistinguishable from Hartree-Fock in the case of the ns orbitals. The single-zeta is inadequate particularly in the case of the np distributions. In the fairly broad distributions such as those of Ne the differences between the calculated distributions of different quality are greater. It is also interesting to note that the better the quality of the wavefunction, the smaller are p_{max} and $p_{1/2max}$.

Although the momentum distributions of Hartree-Fock (and to a lesser extent the double-zeta) wavefunctions are in

excellent agreement with the experimental distributions, there remain some small discrepancies especially at momenta $\geq 1.5a_0^{-1}$ in spectra of the heavier members of the group. These small differences are particularly obvious in the Kr 4s and Xe 5s spectra. It is interesting to note that this discrepancy tends to increase down the group. For instance the Ne 2p and Ne 2s distributions are in quite good agreement with the respective calculations up to $\simeq 2.2a_0^{-1}$ whereas the Xe 5p and Xe 5s tails appear at approximately $1.5a_0^{-1}$. Previous distorted wave calculations by Dixon *et al.* [DMW76] suggested the inadequacy of the plane wave impulse approximation. The trend seen in the present study is consistent with the idea of Dixon *et al.* that distortion of the electron waves is more severe in the high momentum region. This distortion apparently depends upon the spatial extent of the orbital itself. Another possible cause of the discrepancy is the inadequacy of the Hartree-Fock wavefunction itself. The importance of configuration interactions and relativistic effects on the momentum density in the high momentum region still awaits further theoretical investigation. These effects may also be partly responsible for the small discrepancy between the calculations and the experiments in the very low p region. There is also a possibility that the range of validity of the reaction model will vary depending on the nature of the target species.

Perhaps the most noticeable trend of the np and ns

momentum distributions is the increase in momentum probability contraction with principal quantum number. This can be seen quite clearly with the increasingly sharper momentum distribution going down the group and the decreasing p_{max} and $p_{1/2max}$. Similar effects have been seen in the isoelectronic hydrogen halides: HF, HCl, HBr and HI [BH&80, BM&82]. This behavior can be understood in the light of the Fourier transform (FT) properties. As discussed in chapter 2, the four commonly referred to FT effects are the inverse spatial relation, the existence of an inversion centre at the origin of the momentum-space, molecular density directional reversal and molecular density oscillation effects [CD41, ET77, CB82a, CB82b, MB&83]. In the case of atoms, only first two are relevant. The property of spatial reversal is fundamental in the interpretation of the momentum-space chemistry [CD41, ET77] both for atoms and for molecules since the basic LCAO-MO formalism is identical in the two Hilbert spaces and this will be further elaborated below.

Momentum density maps and position density maps are also shown in figures 4.12 and 4.13 in order to facilitate the understanding of the inverse spatial property between position and momentum space. Before discussing this property, it should be noted that the spherical harmonics are invariant under the Fourier transform (see table 2.1). The angular dependence of the atomic wavefunction is therefore preserved in both spaces and only the radial part of the

wavefunction is affected. Hence a totally symmetric function such as the ns orbital has the same shape in both momentum and position space (see figure 4.13). One has to be careful, however, in making the comparison since the somewhat different appearance in the np maps is largely due to the inverse spatial relation and the relative prominence of lobes (nodes) in position and momentum space.

The inverse spatial relation says that a contraction of probability density in one space will lead to an expansion in the other space and vice versa. (This spatial reversal relation is also associated indirectly with the bond directional reversal effect in molecules.) The trend in the momentum distributions is a direct consequence of this inverse spatial relation. It is perhaps easier to see this phenomenon in the np series. Orbital density expansion in position-space from Ne 2p to Xe 5p is demonstrated in the overall contour expansion in the position density maps and particularly in the associated z-axis position density projection plots (figure 4.12), where the redistribution of the np probability density over (n-1) lobes is clearly illustrated. (Each lobe is labelled in the projection plots.) That the position density expansion is associated with the corresponding contraction in the momentum-space can be most clearly seen in figure 4.12, centre column. In contrast to the position density maps, the secondary lobes in the momentum density are much too weak to be seen when

compared to the primary ones even if a log density scale of three decades is used. These secondary lobes occur outside the range of the momentum density maps in figure 4.12 but will be discussed below (see figure 4.14). The majority of the momentum density of the np orbital is therefore concentrated in the first lobe, in contrast to the increased significance of the "higher" secondary lobes in position-space.

For the ns series, the inverse spatial property is not as immediately obvious in the density maps. Also it should be noted that the helium 1s orbital does not lie in the general trend which is not surprising due to the unique nature of the n=1 shell. It is clear in the z-axis density projection plot that the ns position density of the noble gases is distributed over n lobes, with the first (n-1) lobes having the most significant relative intensities (note the log scale on figure 4.13). In the position density maps, the region from -0.5 to 0.5 a_0 is shown in order to emphasize the most significant lobes which "shrink" considerably into the origin with increasing principal quantum number. With this limited range, the last lobes in Ar 3s and Kr 4s and the last two lobes in Xe 5s (the wing of the 4th lobe is just visible at the extremes of the projection plot) cannot be seen. The overall expansion of position density can be observed from figure 4.13 reasonably well in the limited range of the projection plots if only the first (n-1) lobes are

considered.

To further illustrate the idea of position density expansion versus momentum density contraction, extended range logarithmic plots of the spherically averaged (i.e. radial) momentum density and position density functions (both constructed from Hartree-Fock wavefunctions [CR74]) are shown in figures 4.14 and 4.15 respectively. The solid lines correspond to the radial functions of ns orbitals while the dash lines correspond to the radial functions of np orbitals. The range of the radial momentum density function is $0\text{-}25a_0^{-1}$ for all the members except for Xe where the range is doubled to $50a_0^{-1}$ in order to include all 5 lobes of the ns orbital. For the radial position density functions, a somewhat smaller range ($0\text{-}2.5a_0$) is sufficient to show all the lobe and nodal structures. One striking feature found in these radial density functions is that while there are significant portions of the position density distributed over the outer lobes, the momentum density is mainly concentrated in the first lobe (note logarithmic scales). An obvious example is found in the case of neon 2s. It is clear (figure 4.14) that the second lobe of the Ne 2s momentum density does not contribute significantly. This is in contrast to the relatively much larger contribution of the second lobe to the radial density in position-space (figure 4.15). As explained earlier this concentration of the density in momentum-space in the first lobe, corresponds to a contraction while the

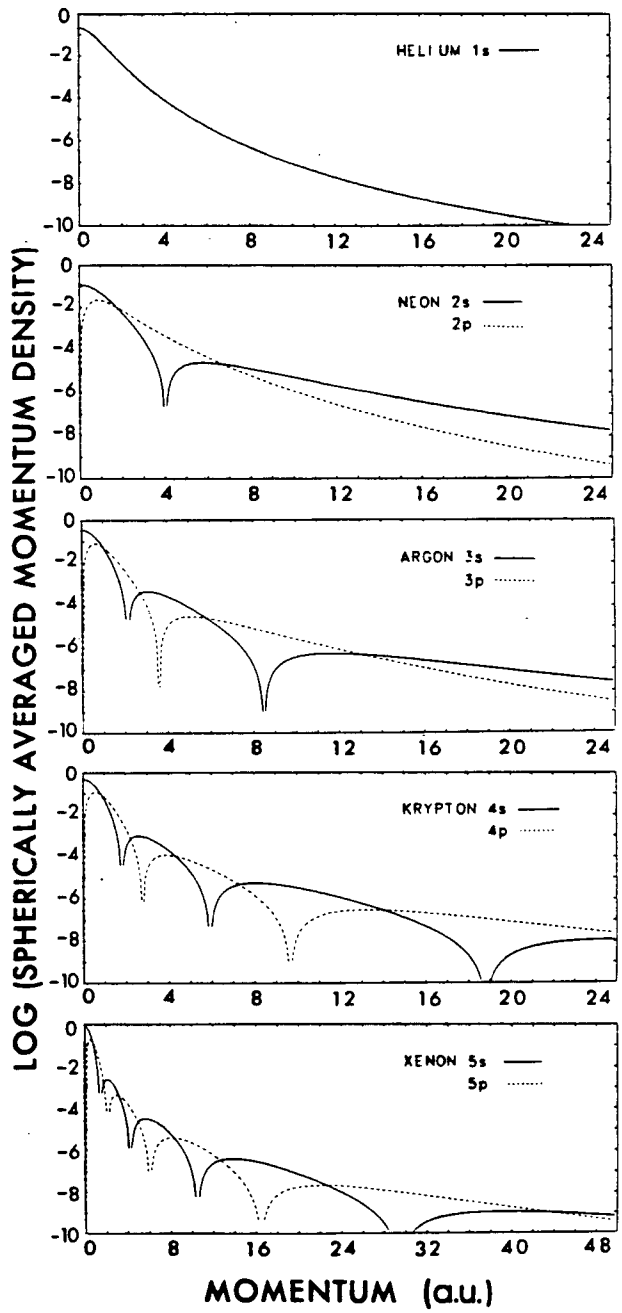

Figure 4.14 - Comparison of extended range Hartree-Fock spherically averaged momentum distributions for np (dotted lines) and ns (solid lines) of Noble Gases. The np and ns distributions exhibit n-1 and n lobes respectively.

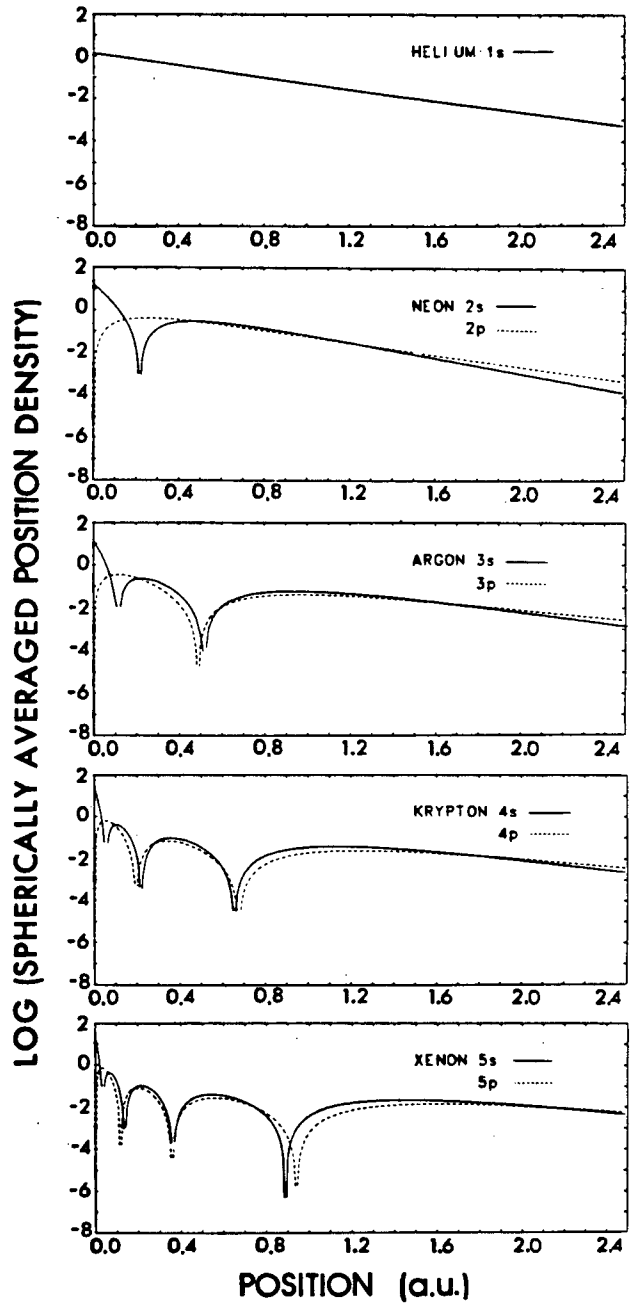

Figure 4.15 - Comparison of extended range Hartree-Fock spherically averaged position distributions for np (dotted lines) and ns (solid lines) of Noble Gases. The np and ns distributions exhibit n-1 and n lobes respectively.

spreading of the position density over all the lobes is related to the reverse behavior, i.e. an expansion.

Figure 4.16 shows the radial position and momentum corresponding to an enclosed 95% probability, which can be virtually regarded as the size of the orbital. The relative increase (from Ne to Xe) in $r_{95\%}$ in the ns and np orbital is clearly seen to be associated with a corresponding relative decrease in $p_{95\%}$. This unambiguously demonstrates the inverse spatial relation. It can also be noted that, as is often invoked in screening arguments, the ns orbitals are more penetrating (localized) in position-space than their np counterparts while the reverse is true in momentum-space. Another interesting feature is the linearity of the orbital spatial extent as a function of the principal quantum number starting from argon (n=3). (See figure 4.16.) This linearity indicates that there is a constant linear orbital expansion (contraction) starting from the n=3 shell in r-space (p-space). The fact that neon deviates from the general linear trend is expected since there is no nd subshell in the first-row (n=2) elements. Helium is also expected to be different again because of its unique electronic structure. Electron screening effects in neon and argon are therefore different from He and also Kr and Xe which have nd electrons.

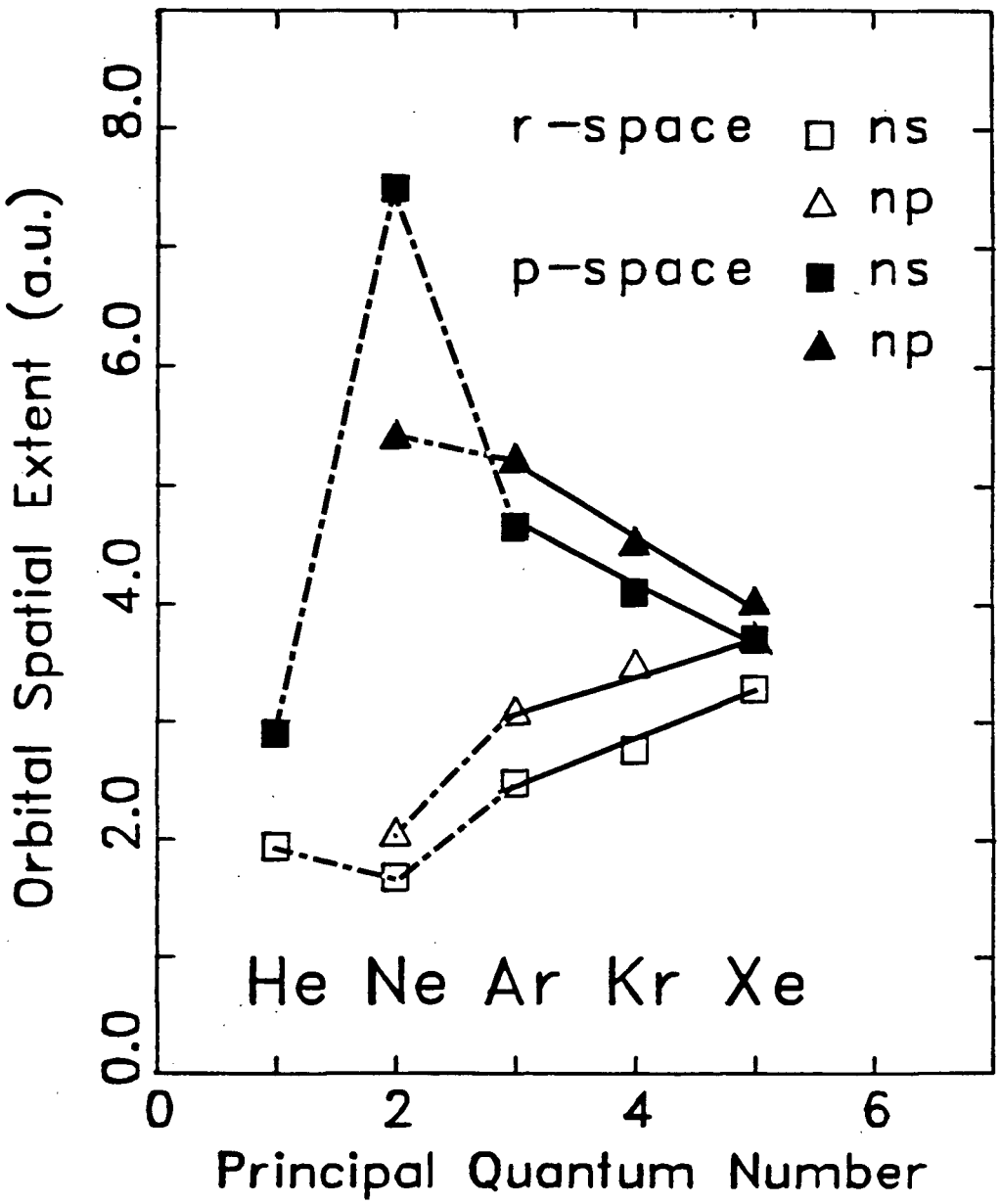

Figure 4.16 - Comparison of the orbital spatial extent of the ns and np orbitals of Noble Gases in position and momentum space. The spatial extent represents an enclosed 95% probability and is effectively the size of the orbital.

Chapter V

TWO ELECTRON SYSTEMS: HELIUM AND MOLECULAR HYDROGEN

5.1 INTRODUCTION

The study of two electron systems (i.e. He and H_2) has attracted a considerable amount of attention not only in the experimental determination of their respective momentum distributions [E70, BW73, HM&73, MU&74, DM&75, DMW76, L77, WM&77, MC&81] but also in the theoretical investigation of their electronic wavefunctions and related properties [W33, KR60, D62, LH67, BS72, LS78]. Since there is only one type of orbital in the ground state of the two electron systems in the simple molecular orbital (MO) picture, i.e. 1s in He and $1\sigma_g$ in H_2, the total electron momentum distributions derived from the experimental Compton profiles obtained using high energy photon Compton scattering techniques [C71] and high energy electron impact spectroscopy [BF74] should be essentially the same[1] as the orbital momentum distributions measured directly by the binary (e,2e) method. The two electron systems therefore provide a unique testing ground for direct comparison of different experimental techniques in

[1] The Compton experiment sees all excited states in addition to ground state. However the latter is overwhelmingly the dominant contribution.

the determination of momentum distributions. There are many measurements of the Compton profiles of He and H_2 using X-ray and γ-ray Compton scattering techniques and high energy electron impact spectroscopy (HEEIS) [E70, BW73, L77]. Measurements of the orbital momentum distributions using binary (e,2e) spectroscopy have also been made for He [HM&73, MU&74, DMW76] and H_2 [DM&75, WM&77, MC&81]. In the case of He, it has been found that there is good agreement between the momentum distributions observed by different binary (e,2e) groups. However, there is a major discrepancy in the reported measurements for the momentum distribution of H_2 $1\sigma_g$. In particular, the recent high momentum resolution measurement of H_2 $1\sigma_g$ by Migdall *et al.* [MC&81] is in significant disagreement with the earlier (e,2e) determinations by Weigold *et al.* [WM&77] and Dey *et al.* [DM&75]. A further independent measurement at high impact energy is called for and this has provided stimulus for the present work. It should be noted that very recently the one electron system H 1s has been investigated by binary (e,2e) spectroscopy [LW81] giving a result in excellent agreement with the exact solution of the Schrodinger equation for the hydrogen atom. No such measurement has been reported to date using Compton scattering.

There are numerous wavefunction calculations for the two electron systems, especially in H_2 because of its fundamental significance in bonding theory. The theoretical atomic

momentum distribution of He 1s calculated from the Hartree-Fock wavefunction [CR74] has been shown to be in excellent agreement with the reported momentum distributions [HM&73, LB83a] (chapter 4). It should be noted that although the Hartree-Fock wavefunction is adequate for the He^+ ground state, a configurational interaction (CI) wavefunction is required for the excited n=2 transitions [MU&74, DMW76, CM&84]. In the case of H_2, accurate theoretical determinations of its electronic ground state wavefunction have to resort to configurational interaction methods in order to represent adequately spatial electron correlation effects in this diatomic molecule [MWY60, FR61, DW66, LH67]. In this respect, H_2 provides the simplest test molecule for applying CI methods. Weigold *et al.* [WM&77] have investigated ground state correlations in H_2 using binary (e,2e) spectroscopy. The results which are a very sensitive probe for the wavefunction were compared with calculations using a CI wavefunction [MWY60]. In addition, H_2 provides a unique prototype covalent bond for the study of chemical binding and bond formation. Earlier works by Berlin [B51] and Roux *et al.* [BD&60, RC62] have focussed upon the use of position density difference distributions to investigate bonding phenomena in diatomics. The study of position density and density difference maps to relate concepts of binding and antibinding has been further extended by Bader *et al.* [BH67, BC68] through the use of forces acting upon the

nuclei and the Hellmann-Feynman theorem. (See also Deb [D73].) A somewhat different approach is the work of Feinberg *et al.* [FRM70, FR71], which examines the behaviour of the kinetic and potential energy upon bond formation and the role of the Virial theorem in bond formation.

In the present work, the momentum distribution of H_2 $1\sigma_g$ is measured and is compared with existing binary (e,2e) measurements as well as with theoretical distributions of different quality ranging from minimal basis, double-zeta basis [SB72], limited Hartree-Fock [FR61], CI [MWY60] and the optimized valence configuration [DW66]. Direct comparison of the momentum distributions of the two electron systems with those derived from the experimental Compton profiles of Lee [L77] is used to compare the two techniques and assess their viabilities since each depends on a different reaction model. In addition, a different qualitative view of covalent chemical binding and bond formation of H_2 $1\sigma_g$ is presented through the use of momentum density [CS&79, BC&82, CB82a, CB82b, MB&83] and momentum density difference maps [HC68, ET77] to extend momentum-space chemical concepts (chapter 2). In particular the momentum density difference map for H_2 $1\sigma_g$ gives a clear picture of the nature of a single covalent bond in momentum-space.

5.2 GROUND-STATE BINDING ENERGY SPECTRA

Figures 5.1 and 5.2 show the binding energy spectra of the He 1s and H_2 $1\sigma_g$ electrons respectively. The He binding energy spectrum provides a direct measure of the instrumental energy resolution function. A Gaussian line shape with a FWHM=1.6eV was found to provide an excellent fit to the data (see also figure 4.1). With the determined instrumental energy resolution function and the experimental width of 2.35eV FWHM of the H_2 $1\sigma_g$ peak (figure 5.2), the Franck-Condon width of the H_2 ground ionic state is determined to be 1.7eV. This is in excellent agreement with the high resolution PES works of Asbrink [A70] and Turner and May [TM66]. (The present study is limited only to the ground states of the two electron systems because of the extremely weak intensities of the excited ionic states [HM&73, MU&74, DMW76, WM&77].)

5.3 SPHERICALLY AVERAGED MOMENTUM DISTRIBUTIONS

Figures 5.3 and 5.4 (a and b) show the momentum distributions of He 1s and H_2 $1\sigma_g$ electrons respectively. Since the momentum density ($\rho(p)$) is related to the Compton profile (J(p)) by the following equation:

$$[5.1] \qquad \rho(p) = -(2\pi p)^{-1}\, dJ(p)/dp,$$

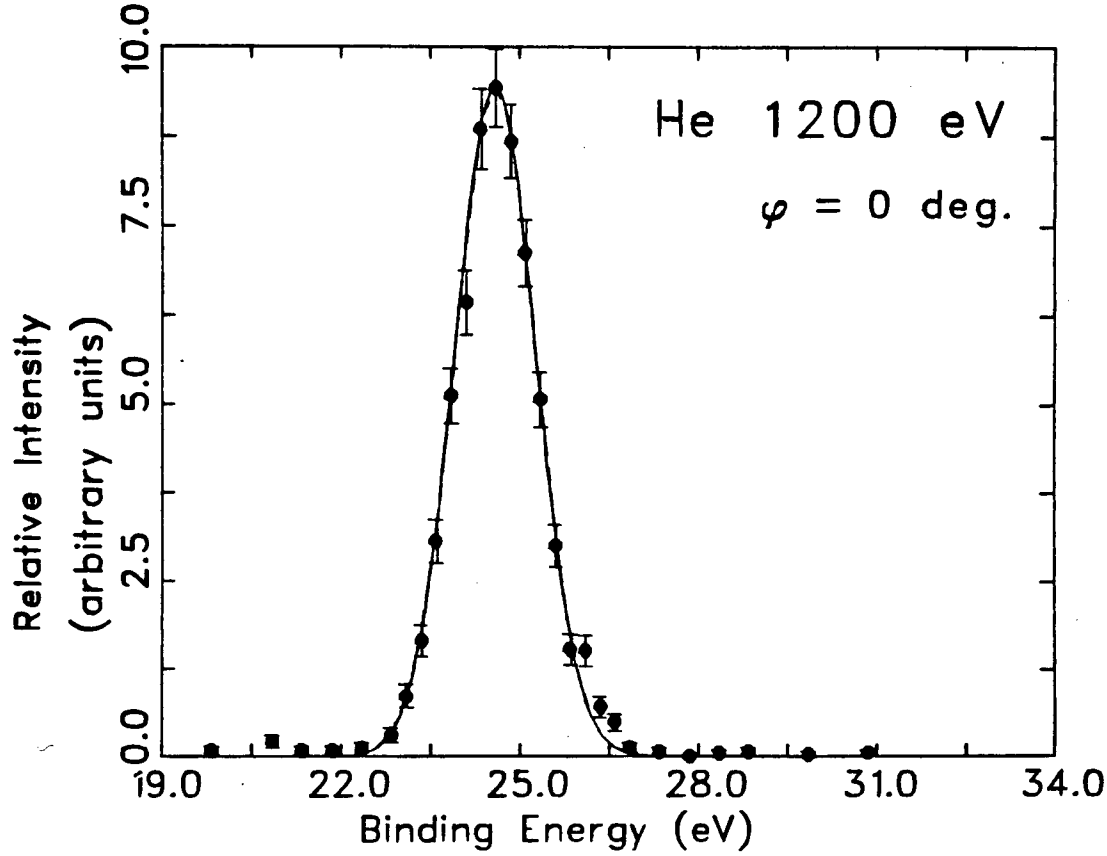

Figure 5.1 - Binding energy spectrum for He 1s ionization at ϕ=0°. The solid line corresponds to a Gaussian lineshape with a FWHM of 1.6eV (the instrumental energy resolution).

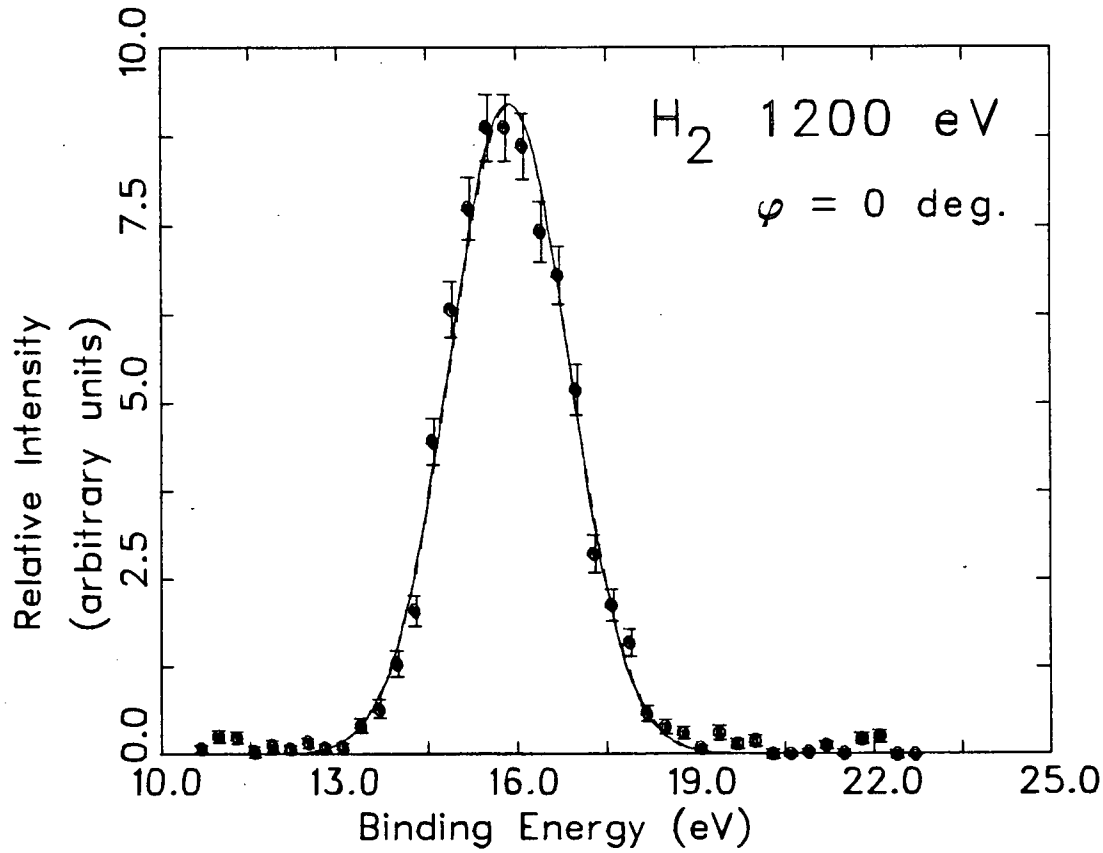

Figure 5.2 - Binding energy spectrum for H_2 $1\sigma_g$ ionization at ϕ=0°. The solid line corresponds to a Gaussian lineshape with a FWHM of 2.3eV.

the momentum distributions can be obtained by differentiating the fitted experimental Compton profiles[2] reported by Lee using high energy electron impact spectroscopy (HEEIS) [L77]. These derived results are presented in both spectra as open squares in figures 5.3 and 5.4. Theoretical momentum distributions calculated from wavefunctions of different quality are also compared with the experimental data. The calculated momentum distributions (spherically averaged) have been convoluted with the momentum resolution function of the binary (e,2e) spectrometer (chapter 3) to facilitate direct comparison with experiment. For He, atomic wavefunctions of Hartree-Fock, double-zeta and single-zeta qualities of Clementi and Roetti [CR74] are used. For H_2, five wavefunctions of quality ranging from minimal basis[3] to the extended Hartree-Fock are used [HL&80, SB72, FR61, MWY60, DW66]. A brief description of these wavefunctions is given in table 5.1. The method of calculating the spherically averaged momentum distributions for CI type wavefunctions for H_2 $1\sigma_g$ and H_2 $1\sigma_u$ orbitals has been discussed by Weigold *et al*. [WM&77]. A similar procedure is used in the present calculation. It should be noted that Migdall *et al*. [MC&81]

---

[2] In the high energy electron impact spectroscopic (HEEIS) work [L77] Lee least-squared fitted the experimental Compton profiles to a sum of differentiable polynominal functions. The resulting experimental parameters (see tables 7 and 8 of ref. [L77]) are used to calculate the momentum distributions.

[3] The minimal basis is the standard STO-3G basis of the Gaussian 76 package [HL&80].

have also compared their result with a wide range of SCF wavefunctions. The HEEIS data and the theoretical distributions are area normalized to the (e,2e) data from $p=0-1.5a_0^{-1}$ for both He and H_2 (figures 5.3 and 5.4b respectively). Clearly only shape comparison is possible in the present relative experimental measurements.

In the atomic case, i.e. the He 1s momentum distribution (figure 5.3), excellent agreement between the (e,2e) data and the theoretical Hartree-Fock [CR74] distribution is observed. The double-zeta calculation is almost indistinguishable from the Hartree-Fock result but the single-zeta wavefunction is inadequate in predicting the experimental distribution. Although there is generally good agreement between the HEEIS data and the (e,2e) data, the HEEIS distribution appears to be very slightly narrower than both the present (e,2e) result and the Hartree-Fock theoretical distribution. This discrepancy may be the result of a noisy Compton profile in the low momentum region, which as pointed out by Lee [L77] requires a five term polynomial fit and some smoothing in order to produce a good fit. Another possibility is the breakdown of the impulse approximation [BS72, LS78]. While there is generally very good agreement between the experimental measurements of the He 1s momentum distribution and the Hartree-Fock theory, it should be noted that limitations in the latter have been demonstrated by measurements of n=2 transitions in He ionization by McCarthy

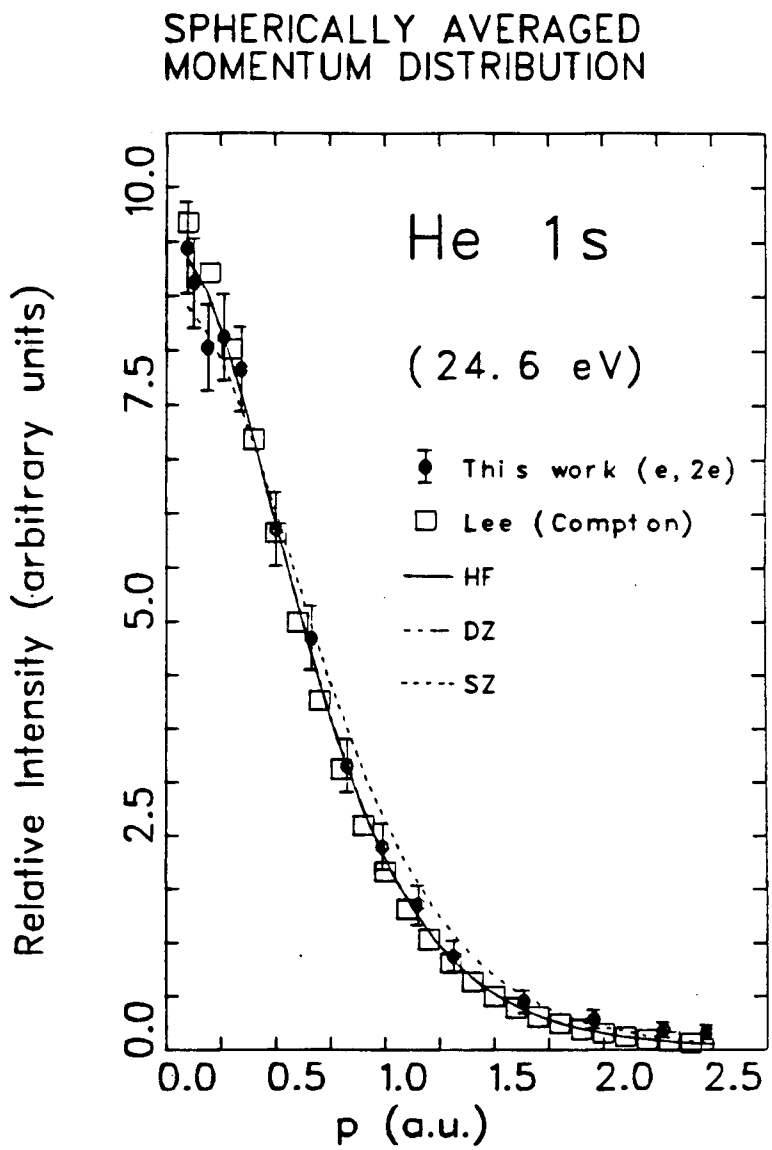

Figure 5.3 - Atomic momentum distribution for He 1s orbital. The open squares (□) give the momentum distribution derived from the Compton scattering (HEEIS) data [L77]. The HF and DZ [CR74] theoretical distributions are indistinguishable from each other.

et al. [MU&74] and Dixon *et al*. [DMW76] using binary (e,2e) spectroscopy.

For the molecular momentum distribution of H_2 $1\sigma_g$, a similar generally good agreement is also found between the Compton scattering (HEEIS) and (e,2e) data (figures 5.4a,b). The HEEIS distribution is as in the case of helium very slightly narrower than the binary (e,2e) momentum distribution. From figure 5.4a it can be seen that the present (e,2e) data is also in excellent agreement with the earlier (e,2e) measurements of Weigold and coworkers [DM&75, WM&77] while there is significant disagreement with the recent (e,2e) measurement of Migdall *et al*. [MC&81]. The experimental (e,2e) distributions of Weigold *et al*. [WM&77] and Migdall *et al*. [MC&81] are point normalized at their respective maxima to the present (e,2e) distribution. (Area normalization of these data does not change the conclusion below.) The latter work [MC&81] gives a significantly broader momentum distribution ($p_{1/2max} \simeq 0.6 a_o^{-1}$) than that obtained both in the present work and in the earlier [DM&75, WM&77] binary (e,2e) works, which all have $p_{1/2max} \simeq 0.5 a_o^{-1}$. It can also be seen that the momentum distribution derived from the differentiated Compton profile [L77] (see the case of He above) is in good agreement with both the present and earlier [DM&75, WM&77] binary (e,2e) determinations.

There are several interesting features associated with the theoretical momentum distributions of the H_2 $1\sigma_g$ orbital.

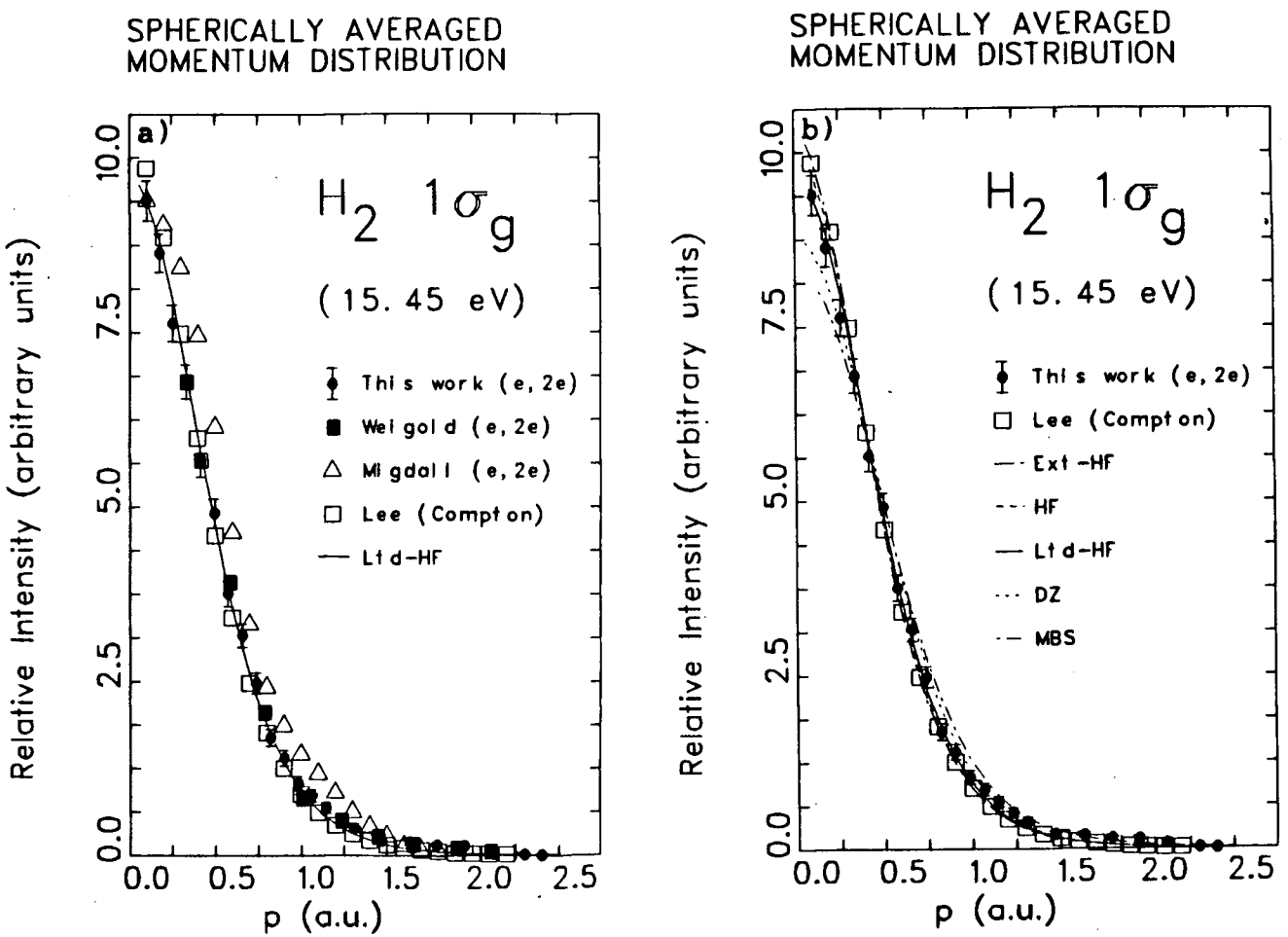

Figure 5.4 - Comparison of a) experimental molecular momentum distributions and b) calculated momentum distributions for H_2 $1\sigma_g$ orbital.

(See figure 5.4b.) First, whereas the minimal basis (MBS) [HL&80] and the double-zeta (DZ) [SB72] wavefunctions both give broader momentum distributions compared to the experimental one, the variationally better quality CI wavefunctions of McLean *et al.* (HF) [MWY60] and of Das and Wahl (Ext-HF) [DW66] both predict slightly narrower distributions. The somewhat more physical single configuration basis, which consists of 1s, 2s and 2pσ functions, of Fraga and Ransil (Ltd-HF) [FR61] gives the best agreement with the experimental (e,2e) distribution. This seems to support the assertion that a variationally superior wavefunction does *not necessarily* provide the best description of the momentum distribution. Such observation has also been made in an earlier molecular (e,2e) study [BC&82]. Finally, there is a small discrepancy between the (e,2e) data and the better quality theoretical distributions in the range $p>1.5a_0^{-1}$. A similar discrepancy has also been observed in the noble gases [MW76a, LB83a] (chapter 4). This is probably due to the breakdown of the PWIA in the high momentum region in the (e,2e) reaction model and to the lack of relativistic and explicit relaxation corrections in the wavefunctions.

To summarize, there is generally good agreement between the present (e,2e) momentum distribution and the better quality theoretical momentum distributions [FR61, MWY60, DW66] as well as with the experimental (e,2e) data of Weigold

et al. [DM&75, WM&77] and the Compton profile (HEEIS) data of Lee [L77] for the H_2 $1\sigma_g$ orbital. The present comparison between experimental (e,2e) data and the HEEIS data shows that the HEEIS distributions of Lee may be somewhat limited by the accuracy of the polynomial fit to obtain the momentum distributions from the experimental Compton profiles and that the (e,2e) data is generally limited by the validity of PWIA above $p=1.5a_0^{-1}$. There is, nonetheless, very good agreement between the (e,2e) data and the HEEIS data at least in the low momentum region and it is clear that the data are reasonably consistent. Since the Compton profile experiments can provide the total momentum distributions and the binary (e,2e) method is most sensitive to individual valence orbital distributions, it seems feasible that by combining data from the two experiments, one may obtain the momentum distributions of the core electrons in other future studies of more complex systems.

5.4 MOMENTUM-SPACE CHEMISTRY AND ORBITAL DENSITY TOPOGRAPHY

5.4.1 Density Mapping Convention

The wavefunctions used in the present study of density maps are the Hartree-Fock atomic wavefunctions of Clementi and Roetti [CR74] for He and the optimized valence configuration molecular wavefunctions of Das and Wahl [DW66]

for H_2. Both of these are considered to be "variationally superior" compared to the other wavefunctions (see table 5.1). The Das and Wahl wavefunction (Ext-HF), although slightly less satisfactory in predicting the observed momentum distribution, is chosen for the present topographical study of chemical bonding phenomena because of its optimization procedure [DW66] and its availability at several internuclear separations.

Unless otherwise stated, the contour values of the density maps (both position and momentum density) are logarithmic; ranging from 0.6, 0.8, 2, 4, 6, 8, 20, 40, 60 to 80% of the maximum density value. The contour values for the density difference maps are also logarithmic and are ±0.6, ±0.8, ±2, ±4, ±6, ±8, ±20, 40, 60 and 80% of the absolute maximum density difference value. The negative contour lines are indicated by dash lines. The plane of the contour map is defined directionally by two unit vectors. In the present case the (0,0,1) vector corresponds to the z axis which is parallel to the internuclear direction and the (0,1,0) vector corresponds to the y axis, the bond-perpendicular direction. The range of the momentum and position is from -2.5 a.u. to 2.5 a.u. in both vector directions. Along with the density maps, line density projection plots parallel to the two axes are also presented in order to better illustrate the general changes in shape and amplitude of the relative density profiles along the axes. The dotted lines across the contour

Table 5.1
Comparison of theoretical wavefunctions.

Orbital	Wavefunction Quality	Total Energy (hartree)	Reference
He 1s			
SZ	Single-zeta	-2.8476562	Clementi-Roetti [CR74]
DZ	Double-zeta	-2.8616726	Clementi-Roetti [CR74]
HF	Hartree-Fock	-2.8616799	Clementi-Roetti [CR74]
H_2 $1\sigma_g$			
MBS	Minimal basis gaussian set	-1.1167	Gaussian 76 STO-3G [HL&80]
DZ	Double-zeta gaussian set	-1.1266	Snyder-Basch [SB72]
Ltd-HF	Single-configuration: 1s, 2s, $2p_\sigma$ STO basis	-1.1335	Fraga-Ransil [FR61]
HF	5 configurations CI, Hartree-Fock quality	-1.1672	McLean et al. [MWY60]
Ext-HF	Optimized valence configuration, extended Hartree-Fock quality	-1.1698	Das-Wahl [DW77]

maps indicate where the projections are taken; for instance the line density plot on the top of the contour map is along the "horizontal" (0,1,0) dotted line. Contour values relative to the maximum density value (linear scale) are indicated on the sides of these projection plots.

The difference density is defined in the present study to be the difference between the molecular (or atomic) orbital density and the averaged density of the independent atoms at a particular internuclear geometry (the independent atoms model, IAM), i.e.

$$[5.2a] \qquad \Delta\rho = 2\rho\{MO\} - \Sigma^{N}_{atom=1}\ \rho\{atom\},$$

where $\rho\{atom\}$ is the one electron density of the independent atoms.

$$[5.2b] \qquad \Delta\rho\{He1s\} = 2\rho\{He1s\} - (\rho\{H1s\}+\rho\{H1s\}) \quad R=0a_o,$$

$$[5.2c] \qquad \Delta\rho\{H_2 1\sigma_g\} = 2\rho\{H_2 1\sigma_g\} - (\rho\{H1s\}+\rho\{H1s\}) \quad R=1.4a_o,$$

where R is the (equilibrium) internuclear separation, which is varied in the study of the bond formation of H_2. (See section 5.4.7.) The wavefunction of the atomic hydrogen 1s orbital is exact.

In the following sections, the Fourier transform (FT) and Virial properties (chapter 2) will be used to investigate some of the most prominent features in the density functions

in the two electron systems with special focus on chemical binding in momentum-space. The nature of the density redistribution accompanying chemical bonding is well illustrated by considering the formation of a "virtual" bond in the simple atomic system discussed below.

5.4.2 He 1s Atomic Orbital

The helium 1s atomic wavefunction (on the basis of the *electronic* structure alone) can be considered to be a special case of the two electron H_2 molecular wavefunction, namely when the internuclear separation between the two H atoms, R, is zero. Figure 5.5 shows the density maps of the He 1s atomic wavefunction and that of the independent atoms model (IAM) wavefunction and their difference density (bond density) maps in both momentum and position-space. Several interesting features can be seen in these maps.

(i) Only the symmetry and the inverse spatial reversal properties apply in the case of atoms. The *shape* of momentum densities of He 1s and of the independent H 1s at R=0 are clearly identical to that of their corresponding position densities. The only difference is, in accord with the inverse spatial reversal relation, an inverse weighting variation in the spatial extent of these density functions in different spaces. This is illustrated in the density maps

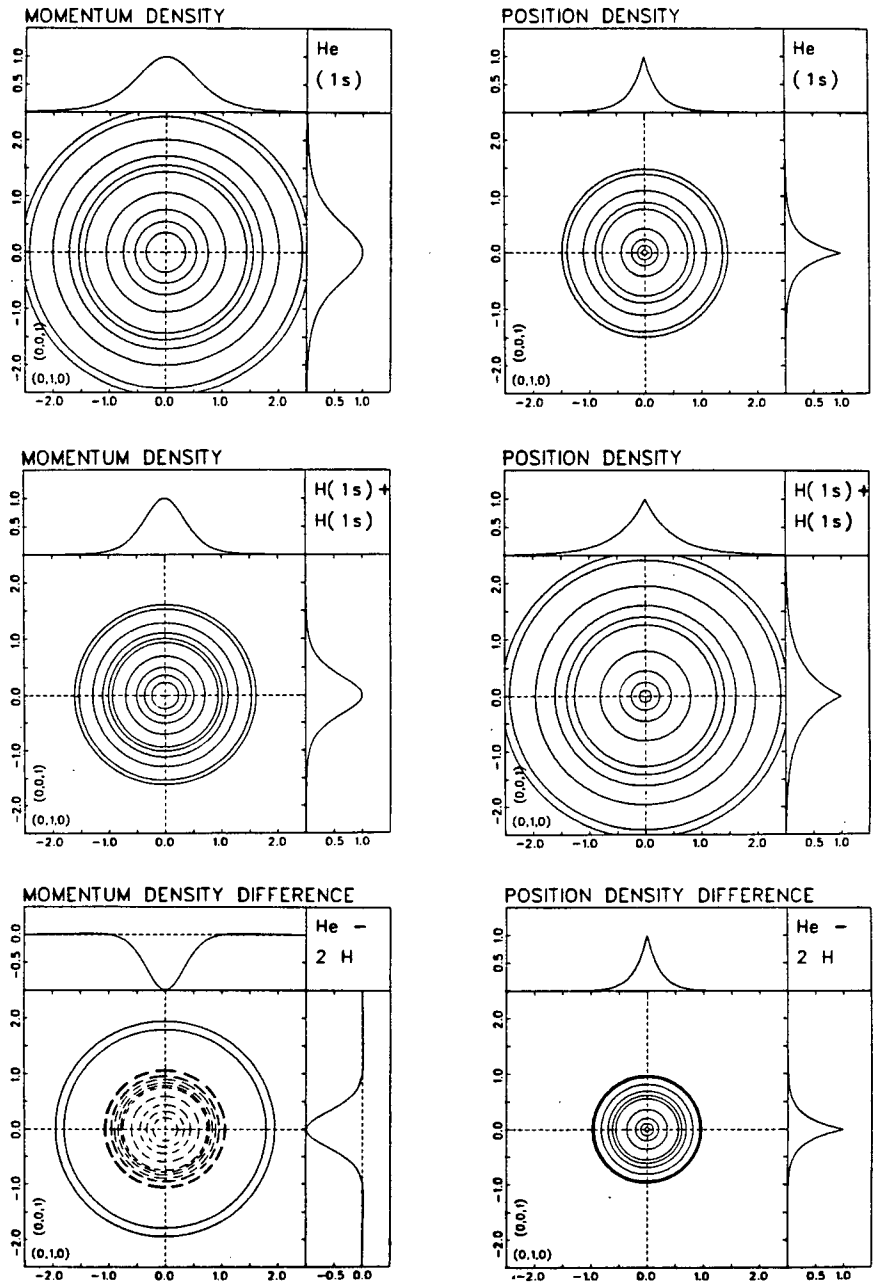

Figure 5.5 - Density contour maps of the He 1s orbital (top), the independent atom model (centre) and density difference maps (bottom) in momentum-space (LHS) and position space (RHS). Negative density contours are represented by dashed lines.

and projection plots where a contraction of r-space orbital density from the IAM case (figure 5.5, centre) to He case (figure 5.5, top) leads to a concomitant expansion in p-space density. Similar behavior has also been observed in the rest of the noble gas group [LB83a] (chapter 4).

(ii) A contraction of the r-space density accompanies the formation of the stable atom from independent atom densities because of the associated decrease in potential energy of the electrons. Such density redistribution is best illustrated by the r-space density difference map (figure 5.5, bottom RHS). In p-space, however, the corresponding transfer of density is from the p-space origin to the outer high momentum region. This is a direct consequence of the Virial relation since the lowering of the potential energy upon the formation of a stable bound system (a virtual bond) corresponds to an increase in the kinetic energy. In the case of He 1s the kinetic energy is raised by transferring density from the p-space origin to the high momentum region isotropically. This is a manifestation of what has been referred to as a "white hole" effect (see chapter 2), in which the density is pushed out from the p-space origin in order to achieve a higher kinetic energy and hence a more stable system. This virtual bond in atomic He has the shape of a "hollow ball" (figure 5.5, bottom LHS).

5.4.3 H_2 $1\sigma_g$ Orbital

For molecules, the density function ρ can be decomposed into a quasi-classical part, ρ^{QC}, which is just the sum of one centre (atomic) terms, and an interaction part, ρ^{I}. (Recall: $\rho=\rho^{QC}+\rho^{I}$, see table 2.1). Such a partition of ρ is useful in understanding bonding phenomena since the quasi-classical part is positive over all space, the key in classifying an orbital in momentum-space as bonding, antibonding or nonbonding, hinges upon the interaction density. Such a density decomposition in momentum and position space for the H_2 $1\sigma_g$ orbital is shown in figure 5.6.

The quasi-classical density can be regarded as density due to IAM (independent atoms model) wavefunctions except with modified orbital exponents. As such, $\rho^{QC}(r)$ is seen (in figure 5.6, top RHS) simply as two partially overlapping spherical charge clouds concentrated around the two H nuclei separated by the equilibrium separation of $1.4a_0$. The small valley seen in the bond-parallel projection plot is caused by summing the tails of the two independent atomic densities. As expected for a bonding orbital, $\rho^{I}(r)$ (figure 5.6, centre RHS) shows a significant accumulation of charge (positive overlap) in the internuclear bond-parallel region. The independent nature of electrons in the quasi-classical density function is perhaps best illustrated in p-space (figure 5.6, top LHS). The Fourier transform of two independent r-space s-type atomic functions separated by R

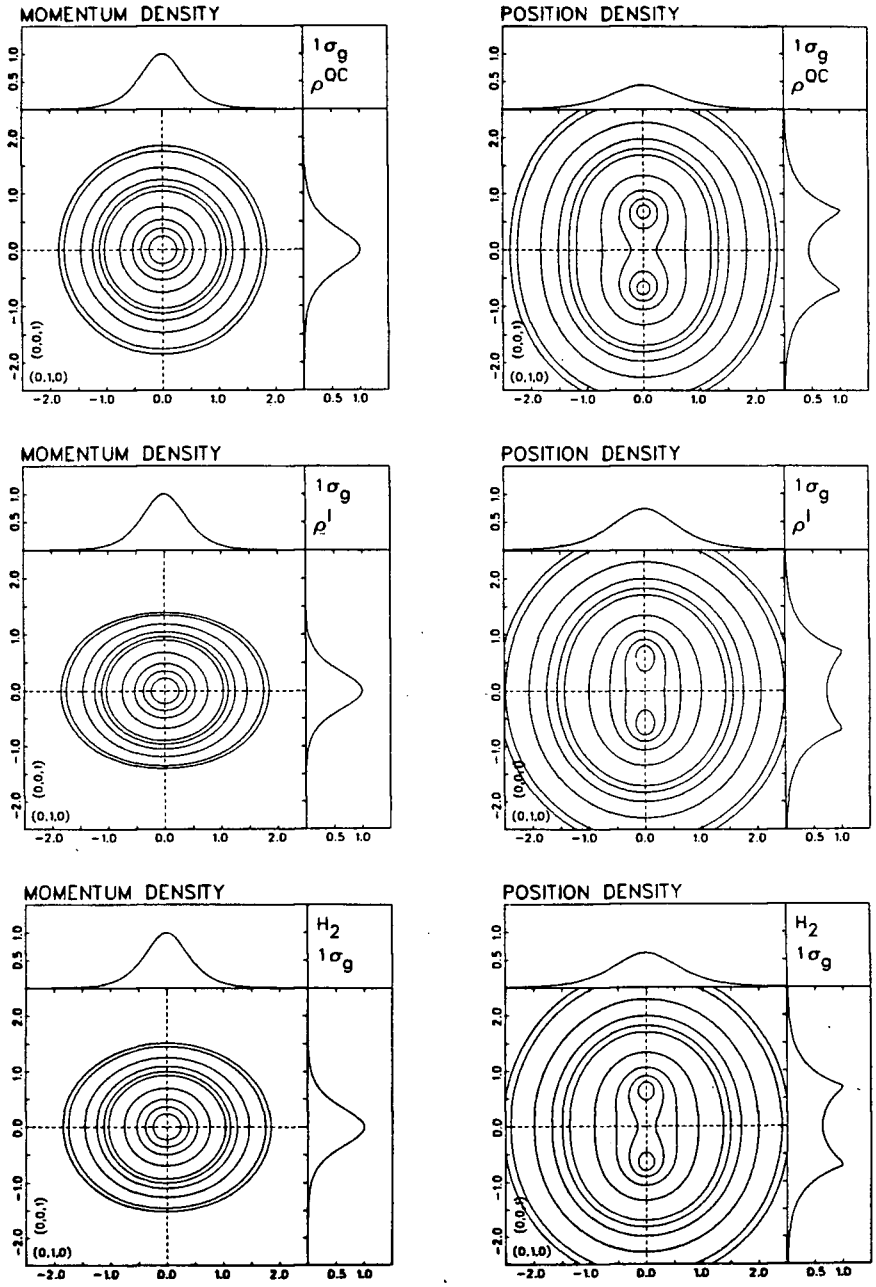

Figure 5.6 - Contour maps of Quasi-Classical density (top), Interaction density (centre) and the molecular density (bottom) for H_2 $1\sigma_g$ in momentum-space (LHS) and position space (RHS).

gives two p-space s-type atomic functions on top of each other in momentum-space to generate the isotropic density distribution as shown (see chapter 2). The internuclear geometry information is absent in the p-space quasi-classical density and can only be recovered by considering the p-space interaction (interference) density (see figure 5.6, centre LHS and a more complete discussion later involving figure 5.11). This interaction momentum density shows an ellipsoidal density accumulation elongated in the bond-perpendicular direction. The interference effects therefore reverse the bonding density concentration from the longitudinal to the transverse direction in p-space. This interaction density seems to dominate the *overall* density appearance (figure 5.6, bottom LHS).

Figure 5.7 shows the density and density difference maps of the H_2 $1\sigma_g$ orbital in r-space and p-space. The IAM p-space density (figure 5.7, centre LHS) is, of course, identical to that of figure 5.5, centre LHS. In addition to the symmetry and inverse spatial reversal FT properties mentioned earlier for the atomic case, the density directional reversal property is clearly observed for the momentum and position densities (figure 5.7, top). In this case, concentration of density in the longitudinal direction in r-space corresponds to density concentration in the transverse direction in p-space. This density reversal property arises from constructive interference of the FT

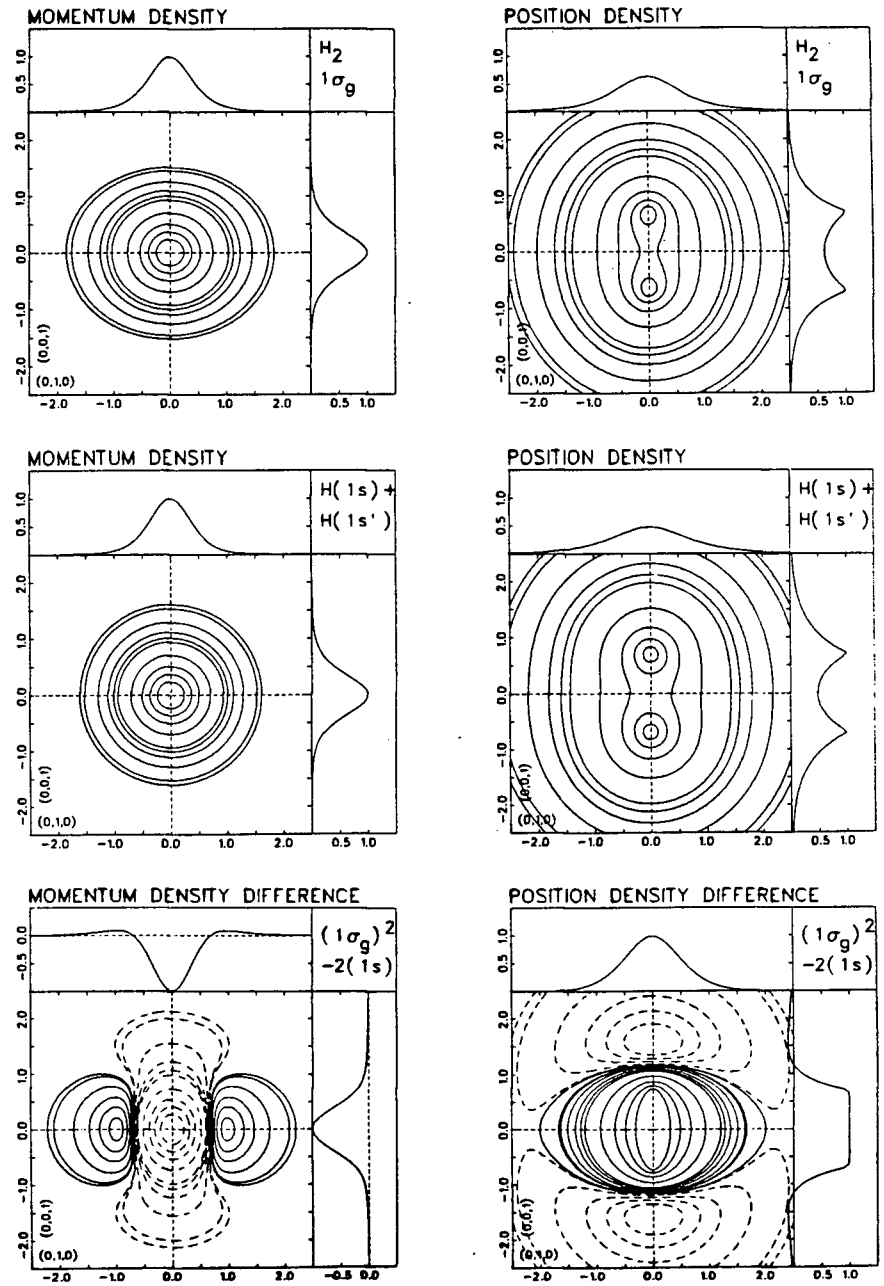

Figure 5.7 - Density contour maps of the H_2 $1\sigma_g$ orbital (top), the independent atom model (centre) and density difference maps (bottom) in momentum-space (LHS) and position space (RHS). Negative density contours are represented by dashed lines.

waves with the density lobes located around the atomic centres.

The density difference maps (figure 5.7, bottom) give the quantum-mechanical pictures of a covalent sigma chemical bond in position and momentum space. A chemical bond in r-space can be thought of as an accumulation of density (fractional charge) in the internuclear region. The amount of density transferred into the r-space binding region provides an attractive electronic-nuclear force to counterbalance the repulsive nuclear-nuclear repulsion [BH67, BC68, D73] for binding the molecule together. (Zero net force is obtained at the equilibrium internuclear separation, $R=1.4a_0$.) This is clearly illustrated in the position density difference map (figure 5.7, bottom RHS) in which density is transferred from the region outside the atoms (negative difference) into the region between them (positive difference).

A complementary view of a chemical bond is shown by the momentum-space density difference map (figure 5.7, bottom LHS). In p-space, the chemical bond can be described physically by "a bone in a donut" picture. A sigma chemical bond in p-space is represented by a redistribution of the density from the bond-parallel high momentum region (the "bone" part) into a bond-perpendicular annular high momentum region (the "donut"). Note that the density is cylindrically symmetric about the bond axis direction, i.e. the (0,0,1)

axis. This density redistribution in p-space can again be explained qualitatively using the Virial relation. If the r-space density maps and their associated projection plots of the $1\sigma_g$ orbital are compared with those of the independent atoms, it is found that the molecular orbital is in fact slightly contracted, which is the result of the larger orbital exponents. (This also accounts for the negative tail seen in the projection plots of the r-space difference map in the bond-parallel direction.) This contraction will lower the potential energy sufficiently so that subsequent localization of charge into the r-space binding region to balance the nuclear repulsion force (a process which makes the potential energy less negative) will not destroy the overall stability of the system. The initial contraction in r-space, which drops the potential energy, corresponds to a density transfer process in p-space which will increase the kinetic energy accordingly. The localization step in r-space will cause a decrease in the bond-parallel component of the kinetic energy since the "filling in" of the binding region lowers the gradient of the wavefunction. This decrease therefore leads to a corresponding decrease in the bond-parallel component in <p> and hence in the momentum density in the bond-parallel direction. The increase in kinetic energy must therefore rely upon the bond-perpendicular components. The result is a decrease in the bond-parallel p-space density (negative difference, see figure 5.7, bottom LHS) to raise the

transverse p-space density (positive difference). The "white hole" effect, i.e. the depletion of the density at the p-space origin, can also be understood as follows. It should be noted that in r-space the transfer of density is from the end regions of the system (where the electrons experience weaker potential) into the internuclear region. This migration of charge density in position-space therefore corresponds to the removal of density near the p-space origin.

5.4.4 H_2 $1\sigma_u$ Orbital

Figure 5.8 shows the quasi-classical and interaction densities of the H_2 $1\sigma_u$ orbital in both momentum and position space. The quasi-classical densities (figure 5.8, top) are similar to those in figure 5.6. As expected, the distinction between a bonding and an antibonding orbital is determined by the interaction densities (figures 5.6 and 5.8, centre). Whereas the symmetric functions of the bonding orbital in r-space produce charge accumulation between nuclei (positive overlap), the antisymmetric functions of the antibonding orbital give rise to charge depletion in the binding region (negative overlap) and charge concentration in the antibinding region outside the nuclei. The corresponding interaction momentum density of the antibonding orbital (figure 5.8, centre LHS), which is obtained from destructive

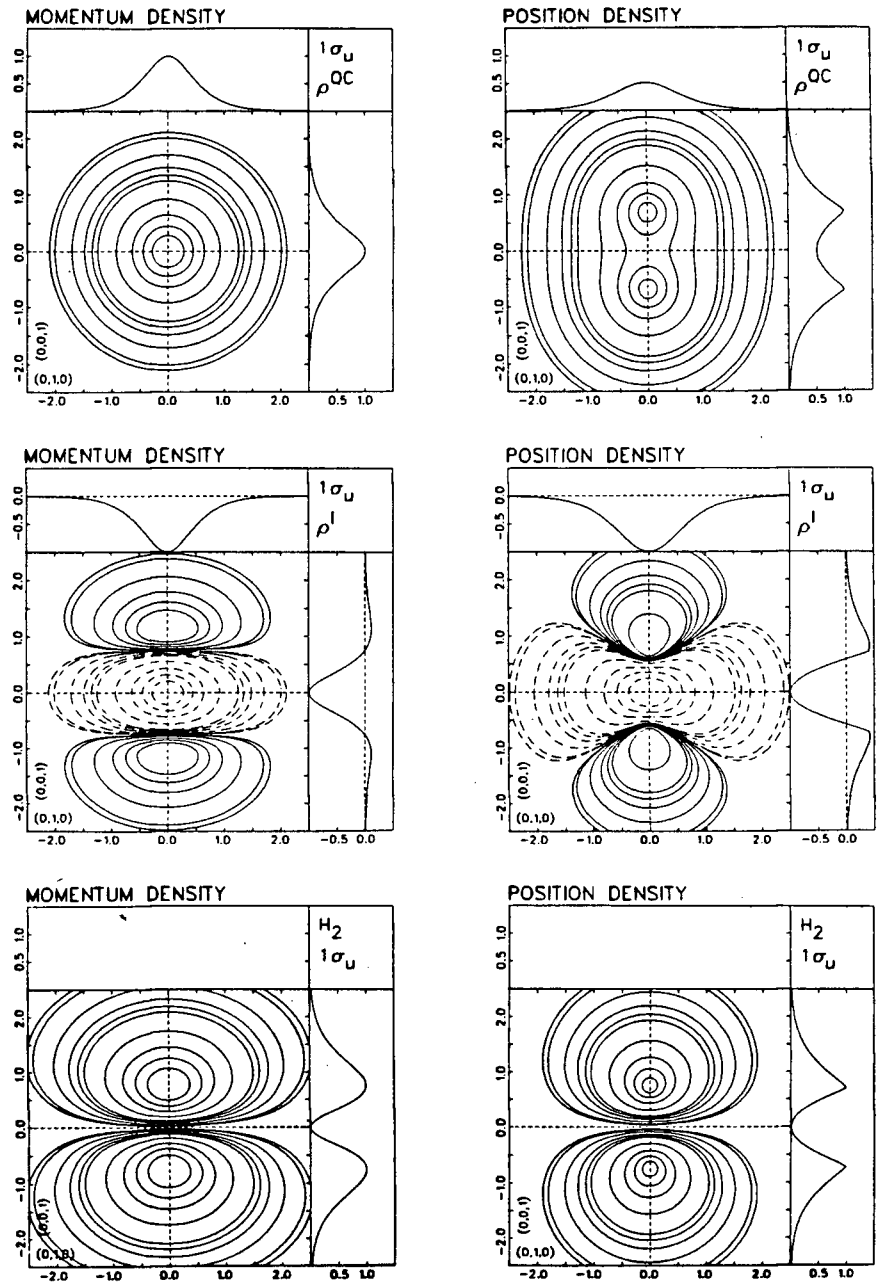

Figure 5.8 - Contour maps of Quasi-Classical density (top), Interaction density (centre) and the molecular density (bottom) for H_2 $1\sigma_u$ in momentum-space (LHS) and position space (RHS).

interference of FT waves with the antisymmetric density lobes, has a somewhat similar appearance to the r-space interaction density (figure 5.8, centre RHS). Density is removed from the p-space origin to the antibinding bond-parallel high momentum region. The sums of ρ^{QC} and ρ^{I} in both spaces give the overall densities (figure 5.8, bottom) of the antibonding orbital, which has a similar appearance to an atomic p orbital (chapter 4). The overall densities are clearly seen to obey the symmetry and inverse spatial reversal FT relations.

The density difference maps of the $1\sigma_u$ orbital are shown in figure 5.9 (bottom). The independent atoms model densities (figure 5.9, centre) are, of course, identical to those in figure 5.7. In r-space, an "antibond" is characterized by a depletion of charge in the internuclear binding region and an accumulation in the antibinding region at the ends of the molecule. On the other hand, the antibinding region in p-space is the bond-parallel high momentum region (figure 5.9, bottom LHS) and the binding region (figure 5.7, bottom LHS) is the bond-perpendicular high momentum region, as defined above.

It is also apparent why the $1\sigma_u$ orbital is antibinding. In p-space, the transfer of density from the p-space origin into the high momentum bond-parallel region corresponds in r-space to a charge transfer from the low potential region to the high potential (i.e. more negative V) region (the Virial

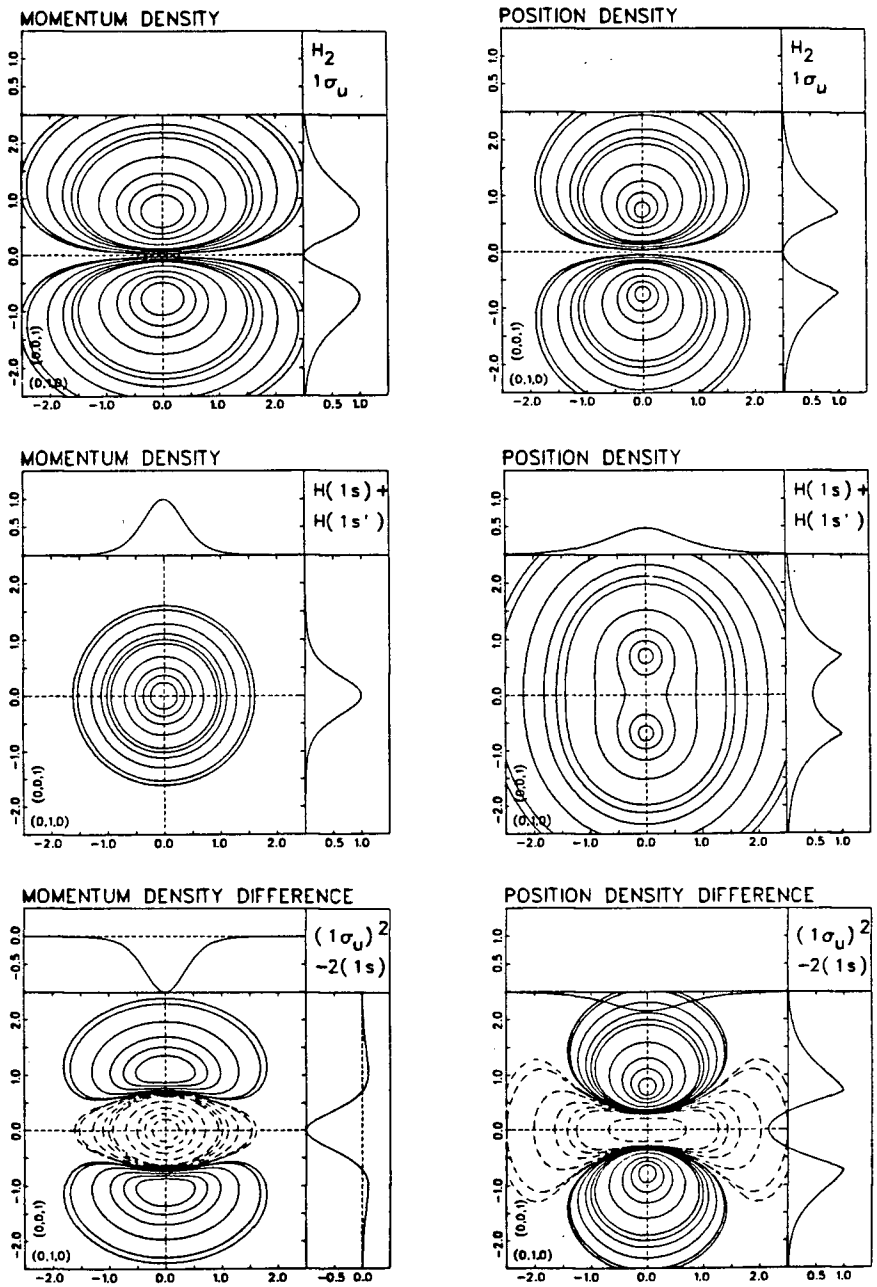

Figure 5.9 - Density contour maps of the H_2 $1\sigma_u$ orbital (top), the independent atom model (centre) and density difference maps (bottom) in momentum-space (LHS) and position space (RHS). Negative density contours are represented by dashed lines.

relation). This results in an overall polarization of charge around the atomic centres at the expense of charge between the nuclei (figure 5.9, bottom RHS). The nuclear-nuclear repulsive force is therefore greatly enhanced because of the poor electronic shielding of the two nuclei. The result is an unstable system.

5.4.5 Molecular Density Directional Reversal In H_2

Figures 5.10 and 5.11 give a three-dimensional visualization[4] of the H_2 $1\sigma_g$ and $1\sigma_u$ orbitals respectively in both momentum and position space. The range of the momentum and position of one side of the "density cube" (which contains the density surface) is -2.5 to 2.5 a.u. except for the final surfaces on the right hand side of figures 5.10 and 5.11 which are shown at 33% reduction (i.e. the range has been tripled). The indicated density values of the (constant) density surfaces correspond, from left to right, to 80, 20, 2, 0.2 and 0.0008% of the maximum density. Two of the three orthogonal vectors which define the density cube are also shown and correspond to the same vector directions as those of the contour maps (see figures 5.6-5.9).

For the H_2 $1\sigma_g$ orbital, the molecular density reversal property is clearly illustrated by the series of constant

---

[4] Details of the three-dimensional orbital visualization procedure are given in ref. [W74]. (See also chapter 10.)

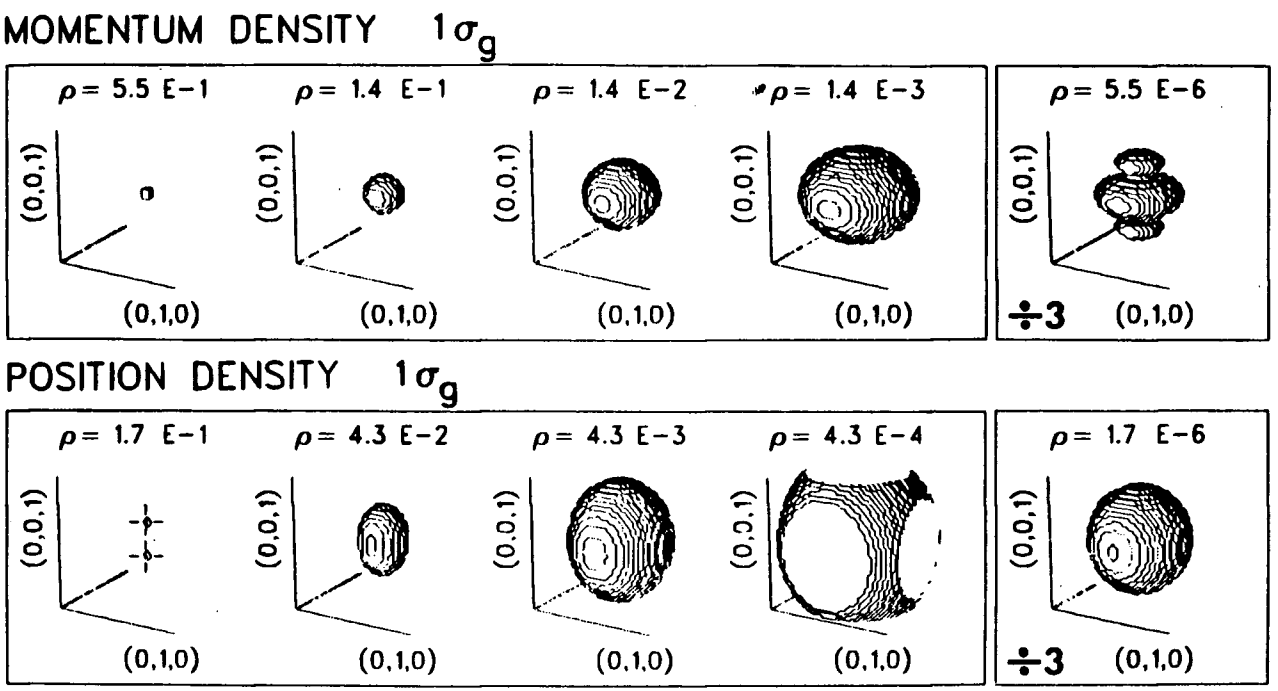

Figure 5.10 - Three-dimensional density surface visualization of H_2 $1\sigma_g$ orbital in momentum-space (top) and position space (bottom). The density values of the surfaces correspond to 80, 20, 2, 0.2 and 0.0008% of the maximum density value.

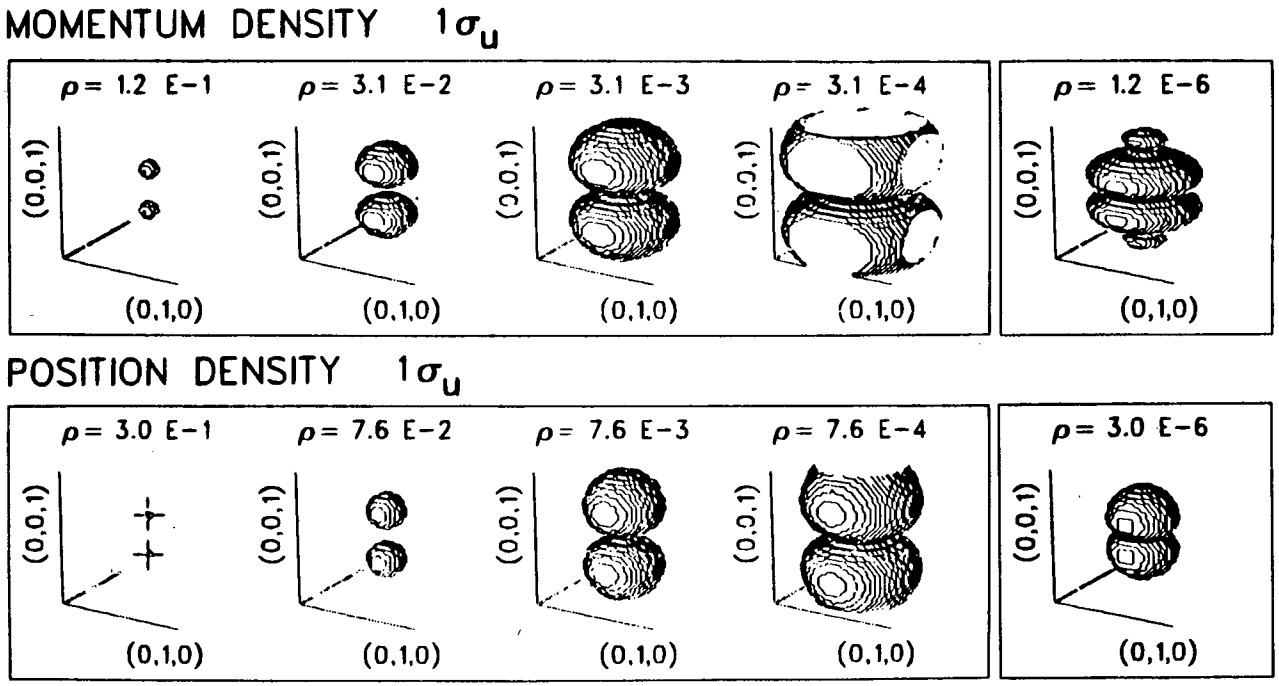

Figure 5.11 - Three-dimensional density surface visualization of H_2 $1\sigma_u$ orbital in momentum-space (top) and position space (bottom). The density values of the surfaces correspond to 80, 20, 2, 0.2 and 0.0008% of the maximum density value.

density surface plots (figure 5.10). It can be seen that the r-space density of the bonding orbital is oriented ellipsoidally with the major axis in the internuclear (the (0,0,1) vector) direction, while the corresponding p-space density is directed perpendicular to the internuclear axis. It can also be seen in r-space (figure 5.10, bottom) that the shape of the density surface changes from ellipsoidal to near spherical as the density value becomes smaller (i.e. the density boundary surface becomes larger). In p-space, on the other hand, the density changes from spherical (high density surface) to ellipsoidal (low density surface). This is in accord, of course, with the inverse weighting behavior (the inverse spatial reversal property) of the density function in momentum and position space as discussed above. There is, however, no direct one-to-one correspondence between the density surface in r-space and that in p-space; namely, a particular density surface in r-space cannot be associated with a corresponding one in p-space and vice versa. Figure 5.11 gives the three-dimensional visualization of the H_2 $1\sigma_u$ orbital. It can be seen, again that the p-space density lobes are significantly elongated in the bond-perpendicular direction as the boundary surface is enlarged. This ellipsoidal growth is a logical consequence of the density oscillations (see below) which appear in the bond-parallel direction for both the $1\sigma_g$ and $1\sigma_u$ orbitals.

Another important FT feature as demonstrated in the

surface plots for the $1\sigma_g$ and $1\sigma_u$ orbitals is that the manifestations of the nuclei are different in position-space and in momentum-space. In r-space the nuclear positions (shown by crosses (+) on the position density surface plots in figures 5.10 and 5.11, lower LHS) can be identified directly by the higher density surface. In p-space, the nuclear separation is manifested by density oscillations giving lobes at large momentum in the bond-parallel direction in the low density surface plots (see upper RHS of figures 5.10 and 5.11 and in the detailed discussions below). The three-dimensional visualizations of the orbital density are therefore very useful in the illustration of *all* of the FT properties discussed above.

5.4.6 Molecular Density Oscillation In H_2

Extended range momentum and position density maps of H_2 $1\sigma_g$ and $1\sigma_u$ orbitals are shown in figure 5.12. The density contours logarithmically span six decades starting from 0.9%, 0.5%, 0.1%, 0.09%, 0.05%, 0.01%, etc. down to 0.000001% of the maximum contour values in order to emphasize the weak modulation features arising from the interference terms in the momentum-space density (see chapter 2). The range is from -12.5 to 12.5 a.u. in both vector directions. Note also the logarithmic scale (9 decades) in the axis projection plots. The extended range momentum density maps clearly

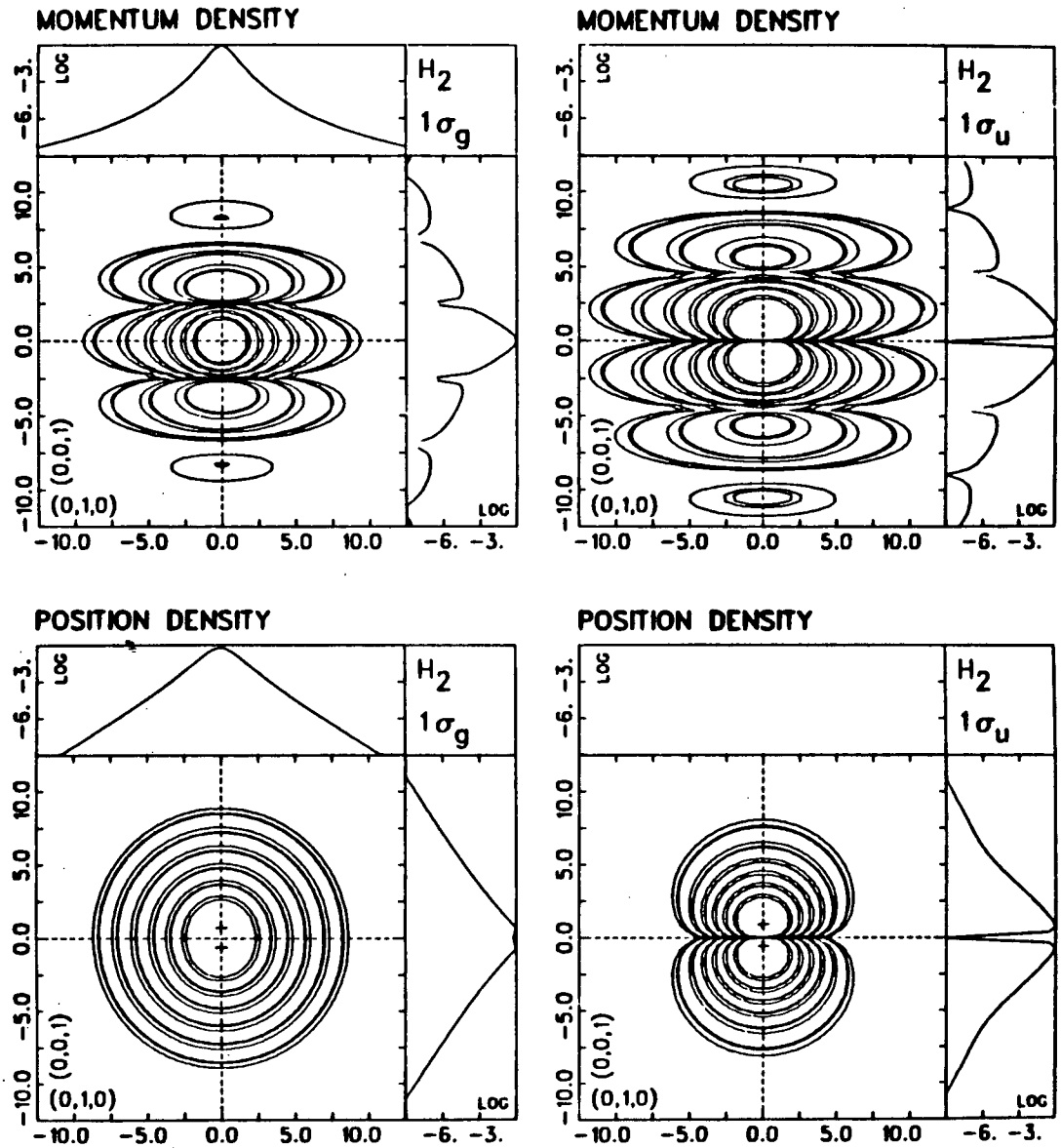

Figure 5.12 - Extended range density contour maps of H_2 $1\sigma_g$ (LHS) and $1\sigma_u$ (RHS) in momentum-space (top) and position space (bottom). The contour values logarithmically span six decades starting from 0.9, 0.5, 0.1, etc. down to 0.000001% of the maximum density.

illustrate the effect of amplitude modulations arising from constructive and destructive interferences of the FT waves with the r-space density lobes around each of the atomic centres [CB82a]. It can also be seen from the bond-parallel axis projection plots that the bonding orbital momentum density oscillates cosinusoidally while the antibonding orbital density oscillates sinusoidally, i.e. 90° out of phase, due to opposite signs of the MO coefficients. The obvious constant periodicity in both of these density oscillations can be obtained from the bond-parallel momentum density projection plots and is found to be $4.49a_0^{-1}$ (= 2π/bond length).[5] Of course the molecular geometry is *directly* shown in the position-space maps (figure 5.12, bottom) where the nuclear positions are shown by crosses (+). It is noteworthy that the momentum density oscillation effect in the $1\sigma_u$ orbital is more severe and more extended than that of the $1\sigma_g$ orbital. This is not surprising since the overlap of FT waves with two well defined density lobes in the $1\sigma_u$ orbital should be more complete than the corresponding overlap with the partially merged lobes in the $1\sigma_g$ orbital (see figure 5.12, bottom and figure 5.7, upper RHS). This is because the significant bonding density in the region between

[5] In H_2 the equilibrium internuclear separation (bond length) is $1.4a_0$. This oscillating phenomenon has also been referred to as "bond oscillation" [ET77]. The relation between momentum density and position density is analogous to that between an X-ray diffraction pattern and the corresponding crystal structure.

the lobes leads to interference cancellation. It is clear that it is unlikely that these density oscillations could be observed experimentally in the spherically averaged momentum distributions of H_2 because of the very small amplitudes of the modulations. (Note that even for oriented H_2 the first oscillation is already at least four decades lower in intensity). Since the binary (e,2e) experiment is most useful and sensitive in the chemically interesting low momentum (large position) region, the observation of the density oscillations is of marginal interest in the study of chemical bonding and reactivity. However the large momentum region in which the density oscillations occur is of importance in the stringent evaluation of the (e,2e) reaction theory of molecules since even in the case of atoms apparent deviations from the PWIA have been observed in momentum densities above $\simeq$ 1-1.5 a_0^{-1} [MW76a, LB83a] (chapter 4) using impact energies below $\simeq$ 1200 eV.

5.4.7 Bond Formation In H_2

At this point, it is instructive to consider the binding and antibinding regions in r-space and p-space for the single covalent sigma bond of the hydrogen molecule. It is interesting to note that in momentum-space the formation of a stable or unstable system (either atomic (figure 5.5) or molecular (figure 5.7)) results in depletions of density in

the low momentum region around the p-space origin (the so-called "white hole"). Addition of density to the bond-perpendicular high momentum region has the effect of increasing the total kinetic energy (and hence lowering the total energy by the Virial relation) and causes the formation of a stable chemical bond. Accumulation of density in the bond-parallel high momentum region is less effective in increasing the kinetic energy since the parallel component is smaller than the perpendicular components [FRM70, FR71]. This also causes outward charge polarization in r-space (in the internuclear direction) which increases the nuclear-nuclear repulsion force, leading to an unstable system.

In order to further investigate the formation of a stable chemical bond, position and momentum density difference maps at a number of internuclear separations are shown in figure 5.13. The wavefunctions used are those of Das and Wahl [DW66], which are reported as a function of internuclear separation. The internuclear separations are 8, 6, 4, 2, 1.4 and $1a_0$ respectively and are so indicated on the maps. The ranges of all momentum density difference maps are the same (from $-2.5a_0^{-1}$ to $2.5a_0^{-1}$) in both directions. The ranges of the position density difference maps are different depending on the nuclear separations. Before discussing these density difference maps, one must keep in mind that comparison of the relative negative and positive amplitudes can only be made within a single density map and its

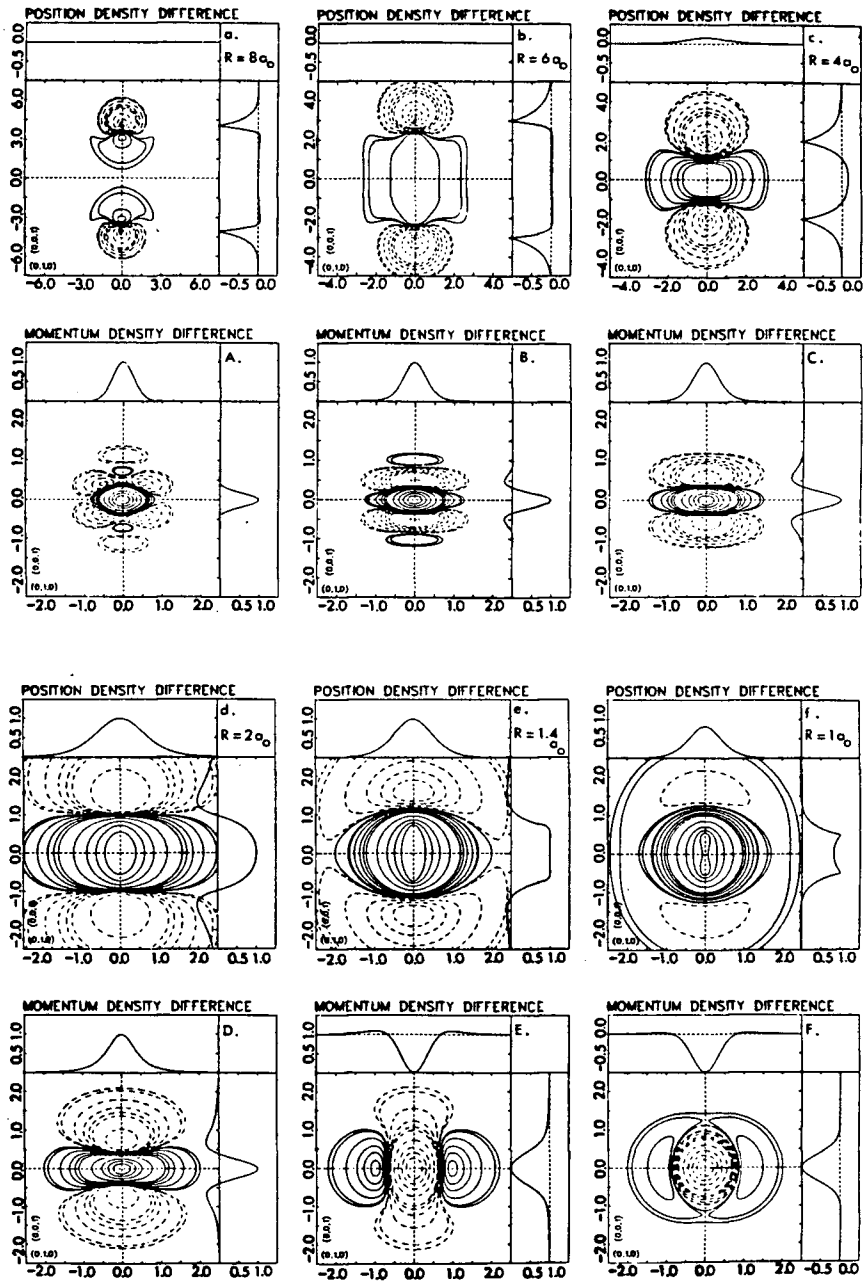

Figure 5.13 - Density difference contour maps in position and momentum space showing the dynamics of the formation of H_2 $1\sigma_g$ orbital as a function of the internuclear separation R. Negative density contours are indicated by dashed lines.

associated projection plots. The absolute maximum density value in each difference map is indicated in table 5.2 in order to give some idea of the global change upon attaining the equilibrium separation.

The most conspicuous pattern seen in the series of position and momentum density difference maps is the gradual transfer of density in the respective space from its antibinding region into its binding region as the internuclear separation approaches the equilibrium value. The r-space topographic sequence of bond formation suggests that the mechanism of bond formation can be viewed as orbital contraction accompanied by density localization into the binding region. The orbital contraction in r-space is illustrated by the bond axis projection plots for R=8 and $6a_0$ (figures 5.13a and b, note the scale change) where relatively large density depletion around each of the atomic centres is clearly observed. The density localization into the binding region can be seen from the position density difference maps and their associated projection plots for R=4, 2, and $1.4a_0$ (figures 5.13c, d and e) where there is an increasingly significant charge accumulation between the atomic centres as R decreases. This is also indicated by the relative magnitudes of the positive and negative segments in the bond-parallel projection plots.

In p-space, the general transfer of density from the bond-parallel high momentum (antibinding) region into the

Table 5.2
Maximum absolute values of density difference for H_2 $1\sigma_g$ as a function of R.

R (a_0)	Maximum density difference (a.u.)	
	r-space	p-space
1	0.284	-0.571
1.4	0.115	-0.251
2	0.049	0.252
4	-0.023	0.505
6	-0.006	0.222
8	-0.005	0.131

bond-perpendicular high momentum (binding) region is clearly observed. It is interesting to find that the initial orbital contraction in r-space (note scale change between figures 5.13a and b) not only results in momentum density spatial expansion (figures 5.13A and B) but also causes oscillations of the difference density between the positive and negative lobes (especially along the bond axis, see figure 5.13B). Such oscillation must not be confused with the previously discussed density oscillation effect which arises purely from Fourier transformation of the r-space LCAO-MO wavefunction. The effect of r-space localization of density into the region between the atomic centres is clearly illustrated by the r-space axis projection plots where there is a transfer of density from the antibinding region (negative density difference) into the binding region (positive density difference). In p-space this corresponds to a loss of density in the free electron region around the p-space origin. See figures 5.13B, C, D and E. As the atoms approach each other the negative lobes are seen to penetrate deeper and deeper into the p-space origin along the bond-parallel direction until the equilibrium geometry is reached where the total effect of contraction and localization gives rise to the "bone in a donut" picture of chemical bonding in momentum-space discussed above. It can be seen that the bond-perpendicular p-space projection plot changes *drastically* going from $R=2a_0$ (figure 5.13D) to $R=1.4a_0$

(figure 5.13E) where the density difference has changed sign from positive to negative around the p-space origin. Changes in this region will be further discussed in the following chapter.

Further closer approach of the atoms at $R=1a_0$ increases the relative density in the high momentum bond-parallel region (figure 5.13F) at the expense of density in the bond-perpendicular region. The corresponding position density difference map (figure 5.13f) shows that charge accumulation between atomic centres becomes saturated, which causes an apparent concentration of charge around the atomic centres. Such a polarization effect increases the electron-electron repulsions and therefore leads to instability. A further decrease in R will eventually fuse the two lobes together (see bond-parallel projection plot) to form a helium atomic system (figure 5.5). Such a change will further increase the density in the bond parallel high momentum region, leading to the "hollow ball" arrangement of the density difference of a stable helium atom in p-space. The hollow ball is again a stable system as discussed above. (See figure 5.5.)

Chapter VI

BOND DENSITY OF MOLECULAR HYDROGEN IN MOMENTUM SPACE

6.1 INTRODUCTION

The ground state electronic wavefunction of molecular hydrogen has been the subject of many experimental investigations including both binary (e,2e) spectroscopy [WM&77, LB83b] and Compton scattering [L77]. In general Compton scattering experiments sample the momentum density due to all the electrons of the target. Binary (e,2e) spectroscopy [MW76a], on the other hand, samples selectively the momentum density of individual orbitals and provides a direct and sensitive experimental evaluation of molecular orbital wavefunctions. In the case of H_2, the total momentum density is to a very good approximation that of the $1\sigma_g$ orbital. The generally good agreement of the momentum distribution of molecular hydrogen observed by the two different techniques has been demonstrated in the preceding chapter (see also ref. [LB83b]). The ground state wavefunction of H_2 has also been investigated by many elaborate theoretical *ab-initio* calculations. The hydrogen molecule is also the simplest test molecule for configurational interaction methods. Moreover, it involves the simplest (covalent) chemical bond and is thus suitable

for the fundamental studies of chemical binding and electronic structural properties. Earlier works by Berlin [B51], Roux and Cornille [RC62] and Bader *et al*. [BH67, BC68] involved position (charge) density difference (bond density) maps and the force concept. Other works by Bader and Preston [BP69] and by Feinberg *et al*. [FRM70, FR71]. examined the behaviour of the kinetic and potential energies upon bond formation and the role of the Virial theorem therein.

The bond density in either position or momentum-space is defined (as in the preceding chapter) to be the density difference between the molecular density ($\rho\{H_2\ 1\sigma_g\}$) and the density due to independent atoms (the independent atom model density, $\rho\{IAM\}$) at positions corresponding to the molecular nuclear geometry, i.e.

[6.1a] $$\Delta\rho = 2\rho\{H_2\ 1\sigma_g\} - \rho\{IAM\} \quad \text{at R},$$

[6.1b] $$\rho\{IAM\} = \rho\{H\ 1s\} + \rho\{H\ 1s\} \quad \text{at R},$$

where R is the internuclear separation and ρ denotes the single electron density. It is possible to obtain the "experimental" (spherically averaged) momentum-space bond density using the experimental momentum distributions of the $H_2\ 1\sigma_g$ orbital and either the experimental or the exact theoretical momentum distribution of the 1s orbital for the H atom. The momentum distribution for the 1s orbital of atomic hydrogen has been determined recently by Lohmann and Weigold

[LW81] using binary (e,2e) spectroscopy. The measured result is found to reproduce the exact solution of the Schrodinger equation in momentum-space. The only difficulty involved in obtaining the bond density is the normalization of the measured spherically averaged momentum density of H_2 $1\sigma_g$ because the noncoplanar symmetric (e,2e) experiment measures (in most cases) only relative cross sections [MW76a]. In the present study, this problem is solved by employing a numerical procedure. The "experimental" momentum-space bond density thus obtained is compared with theoretical calculations using H_2 wavefunctions of different quality including Extended Hartree-Fock (Ext-HF) [DW66], Limited Hartree-Fock (Ltd-HF) [FR61], Double-Zeta (DZ) [SB72] and Minimal Basis Set (MBS) [HL&80]. In addition the dependence of the bond density on the quality of the wavefunction is also examined by directional momentum-space and position-space density difference maps [CD41, B51, RC62, BH67, BC68, HC68, BP69, ET77, LB83b, R83]. The study (chapter 5) of the bonding in H_2 at large step spacings between internuclear separations of R=8 and $1a_0$ has indicated that dramatic changes in momentum-space bond density occur between R=2 and $1a_0$. The topographical study of the momentum-space bond density in H_2 is now extended to explore in detail the critical range of R=2 to $1a_0$ using the extended Hartree-Fock quality wavefunction of Das and Wahl [DW66]. The present study provides a complementary look at chemical bonding

phenomena of H_2 in momentum and position space and further illustrates momentum-space chemical concepts [CD41, ET77, CS&79, CB82b, MTC82, LB83b]. A three dimensional representation is shown for the H_2 $1\sigma_g$ single covalent bond in momentum-space.

6.2 ESTIMATION OF THE ORBITAL MOMENTS AND NORMALIZATION OF THE MOMENTUM DISTRIBUTION

In the present work, the spherically averaged momentum-space bond density of H_2 $1\sigma_g$ is obtained by equation 6.1 using the experimentally determined momentum distribution of the H_2 $1\sigma_g$ orbital (chapter 5) and the exact atomic hydrogen 1s momentum distribution [LW81]. The experimental momentum distribution of the H 1s orbital has been shown to be in excellent agreement with the exact solution (squared) of the Schrodinger equation in momentum-space [LW81]. The procedure for normalization of the relative spherically averaged momentum density of the H_2 $1\sigma_g$ orbital to give an absolute density is outlined below. Briefly, an analytical function is fitted to the experimental spherically averaged momentum distribution using a square residual minimization method [L72c, M81]. The n^{th} order momentum moments of the j^{th} orbital, $\langle p^n \rangle_j$, are then evaluated from the fitted function using standard numerical integration techniques [L72c].

[6.2a] $$\langle p^n \rangle_j = 4\pi \int \{\rho_j(p)\} p^{n+2} dp,$$

where $\{\rho_j(p)\}$ is the spherically averaged momentum distribution of the j^{th} orbital. The experimental distribution and the optimized analytical density function can be normalized by the zeroth order moment. In the case of H_2, one has:

[6.2b] $$\langle p^0 \rangle 1\sigma_g = \text{occupancy number of } 1\sigma_g \text{ orbital} = 2.$$

Three semi-empirical analytical functions are used to approximate $\{\rho(p)\}$ of the H_2 $1\sigma_g$ orbital. These are:

(i) Orbital Local Density Functional (OLDF) density:

$$\{\rho(p)\} = K\ (p^2/2 + a_1 p + a_2)^{-3};$$

(ii) Best Single Zeta (BSZ) density:

$$\{\rho(p)\} = K\ (\zeta^5)\ (\zeta^2 + p^2)^{-4};$$

(iii) Two Term Polynomial (TTP) density:

$$\{\rho(p)\} = K_1(\gamma_1^2 + p^2)^{-4} + K_2(\gamma_2^2 + p^2)^{-5}.$$

The linear parameters (K, K_1 and K_2) are normalization constants. Both the linear (K's) and the nonlinear parameters (a's, ζ and γ's) are optimized by fitting to the experimental momentum distribution in the numerical procedure [M81]. The OLDF density form used here is that given by Pathak *et al.* [PPG82] and should strictly be used for the

total momentum density of atoms in the local density functional approximation [L79]. The BSZ (Best Single Zeta) momentum density corresponds to the square of the Fourier transform of a position-space 1s Slater-Type-Orbital [KT76] with the ζ value optimized to give the best fit to the experimental momentum distribution. The two term polynomial function (TTP) is used by Lee [L77] in his study of the total momentum density of H_2 by high energy electron impact spectroscopy. It should be noted that the two term polynomial function is essentially the BSZ function with an additional high order term.

Figure 6.1 shows the experimental momentum distribution of the H_2 $1\sigma_g$ orbital (see also figure 5.4) along with the fitted analytical density functions. It is obvious that all three semi-empirical density functions give an excellent fit to the experimental data. The BSZ and TTP densities are indistinguishable from each other while the OLDF density is only slightly different from the BSZ and TTP densities in the low and high momentum region.

Table 6.1 shows the orbital momentum moments calculated using the optimized density functions. Orbital moments evaluated directly from *ab-initio* SCF wavefunctions of different quality [HL&80, SB72, FR61, DW66] are also given. These moments are compared with those reported by Lee [L77]. Clearly, there is an overall good agreement between the "experimental" orbital moments (less good for the higher

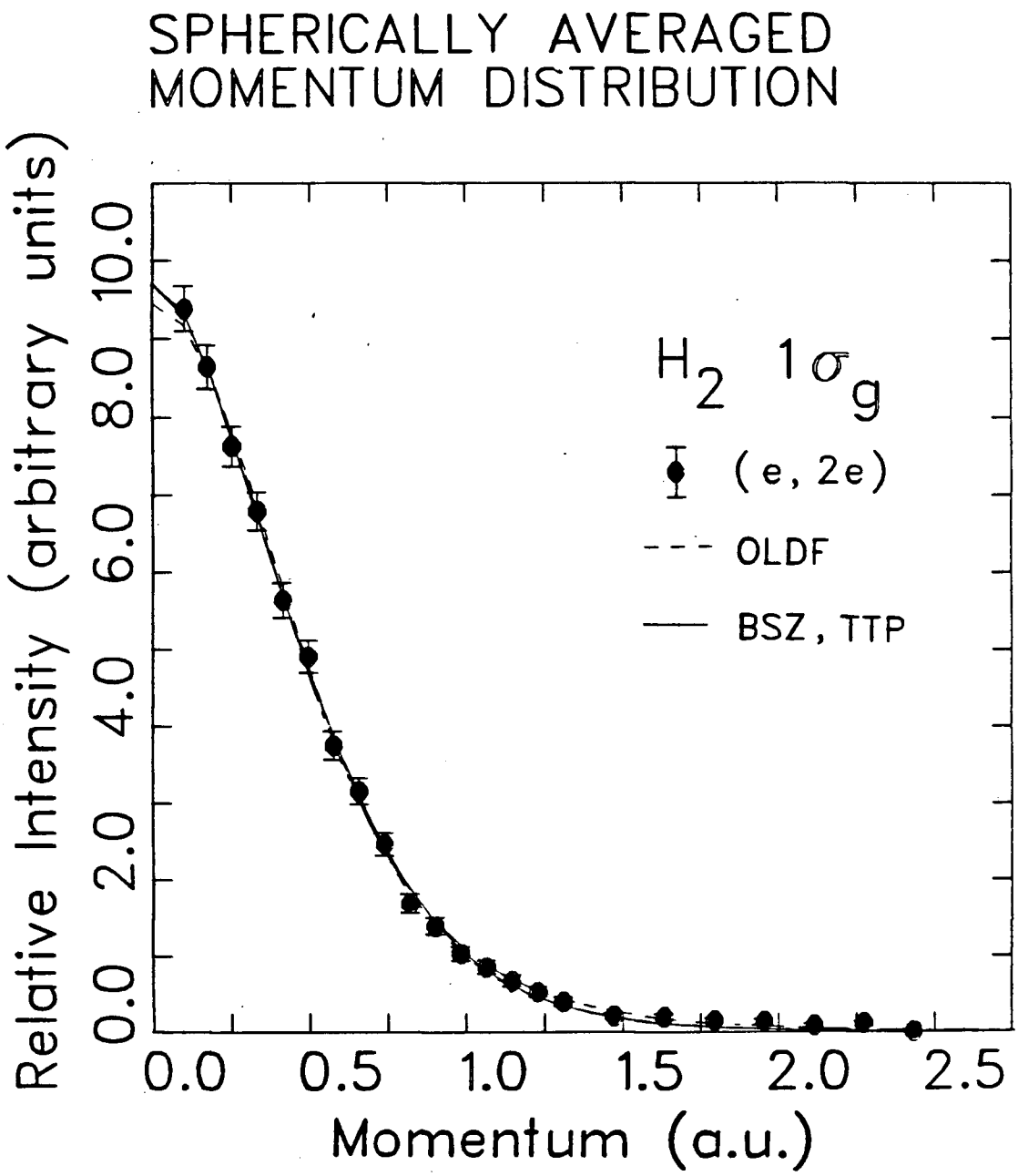

Figure 6.1 - Comparison of the experimental spherically averaged momentum distribution of H_2 $1\sigma_g$ orbital with the fitted semi-empirical density functions: OLDF, BSZ and TTP. The BSZ and TTP functions are indistinguishable from each other.

Table 6.1
Orbital momentum moments (in atomic units) of H_2 $1\sigma_g$ orbital.

Moment	"Experimental"*			Theory**				Lee+
	OLDF	BSZ	TTP	Ext-HF	Ltd-HF	DZ	MBS	
$\langle p^2 \rangle$	6.36	7.56	7.62	8.24	7.86	7.20	6.92	8.32(0.25)
$\langle p^1 \rangle$	2.62	2.96	2.96	3.18	3.02	3.02	2.96	3.08(0.02)
$\langle p^0 \rangle$	2.00	2.00	2.00	2.00	2.00	2.00	2.00	1.99(0.02)
$\langle p^{-1} \rangle$	2.46	1.96	1.92	1.82	1.82	1.84	1.90	1.86(0.02)
$\langle p^{-2} \rangle$	2.86	2.62	2.50	2.26	2.26	2.26	2.40	2.34(0.09)

* The accuracy is expected to be about ±7%.
** The accuracy is about ±4%. Note that the various wavefunctions are: Ext-HF [DW66], Ltd-HF [FR61], DZ [SB72] and MBS [HL&80].
\+ The moments are evaluated by Lee [L77] using a similar two term polynomials optimization of the Compton scattering data. Uncertainties are shown in brackets.

moments $\langle p^2 \rangle$) and the theoretical ones. The semi-empirical BSZ and TTP moments are quite close to each other with the OLDF moments being noticeably different. In particular, the OLDF density significantly underestimates the average orbital moment $\langle p \rangle$. This deficiency is due to the form of the OLDF density, which in general will lead to a broader total momentum distribution even for atoms [PPG82]. The OLDF moments show that the reported form of the OLDF function [PPG82] is not adequate to represent the momentum density of small molecules like hydrogen. It is also evident from table 6.1 that the "experimental" moments are slightly different from the theoretical ones. The estimated averaged orbital momenta $\langle p \rangle$ are generally slightly lower than the theoretical ones. This suggests that the experimental H_2 $1\sigma_g$ orbital is less spatially diffuse (in position-space) than that predicted by the more sophisticated *ab-initio* wavefunctions. It should be noted that the momentum distribution measured at a particular binding energy is in general related to the overlap form factor [MW76a]. In the target Hartree-Fock approximation [MW76a], the form factor can be simplified to the orbital momentum density. It is also possible that small differences in the estimated orbital momenta $\langle p \rangle$ between the experiment and theories may be attributed to the inadequacy of the target Hartree-Fock approximation. The results of binary (e,2e) spectroscopy involve vibrational averaging over the final ion state [MW76a]. The effects of this averaging

on the comparison of experimentally determined momentum distributions and those calculated at a single R value are expected to be negligible as demonstrated by the work of Dey *et al*. [DM&75] on H_2 and D_2.

6.3 SPHERICALLY AVERAGED MOMENTUM-SPACE BOND DENSITY

Figure 6.2 shows the spherically averaged momentum-space bond density of H_2. The right hand section of figure 6.2 shows the detail between $0.5a_0^{-1}$ and $1.5a_0^{-1}$. The constants optimized in the orbital moment estimation procedure are used to normalize the experimental spherically averaged momentum distribution of the H_2 $1\sigma_g$ orbital (chapter 5). The Independent Atom Model density is obtained from the exact solution for the H 1s orbital. Equation 6.1 is then used to calculate the bond density. Theoretical bond densities corresponding to different quality wavefunctions of the H_2 $1\sigma_g$ orbital are also given for comparison.

Several interesting features are apparent. First, the spherically averaged momentum-space (p-space) bond density consists of a negative well and a positive wing tailing off to $p=\infty$ with the zero-crossing point at $p\simeq 0.8a_0^{-1}$. Although the directional information is lost after the spherical averaging, one can see that a sigma bond is characterized by a transfer of momentum density (fractional current) from the low momentum region to the high momentum region. In

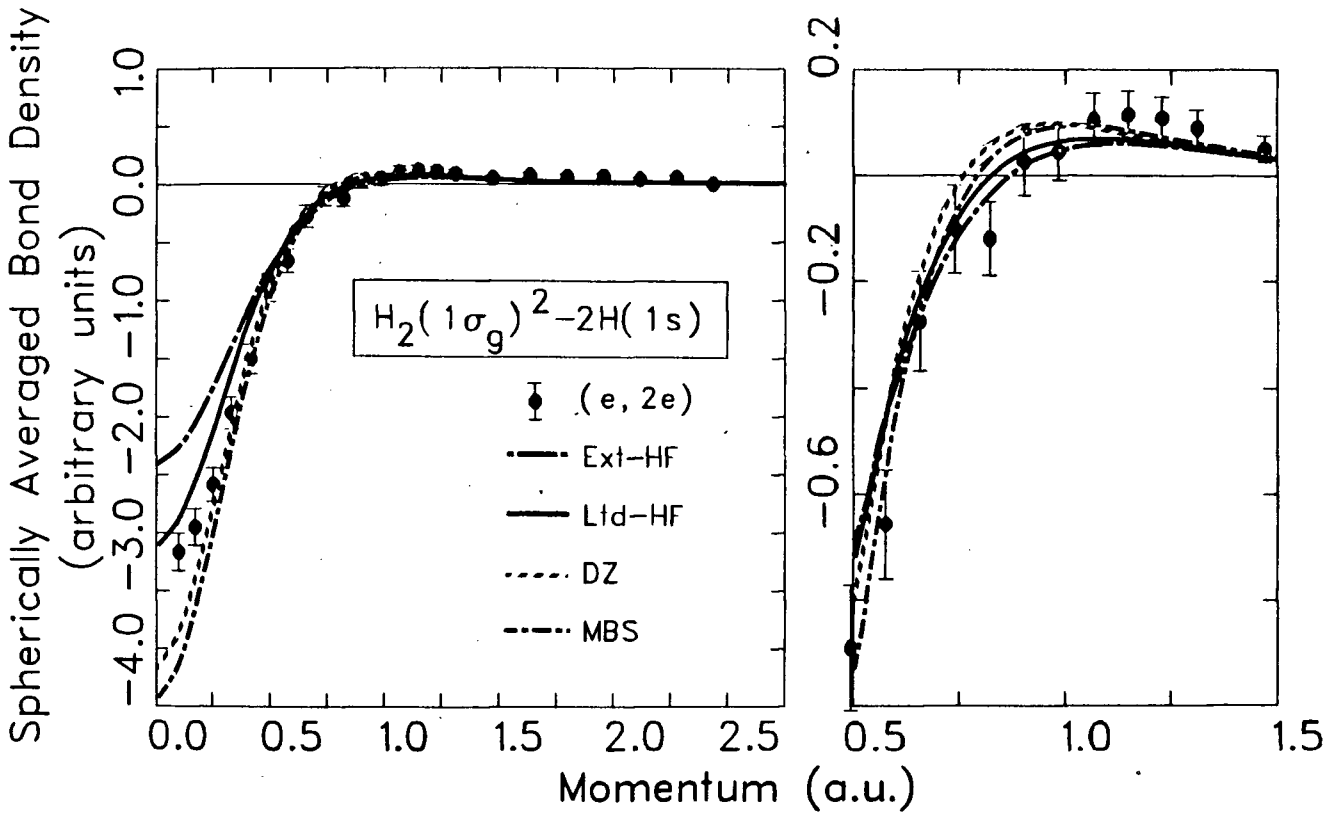

Figure 6.2 - Spherically averaged momentum-space bond density of H_2. An exploded view of the bond density in the range 0.5 to 1.5 a_0^{-1} is given to illustrate the positive "wing" of the bond density.

addition, the variationally less superior DZ [SB72] and MBS [HL&80] wavefunctions have "deeper wells" (i.e. more negative minima) at the p-space origin and slightly sharper "wings" (positive maxima) than the more sophisticated ones [FR61, DW66]. Furthermore, the "experimental" bond density lies between the Limited Hartree-Fock and the Double-Zeta quality bond densities at low momentum. It is, however, in closer agreement with the Limited Hartree-Fock curve near the momentum origin. It should be noted (chapter 5) that the experimental spherically averaged momentum distribution of the H_2 $1\sigma_g$ orbital gives generally good agreement with theoretical density functions calculated using the Limited Hartree-Fock and better quality wavefunctions. The momentum-space bond density shows the differences between different wavefunctions more clearly than straightforward comparison of the momentum distributions (see figure 5.4b). The momentum-space bond density is therefore an alternative way to evaluate wavefunctions by comparing with experimental (e,2e) data, at least in the special case of the hydrogen molecule where the bond density can be readily derived.

6.4 DIRECTIONAL BOND DENSITY

6.4.1 Wavefunction Dependence

Except where otherwise stated, the density contour values of the directional bond density (density difference) maps used throughout the present study correspond to 80, 60, 40, 20, ±8, ±6, ±4, ±2, ±0.8 and ±0.6% of the absolute maximum density difference value. Contours of negative density difference are shown as dashed lines. The directions of the cutting plane are defined by two vectors; i.e. the bond-parallel or internuclear (0,0,1) vector and the bond-perpendicular (0,1,0) vector. The projection plots on the right hand side and on the top of the contour maps show the relative change in magnitude of the bond density function along and perpendicular to the internuclear axis (dotted lines) respectively. The position and momentum are in atomic units.

Figure 6.3 shows the directional density difference maps corresponding to H_2 $1\sigma_g$ wavefunctions of different quality ranging from Extended Hartree-Fock (Ext-HF) [DW66], Limited Hartree-Fock (Ltd-HF) [FR61], Double-Zeta (DZ) [SB72] and Minimal Basis Set (MBS) [HL&80]. The equilibrium internuclear separation ($1.4a_0$) has been used for the calculations shown in figure 6.3. It should be noted that because of the nature of the DZ and MBS wavefunctions, the contour values for the momentum-space (p-space) bond density

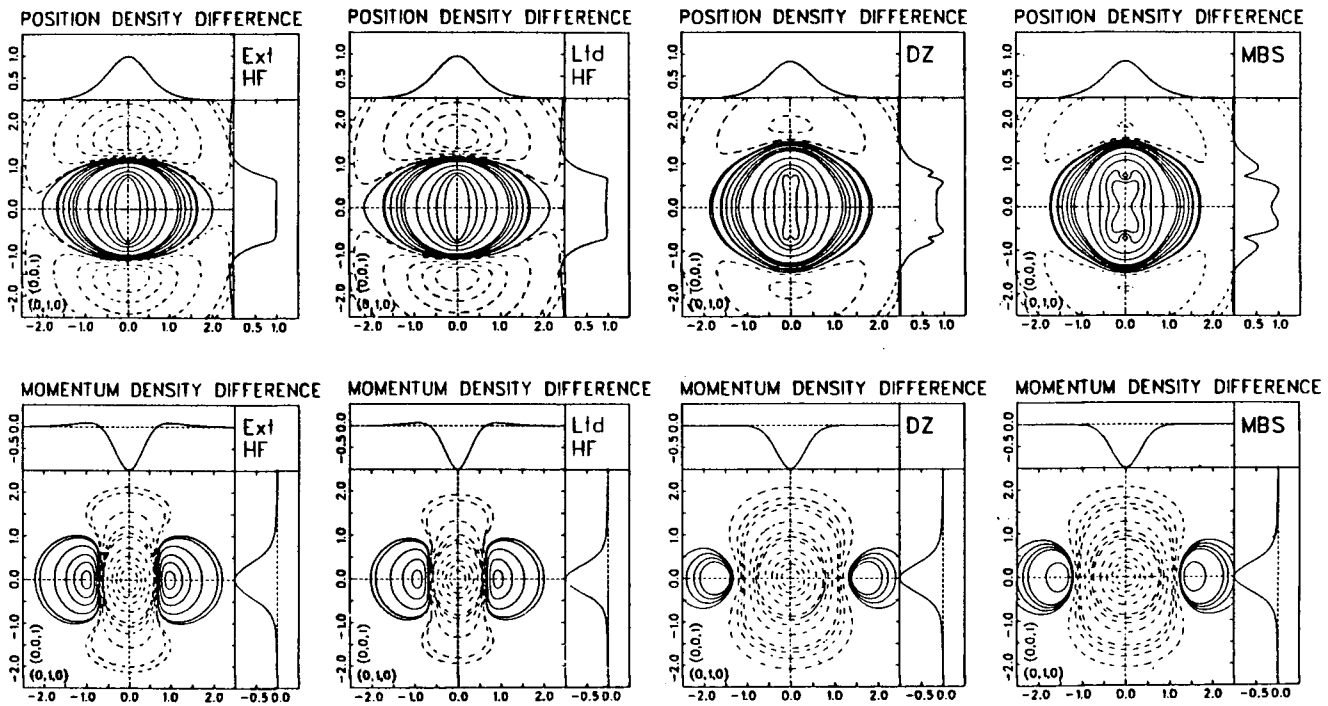

Figure 6.3 - Density difference (bond density) maps in momentum and position space as a function of the type of the H_2 $1\sigma_g$ wavefunction at equilibrium separation. Contours of negative density difference are shown as dashed lines.

(density difference) maps have been extended to include ±0.4, ±0.2, -0.08, -0.06, -0.04, and -0.02% of the *absolute* maximum density difference value.

It is evident that all four wavefunctions provide a qualitatively similar picture for the sigma bond. In general, the sigma bond in H_2 in position-space (r-space) can be associated with the familiar "hamburger" picture; namely, density (fractional charge) accumulation in the internuclear region and density depletion at the end regions of the molecule [BC68]. In momentum-space (p-space) a complementary view of the sigma bond is obtained as discussed in the preceding chapter. In this "bone in a donut" (or torus) model, momentum density (fractional current) is depleted through the p-space origin along the internuclear direction (the "bone" part) and is localized annularly in the high momentum bond-perpendicular region (the "donut"). Similar ideas have also recently been presented by Ramirez [R83]. It should be noted that the cylindrical symmetry of the sigma bond in r-space is preserved in p-space. This is, of course, a direct consequence of the Fourier transform properties discussed previously [ET77, LB83b]. A three-dimensional surface plot of the bond densities generated using the Ext-HF wavefunction [DW66] is shown in figure 6.4 to better visualize the nature of the H_2 $1\sigma_g$ bond in both p-space and r-space. The bond densities for surfaces shown correspond to ±2% of the maximum bond density values in the respective

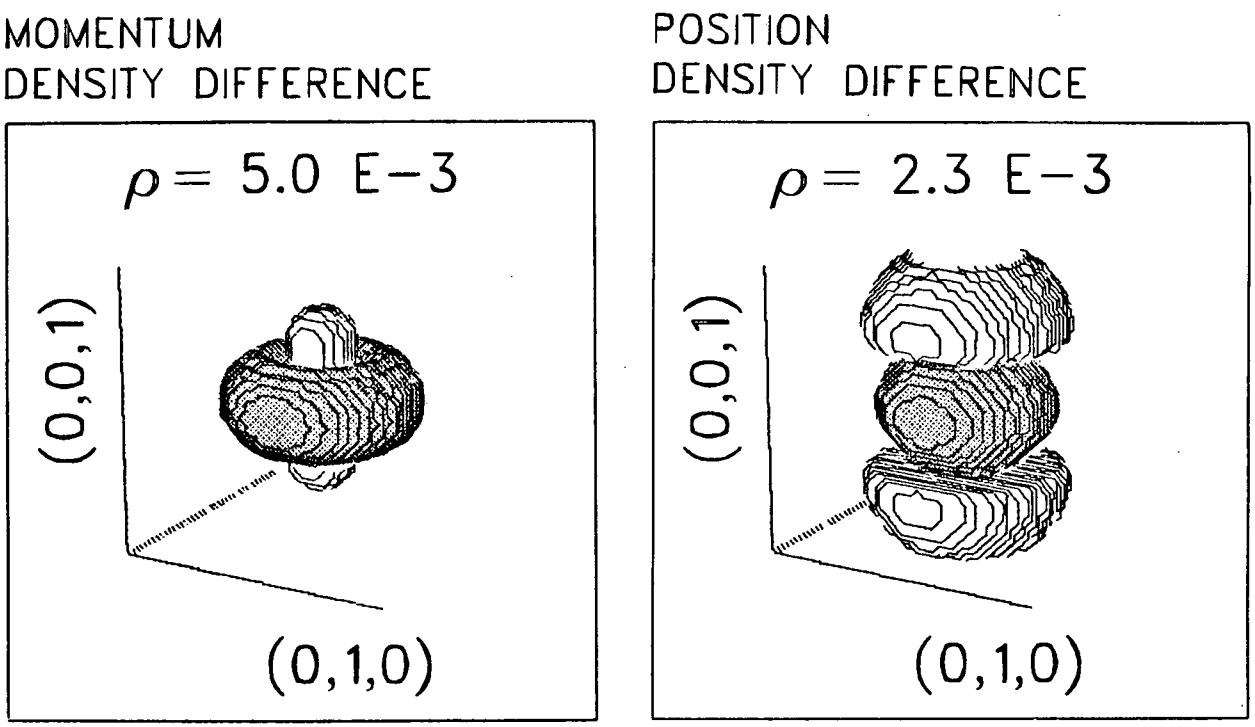

Figure 6.4 - Three-dimensional surface plot of the density difference (bond density) of H_2 in momentum and position space. The bond density surfaces correspond to ±2% of the maximum bond density values. Positive bond density surfaces are shaded.

spaces.

Although all four wavefunctions show the same general density topographical features (see figure 6.3), there are some important differences, especially between the Ltd-HF and DZ. For the Ext-HF and the Ltd-HF bond densities both the r-space and p-space bond densities respectively appear to be quite similar. The only noticeable difference is in the end regions of the "bone" part. The major difference occurs between the Ltd-HF and the DZ bond densities. The pronounced change in the nature of the wavefunction can be seen in the r-space bond density whereby the bond-perpendicular ellipsoidal positive lobe of the Ltd-HF (and Ext-HF) becomes more spherical in the DZ (and MBS). This can be seen more clearly in the bond-parallel projection plots, which show the appearance of four well defined positive maxima for the DZ (and MBS) instead of the flat positive "plateau" for the Ltd-HF (and Ext-HF). The negative lobe of the DZ not only has a relatively smaller amplitude but also is further away from the r-space origin. Even more dramatic differences can be seen in the p-space density difference maps. (Note that more contour lines with smaller bond density values are included for the DZ and MBS bond densities in figure 6.3). The p-space bond of the DZ (and also MBS) is dominated by the negative "bone" structure, which appears also to be considerably broader than that of the Ltd-HF (and Ext-HF) one. The positive "donut" structure can only be seen when

relative contour values below 0.1% of the maximum amplitude are used. In the case of the MBS wavefunction, its r-space bonding structure is even more inadequate as shown by the bond-parallel projection plot. The p-space "donut" structure is also slightly larger compared to the DZ one.

6.4.2 Dependence Of Internuclear Separation

Figure 6.5 shows the directional bond density (density difference) in both p-space and r-space corresponding to the Hartree-Fock quality wavefunction of Das and Wahl [DW66] as a function of internuclear separation R. Earlier work by Bader and Chandra [BC68] reported the r-space bond density maps evaluated using the same Ext-HF wavefunction [DW66] as a function of R. The present work studies the progress of bond formation in p-space over the critical separation range of $1.0a_0 \leq R \leq 2.0a_0$. A preliminary study of bond formation over a more extensive range and wider spacing of selected R values has been given in the preceding chapter. It should be noted that comparison can only be made within a single difference map since contour values are relative to the maximum bond density. The maximum bond densities in the contour planes are shown in table 6.2 to give some indication of the global change as the H atoms approach each other.

Bond formation as represented by this series of sigma bond density maps for H_2 involves the transfer of density

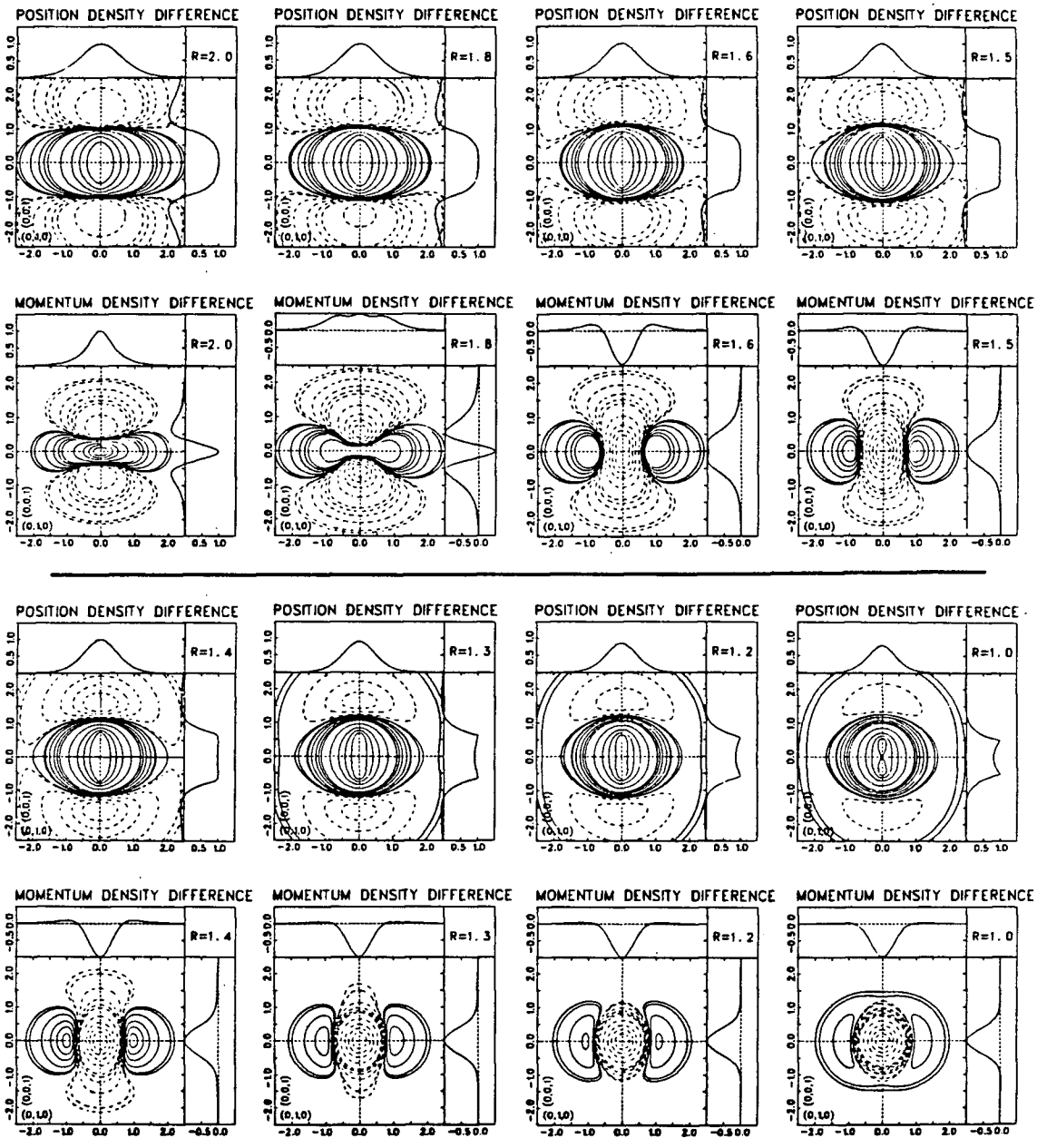

Figure 6.5 - Density difference (bond density) maps in momentum and position space as a function of internuclear separation R. Contours of negative density difference are shown as dashed lines.

Table 6.2
Maximum absolute values of bond density as a function of R.

R (a_0)	Maximum bond density	
	r-space	p-space
2.0	0.0451	0.192
1.8	0.0593	-0.0769
1.6	0.0792	-0.122
1.5	0.0930	-0.197
1.4	0.113	-0.276
1.3	0.142	-0.354
1.2	0.178	-0.433
1.0	0.281	-0.585

* R and the bond density are in atomic units. Note that the equilibrium internuclear separation is 1.4 a_0.

from the antibinding region to the binding region. The r-space binding region is, of course, the small r (i.e. internuclear) region with density extended preferentially in the bond-perpendicular direction while the antibinding region is at large r outside the nuclei extending preferentially in the bond-parallel direction. In contrast the locations of the binding and antibinding regions in p-space are reversed. Specifically, the binding region in p-space is the annular (bond-perpendicular) high p region while the antibinding region is centred at low p and distributed preferentially along the bond-parallel direction. Between $R=2.0a_0$ and the equilibrium separation at $1.4a_0$, the gradual charge accumulation in the r-space binding region is particularly obvious as shown in the bond-parallel projection plots. Further closer approach of the H atoms causes charge saturation in the internuclear region, causing the pile-up of density at the maxima seen particularly clearly at $R=1.0a_0$. A much more dramatic change can be seen in the p-space density difference. At $R=2.0a_0$ the p-space bond density is in fact somewhat similar in shape to its r-space counterpart. In the R range of 2.0 to $1.4a_0$, the penetration of the negative lobe of the p-space bond density into the positive lobe along the bond axis results in the formation of the binding "donut" structure. This dramatic change (in marked contrast to the r-space pictures which only change marginally) is remarkably obvious in both the bond-parallel

and the bond-perpendicular projection plots. Most notable is the change between R=1.8 and $1.6a_0$. Below the equilibrium internuclear distance ($1.4a_0$) closer approach of the H atoms results in the transfer of momentum density back into the antibinding bond-parallel high p region. The enclosure of the negative lobe by the positive lobe generates the unstable oval structure at $R=1.0a_0$.

The difference in density relocation in r-space and p-space is in accord with the Virial property (section 2.2.2) [ET77, LB83b]. The formation of a stable system must be accompanied by the lowering of the total energy, or equivalently by the raising of the kinetic energy. The kinetic energy (T) can be increased more effectively by transferring the density into the high momentum bond-perpendicular region because the parallel component (T_{para}) of the kinetic energy of a diatomic is smaller than the perpendicular component (T_{vert}) [BP69, FRM70, FR71]. The phenomenological change in p-space bond density upon bond formation is indicative of this Virial requirement. In this regard, Bader and Preston [BP69] have shown earlier that the difference between the bond-perpendicular and bond-parallel components of the kinetic energy, $(T_{vert}-T_{para})/T$, reaches its maximum in H_2 between $R=2.0a_0$ and $1.4a_0$. The results of the present investigations are entirely consistent with the theoretical analysis of kinetic energy density in H_2 given by Bader and Preston [BP69]. The presently reported

experimental studies of the distribution of bond density in momentum-space are also consistent with the predictions made in the pioneering theoretical work of Coulson and Duncanson [CD41] in 1941 concerning the electron momentum distribution in a single bond. Finally, the p-space bond density maps complement the r-space bond density maps to provide a more complete bonding picture. Namely, the formation of a stable sigma bond in molecular hydrogen can be regarded as a transformation of the "slow" charge moving with a low momentum along the bond axis at the ends of the molecule to "fast" charge moving with a high momentum perpendicular to the bond axis in the internuclear space of the molecule. Clearly bond formation is manifested, in the present study, much more dramatically in momentum-space than in position-space. Since measurements are possible in p-space but thus far not in r-space, the use of momentum-space concepts and binary (e,2e) spectroscopy promises new vistas of chemical bonding both in theoretical and experimental work.

Chapter VII

CARBON DIOXIDE

7.1 INTRODUCTION

A high momentum resolution ($0.1a_0^{-1}$ FWHM) noncoplanar binary (e,2e) measurement of the momentum distributions of the outer valence orbitals of CO_2 is reported. The electronic configuration of CO_2 can be written as:

$$(1\sigma_u)^2(1\sigma_g)^2(2\sigma_g)^2\ (3\sigma_g)^2(2\sigma_u)^2(4\sigma_g)^2(3\sigma_u)^2(1\pi_u)^4(1\pi_g)^4;{}^1\Sigma^+g.$$

Two earlier binary (e,2e) studies [GT&77, CB82a] of the outer valence orbital momentum distributions of CO_2 have been reported. The measurement by Giardini-Guidoni *et al.* [GT&77], although with comparable momentum resolution ($0.1a_0^{-1}$ FWHM), is limited by the rather low energy resolution (2.6eV FWHM). As a result, only the momentum distribution of the $1\pi_g$ orbital was sampled directly. Also because of the coplanar scattering geometry employed, the orbital momentum distributions are somewhat obscured by the Mott scattering cross section, which varies rapidly with the polar angle theta. The more recent noncoplanar measurements reported by Cook and Brion [CB82a] used higher energy resolution (1.3eV FWHM) but were limited by the rather low

momentum resolution ($0.4a_0^{-1}$ FWHM). Low momentum resolution severely limits observation of details in the measured orbital momentum distributions [CBH80] such as (i) minima at p=0, for instance, in the CO_2 $1\pi_g$ orbital and (ii) the more complex structure of momentum distributions for orbitals made up of symmetric (s-type) and nonsymmetric (p-type) components as for example in the CO_2 $4\sigma_g$ orbital. As in all the earlier studies [GT&77, CB82a], the present experimental energy resolution (1.6eV FWHM) is insufficient to resolve the close lying $A(1\pi_u)^{-1}$ and $B(3\sigma_u)^{-1}$ states. However, direct measurements of the momentum distributions of the $X(1\pi_g)^{-1}$ and $C(4\sigma_g)^{-1}$ states are possible (without the use of the deconvolution method in ref. [CB82a]) by judicious choice of the sitting binding energies. With the improved momentum resolution, the present 1200 eV measurements provide a more detailed picture of the outer valence orbital momentum distributions of CO_2 and resolve earlier uncertainties particularly in the low momentum region of the momentum distribution of the $1\pi_g$ orbital.

7.2 OUTER VALENCE BINDING ENERGY SPECTRUM

The binding energy spectrum of CO_2 has been studied in detail by photoelectron spectroscopy [TB&70], dipole (e,2e) spectroscopy [BT78] and binary (e,2e) spectroscopy [GT&77, CB82a] and also theoretically by the Green's function method

[DC&79]. In the present work, limited range binding energy spectra in the outer valence region measured at ϕ=0°, 8° and 14° are shown in figure 7.1. Individual Gaussian line-shapes (dashed lines) corresponding to the $X(1\pi_g)^{-1}$, $A(1\pi_u)^{-1}$, $B(3\sigma_u)^{-1}$ and $C(4\sigma_g)^{-1}$ states are overlayed in the spectra. The sum of the individual Gaussians is represented by the solid line. The binding energy positions (13.8eV for $1\pi_g$, 17.6eV for $1\pi_u$, 18.1eV for $3\sigma_u$ and 19.4eV for $4\sigma_g$) and the corresponding Franck-Condon widths used in the deconvolution procedures were obtained from high resolution photoelectron spectroscopic data [TB&70]. The labelled arrows (i, ii, iii) in the ϕ=14° spectrum indicate the sitting binding energies selected for the angular correlation measurements (see figures 7.2(i), (ii) and (iii) respectively). Clearly, the energy resolution does not allow a clear separation of the A and B states. However, one can infer some qualitative features about the symmetries of the ionized orbitals from the intensity variation of the Gaussian deconvoluted peaks in the three spectra. The relative intensity distributions of the three outermost orbitals, i.e. the $1\pi_g$, $1\pi_u$ and $3\sigma_u$, all reflect the characteristic (nonsymmetric) p-type distributions with maxima away from p=0. The $4\sigma_g$ orbital, on the other hand, has its maximum in the ϕ=0° spectrum, which indicates a symmetric s-type component in the distribution. In addition, there is significant intensity in the ϕ=14° spectrum which suggests an important nonsymmetric

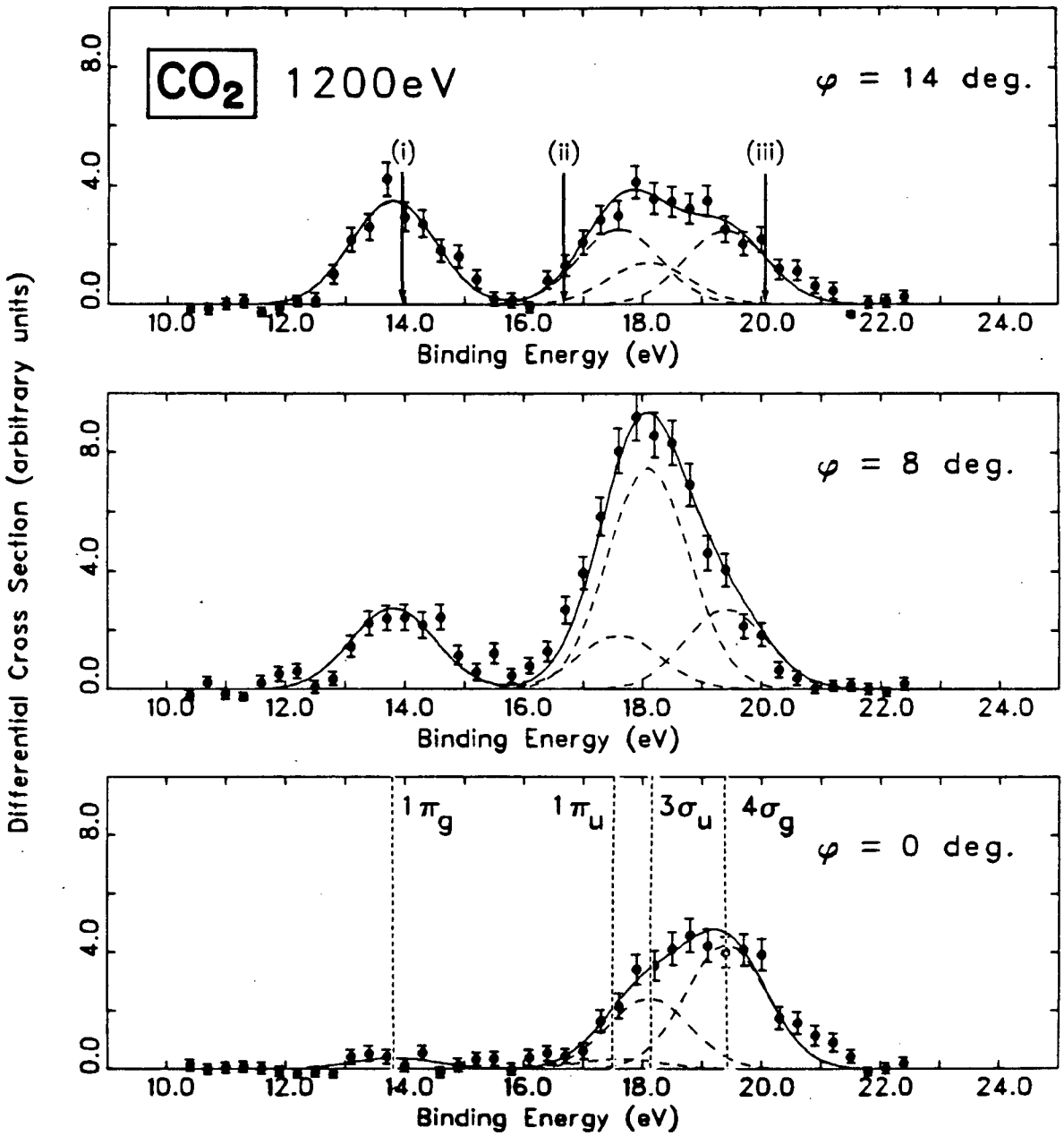

Figure 7.1 - Outer valence binding energy spectra for CO_2 at ϕ=0°, 8° and 14°. The labelled arrows in the ϕ=14° spectrum indicate the sitting binding energies where the momentum distributions are measured (see. figure 7.2).

contribution.

7.3 MOMENTUM DISTRIBUTIONS OF OUTER VALENCE ORBITALS

Figure 7.2 shows the momentum distributions sampled at three different binding energies as indicated by the arrows in figure 7.1. Note that the sitting energies (not the vertical I.P.'s) are indicated in the spectra. Theoretical SCF momentum distributions calculated from the double-zeta basis of Snyder and Basch [SB72] (solid lines) and the standard 4-31G* basis of the GAUSS76 package [HL&80] (dashed lines) as well as an extended Gaussian basis with polarization functions of Langhoff [L84a] (dash-dotted lines) are given for comparison. In figure 7.2(ii) the theoretical momentum distribution due to an admixture of $1\pi_u$ and $3\sigma_u$ orbitals is presented. The mixing coefficients of the individual orbital components (i.e. 0.42 for $1\pi_u$ and 0.58 for $3\sigma_u$) are obtained from the deconvoluted ϕ=8° binding energy spectrum at 16.7eV (figure 7.1). The theoretical distributions are all individually area normalized to the experiment in the momentum range 0 to $1.5a_o^{-1}$.

Generally good agreement between the experiment and the theory is observed. The double-zeta quality wavefunctions of Snyder and Basch [SB72] appear to be marginally superior to both the 4-31G* GAUSS76 wavefunctions [HL&80] and the extended Gaussian basis wavefunctions [L84a]. The present

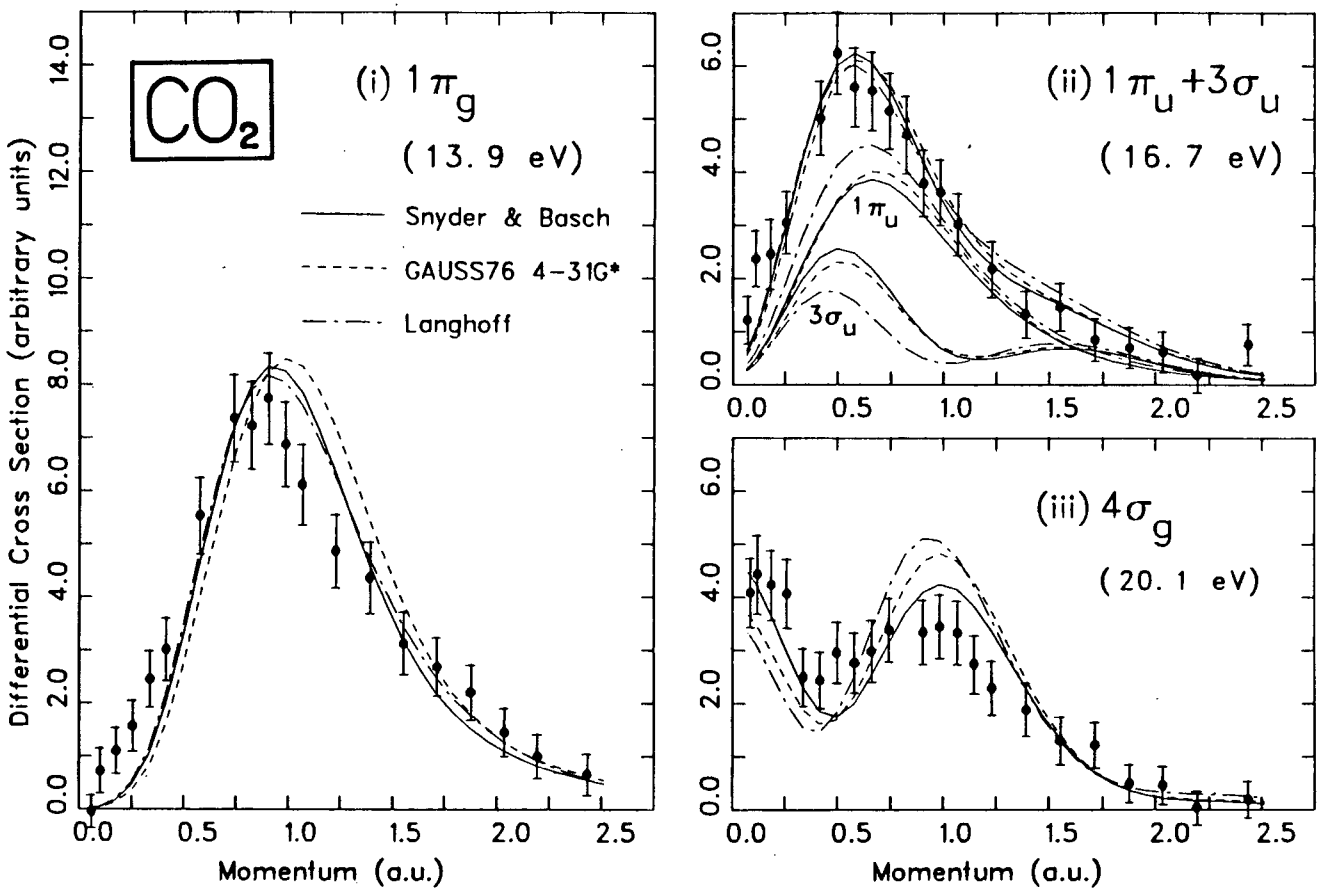

Figure 7.2 - Molecular momentum distributions for CO_2 outer valence orbitals. Theoretical momentum distributions are evaluated using the Snyder and Basch basis [SB72] (solid lines), the 4-31G* GAUSS76 basis [HL&80] (dashed lines) and the extended Gaussian basis of Langhoff [L84a] (dash-dotted lines).

measurements are consistent with those reported earlier [GT&77, CB82a] when the large differences in energy and momentum resolutions are taken into account. Since direct comparison with the momentum distributions of the coplanar work reported by Giardini-Guidoni *et al*. [GT&77] is difficult because the varying Mott scattering cross section distorts the momentum distributions in coplanar studies, comparison is only made with the 400eV noncoplanar measurement of Cook and Brion [CB82a]. It should be noted that the lower accuracy of the momentum distributions reported by Cook and Brion [CB82a] of the $1\pi_u$, $3\sigma_u$ and $4\sigma_g$ orbitals is due to the limited statistical accuracy of the difficult deconvolution procedure [CB82a]. This earlier measurement [CB82a] is also seriously limited by the low angular resolution of the spectrometer which resulted in the measured p-type distributions having considerable intensities at p=0 [CBH80].

For the outermost nonbonding $1\pi_g$ orbital (figure 7.2(i)), there is appreciable intensity in the p=0.2 to $0.5a_0^{-1}$ region not accounted for by any of the theoretical momentum distributions. A similar observation was also made by Cook and Brion [CB82a] in the earlier low momentum resolution measurement at 400eV. However the present measurement clearly rules out any possibility of symmetric components in the wavefunction since the observed momentum distribution goes to zero at p=0 within experimental error. The maximum of the experimental distribution also appears to

be at lower momentum ($p_{max} \simeq 0.8 a_0^{-1}$) when compared to the theory ($p_{max} \simeq 1.0 a_0^{-1}$). These observations suggest an inadequacy in the basis sets of the theoretical wavefunctions for this orbital. Similar behaviour is also found in the outermost 2π orbital of the isoelectronic molecule N_2O [MFW82]. For the $1\pi_u$ and $3\sigma_u$ orbitals, excellent agreement between the experiment and the theory is observed as far as the admixture distribution at 16.7eV (figure 7.2(ii)) indicates. There is also good general agreement between this admixture distribution and a similar distribution reported by Cook and Brion (see figure 7 of ref. [CB82a]) when differences caused by very different momentum resolutions are allowed for. There is, however, a striking difference between the present result and the earlier noncoplanar measurements [CB82a] in the relative intensity ratios of the symmetric and nonsymmetric components in the $4\sigma_g$ orbital (figure 7.2(iii)). The symmetric (s-type) component accounts for the maximum at $p \simeq 0$ while the nonsymmetric (p-type) component is responsible for the second maximum at $p \simeq 1.0 a_0^{-1}$. The present measurement shows significantly better agreement with the theoretical $4\sigma_g$ distributions than does the 400eV measurement [CB82a]. This indicates that the deconvolution method used in ref. [CB82a] was not sufficiently accurate in the low momentum region in that it evidently allowed part of the $3\sigma_u$ intensity to mix in with the $4\sigma_g$ intensity. A more judicious choice of the sitting binding energy for the $4\sigma_g$

orbital in the present work (figure 7.1) also ensures that any overlap of the neighboring $(3\sigma_u)^{-1}$ state is effectively eliminated. It is clear that the theoretical momentum distribution calculated using the Snyder and Basch wavefunction [SB72] gives a better fit to the experiment than that calculated using the 4-31G* wavefunction [HL&80] or the extended Gaussian basis of Langhoff [L84a] although all three theoretical distributions clearly underestimate the ratio of s-to-p components in this orbital. It is interesting to note also that despite the importance of the polarization functions in helping to lower the total energy in the variational method, the addition of more polarization functions as in the 4-31G* and the extended Gaussian basis wavefunctions does not necessarily produce better agreement with the experimental momentum distributions. In the case of the $4\sigma_g$ orbital, inclusion of more polarization functions in fact gives a bigger discrepancy.

7.4 THEORETICAL ORBITAL MOMENTUM DISTRIBUTIONS AND ORBITAL DENSITY TOPOGRAPHY

Figure 7.3 shows the spherically averaged momentum densities of both the valence and the core orbitals of CO_2 calculated using the double-zeta quality wavefunctions of Snyder and Basch [SB72]. The orbitals have been grouped into three classes, namely, the core ($1\sigma_u$, $1\sigma_g$ and $2\sigma_g$), the

valence sigma ($3\sigma_g$, $2\sigma_u$, $4\sigma_g$ and $3\sigma_u$) and the valence pi ($1\pi_u$ and $1\pi_g$) orbitals. The theoretical SCF orbital energies are also given in figure 7.3. It can be seen, in accord with the general chemical intuition, that the momentum distributions of the valence orbitals are concentrated in the low momentum region ($p<3.0a_0^{-1}$) while the momentum distributions of the core orbitals are clearly much more extended into the high p region, and conversely, more constricted in position-space.[1] Another very interesting feature concerning the core ($1\sigma_g$ and $1\sigma_u$) orbitals is the observation of very strong density oscillations [CD41, ET77, CB82a, CB82b]. The periodicities of the modulations manifest the "hidden" information of the (equilibrium) molecular geometry. It should be noted that the periodicities observed in the momentum distributions should only be roughly constant due to the fact that the momentum densities have been spherically averaged. The spherically averaged momentum densities are presented here in

---

[1] The momentum-space (p-space) wavefunction involves an integral of the sum of powers of the gradient of the position-space (r-space) wavefunction over all space (see chapter 2). In the case of atomic orbitals where a large change in the r-space wavefunction occurs only near the nucleus, the small r part of the r-space wavefunction contributes most significantly to the large p part of the p-space wavefunction (the inverse spatial reversal relation). In the case of molecular orbitals, however, the spatial reversal relation, although still qualitatively correct, must be applied with caution since any region where there is a rapid change in the r-space wavefunction will contribute significantly to the high p part of the p-space wavefunction. Such rapid change can occur between atomic centres, for instance across a nodal plane. A clear example of this is the CO_2 ($1\pi_g$) orbital.

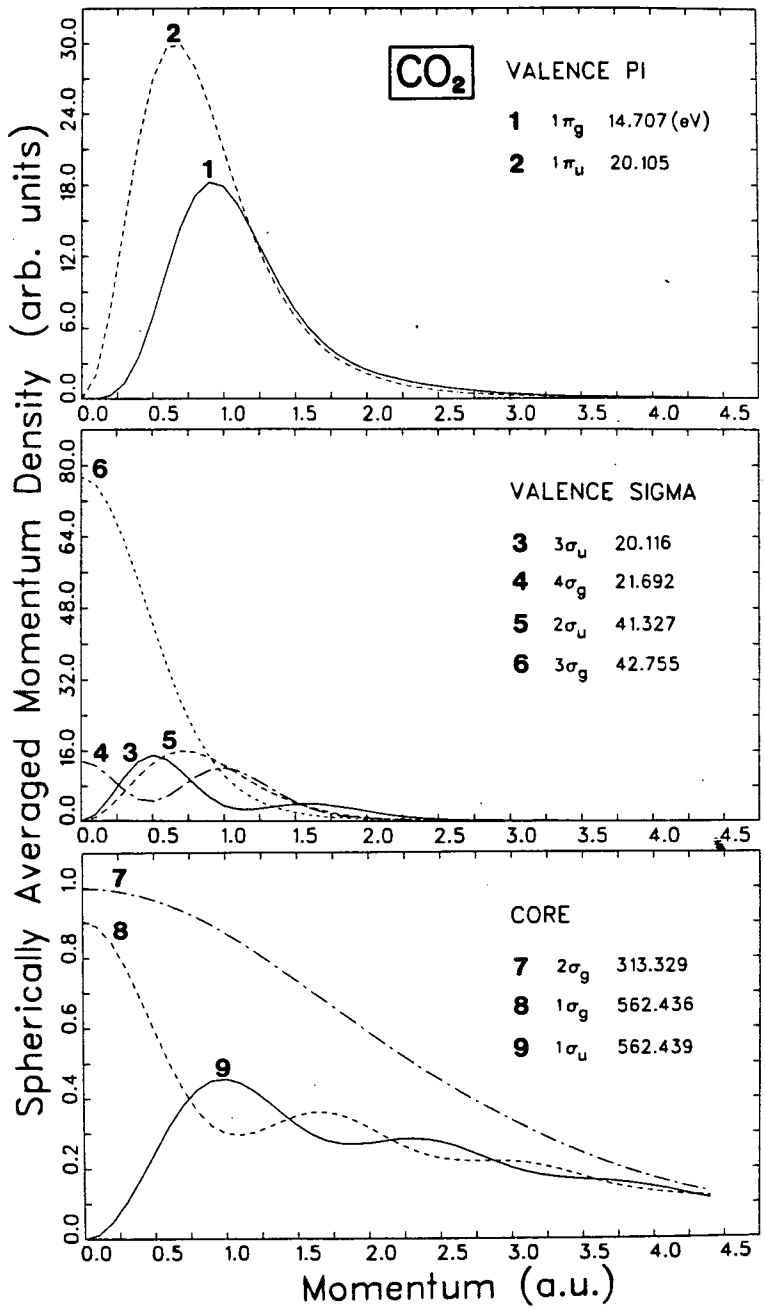

Figure 7.3 - Theoretical orbital momentum distributions for CO_2 evaluated using the Snyder and Basch wavefunction [SB72]. The indicated energies are the theoretical orbital energies.

order to demonstrate the possibility of direct experimental observation of these density oscillation effects using a gaseous target. The experimental investigation of these density oscillation effects is, however, technically not feasible at present because of the very high orbital energies of these core orbitals, which require a very high impact energy in order to satisfy the (e,2e) reaction model [MW76a]. The almost degenerate orbital energies of the $1\sigma_u$ and $1\sigma_g$ orbitals also do not allow observation of individual momentum distributions with the presently available energy resolution. It should also be pointed out that the measurement of the momentum distributions of the inner valence sigma orbitals ($2\sigma_u$ and $3\sigma_g$) are not possible with the present energy resolution because the broad band in the inner valence region is composed of numerous intermixed many-body lines arising from the ionizations of these orbitals. This many-body structure in the inner valence region has been observed experimentally [DC&79, CB82a] and also predicted theoretically by the Green's functions calculations [DC&79]. Finally, figure 7.3 demonstrates one general feature of momentum distributions arising from the parity of the sigma orbitals in molecules with $D_{\infty h}$ symmetry. Namely, the momentum distributions of σ_g orbitals are characterized by maxima at p=0 (s-type) while those of σ_u orbitals have maxima at p≠0 (p-type). This difference in the appearance of the momentum distributions of σ_g and σ_u orbitals provides binary

(e,2e) spectroscopy with a symmetry probing advantage over conventional spectroscopies. This was also earlier pointed out in the case of CO and N_2 by Camilloni *et al*. [CS&79].

These features, seen in the spherically averaged momentum densities, can be further illustrated with directional orbital density contour maps calculated using theoretical wavefunctions of double-zeta quality [SB72] in momentum-space (p-space) and position-space (r-space) (figures 7.4-7.6). The density maps of the valence orbitals of CO_2 have been discussed earlier by Cook and Brion [CB82a, CB82b]. In the present work, the range of the density maps has been extended to 4 atomic units to exhibit additional (weak) features which occur in the high momentum region. In addition, axis projection plots [LB83b] are included to show the relative changes in amplitude along the projection lines. Contour values have also been selected so as to extend logarithmically over three decades relative to the maximum density values. These provide better perspectives into the often small but important features associated with some of the momentum-space chemical concepts [CD41, ET77, CB82b, LB83b]. The density mapping convention used in the present work is the same as that given in chapter 5 (section 5.4.1).

As discussed in the preceding chapters, there are four general momentum-space properties arising essentially from the Fourier transform of position-space wavefunctions [CD41, ET77, LB83b]. In the case of CO_2, the symmetry invariance

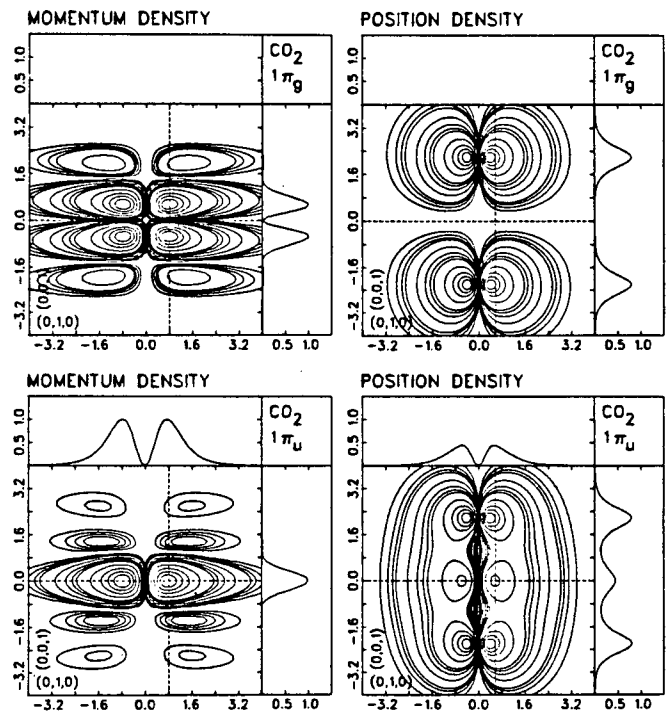

Figure 7.4 - Density contour maps for $1\pi_g$ and $1\pi_u$ orbitals in momentum-space (left) and position-space (right).

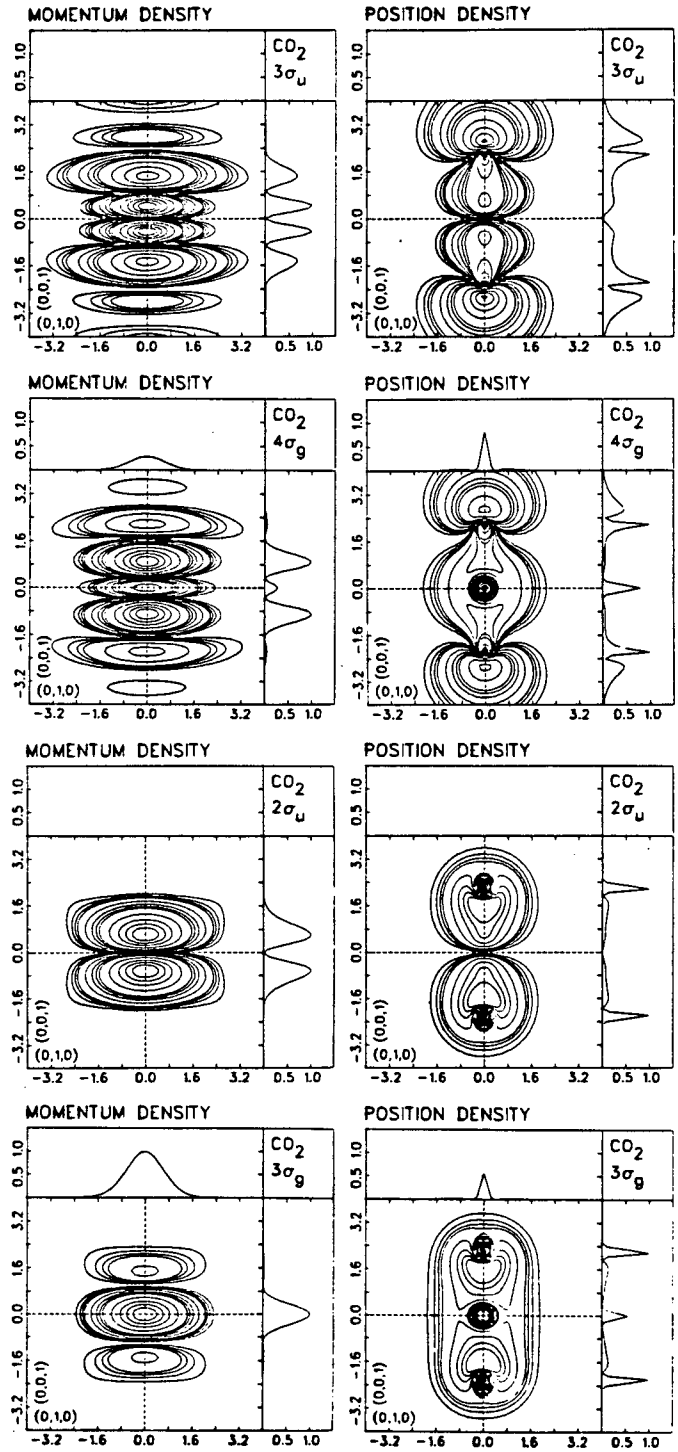

Figure 7.5 - Density contour maps for $3\sigma_u$, $4\sigma_g$, $2\sigma_u$ and $3\sigma_g$ orbitals in momentum-space (left) and position-space (right).

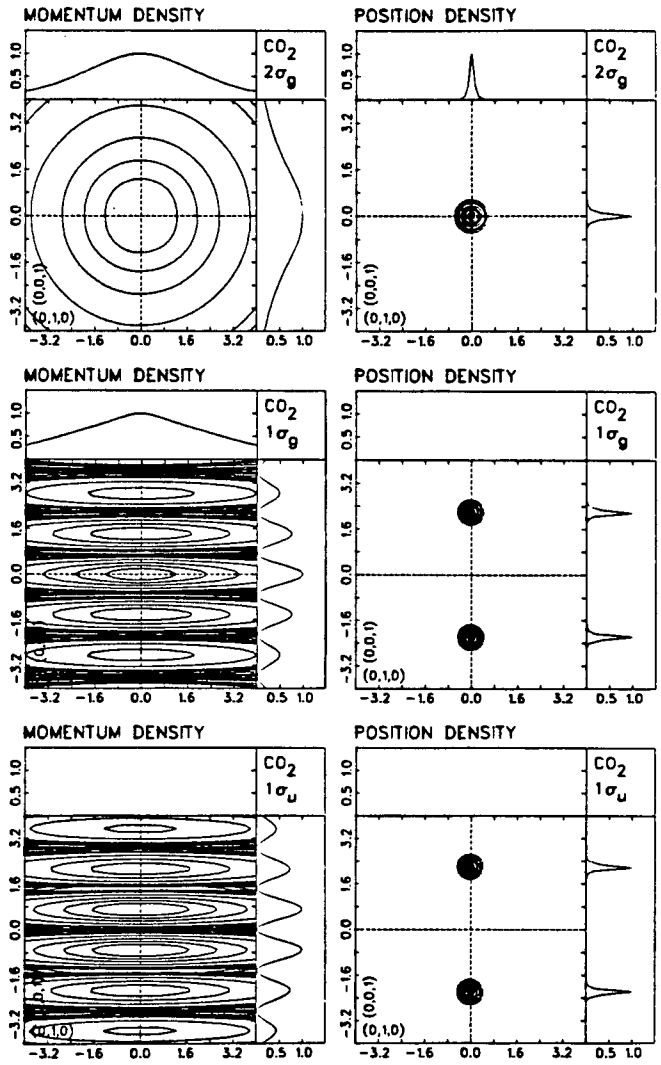

Figure 7.6 - Density contour maps for $2\sigma_g$, $1\sigma_g$ and $1\sigma_u$ orbitals in momentum-space (left) and position-space (right).

property is very clearly demonstrated by the valence orbitals (both the π and σ orbitals) where the p-space and r-space wavefunctions (and their densities) possess identical symmetry elements such as reflection planes. The inverse weighting property can also be seen in the valence orbital density maps and their associated projection plots, which indicate that the p-space density lobes are concentrated in the small p region while the r-space density lobes are located in the large r region. The molecular density directional reversal is illustrated by the fact that individual p-space density lobes are elongated in the bond-perpendicular direction while the r-space lobes are pointing in the bond-parallel direction. Finally, the molecular p-space density oscillation effect is perhaps best demonstrated by the strong lobe modulations along the internuclear axis in the core $1\sigma_u$ and $1\sigma_g$ orbitals (figure 7.6). The weak density oscillations in valence orbitals are shown by the appearance of secondary lobes in the p-space density maps of the outer valence orbitals ($1\pi_g$, $1\pi_u$, $3\sigma_u$ and $4\sigma_g$, see figures 7.4 and 7.5 respectively) where density contours below 1% of the maximum density values are necessary for revealing these structures. These momentum-space properties can be further visualized by using three dimensional constant density surface plots (see section 5.4.5). In figure 7.7, the constant surfaces with density values corresponding to 0.2% of the respective maximum density values for the four

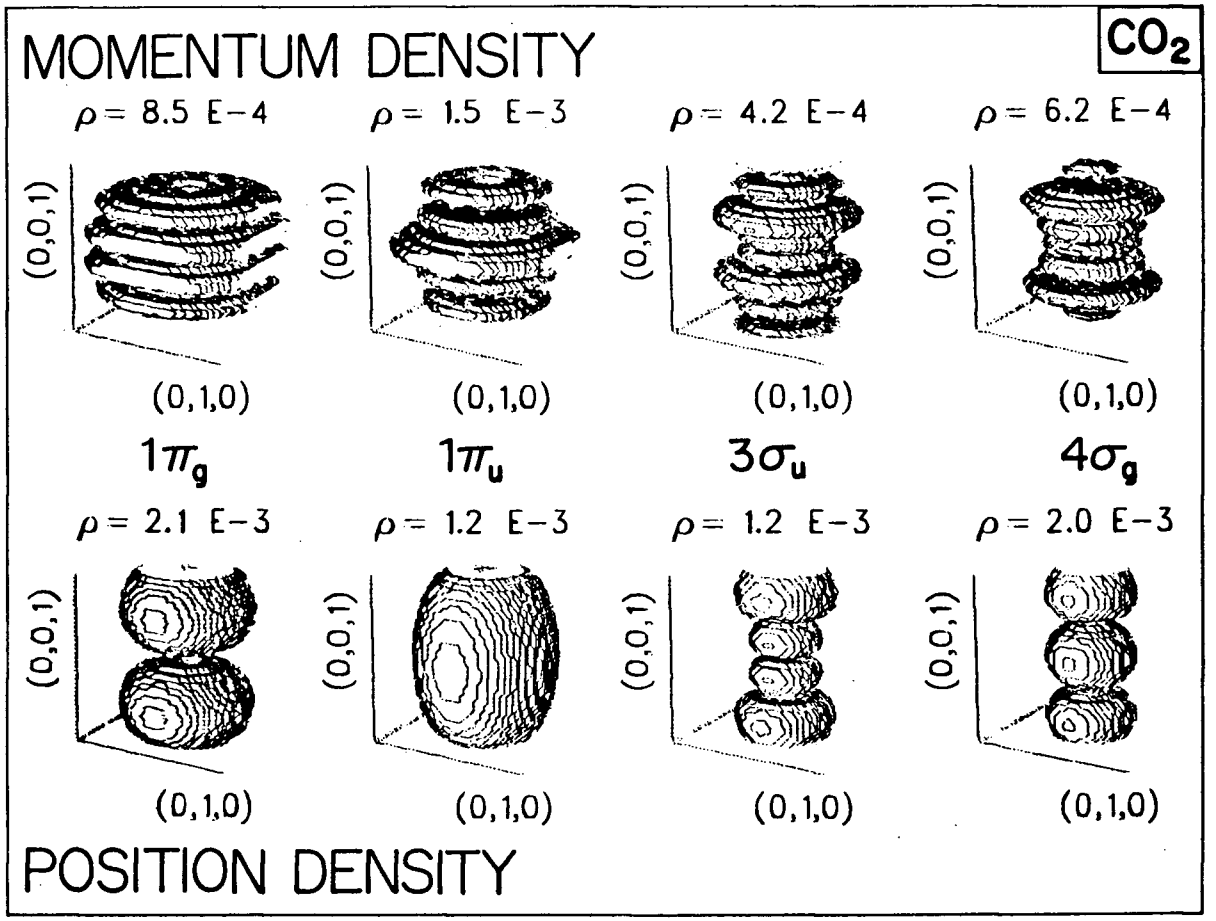

Figure 7.7 - Three-dimensional constant density surface plots for CO_2 $1\pi_g$, $1\pi_u$, $3\sigma_u$ and $4\sigma_g$ orbitals in momentum-space (top) and position-space (bottom). The density values of the surfaces correspond to 0.2% of the respective maximum densities. The range of the density cube is from -4.0 a.u. to 4.0 a.u. in each of the three directions (same as that of the density maps).

outermost orbitals are shown. Clearly, the orbital density of the π symmetry orbitals differ from that of the σ symmetry orbitals by the presence of the "nodal lines" in the internuclear direction. The other symmetry elements such as reflection (and nodal) planes are easily seen. Also, complex secondary disk-like lobes of the p-space densities reflect the molecular density oscillation and directional reversal properties in momentum-space.

Chapter VIII

CARBON DISULPHIDE

8.1 INTRODUCTION

The valence electronic structure of CS_2 has been investigated by several techniques including photoelectron [TB&70, AG&72, PW74, SD&79, HD&80, CKG82, K83], Penning ionization [BY77] and dipole (e,2e) [CWB81] spectroscopies, all of which have provided valuable information on the valence-shell binding energy spectrum of CS_2. In addition, the valence-shell binding energy spectrum of CS_2 has also been calculated using the many-body 2ph-TDA Green's Function (GF) method [SD&79] and more recently using the symmetry adapted cluster configuration interaction (SAC-CI) method [N83]. These theoretical works [SD&79, N83] have shown extensive population splittings in the inner valence ionization region of CS_2, indicating a significant breakdown of the single particle ionization picture. In the present work, the binding energy spectra in the 2-48eV region measured at two relative azimuthal angles (ϕ=0° and 8°) are reported. Relative intensities of binding energy spectra obtained at several relative azimuthal angles by binary (e,2e) spectroscopy are proportional to the momentum probability densities at the corresponding binding energies.

The relative intensities in these spectra can therefore be used to identify aspects of the symmetry and character of the ionized orbitals associated with the particular energy bands especially in the inner valence region. This has also been used to unambiguously assign the identity and ordering of molecular orbitals in molecules such as H_2CO [HHB76b]. Moreover if the momentum distribution sampled at a given binding energy is integrated over the momentum, the resulting momentum-integrated intensity is proportional to the spectroscopic pole-strength and thus can be compared directly with theoretical results obtained by the GF [SD&79] or the SAC-CI [N83] methods. Such a direct comparison of measured and calculated intensities is not possible in the case of photoelectron studies because of the energy dependent dipole matrix element [MUP78]. In the present work, momentum distributions measured at several binding energies are compared with theoretical momentum distributions calculated using wavefunctions of the GAUSS76 431G basis [HL&80] and the extended Gaussian basis of Langhoff [L84b]. The momentum-integrated intensities of the corresponding momentum distributions are used to compare directly with the predicted intensities of the theoretical binding energy spectra [SD&79, N83]. The measured momentum distributions provide the first direct look at the molecular bonding orbitals associated with the C=S bond in CS_2. These distributions are compared with those of the corresponding valence orbitals in CO_2 [LB84b]

(chapter 7). Differences in the orbital momentum distributions of CS_2 and those of CO_2 are interpreted using the respective calculated orbital density contour maps in position and momentum space.

8.2 VALENCE-SHELL BINDING ENERGY SPECTRUM

Carbon disulfide is a 38-electron system with $D_{\infty h}$ point group symmetry. The ground state electronic configuration of CS_2 is:

$$(core)^{22}(5\sigma_g)^2(4\sigma_u)^2(6\sigma_g)^2(5\sigma_u)^2(2\pi_u)^4(2\pi_g)^4.$$

Two sets of angular correlated binding energy spectra are reported. Figure 8.1 shows the outer valence (7-20eV) binding energy spectra measured at ϕ=0°, 4°, 8°, 12° and 16°. Binding energy spectra extending into the inner valence region (up to 48eV) measured at ϕ=0° and 8° are shown in figure 8.2. The four outer valence states: $X(2\pi_g)^{-1}$, $A(2\pi_u)^{-1}$, $B(5\sigma_u)^{-1}$ and $C(6\sigma_g)^{-1}$ as well as the D state are identified in both figures 8.1 and 8.2 by a Gaussian deconvolution procedure. The energy positions (X(10.07eV), A(12.85eV), B(14.47eV), C(16.18eV) and D(17.05eV)) and the corresponding Franck-Condon widths used in the deconvolution procedure are obtained from high resolution PES data [PW74, SD&79, HD&80, CKG82]. The sums of the individual Gaussians

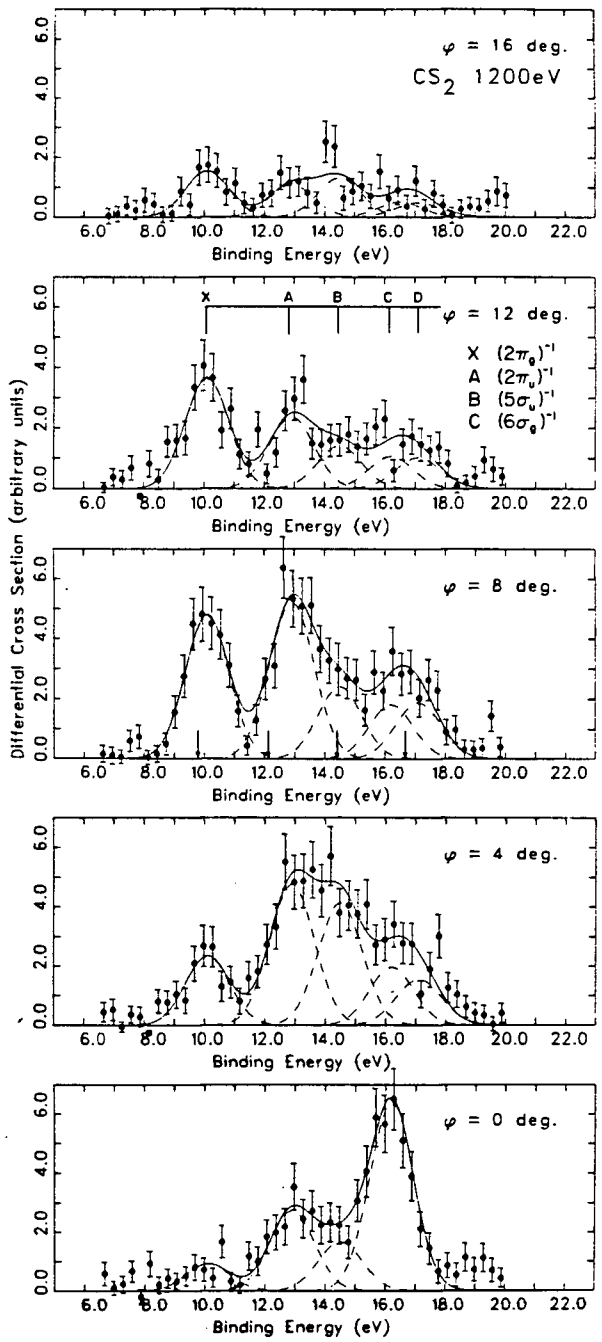

Figure 8.1 - Outer valence binding energy spectra for CS_2 at ϕ=0°, 4°, 8°, 12° and 16°. Least-squares Gaussian fits of the the experimental data are indicated by the solid lines. The labelled arrows in the ϕ=8° spectrum indicate the sitting binding energies where the momentum distributions are measured.

(dotted lines) are represented by solid lines. In general, there is excellent overall agreement between the Gaussian convoluted envelopes and the experimental data. The existence of a contribution from the D state at 17.05eV (which escaped attention in the earlier XPS [AG&72] and dipole (e,2e) [CWB81] works) is also quite evident in the spectra (figures 8.1 and 8.2).

The relative intensity variations of individual deconvoluted (Gaussian) peaks with respect to the azimuthal angle ϕ depend on the momentum distributions (MDs) of the associated characteristic orbitals. It is clear from figure 8.1 that the $X(2\pi_g)^{-1}$, $A(2\pi_u)^{-1}$ and $B(5\sigma_u)^{-1}$ states all have maximum intensities at $p\neq0$, indicating a general p-type dependence in the MDs of the respective orbitals. The $C(6\sigma_g)^{-1}$ state, on the other hand, has maximum intensity at $p\simeq0$ (i.e. in the $\phi=0^\circ$ spectrum). The corresponding MD therefore has a symmetric (s-type) component.

The high resolution PES data [PW74, SD&79, HD&80, CKG82] indicate the presence of two many-body states (satellites) in the outer valence region, namely at 14.07eV and 17.05eV. The intensity of the D state appears to vary in a similar fashion to that of the $A(2\pi_u)^{-1}$ state. This is in good qualitative agreement with the symmetry adapted cluster configuration interaction (SAC-CI) calculation [N83], which predicts a $2\pi_u$ pole next to the primary $6\sigma_g$ pole (see figure 8.3). The other outer valence many-body state at 14.07eV is only

marginally observable in high resolution PES works [SD&79, HD&80] and will not be considered in the present work because of its very small intensity. It should be noted that this many-body state is predicted in the many-body Green's function calculation [SD&79] but not in the SAC-CI calculation [N83].

The long range angular correlated binding energy spectrum (figure 8.2) shows extensive many-body structures in the inner valence region (>20eV) rather than just two peaks which would be expected from the single particle ionization model for the $(4\sigma_u)^{-1}$ and $(5\sigma_g)^{-1}$ processes. These extensive structures were also observed in the earlier XPS [AG&72] and dipole (e,2e) [CWB81] studies.[1] Three prominent overlapping bands in the 22-34eV region can be observed in the ϕ=0° spectrum (figure 8.2). The many-body states above 22eV have higher relative intensities at ϕ=0° than at ϕ=8°, indicating a general s-type behavior of the momentum distributions associated with these ionic states. The structure between 20eV and 22eV (figure 8.2) however appears to have an appreciable p-type contribution.

Theoretical valence-shell binding energy spectra have been calculated by Schirmer *et al*. [SD&79] using the many-

---

[1] It should be noted that spectra obtained by different techniques will have different global appearances due to the different dependences of the spectral intensity upon the experimental kinematic conditions. For a discussion of these differences see ref. [CW&81].

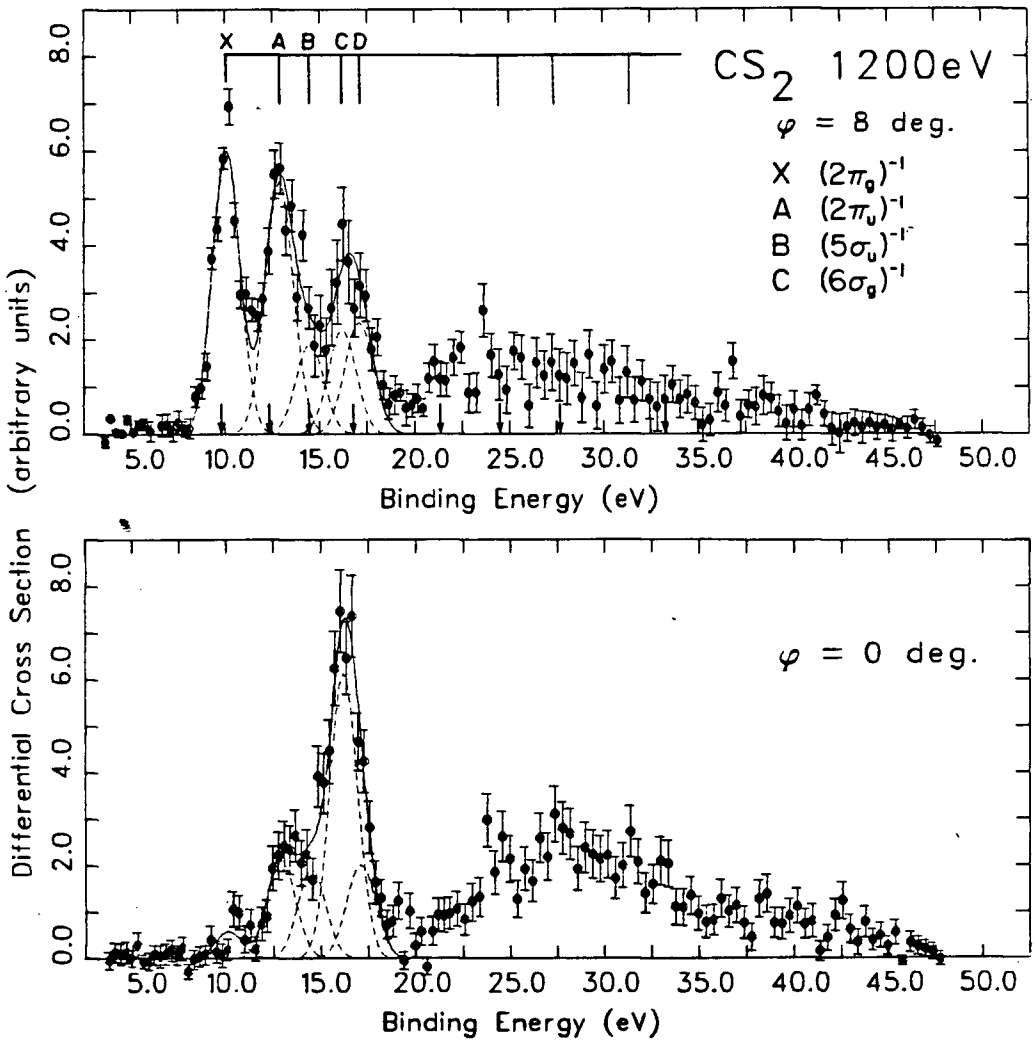

Figure 8.2 - Valence shell binding energy spectra for CS_2 at ϕ=0° and 8°. Least-squares Gaussian fits of the the experimental data in the outer valence region are indicated by the solid lines. The labelled arrows in the ϕ=8° spectrum indicate the sitting binding energies where the momentum distributions are measured.

body 2ph-TDA Green's function (GF) method and more recently by Nakatsuji [N83] using the symmetry adapted cluster configuration interaction (SAC-CI) method. (The SAC-CI spectrum presented here corresponds to the pole-strength spectrum calculated by Nakatsuji using basis II in ref. [N83].) The poles calculated according to the theories are shown in figure 8.3 and have been convoluted with Gaussians of the experimental instrumental width (1.7eV FWHM) to generate the indicated overall envelope to enable a reasonable comparison with the experimental binding energy spectra (figure 8.2). Momentum-integrated intensities of momentum distributions (see below) measured at several selected binding energies (solid squares in figure 8.3) are normalized (relative to each other) to the Gaussian convoluted envelope at 9.8eV. It should be noted that the indicated pole assignments, especially in the inner valence region of the calculated spectra (figure 8.3), each corresponds to the dominant configuration contributing to that pole.

There is generally excellent agreement in the outer valence region between the measured binding energies (figure 8.2) and those calculated by the SAC-CI method [N83] (figure 8.3). Good agreement in the outer valence region between the measured spectra and the GF spectrum [SD&79] can also be obtained if the second band (i.e. the A, B and C envelope) is shifted by approximately 0.8eV to high energy. This and

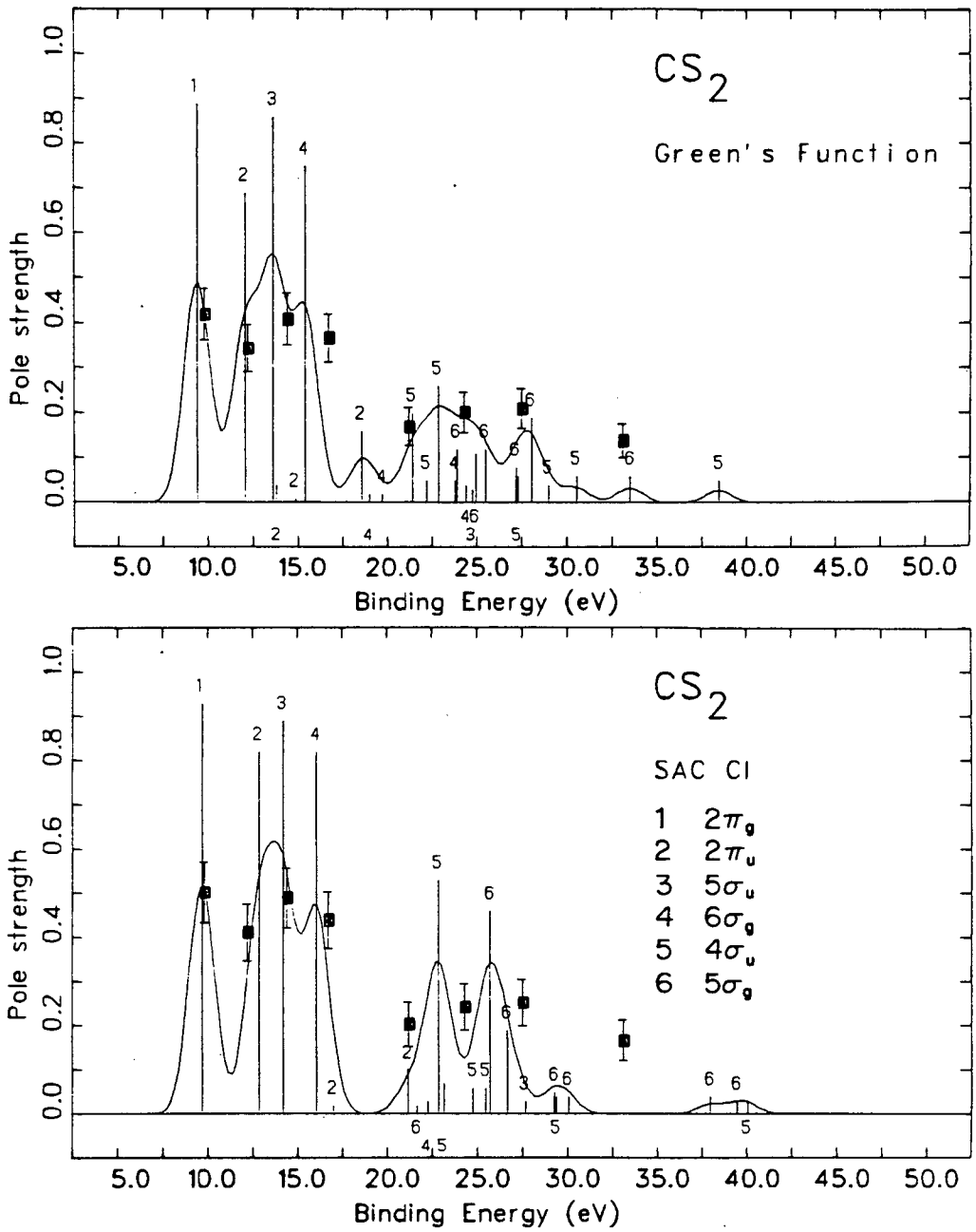

Figure 8.3 - Theoretical valence-shell binding energy spectra for CS_2. The poles calculated by the 2ph-TDA Green's function method [SD&79] (top) and by the symmetry adapted cluster configuration interaction method [N83] (bottom) are convoluted with Gaussians of the instrumental width.

similar discrepancies (see later) in the GF calculated spectrum are often attributed to the inherent limitations of the two particle-hole approximation as well as limitation in the quality of the employed basis set [SD&79]. The *experimental* pole-strengths, as approximated by numerical integration of the momentum distributions measured at the respective energies in the inner valence region, are also in good agreement (at least below 30eV) with the Gaussian convoluted envelopes of both the SAC-CI and the "shifted" GF spectra (see figure 8.3). The inner valence regions of both theoretical spectra [SD&79, N83] show an intense intermixing of (mostly) the $(4\sigma_u)^{-1}$ and $(5\sigma_g)^{-1}$ poles. Similar intermingling of poles has also been observed and predicted in the corresponding inner valence binding energy spectra of CO_2 [DC&79, N83]. In the overall inner valence region, only qualitative agreement between experiment (figure 8.2) and literature calculations [SD&79, N83] (figure 8.3) is found for CS_2. In particular, the many-body structures in both the GF and SAC-CI calculated spectra appear to be restricted to the 20-30eV region, in contrast to the considerable intensity distribution of many-body states observed above 30eV in the experimental spectra (figure 8.2). The experimental energy positions and pole-strengths below 30eV in the inner valence region (figure 8.3) are in better agreement with the GF envelope than with the SAC-CI envelope. The SAC-CI envelope above 20eV must be shifted towards the low energy side by

approximately 1.2eV in order to obtain a reasonable agreement with the experimental pole-strengths estimated at 21.2eV and 24.3eV. It is important to note also that such a downward shift of the SAC-CI spectrum is necessary in order for the poles (as assigned by the calculations) to be consistent with the momentum distributions measured at the corresponding energies (see later). No such shifts are required in the GF spectrum. Momentum distributions measured in the inner valence region can be used in this way to identify the orbital character of the many-body states and to substantiate theoretical assignments of the complex many-body states.

8.3 SPHERICALLY AVERAGED MOMENTUM DISTRIBUTIONS

Figures 8.4-8.9 show the momentum distributions (MDs) measured at selected sitting binding energies of 9.8eV, 12.2eV, 14.4eV, 16.7eV, 21.2eV and 33.1eV respectively. Theoretical MDs calculated using the GAUSS76 431G wavefunction [HL&80] (dashed lines) and the extended Gaussian basis wavefunction of Langhoff [L84b] (solid lines) are height normalized at the maximum for p-type distributions (figures 8.4, 8.5, 8.6 and 8.8) and are area normalized in the range 0-1.5 a_0^{-1} for s-type or sp-type distributions (figures 8.7 and 8.9). It should be noted that the indicated energies in the figures are not the vertical I.P.'s and correspond only to the sitting binding energies (selected so

as to minimize the overlap from neighboring states —— see figures 8.1 and 8.2). Although absolute cross sections are not measured, relative normalization is maintained between the various experimental MDs. In addition, momentum-space (p-space) density and position-space (r-space) density contour maps of individual orbitals calculated using the GAUSS76 431G wavefunction are also presented. The density mapping convention is the same as that used in chapter 5 (section 5.4.1).[2]

8.3.1 Outer Valence Orbitals

The sitting binding energies at which the corresponding MDs are measured have been judiciously chosen in order to minimize contributions from the neighboring states. It is clear from figures 8.1 and 8.2 that the MDs measured at 9.8eV, 12.2eV and 14.4eV can be assigned essentially to the $2\pi_g$, $2\pi_u$ and $5\sigma_u$ orbitals respectively. The MD sampled at 16.7eV however contains significant contributions from both the C and D states because the small natural separation

---

[2] Briefly, the contour plane is defined by two orthogonal directional vectors with the (0,0,1) vector indicating the bond-parallel internuclear direction. Contour lines of density values corresponding to 80, 60, 40, 20, 8, 6, 4, 2, 0.8, 0.6, 0.4 and 0.2% of the maximum densities are shown. Projection plots of the density function along the indicated (dashed) lines are used to show clearly the relative change in magnitude of the density functions. The momentum and position are in atomic units.

between the two states is beyond the instrumental energy resolution.

The experimental and theoretical MDs of the $2\pi_g$ orbital, along with the corresponding density maps are shown in figure 8.4. The position density map clearly indicates the "nonbonding" (lone-pair) character of the $2\pi_g$ orbital which consists mainly of the $S(3p_x, 3p_y)$ atomic orbitals. The slight distortion of the position density near the σ_h plane is due to the negative overlap of the contributing $S(3p_x, 3p_y)$ atomic orbitals. The corresponding momentum density map also shows a pseudo-d type main structure with weak secondary lobes in the high p region. There is fair agreement between the experimental MD and those calculated by the extended Gaussian basis wavefunction [L84b] and by the GAUSS76 431G wavefunction [HL&80] in the region $p>0.5a_o^{-1}$. The theoretical MD calculated using the GAUSS76 431G basis is slightly shifted to higher momentum. In the region $p<0.5a_o^{-1}$, the experimental MD lies closer to the origin than the calculated MDs. A similar discrepancy is also observed in the MD of the corresponding CO_2 $1\pi_g$ orbital [LB84b] (chapter 7). This suggests that the CS_2 $2\pi_g$ orbital, like the CO_2 $1\pi_g$ orbital, may in fact be somewhat more diffuse (i.e. more extended in r-space) than that modelled by either of the theoretical wavefunctions.

A similar discrepancy between the experimental MD of the $2\pi_u$ orbital (figure 8.5) and the calculated MDs is also

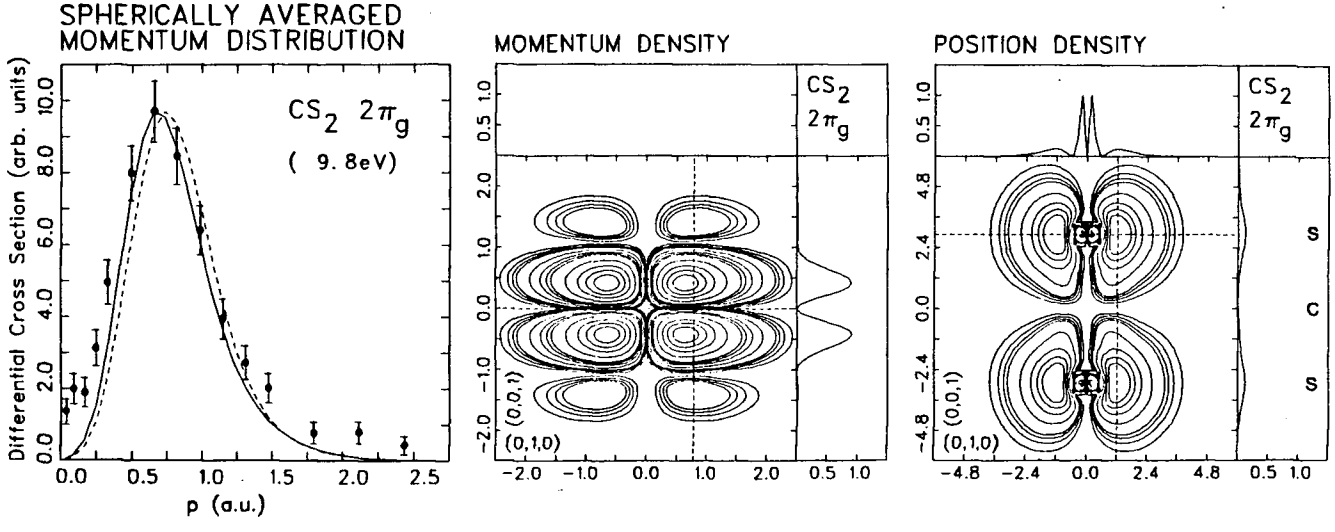

Figure 8.4 - Molecular orbital momentum distributions (left), momentum density (centre) and position density (right) maps of the CS_2 $2\pi_g$ orbital. Theoretical momentum distributions are evaluated using wavefunctions of the extended Gaussian basis [L84b] (solid lines) and the GAUSS76 431G basis [HL&80] (dashed lines).

observed in the region below $0.5a_0^{-1}$, despite good agreement in the higher momentum region at least up to $1.5a_0^{-1}$. The $2\pi_u$ orbital, as is clearly evident from the position density map, represents the bonding (positive) overlap between $S(3p_x, 3p_y)$ and $O(2p_x, 2p_y)$ orbitals. The CS_2 $2\pi_u$ orbital is, of course, similar to the corresponding $1\pi_u$ orbital in CO_2 [CB82a] (chapter 7). There is, however, significantly less relative intensity in the secondary lobes in the high momentum region of the CS_2 $2\pi_u$ orbital momentum density map in comparison with the corresponding CO_2 $1\pi_u$ counterpart. Since Fourier transformation involves the sums of powers of gradients of the r-space wavefunction (chapter 2) the high momentum part of the p-space wavefunction is related therefore to the more rapidly varying parts of the r-space wavefunction over the whole Hilbert space. The change in the $C(2p_x, 2p_y)$-$S(3p_x, 3p_y)$ overlap in CS_2 (in r-space) is evidently much smoother (small gradient) than the corresponding $C(2p_x, 2p_y)$-$O(2p_x, 2p_y)$ overlap in CO_2 (figure 7.4), as indicated by the bond-parallel projection plots of the respective position density maps. Consequently the secondary lobes in the high momentum region for the $2\pi_u$ (and also the $2\pi_g$) orbital(s) of CS_2 are less intense than those for the corresponding orbital(s) of CO_2 (chapter 7).

It is interesting to note that the positions of the maxima in the $2\pi_g$ ($p_{max} \simeq 0.7a_0^{-1}$) and $2\pi_u$ ($p_{max} \simeq 0.5a_0^{-1}$) MDs of CS_2 are generally at lower momentum than those of the $1\pi_g$

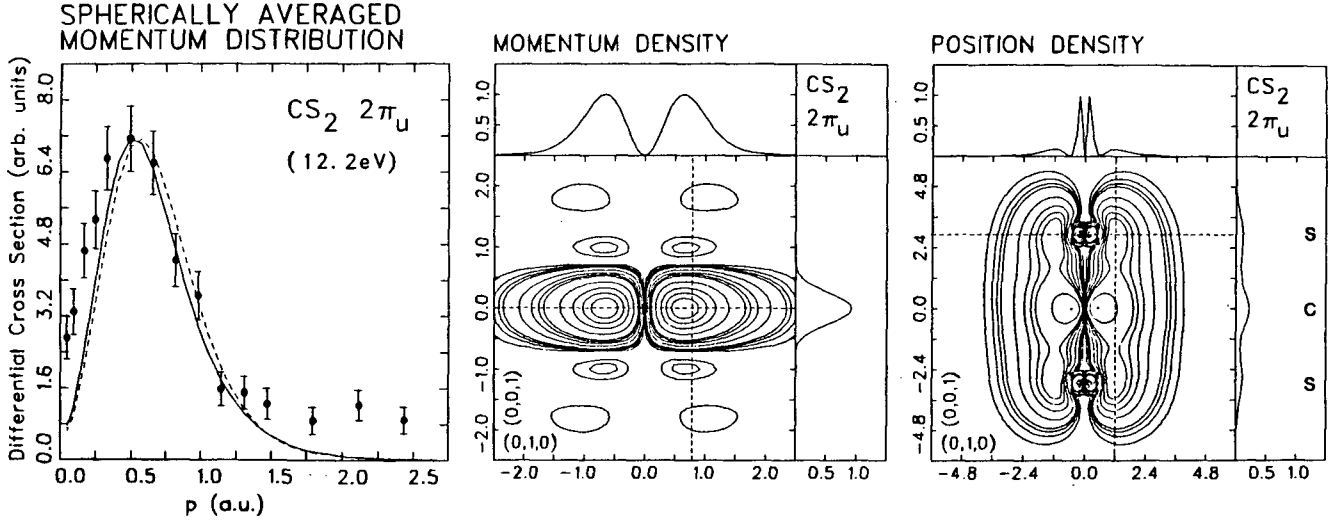

Figure 8.5 - Molecular orbital momentum distributions (left), momentum density (centre) and position density (right) maps of the CS_2 $2\pi_u$ orbital. Theoretical momentum distributions are evaluated using wavefunctions of the extended Gaussian basis [L84b] (solid lines) and the GAUSS76 431G basis [HL&80] (dashed lines).

($p_{max} \simeq 0.9 a_0^{-1}$) and $1\pi_u$ ($p_{max} \simeq 0.7 a_0^{-1}$) MDs of CO_2 [CB82a] (chapter 7) respectively. This is again consistent with the earlier observation that the π orbitals in CS_2 are more extended in position-space than the corresponding orbitals in CO_2, principly because of the inherently more diffuse nature of the S 3p atomic orbitals as compared with O 2p orbitals. The MDs of the π orbitals in CS_2 are also sharper than those of the π orbitals in CO_2 as expected from a consideration of the inverse spatial reversal relation (chapter 2).

The position density map of the $5\sigma_u$ orbital (figure 8.6) indicates that it is made up of bonding (positive) overlaps between the S(3s, $3p_z$) and C($2p_z$) orbitals. Very intense secondary lobes (figure 8.6, bond-parallel projection plot) are present in the momentum density contour map. The first set of secondary lobes are not due to density (bond) oscillations [CD41, ET77, CB82b, LB83b] but are the (symmetry required) counterparts of the secondary lobes outside the S atoms in the position density map. These structures in the momentum density map give rise to the second maximum observed in the MD of this orbital. The intensity of the second lobe is also reduced relative to that of the first in the MD in comparison with the situation in the density map. This is due to the effects of spherically averaging implicit in the use of (randomly oriented) gaseous targets in the experiment. There is a reasonable agreement between the experimental and theoretical MDs in the region $p<0.7 a_0^{-1}$. The experimental MD

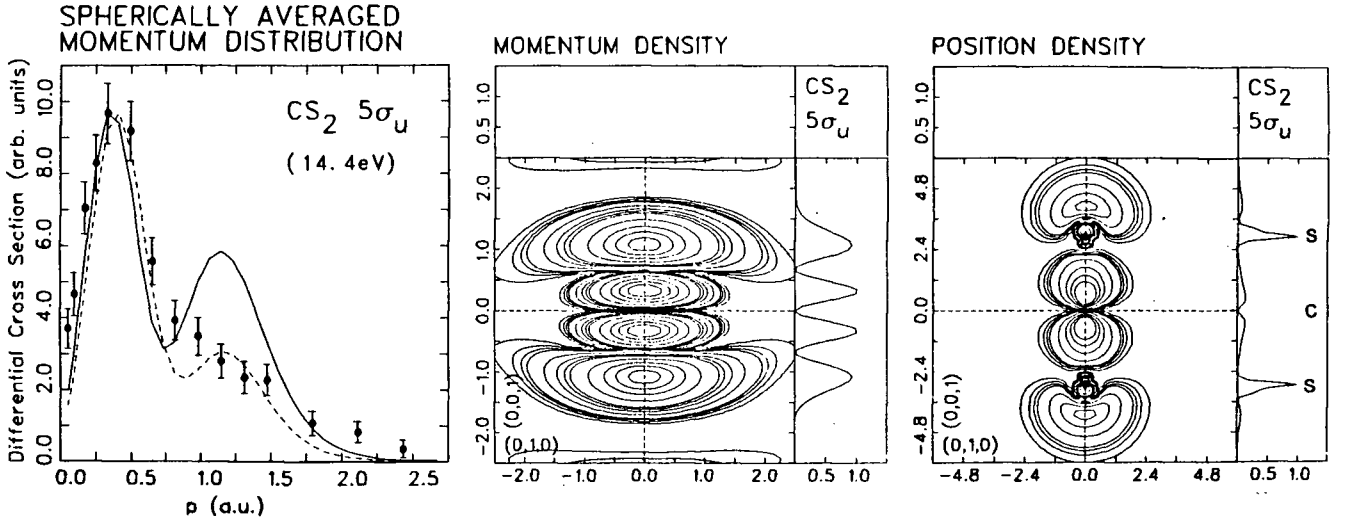

Figure 8.6 - Molecular orbital momentum distributions (left), momentum density (centre) and position density (right) maps of the CS_2 $5\sigma_u$ orbital. Theoretical momentum distributions are evaluated using wavefunctions of the extended Gaussian basis [L84b] (solid lines) and the GAUSS76 431G basis [HL&80] (dashed lines).

has a shoulder above $0.7a_o^{-1}$ occurring in approximately the same region as the well defined second maxima of the calculated MDs. The extended Gaussian basis wavefunction [L84b] severely overestimates the second maximum in the MD. The remarkably sharp peak in the measured MD represents the lowest p_{max} ($\simeq 0.3a_o^{-1}$) for any MD observed to date using binary (e,2e) spectroscopy.

Figure 8.7 shows the MD measured at 16.7eV, and the density maps of the $6\sigma_g$ orbital in momentum-space and position-space. The $6\sigma_g$ orbital consists essentially of antibonding (negative) overlaps between S(3s, $3p_z$) and C(2s) orbitals (see position density map). Because of the symmetry properties of the molecule in momentum-space, the lobe at the p-space origin can only come from the C(2s) orbital located at the r-space origin. As expected, the p-space density map of the CS_2 $6\sigma_g$ orbital is of sp-type and is very similar in appearance to that of the CO_2 $4\sigma_g$ orbital (see figure 7.5). The MD measured at 16.7eV (represented by open squares in figure 8.7) contains comparable contributions from both the C and D states because of the proximity of these two states (figure 8.1). According to the SAC-CI calculated binding energy spectrum (figure 8.3), the D state is due to part of the ionization of the $2\pi_u$ orbital. Therefore in order to "filter out" the $2\pi_u$ contribution, the $2\pi_u$ orbital MD measured at 12.2eV is appropriately scaled according to the Gaussian deconvoluted binding energy spectra (figure 8.1) and

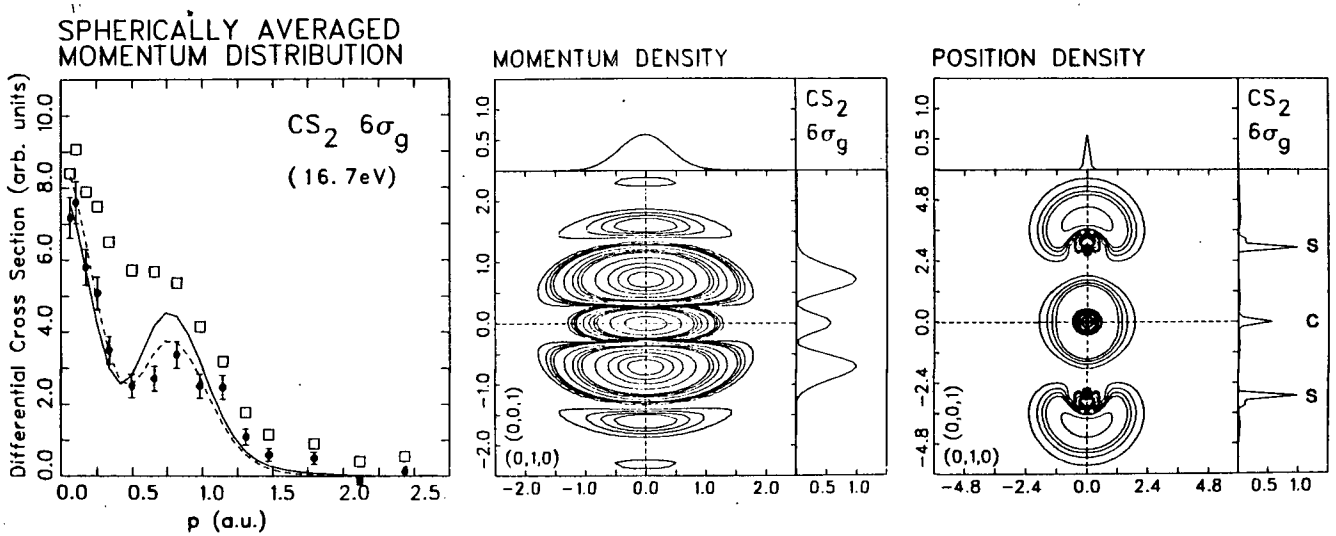

Figure 8.7 - Molecular orbital momentum distributions (left), momentum density (centre) and position density (right) maps of the CS_2 $6\sigma_g$ orbital. The open squares represent the momentum distribution measured at 16.7eV, which contains contributions from both the C and the D states. The solid circles correspond to the "filtered" momentum distribution of the $6\sigma_g$ orbital (C state). (See also caption of fig. 8.6.)

is subtracted off from the MD measured at 16.7eV (represented by open squares). The "filtered" MD (represented by solid circles in figure 8.7) corresponds to the MD of the separate $6\sigma_g$ orbital measured at 16.7eV. There is an excellent agreement between the "filtered" MD and the calculated MDs (particularly for the GAUSS76 431G wavefunction) of the $6\sigma_g$ orbital (figure 8.7). The extended Gaussian basis wavefunction [L84b] again somewhat overestimates the nonsymmetric orbital component of the orbital as was also observed in the case of the $5\sigma_u$ orbital (figure 8.6). This discrepancy may be due to the large amount of polarization functions employed in the extended Gaussian basis wavefunction [L84b]. It is of interest to note that the nonsymmetric (p-type) component in the measured ("filtered") MD of the $6\sigma_g$ orbital in CS_2 is less than that in the MD of the $4\sigma_g$ orbital in CO_2, each relative to the symmetric (s-type) component in the respective MD. This observation is again consistent with the generally more diffuse overlap between the C and S centres in CS_2.

8.3.2 Inner Valence Orbitals

The binding energy spectra (figures 8.2 and 8.3) have been seen to exhibit intense population splittings for the ionization of orbitals above 20eV due to many-body effects. The MDs measured in such an inner valence region can be used

to identify the dominant (if any) characteristic orbital associated with a particular many-body state. In the present work, four MDs have been obtained at energies (21.2eV, 24.3eV, 27.5eV and 33.1eV) corresponding approximately to the band maxima in the ϕ=0° binding energy spectrum (figure 8.2). On the basis of the theoretical binding energy spectrum calculated using the 2ph-TDA Green's function technique, the MD measured at 21.2eV corresponds essentially to the $4\sigma_u$ (pole #5) orbital while MDs measured at other energies (24.3eV, 27.5eV and 33.1eV) can be assigned primarily to the $5\sigma_g$ orbital (pole #6). The theoretical binding energy spectrum calculated using the SAC-CI method also gives similar assignments if the calculated spectrum is shifted by 1.2eV towards the low energy. It should be emphasized that the indicated orbital assignments in figures 8.8-8.11 refer only to the dominant characteristic orbitals present at the respective energies according to the calculations.

Figures 8.8 and 8.9 show respectively the MDs measured at 21.2eV and at 33.1eV as well as theoretical MDs of the dominant orbitals. The position and momentum density contour maps of the $4\sigma_u$ and $5\sigma_g$ orbitals are also given in the corresponding figures. There is a remarkably good agreement between the experimental MD measured at 21.2eV (figure 8.8) and the corresponding calculated MDs of the $4\sigma_u$ orbital in the region $p<1.2a_0^{-1}$. The MD calculated using the extended Gaussian basis [L84b] apparently gives a slightly better

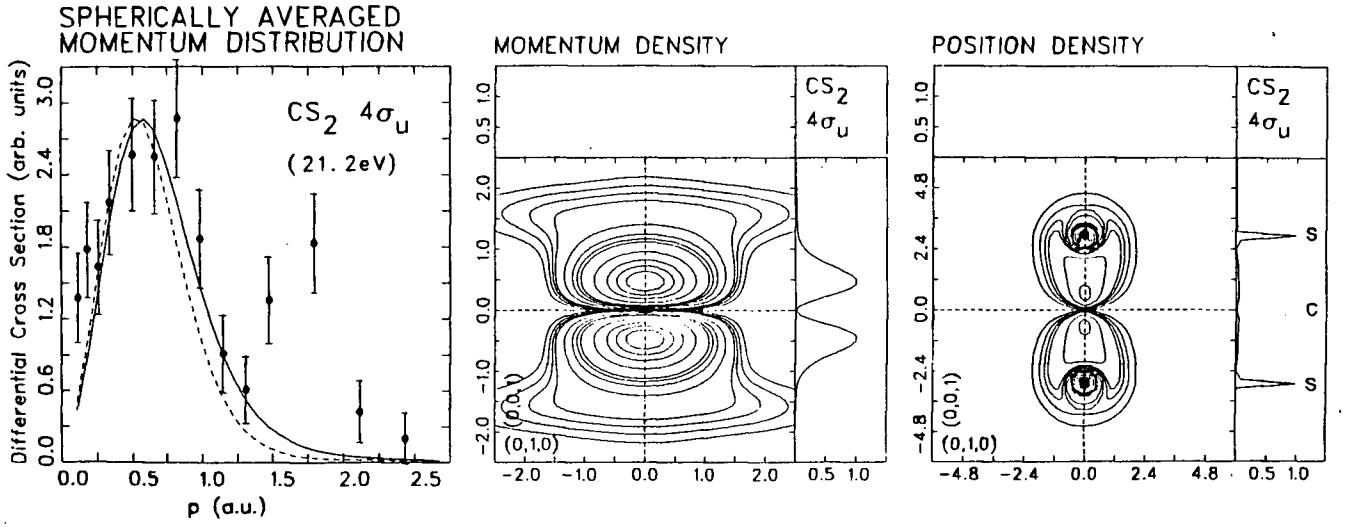

Figure 8.8 - Momentum distribution (left) measured at 21.2eV, momentum density (centre) and position density (right) maps of CS_2 $4\sigma_u$ orbital. Theoretical momentum distributions of the $4\sigma_u$ orbital are evaluated using wavefunctions of the extended Gaussian basis [L84b] (solid lines) and the GAUSS76 431G basis [HL&80] (dashed lines).

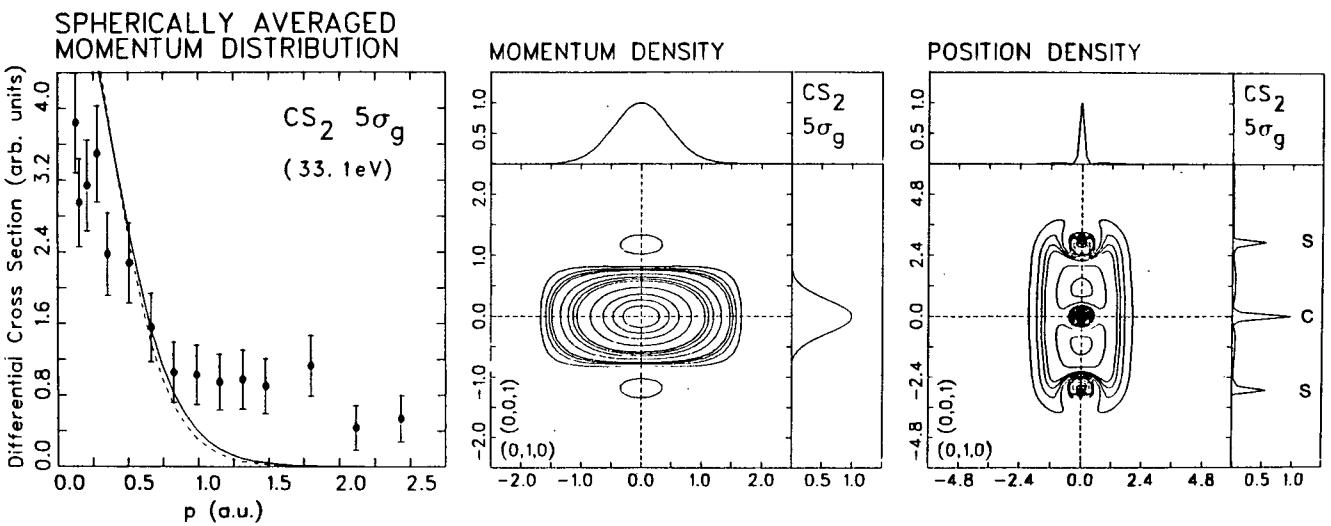

Figure 8.9 - Momentum distribution (left) measured at 33.1eV, momentum density (centre) and position density (right) maps of CS_2 $5\sigma_g$ orbital. Theoretical momentum distributions of the $5\sigma_g$ orbital are evaluated using wavefunctions of the extended Gaussian basis [L84b] (solid lines) and the GAUSS76 431G basis [HL&80] (dashed lines).

agreement to the experiment than that calculated using the GAUSS76 431G basis [HL&80]. There is, however, an apparent second peak occurring near $p \simeq 1.7 a_0^{-1}$ in the experimental MD, a feature which is not accountable for by any of the theoretical orbital MDs. This may indicate the presence of configuration interaction [MW76a] in the inner valence region of CS_2. In the case of the $5\sigma_g$ orbital (figure 8.9), there is only a qualitative agreement between the MD measured at 33.1eV and the calculated MDs of the $5\sigma_g$ orbital. The s-type behavior of the MD measured at 33.1eV is very similar to that observed in the MDs measured at 24.3eV (figure 8.10) and at 27.5eV (figure 8.11). In all cases, the theoretical MDs of $5\sigma_g$ orbital are much too steep to account for the broader experimental MDs. The relatively high intensities of the experimental MDs in the high momentum region again support possible many-body effects caused by configuration interaction (i.e. breakdown of the target Hartree-Fock approximation in the inner valence region). Contamination by other many-body states could also influence the observed shapes of these MDs. The qualitative agreement of the orbital character as indicated by MDs measured at the sitting binding energies of 21.2eV, 33.1eV, 27.5eV, and 24.3eV with those predicted by the theories, however, gives support for the essential correctness of the pole spectral distribution as calculated by the GF and SAC-CI methods.

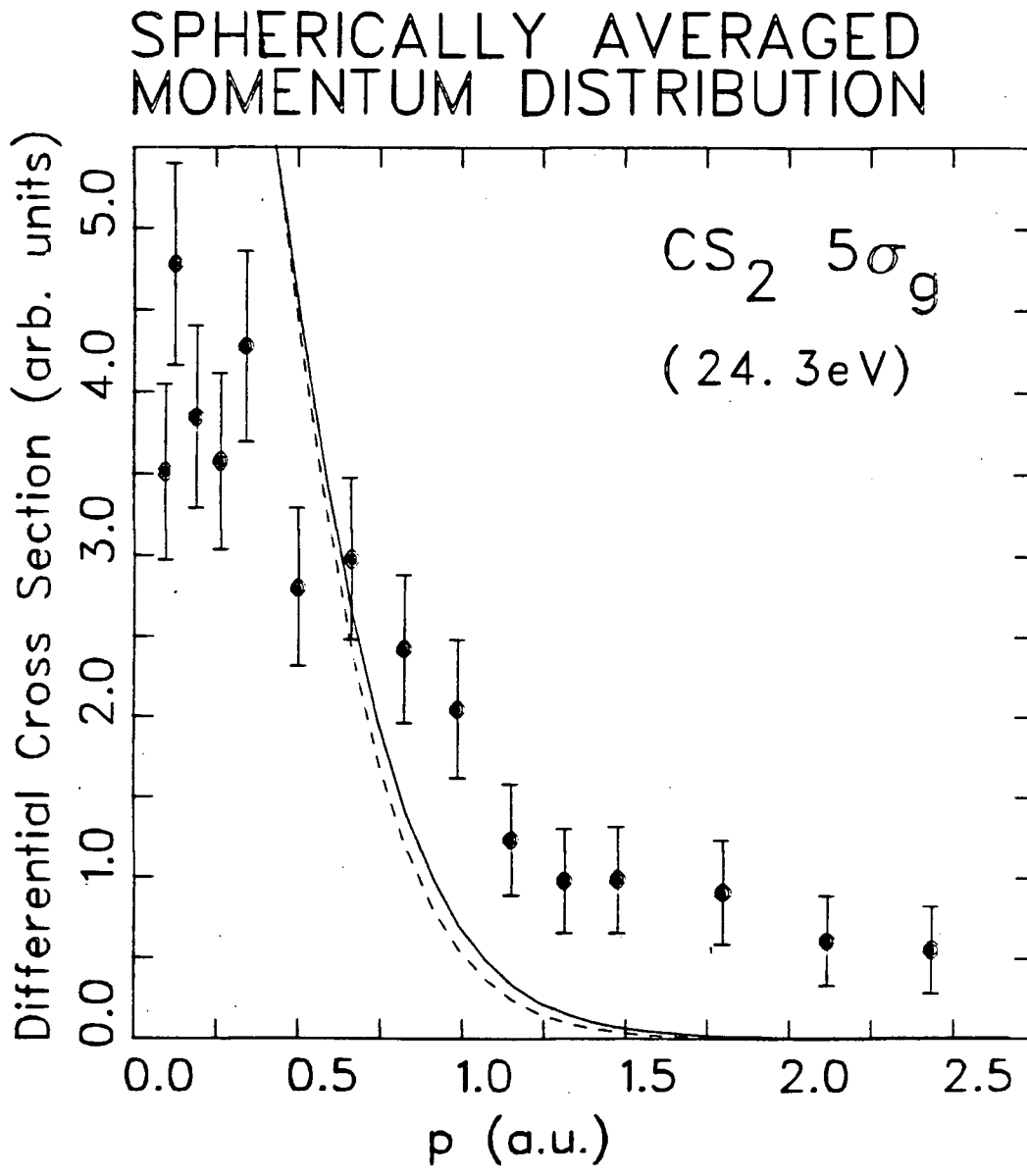

Figure 8.10 - Momentum distribution measured at 24.3eV. Theoretical momentum distributions of the $5\sigma_g$ orbital are evaluated using wavefunctions of the extended Gaussian basis [L84b] (solid lines) and the GAUSS76 431G basis [HL&80] (dashed lines).

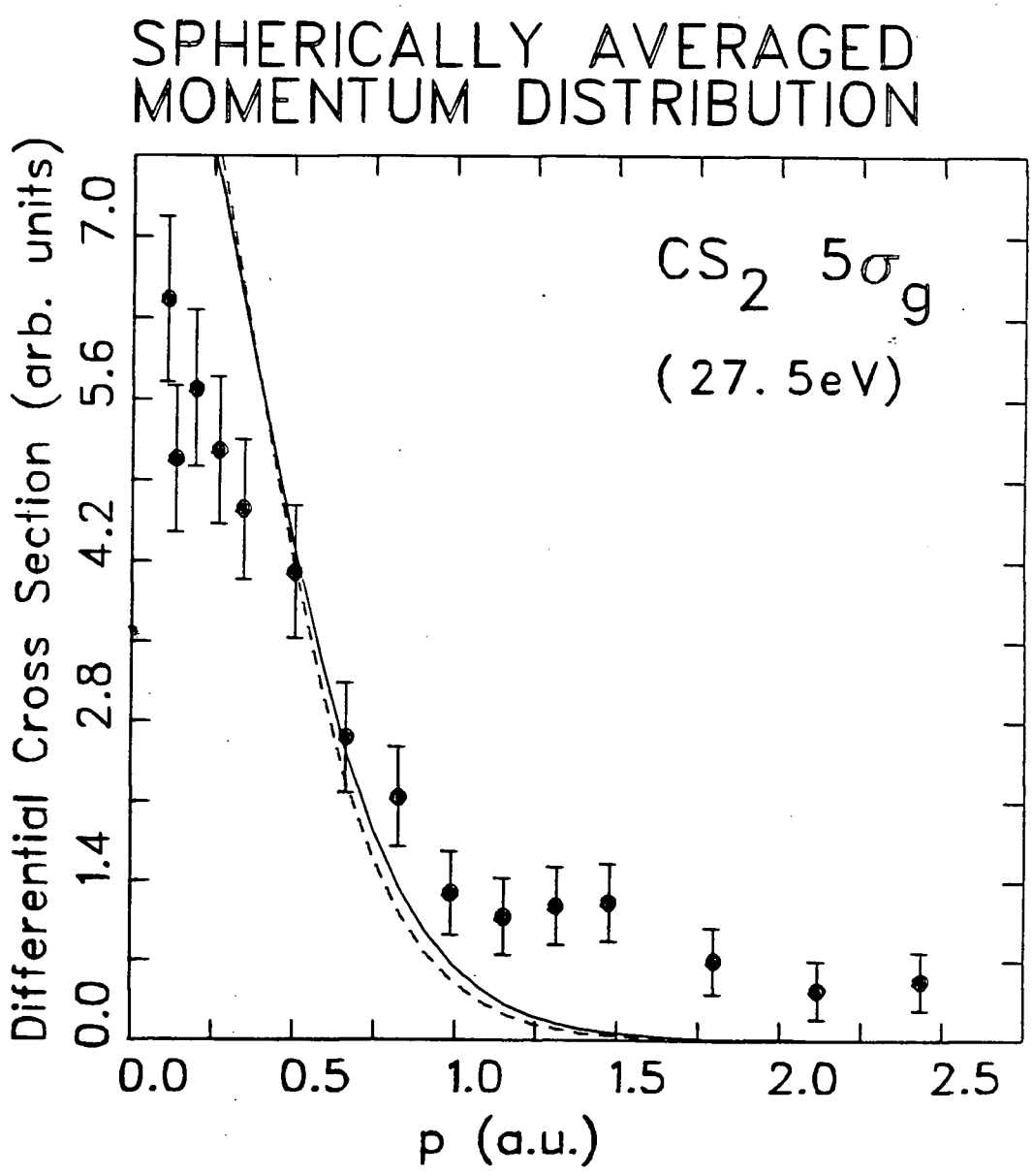

Figure 8.11 - Momentum distribution measured at 27.5eV. Theoretical momentum distributions of the $5\sigma_g$ orbital are evaluated using wavefunctions of the extended Gaussian basis [L84b] (solid lines) and the GAUSS76 431G basis [HL&80] (dashed lines).

8.4 SUMMARY

The present binary (e,2e) measurements of the valence-shell binding energy spectra and momentum distributions of CS_2 provide further confirmation of the general breakdown of the independent particle ionization picture, especially in the inner valence region. Experimental pole-strengths estimated by numerical integration of the measured momentum distributions provide a more quantitative evaluation of theoretical binding energy spectra calculated by the 2ph-TDA Green's function method [SD&79] and by the symmetry adapted cluster configuration interaction method [N83]. Generally good semi-quantitative agreement with the experiment is obtained by both theories, at least below 30eV. The GF spectrum appears to compare more favorably with the experimental spectra in the inner valence region while the SAC-CI spectrum is in better agreement with the experiment in the outer valence region in the case of CS_2. This is in contrast to the situation in H_2O where the SAC-CI calculations [NY82] are very effective [BL&84].

With the exception of the outer valence σ orbitals ($5\sigma_u$ and $6\sigma_g$), theoretical momentum distributions calculated using the extended Gaussian basis wavefunction [L84b] are in somewhat better overall agreement with the experimental MDs than those calculated using the GAUSS76 431G wavefunction [HL&80]. For the outer valence π orbitals ($2\pi_g$ and $2\pi_u$) both theoretical wavefunctions for CS_2 underestimate the density

in the low momentum region ($p<0.5a_0^{-1}$). This suggests that the S($3p_x$, $3p_y$) atomic orbitals used in the theoretical wavefunctions for CS_2 are not sufficiently extended in position-space. There is good agreement between experimental MDs of the $5\sigma_u$ and $6\sigma_g$ orbitals and those calculated using the GAUSS76 431G wavefunction. The extended Gaussian basis wavefunction overestimates the second maxima in both orbital MDs. Momentum distributions measured in the inner valence region (i.e. at 21.2eV, 24.3eV, 27.5eV and 33.1eV) are in qualitative agreement with theoretical MDs of the respective $4\sigma_u$ and $5\sigma_g$ orbitals. These experimental MDs also appear to have significant density in the high momentum region ($p>1.2a_0^{-1}$), possibly indicating significant correlation effects. The good qualitative agreement between the experimental MDs and the theoretical MDs of the expected dominant orbitals provides further support for the pole assignments given by the GF calculation. Finally, general comparison between the CO_2 and CS_2 orbital density maps both in position and momentum space helps to understand the differences between the observed MDs of the corresponding molecules. In particular, the general shift of the momentum density to the lower momentum region observed in the MDs of CS_2 is consistent with the more delocalized nature of the C=S double bond. Investigation of the orbital MDs of the remaining member of the valence isoelectronic series, i.e. OCS, should provide further insights into the nature of

the C=O and C=S bonds (chapter 9).

Chapter IX

CARBONYL SULPHIDE

9.1 INTRODUCTION

Recent binary (e,2e) studies of the orbital momentum distributions (MDs) of CO_2 [CB82a, LB84b] (chapter 7) and CS_2 [LB84c] (chapter 8) have revealed many interesting aspects of the C=O and C=S molecular orbital bonding structures in the respective $D_{\infty h}$ triatomic molecules. In particular, experimental MDs of the outermost antibonding π_g orbitals in CO_2 (chapter 7) and CS_2 (chapter 8) have indicated that theoretical *ab-initio* SCF wavefunctions of double-zeta quality tend to underestimate the low momentum ($<0.5a_0^{-1}$) region. This suggests that the spatial extents (in position-space) of the nonbonding orbitals are larger than those anticipated by existing molecular orbital theories. This has obvious implications for chemical reactivity and molecular bonding which occur primarily on the outer large r portions of the orbitals. Variationally determined SCF wavefunctions are not necessarily sensitive to these outer spatial parts of the wavefunctions. Moreover, p-type MDs of CS_2 (chapter 8) are generally sharper with the maximum located closer to p=0 than the corresponding MDs of CO_2 [CB82a] (chapter 7). This observation is of course consistent with the chemical

conception that the atomic S(3s, 3p) orbitals used for the formation of the molecular orbitals in CS_2 are generally more spatially diffuse than the O(2s, 2p) orbitals used for the formation of the molecular orbitals in CO_2. This difference in the molecular bonding structure between CS_2 and CO_2 has also been demonstrated in the various momentum-space density maps of individual orbitals computed using theoretical wavefunctions (chapters 7 and 8). In the present work, the nature of the C=O and C=S bonds is further examined experimentally by using binary (e,2e) spectroscopy to study the remaining member of the valence isoelectronic triatomic group, namely, OCS. The effect of molecular symmetry upon MDs of individual molecular orbitals should be of particular interest.

The valence-shell ionization (binding) energies of OCS have been studied extensively by photoelectron [TB&70, AG&72, PW74, DH&80, CKG82, K83], Penning ionization [BY77] and dipole (e,2e) [WLB81] spectroscopies. An earlier binary (e,2e) work on the valence-shell binding energy spectra measured at two relative azimuthal angles using 400eV impact energy was carried out by Cook *et al*. [CW&81]. Theoretical calculation of the binding energy spectrum using the many-body 2ph-TDA Green's function (GF) method was also reported in this earlier work [CW&81]. Recently, the binding energy spectrum has also been calculated by Nakatsuji [N83] using the so-called symmetry adapted cluster configuration

interaction (SAC-CI) method. Both experimental [AG&72, WLB81, CW&81] and theoretical [CW&81, N83] studies of the valence-shell electronic structure of OCS have shown extensive population splittings due to many-body effects in the inner valence region, indicating a major breakdown of the independent particle ionization picture. The present work provides binary (e,2e) measurements of the binding energy spectra (in the 8-44eV range) obtained at ϕ=0° and 8° using 1200eV impact energy. In addition, individual orbital momentum distributions for OCS measured at a series of binding energies carefully chosen so as to minimize contributions from neighboring states are reported. These experimental MDs are compared with the corresponding theoretical MDs calculated using wavefunctions of minimal basis quality [C62] and near Hartree-Fock [MY67] quality. Density contour maps in momentum and position space calculated using the near Hartree-Fock wavefunction [MY67] are used to assist interpretation of the measured spherically averaged MDs and to further explore momentum-space chemical concepts [CD41, ET77, CB82b, LB83b] (chapter 2). The present study of MDs of individual orbitals in OCS extends the earlier investigations of the C=O and C=S bonds in the valence isoelectronic members CO_2 [CB82a] (chapter 7) and CS_2 (chapter 8) respectively. This also enables a comparative study to be made of the momentum-space chemistry of this series of linear triatomic molecules.

9.2 VALENCE-SHELL BINDING ENERGY SPECTRUM

Carbonyl sulfide is a 30-electron system with $C_{\infty v}$ symmetry. The valence-shell ground state configuration can be written as:

$$(\text{core})^{14}(6\sigma)^2(7\sigma)^2(8\sigma)^2(9\sigma)^2(2\pi)^4(3\pi)^4.$$

Figure 9.1 shows binding energy spectra of OCS (8-44eV) measured at ϕ=0° and ϕ=8° using 1200eV (+binding energy) impact energy. Four Gaussian line-shapes (dotted lines) are fitted to the data in the 8-20eV region in order to identify the four well known outer valence states: $X(3\pi)^{-1}$, $A(2\pi)^{-1}$, $B(9\sigma)^{-1}$ and $C(8\sigma)^{-1}$. The energy positions and widths used for the Gaussians are obtained from high resolution photoelectron spectroscopic data [DH&80, K83]. The relative peak intensities of the individual Gaussians in the ϕ=0° and in the ϕ=8° spectra clearly indicate that the three outermost states: $(3\pi)^{-1}$, $(2\pi)^{-1}$ and $(9\sigma)^{-1}$ have generally p-type momentum distributions (MDs).[1] The $(8\sigma)^{-1}$ state, however, has a generally s-type (symmetric) component in the corresponding MD. In the inner valence region (>20eV), extensive structures due to the many-body states are observed. The global decrease in the intensity of these structures in going

---

[1] A p-type momentum distribution has maximum away from p=0 while a s-type momentum distribution has maximum at p=0.

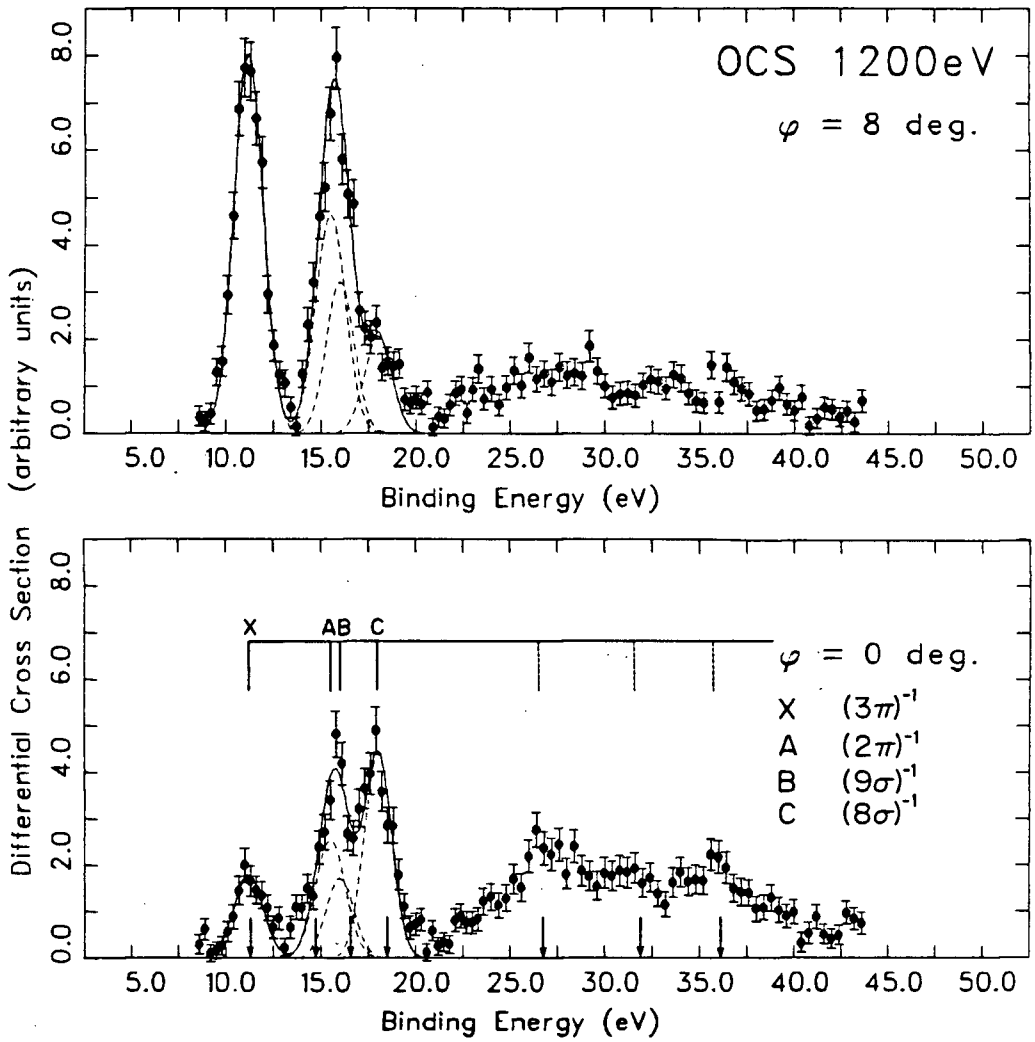

Figure 9.1 - Valence-shell binding energy spectra for OCS at ϕ=0° and 8°. Least-squares Gaussian fits of the experimental data in the outer valence region are indicated by the solid lines. The labelled arrows in the ϕ=0° spectrum indicate the sitting binding energies where the momentum distributions are measured.

from ϕ=0° to ϕ=8° (see figure 9.1) suggests that the majority of the many-body states comes from ionization of orbitals with symmetric (s-type) components. Significant many-body states have also been observed earlier in the X-ray photoelectron [AG&72] and dipole (e,2e) [WLB81] spectra of OCS. The present binary (e,2e) measurements of the binding energy spectra using 1200eV impact energy are also consistent with the earlier binary (e,2e) study by Cook *et al.* [CW&81] using 400eV impact energy. The second peak in the outer valence region (i.e. corresponding to the unresolved A+B states) reported in earlier work [CW&81] showed a higher intensity at ϕ=0° (than at ϕ=15°), in contrast to the smaller intensity at ϕ=0° (than at ϕ=8°) observed in the present work. It should be noted that this effect is due to differences in the instrumental angular resolutions used in the earlier [CW&81] and the present works, as well as the effective sitting momenta (i.e. different ϕ's) used for the binding energy spectra in each case.

Figure 9.2 shows the theoretical binding energy spectrum calculated using the many-body 2ph-TDA Green's function (GF) method [CW&81] and that calculated using the symmetry adapted cluster configuration interaction (SAC-CI) method [N83]. The poles calculated by the theories [CW&81, N83] have been convoluted with Gaussians of the instrumental width (1.7eV FWHM) to generate an overall envelope. Both theoretical spectra (figure 9.2) give good qualitative agreement with the

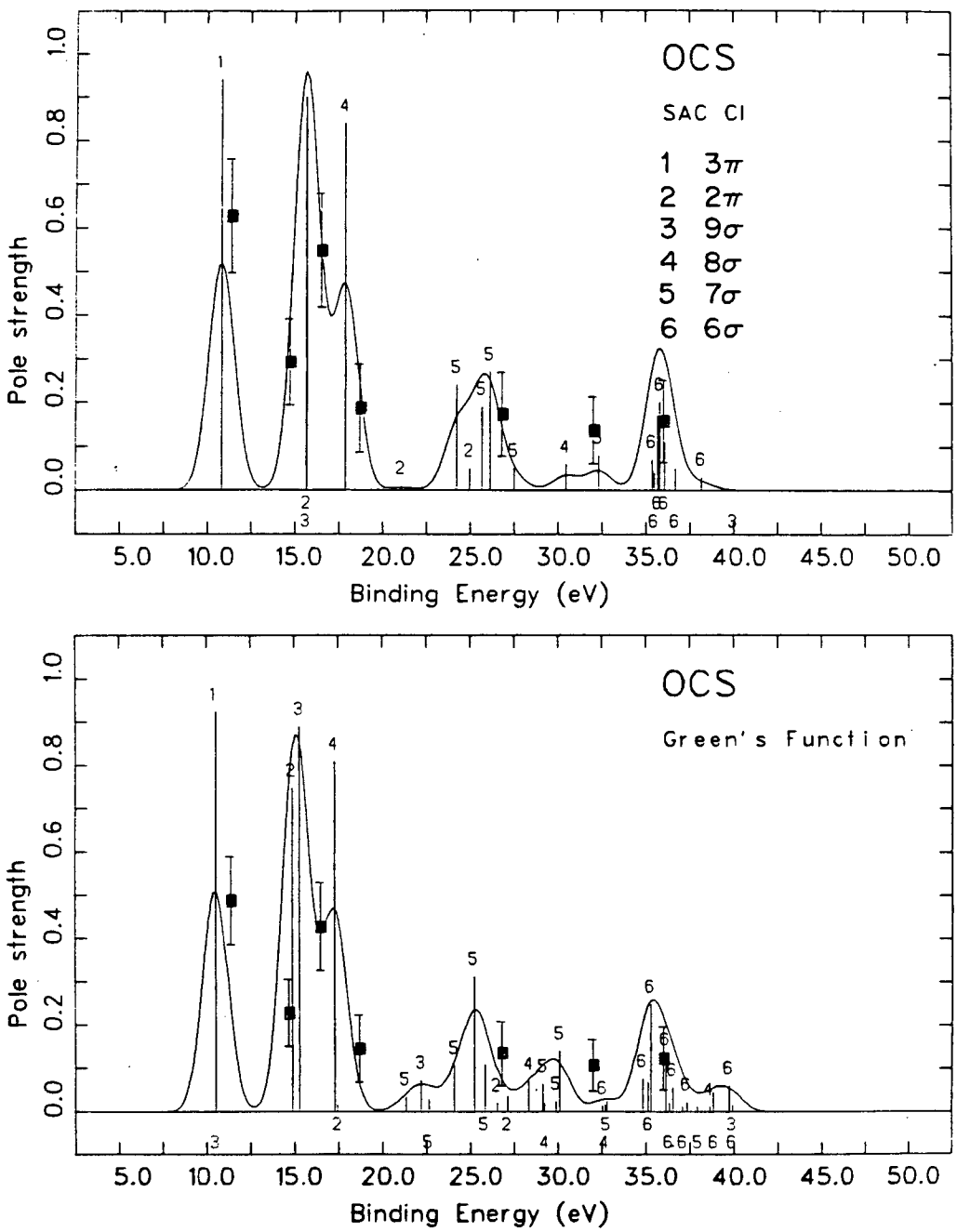

Figure 9.2 - Theoretical valence-shell binding energy spectra for OCS. The poles calculated by the 2ph-TDA Green's function method [CW&81] (bottom) and by the symmetry adapted cluster configuration interaction method [N83] (top) are convoluted with Gaussians of the instrumental width (1.7eV) (solid curves).

experiment (figure 9.1) in describing the many-body structure in the inner valence region. In particular extensive population splittings among the 7σ and 6σ holes are predicted by both theories [CW&81, N83]. It should be noted that in contrast to the intense intermixing between poles observed and calculated in the inner valence spectral region for CO_2 [CB82a] and CS_2 (chapter 8), the 7σ and 6σ poles of OCS do not intermingle appreciably with each other. The many-body effects appear to split a single "independent particle" pole into a "cluster" of smaller "many-body" poles centered approximately 4eV below the theoretical orbital energies of the respective orbitals.[2]

In order to make a more direct comparison with the pole-strengths calculated by the theories [CW&81, N83], experimental pole-strengths (solid squares in figure 9.2) are estimated by numerical integration (over the experimental momentum range) of momentum distributions measured at several binding energies (figures 9.3-9.8). It should be noted that such a comparison depends upon the accuracy and the range of the numerical integration procedure as well as the statistics of the available data over the experimental momentum range. The experimental pole-strengths have been height normalized

---

[2] The orbital energy of the 7σ orbital in the near Hartree-Fock wavefunction of McLean and Yoshimine [MY67] is 29.8eV while that of the 6σ orbital is 40.9eV. The independent particle orbital energy is expected to lie at the "centre of gravity" of the energies of the many-body poles [MW76a].

(relative to each other at 16.5eV) to the Gaussian convoluted envelopes (figure 9.2). Clearly, there is a reasonable agreement between the normalized experimental pole-strengths and the (convoluted) theoretical spectra. The SAC-CI spectrum [N83] gives a marginally better agreement with the experiment than the GF spectrum [CW&81] in the outer valence region. The pole-strength at 36.0eV appears to have been overestimated by both theories [CW&83, N83]. The theories are inherently limited by the amount of the excitation processes included as well as by the quality of the basis sets employed.

9.3 SPHERICALLY AVERAGED MOMENTUM DISTRIBUTIONS

Figures 9.3-9.8 show the spherically averaged momentum distributions (MDs) measured at 11.4eV, 14.7eV, 16.5eV, 18.7eV, 26.8eV and 36.0eV respectively. The indicated sitting binding energies are not necessarily the vertical ionization potentials (I.P.'s) but are carefully selected values so as to minimize any contribution from the neighboring states. Theoretical MDs of individual orbitals are calculated using wavefunctions of near Hartree-Fock (NHF) quality [MY67][3] and of minimal basis set (MBS) quality [C62].

---

[3] The near Hartree-Fock quality wavefunction [MY67] consists essentially of a double-zeta basis set with polarization functions.

Both basis sets [MY67, C62] employ Slator-type orbitals. The theoretical MDs have been individually area normalized from 0-1.5 a_0^{-1} to the respective experimental MDs. Momentum density and position density contour maps of individual orbitals have also been evaluated using the near Hartree-Fock quality wavefunction of McLean and Yoshimine [MY67]. The mapping convention is identical to that used in chapter 5 (section 5.4.1).[4] In the position density maps, the S atom is located in the negative z direction while the O atom is in the positive z direction. The C atom is situated at the origin of the plane in position-space. In momentum-space the nuclear region is at infinity on the p-space virtual boundary (chapter 2).

9.3.1 Outer Valence Orbitals

Figure 9.3 shows the MDs, momentum density and position density contour maps of the 3π orbital. The position density map clearly shows the "nonbonding" nature of the orbital, which is essentially composed of $O(2p_x, 2p_y)$ and $S(3p_x, 3p_y)$

[4] Briefly, the contour plane of the density function is defined by two orthogonal directional vectors. In the present case, the (0,0,1) vector (or the z-axis) corresponds to the bond-parallel direction (i.e. along the internuclear axis). Density contour values of 80, 60, 40, 20, 8, 6, 4, 2, 0.8, 0.6, 0.4 and 0.2% of the maximum are used. Projection plots along the indicated (dashed) lines are employed to better illustrate the variation of the magnitude of the density function.

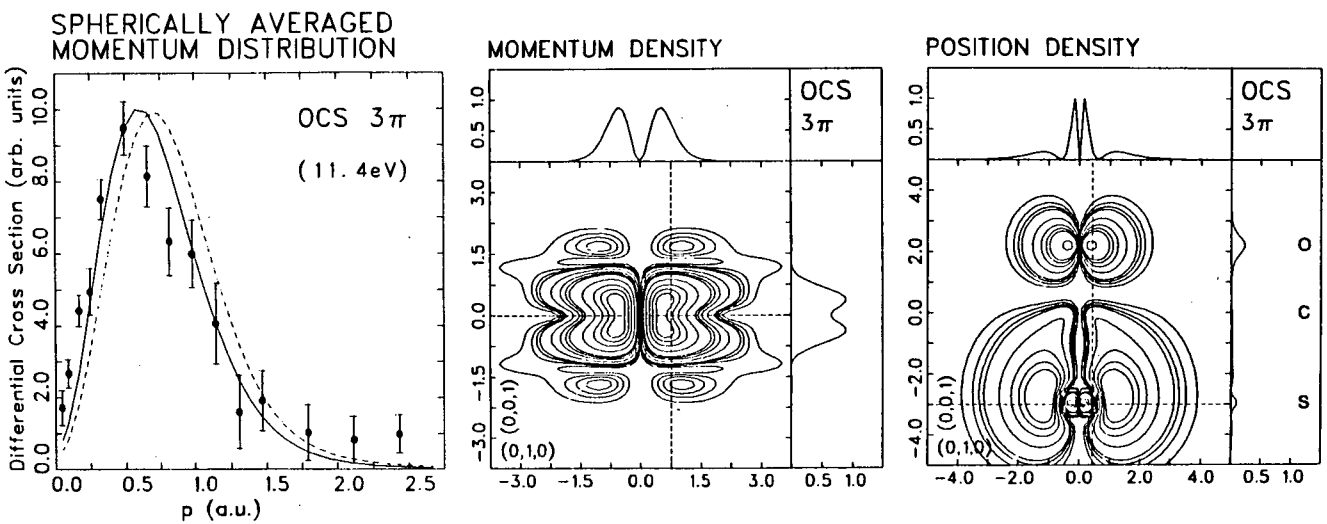

Figure 9.3 - Molecular orbital momentum distributions (left), momentum density (centre) and position density (right) maps of the OCS 3π orbital. Theoretical momentum distributions are evaluated using wavefunctions of near Hartree-Fock [MY67] quality (solid lines) and of minimal basis set [C62] quality. (dashed lines).

orbitals. The corresponding momentum density map of the 3π orbital can be considered as a pseudo-d orbital with the primary lobes merging at the p_z=0 plane. A similar situation exists in the case of other linear heteronuclear molecules such as the case of the 2π orbital of NO [BC&82]. It is important to note that the additional inversion centre at the p-space origin changes the overall symmetry of the symmetry orbital[5] from $C_{\infty v}$ in r-space to $D_{\infty h}$ in p-space (chapter 2). This situation results in the presence of momentum density in the p_z=0 reflection plane. The only apparent distinction between the momentum densities of the $C_{\infty v}$ (e.g. OCS) and $D_{\infty h}$ (e.g. CO_2 or CS_2) molecules in the case of antibonding π orbitals therefore depends upon whether or not the orbital has any density at the "lateral" reflection plane (i.e. the p_z=0 plane) in momentum-space. For instance, the momentum density of the CO_2 $1\pi_g$ orbital has a nodal plane at p_z=0 (see figure 7.4) while that of the OCS 3π orbital has a reflection plane at p_z=0. In general, the presence of nodal *curvatures* (surfaces) in position-space (as in OCS, for instance) will

---

[5] A symmetry orbital is the sum of a set of degenerate orbitals with the same orbital symmetry. It should be noted that the degenerate orbitals (e.g. the three components of the $1t_1$ orbital in CF_4 (chapter 10) or the five components of atomic d orbitals) contributing to a symmetry orbital may have different individual momentum profiles even though they have identical orbital energies. In this connection, it is also of importance to note that in binary (e,2e) spectroscopy it is the MDs of symmetry orbitals which are measured since orbital selection is obtained by choosing appropriate (binding) energies.

lead to reflection planes with nonzero density in momentum-space. Nodal *planes*, on the other hand, remain unchanged in both position and momentum space. For any π symmetry orbital, the characteristic nodal line along the internuclear axis is also invariant in both momentum and position space.

There is generally good agreement between the experimental MD of the 3π orbital and the theoretical MD calculated using the NHF wavefunction [MY67]. It is not surprising that MD calculated using the poorer quality MBS wavefunction [C62] does not agree with the experimental MD and is found to be shifted towards the higher momentum region. The small discrepancy in the $p<0.3a_0^{-1}$ region between the experimental MD and the calculated NHF MD indicates that the NHF wavefunction underestimates the low momentum part of the orbital. The spatial extent (in r-space) of the 3π orbital is therefore larger than that prescribed by the NHF wavefunction. It should be noted that the maximum of the experimental MD of the OCS 3π orbital occurs at an unusually small p value ($p_{max}\simeq0.50a_0^{-1}$) with respect to those of the CO_2 $1\pi_g$ orbital ($p_{max}\simeq0.85a_0^{-1}$) (chapter 7) and the CS_2 $2\pi_g$ orbital ($p_{max}\simeq0.67a_0^{-1}$) (chapter 8). The small p_{max} in the OCS 3π MD is a manifestation of the density lobe merging effects at the $p_z=0$ plane, which causes the effective maxima of the fused lobes to occur at smaller p values (figure 9.3, momentum density map).

The 2π orbital (figure 9.4, position density map) can be

considered essentially as bonding overlap between the $O(2p_x, 2p_y)$ and $C(2p_x, 2p_y)$ orbitals (see bond-parallel projection plot of figure 9.4). The momentum density map of the OCS 2π orbital appears to be quite similar to that of the CO 1π orbital [CS&79]. This orbital accounts for most of the π bonding in the C=O double bond. Both theoretical MDs of the 2π orbital lie in the higher momentum region with respect to the experimental one. The half width of the MBS MD is much too broad, again indicating the inadequacy of the MBS wavefunction. This overemphasis of the high momentum part in the theoretical wavefunctions again indicates the need for more diffuse atomic functions to be used in the formation of the π bond in OCS. It is also observed that the experimental MD of the 2π orbital closely resembles that of the 3π orbital, despite the different atomic compositions of the two orbitals.

The small natural separation between the $A(2\pi)^{-1}$ and $B(9\sigma)^{-1}$ states does not allow a "clean" measurement of the MD of the 9σ orbital with the present instrumental energy resolution. (The MD of the 2π orbital was measured at the low energy side of the A state (figure 9.1), which accounts for the relatively large error bars in the MD in figure 9.4.) The MD measured at 16.5eV (figure 9.5) is therefore due to a mixture of significant contributions from each of the 2π and 9σ MDs. Theoretical MDs are obtained by summing the corresponding theoretical MDs of the 2π and 9σ orbitals. The

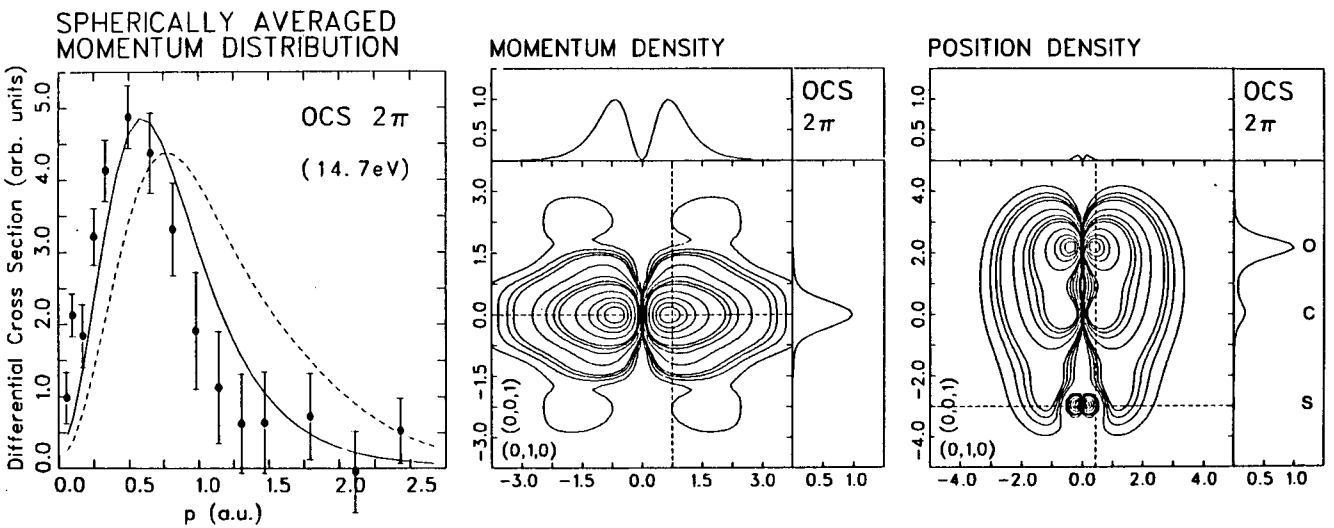

Figure 9.4 - Molecular orbital momentum distributions (left), momentum density (centre) and position density (right) maps of the OCS 2π orbital. Theoretical momentum distributions are evaluated using wavefunctions of near Hartree-Fock [MY67] quality (solid lines) and of minimal basis set [C62] quality. (dashed lines).

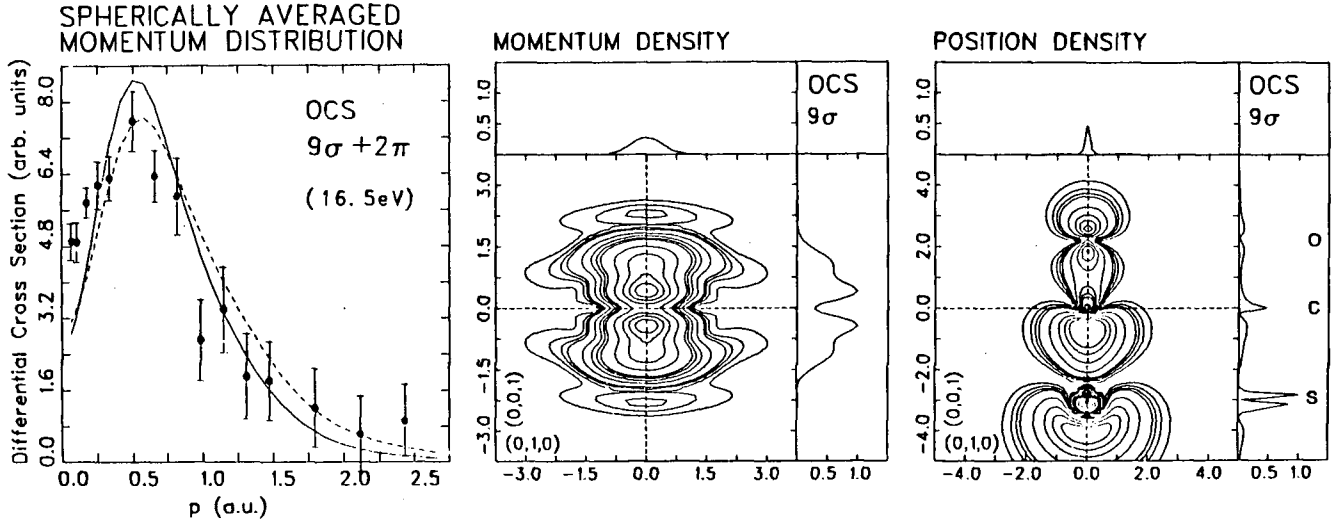

Figure 9.5 - Molecular orbital momentum distributions measured at 16.5eV (left), momentum density (centre) and position density (right) maps of the OCS 9σ orbital. Theoretical momentum distributions, corresponding to a weighted sum (see text) of the 2π and 9σ distributions, are evaluated using wavefunctions of near Hartree-Fock [24] quality (solid lines) and of minimal basis set [25] quality (dashed lines).

mixing coefficients of the two orbitals are obtained from consideration of the intensity ratio of the A and B states at 16.5eV in the ϕ=8° binding energy spectrum (figure 9.1). Figure 9.5 shows that the composite theoretical MDs are in reasonable agreement with the experimental MD measured at 16.5eV. There is, however, a discrepancy between theories and experiment in the $p<0.3a_0^{-1}$ region. The OCS 9σ orbital is primary antibonding between the O(2s, $2p_z$), C(2s, $2p_z$) and S($3p_z$) orbitals. The symmetric (s-type) component in the 9σ MD is clearly being underestimated by both theoretical wavefunctions. This suggests that the C(2s) contribution in the 9σ orbital should be increased in order to obtain a better agreement. The position density map of the 9σ orbital (figure 9.5) is analogous to those of the $CO_2(3\sigma_u)$ (figure 7.5) and $CS_2(5\sigma_u)$ (figure 8.6) orbitals. The corresponding momentum density of the OCS 9σ orbital is also similar to those of CO_2 $(3\sigma_u)$ and CS_2 $(5\sigma_u)$ orbitals except that there is a general merging between density lobes in the case of the 9σ orbital. This merging effect is indicative of the differences in molecular symmetries between OCS and its valence isoelectronic $D_{\infty h}$ counterparts CO_2 and CS_2.

The position density map of the 8σ orbital (figure 9.6) shows that the 8σ orbital is bonding between the C(2s, $2p_z$) and O(2s, $2p_z$) orbitals. The s-p composite nature of the orbital is clearly evident in the momentum density map (see also the bond-parallel projection plot). There is excellent

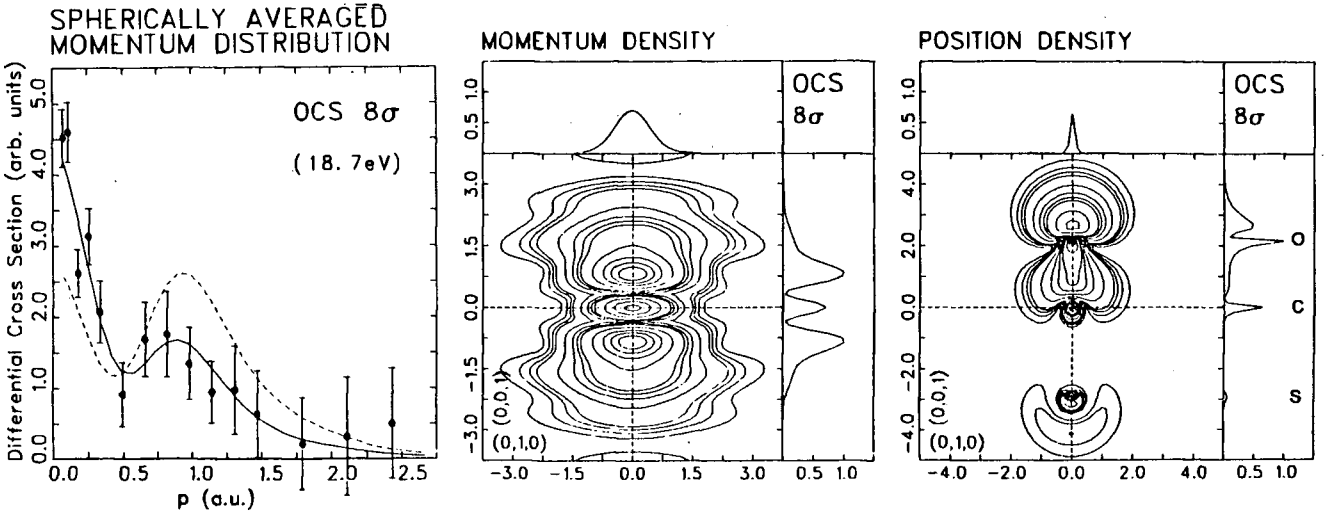

Figure 9.6 - Molecular orbital momentum distributions (left), momentum density (centre) and position density (right) maps of the OCS 8σ orbital. Theoretical momentum distributions are evaluated using wavefunctions of near Hartree-Fock [MY67] quality (solid lines) and of minimal basis set [C62] quality. (dashed lines).

agreement between the experimental MD and the calculated NHF MD for the 8σ orbital. The calculated MBS MD severely underestimates the s-to-p ratio (as indicated by the ratio of intensities at p=0 and at $p=0.8a_0^{-1}$). It is interesting to note that the experimental s-to-p ratio for the OCS 8σ orbital is much higher than those of the corresponding CO_2 $4\sigma_g$ orbital (figure 7.2) and CS_2 $6\sigma_g$ orbital (figure 8.7).

9.3.2 Inner Valence Orbitals

The broad structures in the inner valence region observed in the binding energy spectra (figure 9.1) have been attributed to many-body (or electron correlation) effects. This observation confirms the general breakdown of the independent particle (Koopmans-like) ionization picture. Both the GF [CW&81] and the SAC-CI [N83] calculations of the binding energy spectrum (figure 9.2) have indicated that there are severe population splittings in the 7σ and 6σ hole states. More importantly, both theories [CW&81, N83] show that there are clusters of 7σ and 6σ poles centering approximately at 26eV and 36eV respectively (figure 9.2). On the basis of the theoretical interpretation of the inner valence structure, the MDs measured at 26.8eV and 36.0eV can be associated with the 7σ and 6σ orbitals respectively. The chosen sitting binding energies correspond approximately to the positions of two of the prominent band maxima in the $\phi=0°$

binding energy spectrum (figure 9.1). There is excellent agreement between the experimental MDs and the calculated MDs for the 7σ (figure 9.7) and 6σ (figure 9.8) orbitals. It should be noted that theoretical MDs of the inner valence orbitals calculated by NHF and MBS wavefunctions (figures 9.7 and 9.8) are very similar to each other. Differences between the qualities of the two wavefunctions are more clearly seen in the MDs of the outer valence orbitals.

The position density maps of the 7σ and 6σ orbitals indicate that the 7σ and 6σ orbitals can be considered as C(2s)-S(3s) and C(2s)-O(2s) overlaps respectively. There is no correspondence between the composition of the OCS 7σ orbital and those for the corresponding CO_2 $2\sigma_u$ (chapter 7) and CS_2 $4\sigma_u$ (chapter 8) orbitals. The OCS 6σ orbital (figure 9.8), on the other hand, closely resembles half of the CO_2 $3\sigma_g$ orbital in the respective position density maps. There is, however, a distinct difference in appearance between the momentum density map of the two orbitals. In particular, the momentum density of the OCS 6σ orbital is much more isotropic than that of the $3\sigma_g$ orbital in CO_2 which has secondary lobal structures (see figure 7.5). The degree of isotropy of molecular density in p-space is of course related to that in r-space by the molecular density directional reversal relation [CD41, ET77, CB82b, LB83b] (chapter 2). The (single) C(2s)-O(2s) overlap in the OCS 6σ orbital in r-space (figure 9.8) is clearly more spherical than the more

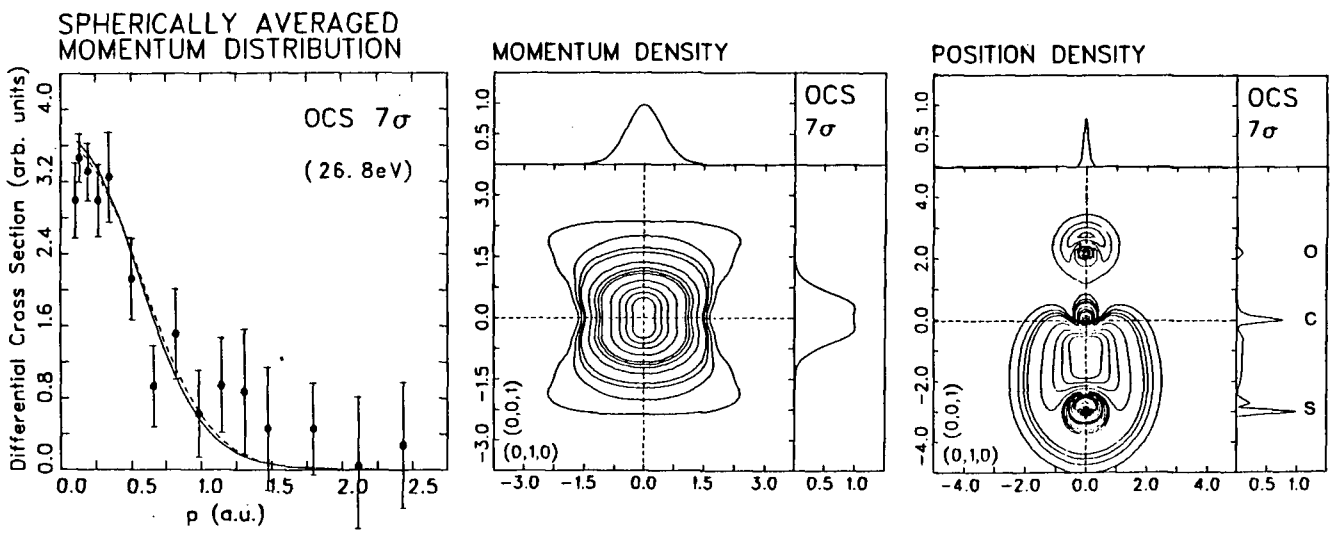

Figure 9.7 - Molecular orbital momentum distributions (left), momentum density (centre) and position density (right) maps of the OCS 7σ orbital. Theoretical momentum distributions are evaluated using wavefunctions of near Hartree-Fock [MY67] quality (solid lines) and of minimal basis set [C62] quality. (dashed lines).

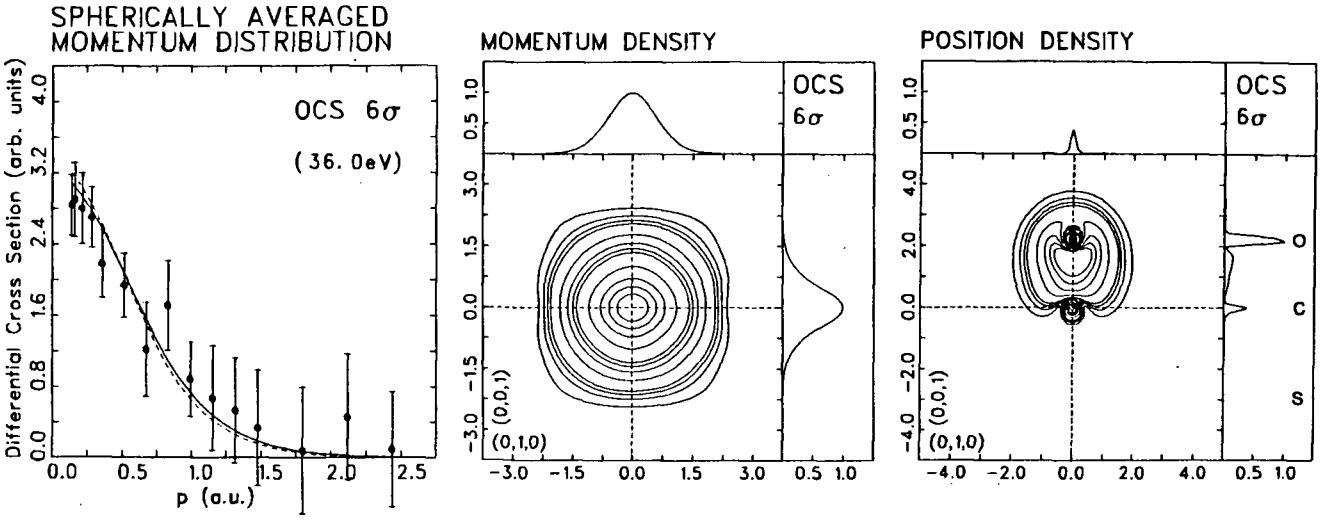

Figure 9.8 - Molecular orbital momentum distributions (left), momentum density (centre) and position density (right) maps of the OCS 6σ orbital. Theoretical momentum distributions are evaluated using wavefunctions of near Hartree-Fock [MY67] quality (solid lines) and of minimal basis set [C62] quality. (dashed lines).

elongated O(2s)-C(2s)-O(2s) overlap (i.e. a double C-O overlap) in the CO_2 $3\sigma_g$ orbital.

9.4 MANY-BODY STRUCTURE OF CO_2, CS_2 AND OCS

It is instructional to review some of the important aspects of the valence electronic structure of the linear triatomic group: CO_2, CS_2 and OCS. Detailed studies of CO_2 and CS_2 using binary (e,2e) spectroscopy are given in chapter 7 and chapter 8 respectively. Figure 9.9 shows the valence-shell binding energy spectra of CO_2 [CB82a], CS_2 (chapter 8) and OCS (figure 9.1) measured at ϕ=0°. It should be noted that the binding energy spectrum of CO_2 reported by Cook and Brion [CB82a] was obtained using 400eV impact energy while the binding energy spectra of CS_2 (chapter 8) and OCS (figure 9.1) were measured using 1200eV impact energy. In addition, theoretical binding energy spectra above 20eV calculated using the many-body 2ph-TDA Green's function technique for CO_2 [DC&79], CS_2 [SD&79] and OCS [CW&81] (see also figure 9.2) are shown as inserts in figure 9.9. The calculated poles have been convoluted with the corresponding experimental half-widths in each case.

Several interesting features can be seen from figure 9.9. There is a general shift of the valence-shell binding energy profile towards the low energy side progressing from CO_2 (top), OCS (bottom) and finally to CS_2 (middle). This is

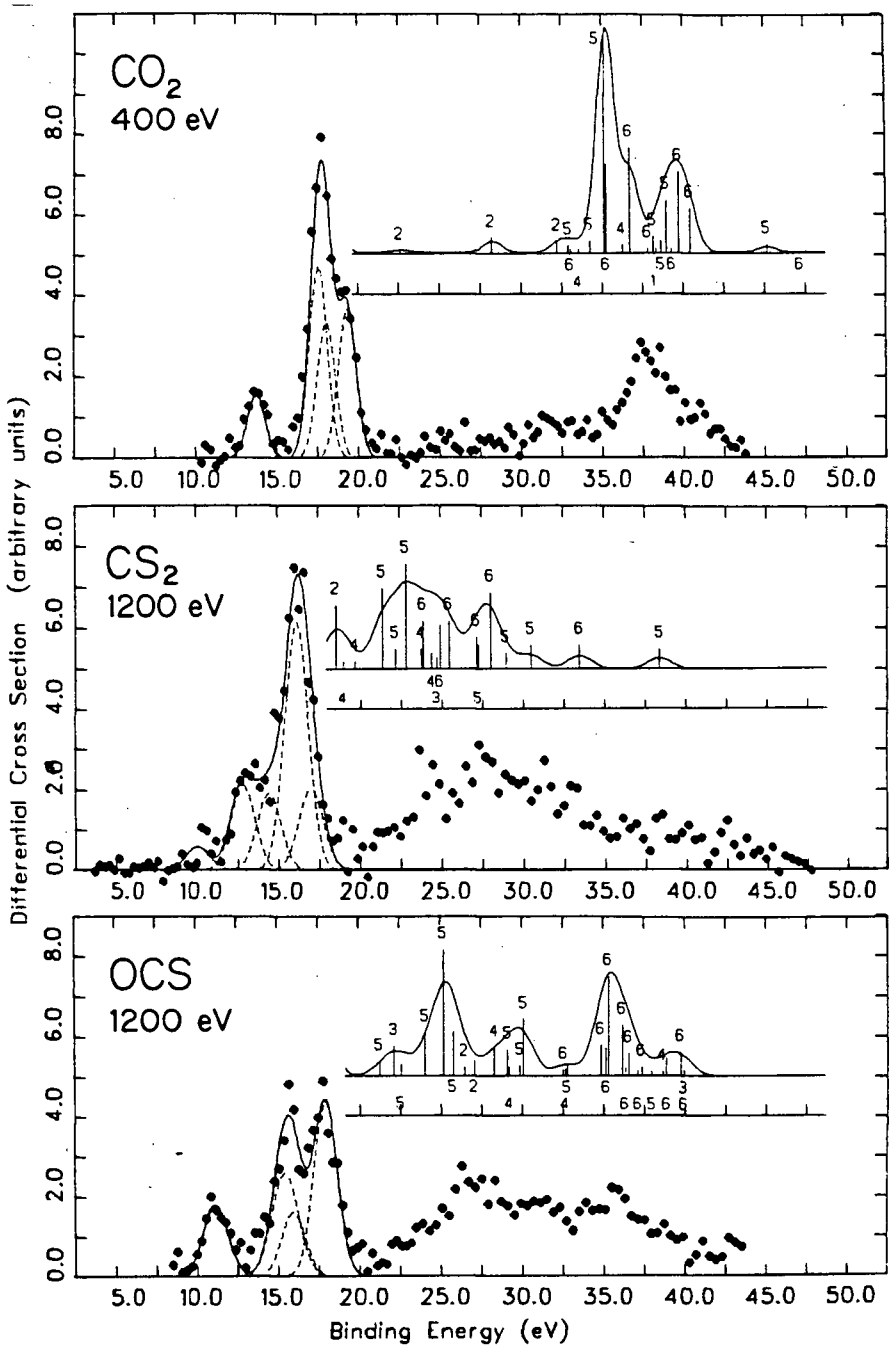

Figure 9.9 - Comparison of the valence-shell binding energy spectra for CO_2 [CB82a], CS_2 (chapter 8) and OCS at ϕ=0°. Inner valence-shell binding energy spectra calculated by the 2ph-TDA Green's function method for CO_2 [DC&79], CS_2 [SD&79] and OCS [CW&81] are shown as inserts.

of course in accord with the opposite trend associated with the size of the valence isoelectronic orbitals in the group, namely, CS_2 > OCS > CO_2. The energy required for ionizing an electron in a more spatially extended orbital is in general less than that in a more tightly bound (i.e. more localized) orbital. Moreover, there is an intense population splitting in the inner valence region of each spectrum, indicating a general breakdown of the independent particle ionization picture throughout this linear triatomic series. The energy profile of the many-body states of OCS also lies intermediate between those of CS_2 (lower energy) and CO_2 (higher energy). A similar spectral pattern of the many-body states in CO_2, CS_2 and OCS can be seen in the earlier XPS work [AG&72] and is also predicted in calculations using the many-body 2ph-TDA Green's function (GF) technique [DC&79, SD&79, CW&81] (figure 9.9 inserts) and in those using the symmetry adapted cluster configuration interaction (SAC-CI) method [N83].[6] There is generally good qualitative agreement between the experimental binding energy spectra and the corresponding GF calculated spectra for CO_2, CS_2 and OCS. However, small energy shifts

[6] The SAC-CI method should inherently provide a better description of electron correlation effects because of the inclusion of four electron excited configurations [N83]. It appears, however, that the SAC-CI calculated spectra of CS_2 and OCS compare less favorably with the corresponding experimental binding energy spectra than the GF calculated spectra. This may be due to the difference in the quality of the basis sets involved. The GF calculated spectra give broader breakdown patterns and are used in the present comparison study (figure 9.9).

of the various bands in the inner valence region are often needed in the GF spectra to provide better spectral correspondence with the experimental spectra. The GF calculations also appear to have underestimated the amount of many-body states in the 35-45eV region of CS_2 and in the 27-32eV region of CO_2. These deficiencies in the GF calculations are attributed to the inherent limitations of the two particle-hole Tamm Dancroff approximation as well as the quality of the employed basis sets. It should be noted that intermixing of poles between the inner valence orbitals (labelled by 5 and 6 in figure 9.9) appear to be more severe in CO_2 and CS_2 than in OCS. The GF calculated spectrum of OCS generally shows poles from the same orbital clustering together to give the calculated band maxima.

9.5 MOMENTUM-SPACE CHEMISTRY OF CO_2, CS_2 AND OCS

Some of the most conspicuous features in the orbital pattern of the CO_2, CS_2 and OCS molecules are now discussed. Figures 9.10 and 9.11 show the momentum distributions (MDs) and the corresponding theoretical momentum and position density contour maps of the outer valence antibonding π orbitals and of the outer valence bonding σ orbitals of the linear triatomic group respectively. Theoretical wavefunctions used for computing the momentum distributions and the associated density maps of CO_2 [SB72], CS_2 [HL&80]

and OCS [MY67] are of double-zeta or better quality. The calculated MDs for the outer valence antibonding π orbitals (figure 9.10) are height normalized at the respective maxima and those for the outer valence bonding σ orbitals (figure 9.11) are area normalized from 0-1.5 a_0^{-1}, each to the respective experimental MD.

9.5.1 Outer Valence Antibonding π Orbitals

As shown in figure 9.10, the experimental MDs of the $CO_2(1\pi_g)$, $CS_2(2\pi_g)$ and $OCS(3\pi)$ orbitals are generally in good agreement with the corresponding MDs calculated using wavefunctions of at least double-zeta quality. There is, however, a notable discrepancy in the low momentum ($<0.5a_0^{-1}$) region between the experimental and calculated MDs of the respective π orbitals. In all cases, the calculated MDs not only underestimate the density in the low momentum region but also appear to have slightly overestimated the location of the maximum, p_{max}, by approximately $0.1a_0^{-1}$. These small inadequacies suggest that the atomic orbitals involved in the formation of the essentially nonbonding molecular orbitals should be more spatially extended (in position-space) i.e. more delocalized. Similar discrepancies have also been observed in the "lone-pair" nonbonding orbitals of the first-row hydrides: HF [BH&80], H_2O [DD&77a, HHB77, BL&84] and NH_3 [CS&76, HHB76a].

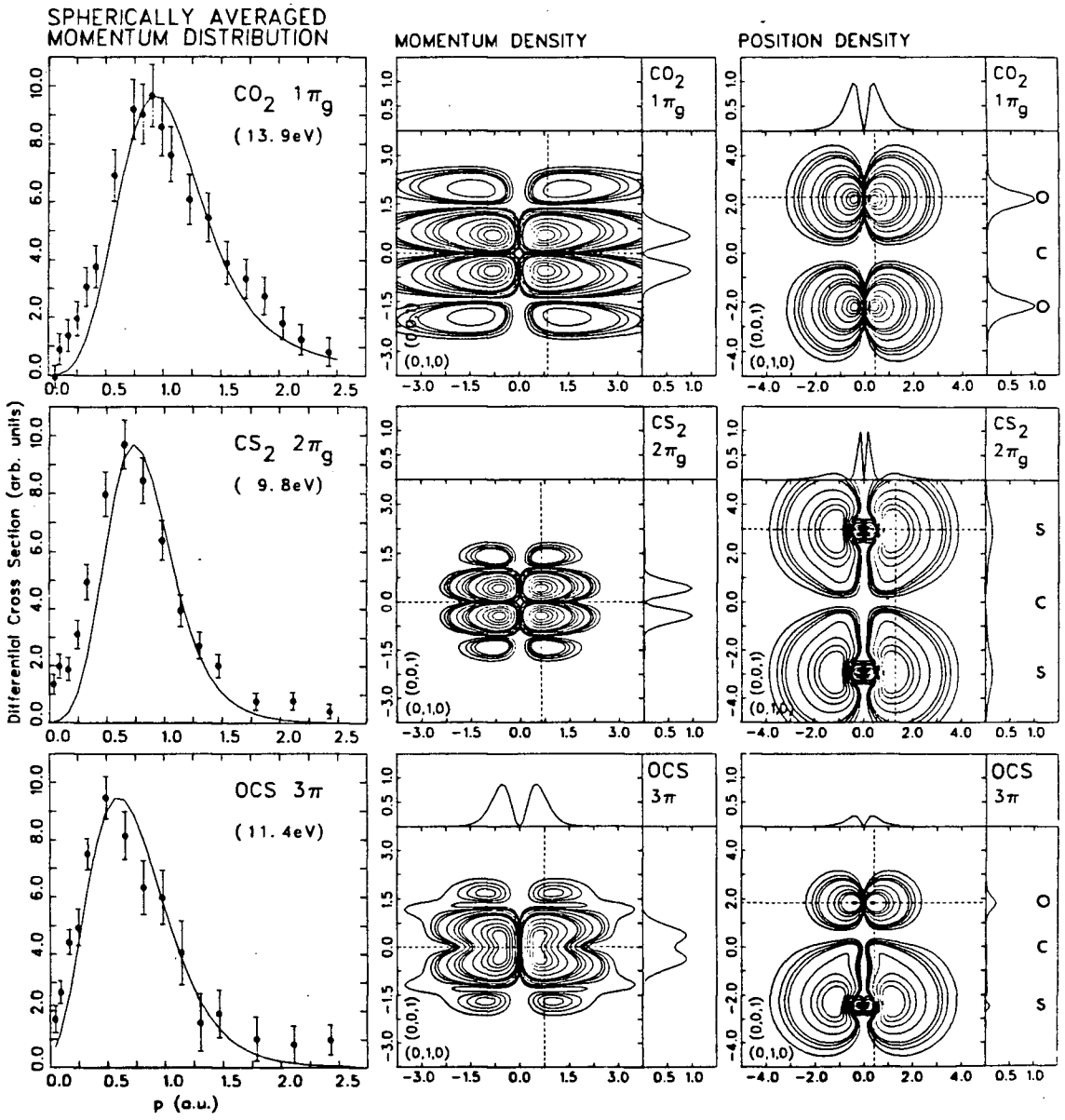

Figure 9.10 - Comparison of momentum distributions (left), momentum density (centre) and position density (right) maps of the CO_2 $1\pi_g$, CS_2 $2\pi_g$ and OCS 3π orbitals.

One striking trend in the experimental MDs of the valence isoelectronic group is the progressive contraction of density into the lower momentum region from the $CO_2(1\pi_g)$, $CS_2(2\pi_g)$ to $OCS(3\pi)$ orbitals as evidenced by the changes in p_{max}. This is clearly shown by contrasting the broad $CO_2(1\pi_g)$ MD with the relatively sharp $CS_2(2\pi_g)$ MD. The $CO_2(1\pi_g)$ MD also has a much slower fall-off in the high momentum region than the $CS_2(2\pi_g)$ MD, which has very small intensity beyond $1.7a_0^{-1}$. The width of the $OCS(3\pi)$ MD is somewhat intermediate between those of the two other distributions. Similar changes in the broadness and p_{max} of the experimental MDs of valence isoelectronic orbitals have also been observed in the hydrogen halides [BH&80, BM&82] and the noble gases [LB83a] (chapter 4). In these latter works [BH&80, BM&82, LB83a], it was demonstrated that the experimental MDs of the valence orbitals become more contracted into the lower momentum region with sharper profile as the principal quantum number n of the heavy atom increases. This change in the MDs of the valence isoelectronic orbitals is a clear manifestation of the inverse spatial reversal property.[7] The position density maps

[7] There are four momentum-space chemical properties which are associated with the Fourier transformation. These are: (i) symmetry invariance with an automatic inversion centre at the p-space origin; (ii) inverse spatial reversal; (iii) molecular density directional reversal; and (iv) molecular density oscillation. Detailed discussions of these properties are given in chapter 2.

(figure 9.10) clearly show that the order of the orbital extent in r-space is $CO_2(1\pi_g)$ < $OCS(3\pi)$ < $CS_2(2\pi_g)$. This trend is expected because the replacement of the smaller atomic O(2p) with the larger (and more spatially extended) atomic S(3p) involved in the formation of the antibonding π orbitals of the group: CO_2, OCS and CS_2 increases the overall size of the molecular orbital. The corresponding momentum density maps (figure 9.10) indicate that the order of orbital extent in p-space follows the reverse trend: $CO_2(1\pi_g)$ > $OCS(3\pi)$ > $CS_2(2\pi_g)$. In the case of $D_{\infty h}$ triatomics, there is a drastic contraction of the pseudo d-like lobes in the momentum density of $CS_2(2\pi_g)$ orbital relative to that of the $CO_2(1\pi_g)$ orbital (figure 9.10). In particular, the extent of the outermost (0.2%) contours of the momentum density of $CS_2(2\pi_g)$ orbital is reduced by almost 50% in the bond-perpendicular direction when compared with that of the $CO_2(1\pi_g)$ orbital. Such a large change in the width of the pseudo-d like lobes of the momentum density is responsible for the observed changes in the broadness as well as in the tailing behavior of the MDs of the antibonding π orbitals (see figure 9.10). The size of both the position and momentum densities of the $OCS(3\pi)$ orbital is intermediate between those of the respective densities of the $CO_2(1\pi_g)$ and $CS_2(2\pi_g)$ orbitals.

Other momentum-space properties can also be seen in the density maps of the antibonding π orbitals (figure 9.10) of

the linear triatomic group. The change in the longitudinal direction of individual density lobes from the bond-parallel (0,0,1) direction in r-space to the bond-perpendicular direction in p-space demonstrates the molecular density directional reversal property. Moreover, secondary lobes occurring in the bond-parallel direction are clearly present in the momentum density maps (figure 9.10) of the antibonding π orbitals. This molecular density oscillation (chapter 2) effect retains the information concerning the equilibrium nuclear geometry just as a diffraction pattern in X-ray crystallography contains information related to interatomic distances in crystals. In the case of the antibonding π orbitals of the linear triatomics X=C=Y (where X and Y are either O and/or S atoms), the p-space periodicity, P, of the bond-parallel oscillations is related to the internuclear separation between atoms X and Y, R_{X-Y}, by the following equation:

$$P = 2\pi n \; / \; R_{X-Y}; \; n=1,2,3,... \quad \text{(in atomic units)}.$$

Table 9.1 clearly illustrates the validity of the above relation (for n=1) where the distances R_{X-Y} are obtained from the literature [C62]. A similar relation between the p-space periodicities of the density oscillations and the corresponding r-space internuclear separations has also been verified in chapter 5.

Table 9.1
P-space periodicities of momentum density oscillations and internuclear separations of antibonding π orbitals.*

Linear Triatomic X=C=Y	Separation between X and Y in X=C=Y R_{X-Y}**	$2\pi / R_{X-Y}$	P-space periodicity
O=C=O	4.389	1.43	1.41
S=C=S	5.873	1.07	0.94
O=C=S	5.146	1.22	1.29

* All the values are in atomic units.
** See, for example, reference [C62].

Finally, the property of symmetry invariance in momentum-space is demonstrated in the density maps of the $CO_2(1\pi_g)$ and $CS_2(2\pi_g)$ orbitals. In particular the characteristic symmetry elements, namely the bond-parallel nodal line and the bond-perpendicular nodal plane, are present in both momentum and position density maps (figure 9.10). The presence of the (automatic) inversion centre at the p-space origin alters the overall symmetry of the OCS(3π) orbital from $C_{\infty v}$ in r-space to $D_{\infty h}$ in p-space. In this case only the nodal line is invariant in both momentum and position space. The p_z=0 plane becomes a reflection plane. There is also a general merging between density lobes in the bond-parallel direction. This merging effect accounts for the abnormally low p_{max} observed in the MD of the OCS(3π) orbital.

9.5.2 Outer Valence Bonding σ Orbitals

Figure 9.11 shows that there is good agreement particularly in the low momentum region between the experimental and calculated MDs of the outer valence bonding σ orbitals. With the exception of the OCS(8σ) MD which is in excellent agreement with the calculated MD, the calculated MDs of both the $CO_2(4\sigma_g)$ and $CS_2(6\sigma_g)$ orbitals, however, slightly overestimate the nonsymmetric component in the respective MDs. Of particular interest is the observation

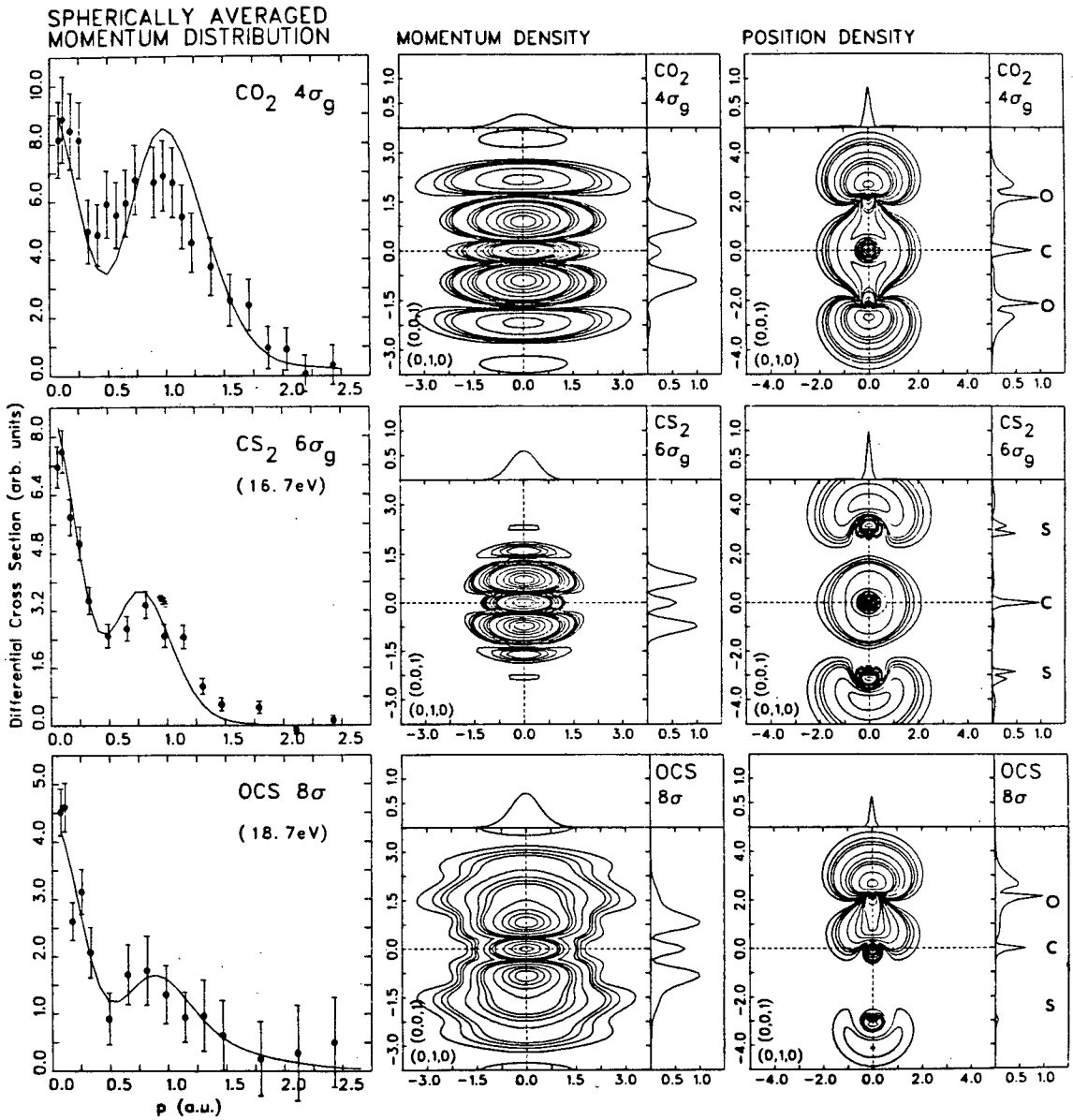

Figure 9.11 - Comparison of momentum distributions (left), momentum density (centre) and position density (right) maps of the CO_2 $4\sigma_g$, CS_2 $6\sigma_g$ and OCS 8σ orbitals.

that the ratio of the nonsymmetric to symmetric components[8] in the MD of the OCS(8σ) orbital is approximately 50% of that of the MD of the $CO_2(4\sigma_g)$ orbital. The position density map of the OCS(8σ) orbital indicates that the 8σ orbital is essentially composed of C-O bonding overlap, which is very similar to the C-O overlap in "half" of the $CO_2(4\sigma_g)$ orbital. This similarity is clearly shown in the bond-parallel projection plots of position density maps of the OCS(8σ) and the $CO_2(4\sigma_g)$ orbitals. It is therefore not surprising to see that the correponding momentum density maps of the two orbitals bear some similarity to each other in their overall general appearance. The momentum density map of the OCS(8σ) orbital can be effectively simulated by merging of the oscillatory lobes in that of the $CO_2(4\sigma_g)$ orbital. The observed change of the p-to-s ratios of the MDs of the two orbitals are consistent with the fact that there is effectively twice as much C-O overlap in the $CO_2(4\sigma_g)$ orbital than in the OCS(8σ) orbital. The density at the O atom is responsible for the nonsymmetric component observed in the experimental MD. The symmetric component of the MD is mainly due to the C(2s) orbital.

Comparison of the position density map of the $CS_2(6\sigma_g)$ orbital with that of the $CO_2(4\sigma_g)$ orbital clearly shows the

---

[8] The ratio of the nonsymmetric to symmetric components can be approximated by the relative intensity ratio of the peak maxima at $p\neq0$ (nonsymmetric component) and at $p=0$ (symmetric component).

more spatially extended nature of the $CS_2(6\sigma_g)$ orbital. There is also a concomitant contraction of the momentum density of the $CS_2(6\sigma_g)$ orbital relative to that of the $CO_2(4\sigma_g)$ orbital, in accord with the inverse spatial reversal property. This contraction is reflected in the MD by the very fast fall-off of the $CS_2(6\sigma_g)$ MD, in contrast to the relatively high momentum tail in the corresponding $CO_2(4\sigma_g)$ MD. The C-S overlap in the $CS_2(6\sigma_g)$ orbital also appears to be weaker than the C-O overlap in the $CO_2(4\sigma_g)$ orbital. This is substantiated by the ratios of the nonsymmetric to symmetric components in the respective orbitals. The p-to-s ratio of the $CS_2(6\sigma_g)$ MD is approximately 40% smaller than that of the $CO_2(4\sigma_g)$ MD. The molecular density directional reversal and molecular density oscillation properties as well as the symmetry invariance property are clearly evident in the momentum density maps of the $CO_2(4\sigma_g)$ and $CS_2(6\sigma_g)$ orbitals. The automatic inversion centre at the p-space origin again generates general merging between density lobes, which results in a more gradual fall-off in the high momentum region of the MD of the $OCS(8\sigma)$ orbital.

Chapter X

CARBON TETRAFLUORIDE

10.1 INTRODUCTION

In the present work detailed measurements of binding energy spectra and momentum distributions for CF_4 are obtained. Earlier studies of substituted fluoromethanes by Cambi *et al.* [CC&81, CC&82] using binary (e,2e) spectroscopy and Green's function theoretical techniques have shown that these molecules exhibit a breakdown of the independent particle ionization picture. These latter works [CC&81, CC&82], however, provided only a limited amount of information on the momentum distributions (MDs) of individual molecular orbitals. The MDs of these fluoromethanes are of interest because of (i) the C-F sigma bonding orbitals and (ii) the nonbonding orbitals which are due primarily to the "lone-pair" fluorine 2p electrons. In particular, discrepancies between the experimental MDs of lone-pair electrons (i.e. nonbonding) and the theoretical MDs evaluated using double-zeta quality SCF wavefunctions have been consistently observed for a number of different molecules. Classic examples of this behavior are the outermost orbitals of the first-row hydrides: $HF(1\pi)$ [BH&80], H_2O $(1b_1)$ [DD&77a, HHB77] and $NH_3(3a_1)$ [CS&76, HHB76b] and of the linear

triatomic group: CO_2 [LB84b], CS_2 [LB84c] and OCS [LB84d] (chapters 7-9). The recent study of CF_4 by Cambi *et al.* [CC&82] is seriously limited by low energy resolution (2.6eV FWHM) and as a result, most of the reported MDs sampled at various binding energies have contributions due to more than one characteristic orbital. This has complicated direct comparison between experimental and theoretical MDs on an orbital basis. The present binary (e,2e) study of CF_4 has been conducted using a binary (e,2e) spectrometer (chapter 3) with high momentum resolution ($0.1a_0^{-1}$) and considerably better energy resolution (1.6eV FWHM). Except for the $4t_2$ orbital, MDs of all the other orbitals can be obtained directly by measuring at judiciously chosen binding energies. The present study is the most detailed set of measurements to date of MDs of individual orbitals of CF_4. The experimental MDs are further compared with theoretical MDs computed using different quality wavefunctions. In addition density topographical diagrams are used to interpret various features in the spherically averaged MDs. This phenomenological contour mapping approach of investigating momentum-space molecular orbital (MO) concepts [CD41, ET77, CS&79, BC&82, CB82a, CB82b, MB&83, LB83b] (chapter 2) has been further extended by using three-dimensional constant density surface plots (chapter 5) of the MO density in both position-space and momentum-space. This permits a fuller exploration of the three-dimensional nature of the symmetry orbitals associated

with a nonlinear molecule such as CF_4.

10.2 VALENCE BINDING ENERGY ELECTRONIC STRUCTURE

Carbon tetrafluoride is a 42-electron system with T_d symmetry. In simple molecular orbital (MO) theory, the ground state electronic configuration can be written as:

$$\underbrace{(1a_1)^2(2a_1)^2(1t_2)^6}_{\text{core}}\underbrace{(3a_1)^2(2t_2)^6}_{\text{inner valence}}\underbrace{(4a_1)^2(3t_2)^6(1e)^4(4t_2)^6(1t_1)^6}_{\text{outer valence}}$$

An approximate MO diagram is given in figure 10.1 to show the major atomic components in individual valence MOs. The first three symmetry orbitals are essentially due to lone-pair electrons on the F atoms. Bonding orbitals (positive overlaps between atomic orbitals) are the $3t_2$ and $3a_1$ orbitals. Antibonding orbitals (negative overlaps between atomic orbitals) include the $4a_1$ and $2t_2$ orbitals. Clearly, only momentum distributions (MDs) of the a_1 orbitals are of pseudo s-type character. The MDs of other symmetry orbitals are of pseudo p-type character.[1]

The binding energy spectra (12-60eV) measured at $\phi=0°$

[1] The pseudo s-type and pseudo p-type terminology used here are intended to qualify MDs of molecular orbitals with shapes similar to those of the MDs of atomic s and p orbitals. A (pseudo) s-type MD has maximum at p=0 while a (pseudo) p-type MD has maximum at p≠0.

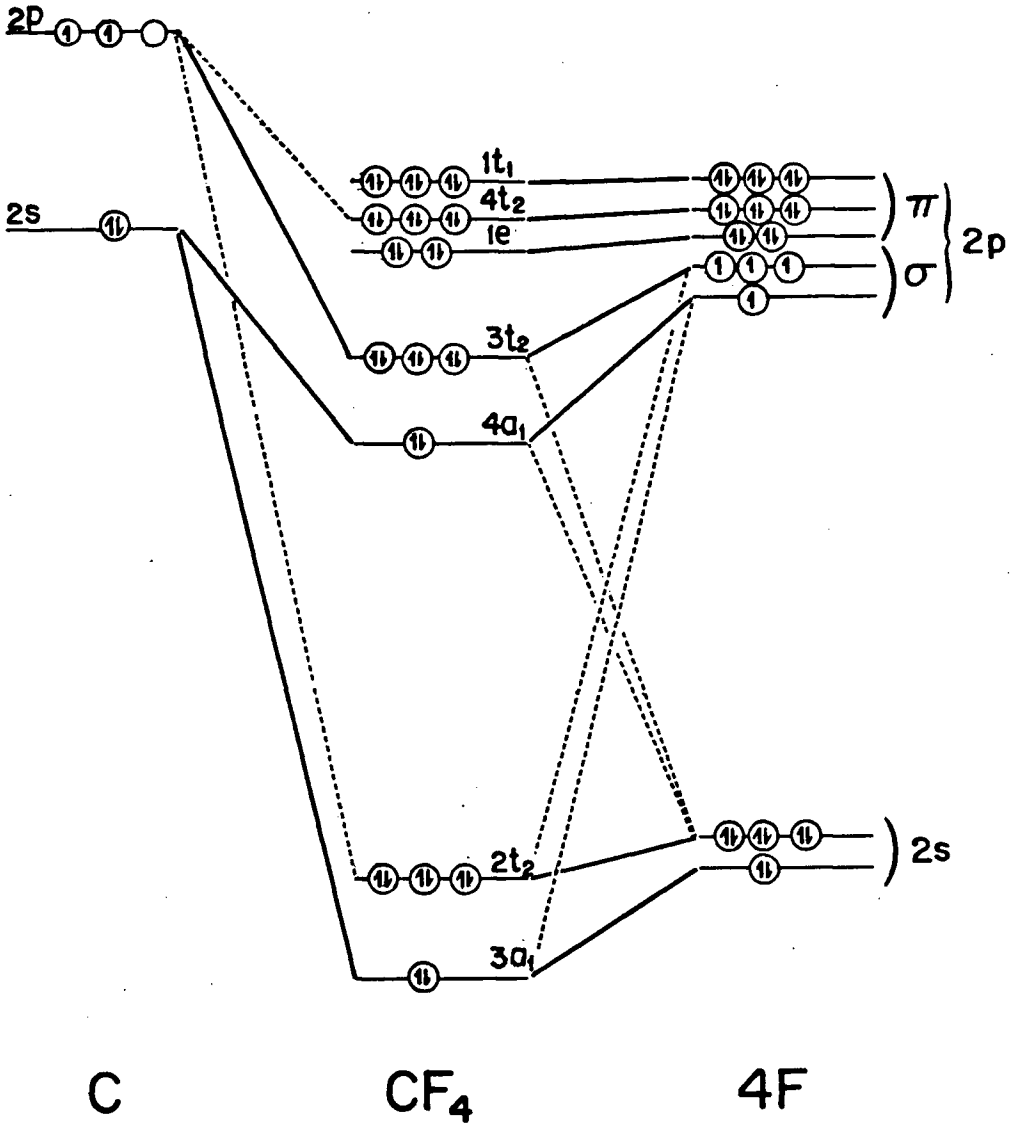

Figure 10.1 - Approximate molecular orbital diagram for the valence-shell of CF_4. Solid lines between energy levels indicate large contributions from the atomic orbitals. Dashed lines are used to indicate smaller contributions.

and 8° are shown in figure 10.2. Figure 10.3 shows the outer valence region (10-30eV) in more detail at a series of azimuthal angles ϕ. Gaussian deconvolution is used to separate bands due to different ionic states. The energy positions and Franck-Condon widths for the individual Gaussians are obtained from photoelectron studies [S&69, BRB70, BM&74, BS&81]. The excellent agreement between the fitted envelopes (sum of individual Gaussians) and the experimental spectra at the respective ϕ angles can be seen in figures 10.2 and 10.3. It is evident from the ratios of relative intensities of the fitted individual Gaussians at ϕ=0° and ϕ=8° (figure 10.2) that only peak 5 (assigned to the $(4a_1)^{-1}$ state) and peak 7 (assigned to the $(3a_1)^{-1}$ state) have higher intensities at ϕ=0°. This indicates that the corresponding MDs have a pseudo s-type behaviour. The other peaks exhibit higher intensities at ϕ=8° and the MDs corresponding to these ionized orbitals are therefore of pseudo p-type character. There is generally good agreement between the present binding energy spectra and those previously reported by Cambi *et al.* [CC&82], given the differences in energy resolution and the sampling ϕ angles in the two studies. Some of the structure has been "broadened" out in the earlier work [CC&82] because of the limited energy resolution.

Many-body Green's function calculations [CD77] of the valence-shell binding energy spectrum of CF_4 using the two-

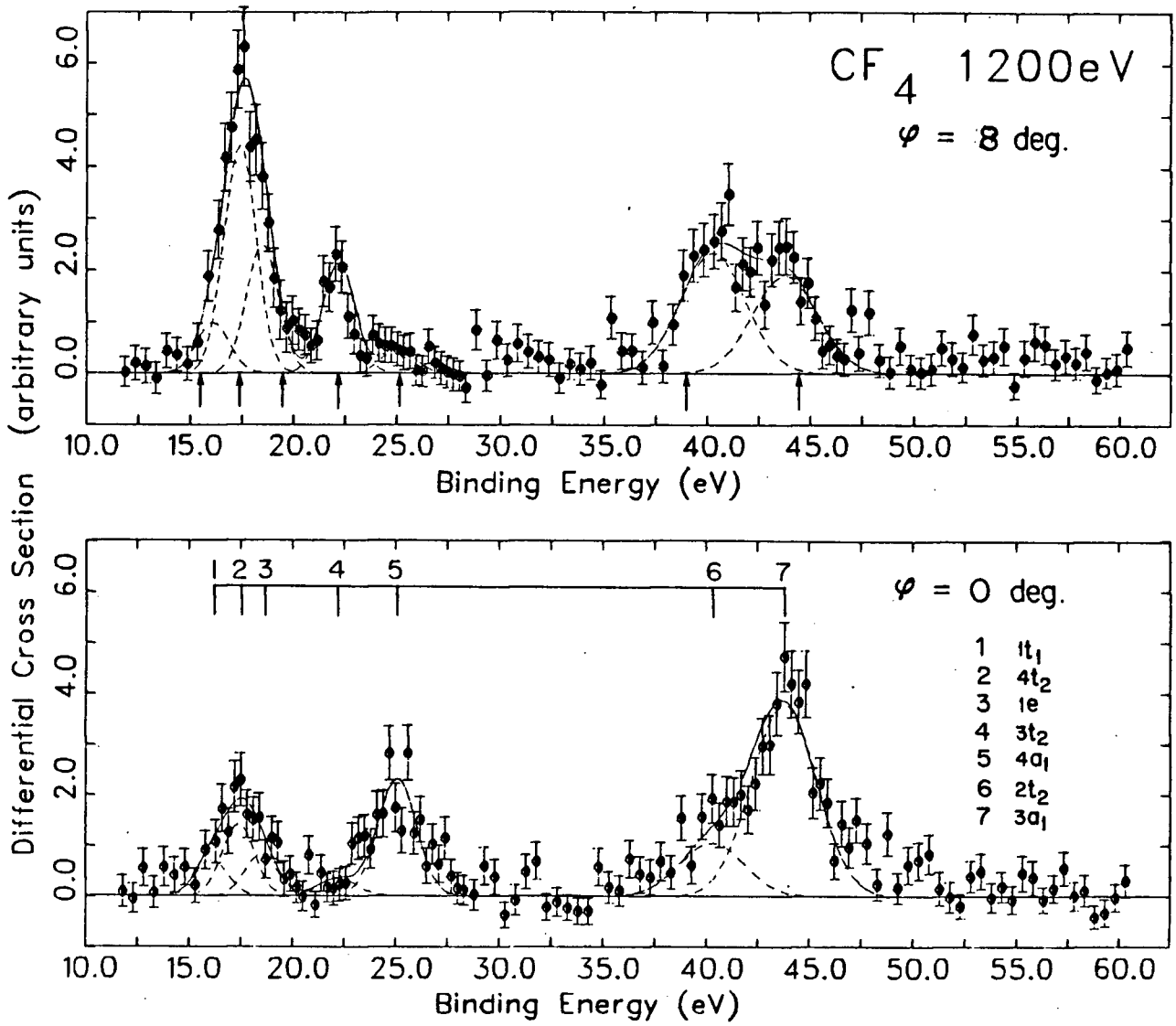

Figure 10.2 - Valence-shell binding energy spectra for CF_4 at ϕ=0° and 8°. Least-squares Gaussian fit of the experimental data is indicated by the solid lines. The arrows in the ϕ=8° spectrum indicate the sitting binding energies where the momentum distributions are measured (see figures 10.6-10.12).

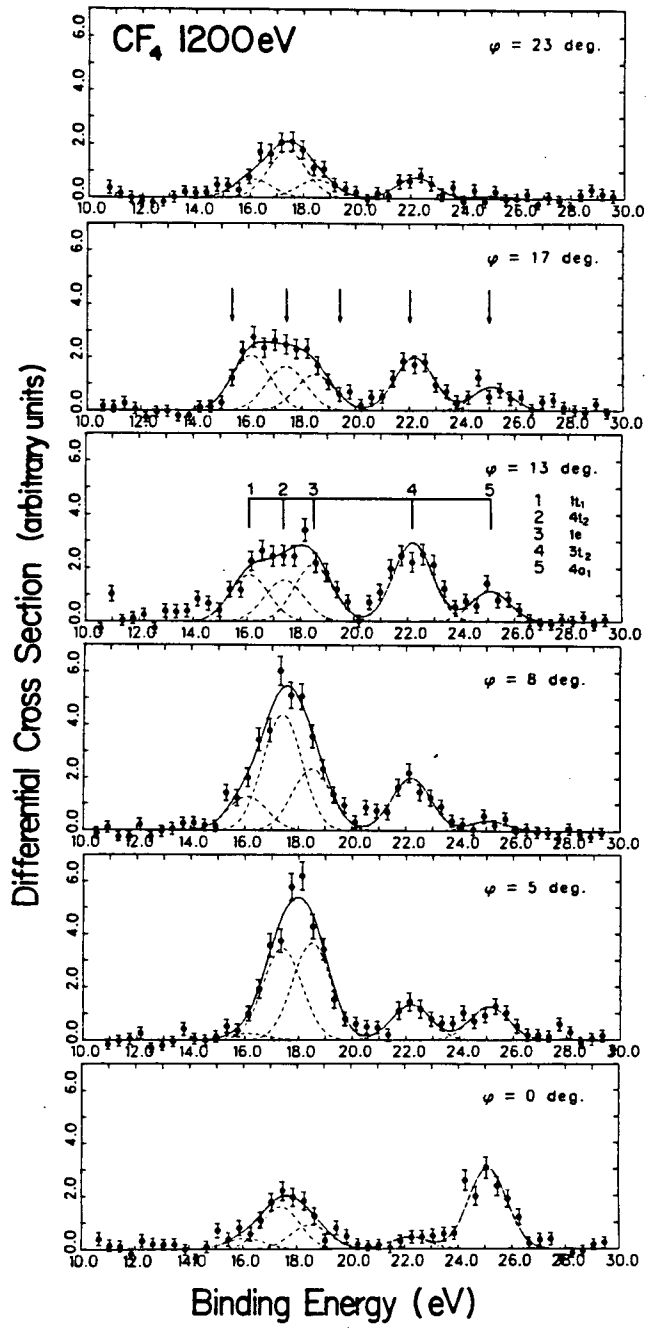

Figure 10.3 - Outer valence binding energy spectra for CF_4 at ϕ=0°, 5°, 8°, 13°, 17° and 23°. Least-squares Gaussian fit of the the experimental data is indicated by the solid lines. The arrows in the ϕ=13° spectrum indicate the sitting binding energies where the momentum distributions are measured (see figures 10.6-10.10).

particle-hole Tamm-Dancoff approximation (2ph-TDA) have been reported in the previous work of Cambi *et al*. [CC&82]. In figure 10.4 and table 10.1, the calculated pole-strengths [CC&82] associated with the ionization of each of the characteristic orbitals are shown. Gaussian convolutions using the corresponding widths (see table 10.1), with areas normalized to the corresponding pole-strengths, are performed to give the global energy profile shown in figure 10.4. Generally good agreement in the energy positions between the experimental binary (e,2e) spectra (figure 10.2) and the theoretical spectrum (figure 10.4) can be found in the outer valence region (<30eV). In the inner valence region, however, there is a global shift of the theoretical band to high energy by approximately 3.5eV. Such an energy discrepancy in the inner valence region in the Green's function derived spectrum is not uncommon [DC&79]. This is usually attributed to the inherent limitations of the 2ph-TDA (which includes only single excitation processes) and also to the quality of the basis set employed. In order to provide a more direct comparison with the present experiment, integrated intensities (over momentum) of the experimental MDs at selected sitting binding energies are compared with the Gaussian convoluted envelope (figure 10.4). These points (solid squares in figure 10.4) are obtained by numerical area integration of the respective MDs in the momentum range 0-$2.5a_0^{-1}$ and are point normalized (relative to each other) to

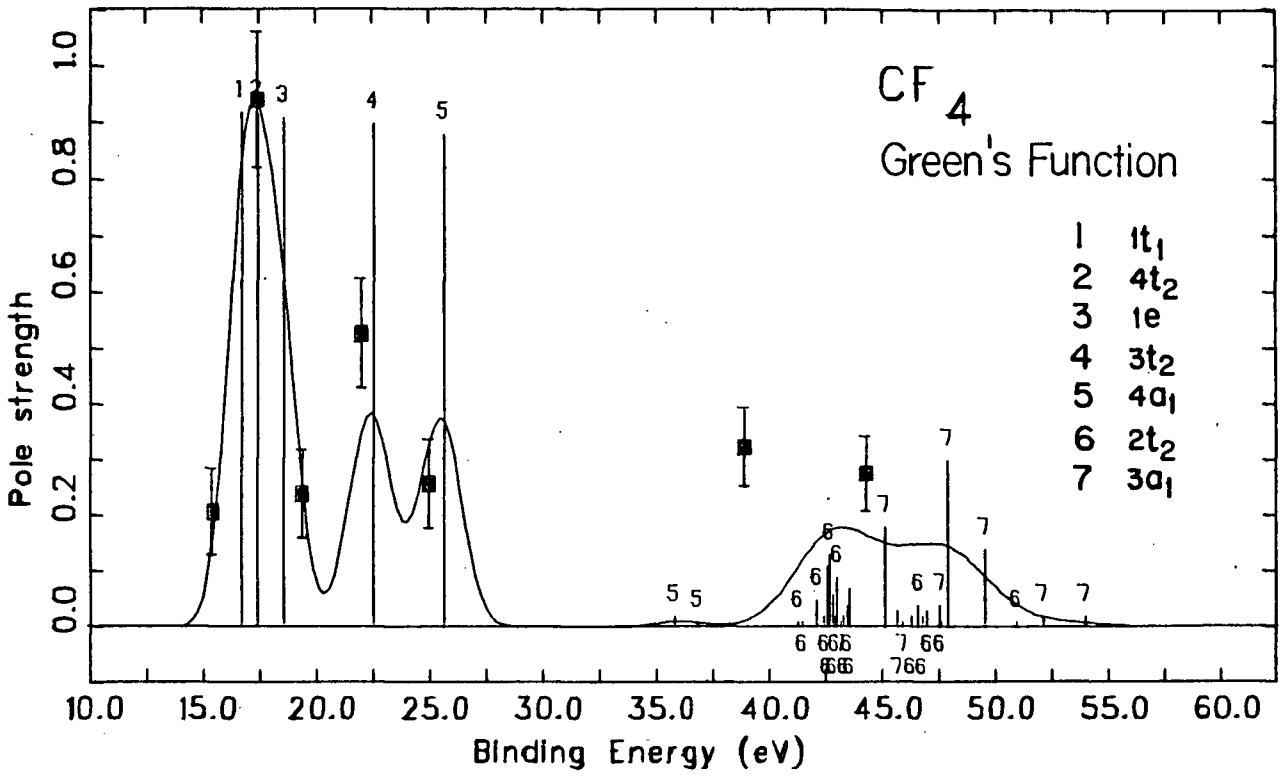

Figure 10.4 - Theoretical valence-shell binding energy spectra for CF_4 calculated using the many-body 2ph-TDA Green s function method. Gaussian convolution of the computed poles [CC&82] using the experimental widths (see table 10.1) is indicated by the solid lines.

Table 10.1
Experimental and theoretical binding energies and pole-strengths for CF_4.

Characteristic Orbital	Binding Energies (eV)		
	Experimental*	Theoretical**	
		SB	2ph-TDA
$1t_1$	16.1 (1.8)	19.38	16.74 [0.92]
$4t_2$	17.4 (1.8)	19.64	17.45 [0.92]
1e	18.5 (1.8)	21.33	18.59 [0.91]
$3t_2$	22.2 (2.2)	24.88	22.54 [0.90]
$4a_1$	25.1 (2.2)	28.14	25.68 [0.88] 35.83 [0.02] 36.89 [0.01]
$2t_2$	40.3 (3.7)	46.62	41.33 [0.01] 41.55 [0.01] 42.16 [0.05] 42.51 [0.02] 42.65 [0.11] 42.73 [0.13] 42.90 [0.06] 42.99 [0.02] 43.06 [0.09] 43.37 [0.02] 43.55 [0.04] 43.61 [0.07] 46.35 [0.02] 46.66 [0.04] 46.85 [0.02] 47.07 [0.03] 47.64 [0.01] 51.00 [0.01]
$3a_1$	43.8 (3.7)	50.46	43.23 [0.01] 45.19 [0.18] 45.71 [0.03] 45.97 [0.01] 47.62 [0.04] 47.94 [0.30] 49.58 [0.14] 52.15 [0.02] 54.00 [0.02] 62.61 [0.01]

* The widths used for the gaussian convolutions are given in round brackets. These widths include the instrumental resolution as well as the Franck-Condon width.

** SB denotes the double-zeta quality SCF wavefunction of Snyder and Basch [SB72]. 2ph-TDA denotes the Green's function calculation in the 2 particle-hole Tamm-Dancoff Approximation by Cambi et al. [CC&82]. The pole-strengths are given in square brackets.

the Gaussian envelope at 17.4eV. It is evident that there is generally excellent agreement in the outer valence region. However, the experimental points in the inner valence region at 38.9eV and 44.3eV are generally higher than the corresponding fitted envelope even after shifting the envelope down by 3.5eV (see earlier comment). The relative intensity distribution of the two points is however in good agreement with the calculations. The reported theoretical Green's function calculation by Cambi *et al*. [CC&82] clearly predicts population splitting among the hole states in the inner valence region, generating broad band structure of the type observed (see figures 10.2 and 10.3).

It is of interest to note from table 10.1 that although significant population splitting is present in the inner valence states (i.e. $(2t_2)^{-1}$ and $(3a_1)^{-1}$), there is little intermixing between these two states and therefore it should be possible to measure the separate MDs of the two contributing orbitals. This situation is similar to that in OCS [CW&81] (chapter 9) but in marked contrast to that in CO_2 [DC&79]. Such a difference in behavior is probably due to the symmetries of the orbitals involved. It is also noteworthy that the orbital energies of the double-zeta quality SCF wavefunction of Snyder and Basch [SB72] can be corrected empirically to approximate the experimental binding energies by a multiplicative factor of 0.88. This is similar to the earlier correction factor of 0.92 for fluoro-

substituted methanes suggested by Brundle *et al.* [BRB70].

10.3 ORBITAL MOMENTUM DENSITIES

The experimental and theoretical spherically averaged momentum distributions as well as the theoretical density contour and surface plots in both momentum-space (p-space) and position-space (r-space) have been determined for each of the valence orbitals of CF_4 (see figures 10.6-10.12). The MO diagram shown in figure 10.1 indicates the major overlapping atomic orbitals in each MO. Theoretical momentum distributions (MDs) have been evaluated using both the Snyder and Basch [SB72] and the GAUSS76 431G* [HL&80] wavefunctions. Both wavefunctions employ Gaussian-type basis sets of essentially double-zeta quality. The GAUSS76 431G* wavefunction [HL&80] has additional polarization functions. The density maps and surface plots have been evaluated using the Snyder and Basch wavefunction [SB72]. The experimental MDs are sampled at sitting binding energies (indicated in brackets on each figure) judiciously chosen so as to minimize contributions from neighbouring states. Consequently all the measured MDs are effectively due to individual characteristic orbitals except for the MD at 17.4eV (see figure 10.7 and

discussion below).[2] The theoretical MDs have been height normalized to the experimental MDs at their respective maxima except for the pseudo s-type $3a_1$ orbital where area normalization in the p range $0\text{-}1.5a_0^{-1}$ is used.

The density topographical convention used in the present study is the same as that in chapter 5 (section 5.4.1). Briefly, the nuclear geometry of the molecule is referenced with respect to a set of cartesian coordinates. In the present case, the C atom is located at the origin and the F-F direction in one of the F-C-F planes of the molecule is oriented parallel to the diagonal of the xy plane (i.e. along the (1,1,0) vector). The two orthogonal directions of the contour plane are then defined by two vectors, which are the (1,1,0) and (0,0,1) vectors in the present case as shown in figure 10.5. It should be noted that in figures 10.6-10.12 the carbon atom is at the origin of the coordinate system in *position-space*. The vectors: (1,1,0) and (0,0,1) refer only to the directions of the contour plane (and the surface plots) and their intersection as shown is not the actual origin in either p-space or r-space. The centres of the

---

[2] It has been shown theoretically [CC&82] that there is little mixing between the two inner hole states (section 10.2). It is therefore reasonable to assume that the two bands in the inner valence region are due primarily to the ionization of the $2t_2$ and $3a_1$ orbitals respectively (figure 10.2). The splitting in population would only broaden the width of each of the respective bands. The sitting binding energies are chosen to minimize any band overlap in the inner valence region.

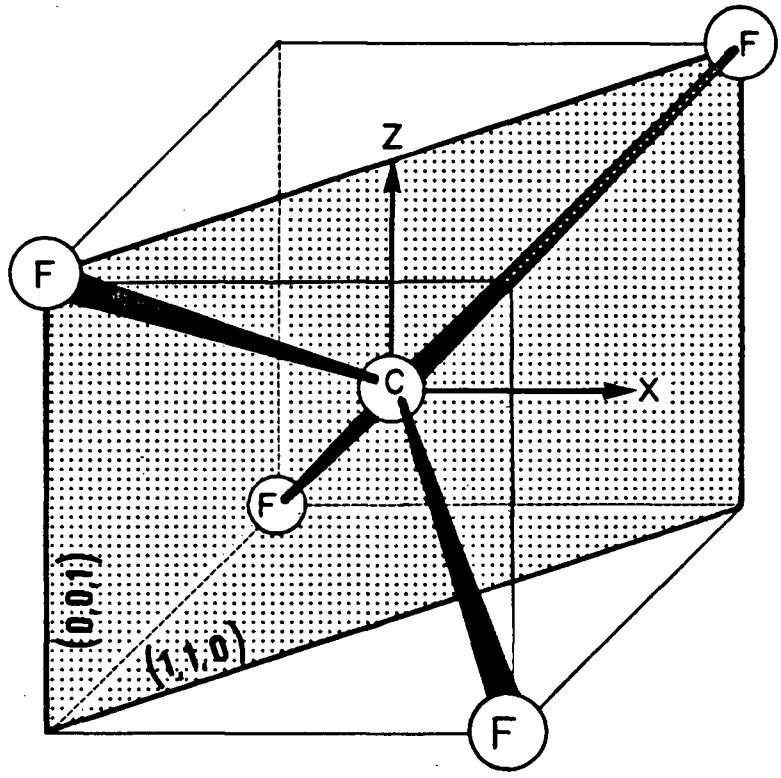

Figure 10.5 - Molecular geometry of CF_4 and the definition of the contour plane.

density maps correspond to the respective origins which are located at the centres of gravity of the surface plots shown in the lower portions of each figure. The contour values span logarithmically over 3 decades and correspond to 80, 60, 40, 20, 8, 6, 4, 2, 0.8, 0.6, 0.4 and 0.2% of the respective maximum density values of the orbitals. Line projection plots are used to show changes in the relative magnitudes of the density function along the lines of projections (dashed lines in the contour maps). Moreover, constant density surface plots are included to show the global 3-dimensional structures of the orbital densities in both p-space and r-space. The density values of the surfaces correspond (from left to right in the plots) to 20, 2 and 0.2% of the maximum density values. The open areas evident in many of the 0.2% surfaces are simply due to "cut-off" resulting from the limits selected for the 3D visualization. It should be noted that the contour map corresponds to the mid-plane perpendicular to the (1,-1,0) direction (i.e. the F-C-F plane itself) of the associated density surfaces. The intersection of the three axes again does not correspond to the true origin. Details of the hidden line removal 3-dimensional computer graphic package are described in ref. [W74]. The position and momentum coordinates as well as the density in both position and momentum-space are in atomic units.

10.3.1 Spherically Averaged Momentum Densities

It is, in general, difficult to compare the spherically averaged momentum densities or momentum distributions (MDs) reported by Cambi *et al*. [CC&82] with those in the present work. This is because some of the reported MDs were sampled at energies where contributions from more than one state are important given the limited energy resolution (2.6eV FWHM) used [CC&82]. For instance separate MDs due to each of the individual outermost orbitals ($1t_1$, $4t_2$ and 1e) were not obtained by Cambi *et al*. [CC&82]. The present work gives more detailed information on most of the separate MDs since the present instrumental energy resolution (1.6eV FWHM) permits measurements to be made at energies where overlaps from other states are minimal (see figure 10.3). In cases where contributions from other orbitals can be ignored in the previous work [CC&82], there is good agreement with the present work. In particular, the MDs at 27.0eV and 45.0eV in the previous work [CC&82] are in good agreement with the respective MDs obtained at 25.0eV (figure 10.10) and 44.3eV (figure 10.12) in the present work. There is, however, some confusion concerning the earlier reported MD obtained at 20.0eV by Cambi *et al*. [CC&82]. Given the reported sitting binding energy (i.e. 20.0eV) and the employed energy resolution (2.6eV FWHM) of the previous work [CC&82], the MD obtained at 20.0eV should have almost equal contributions from both the 1e (I.P. = 18.5eV) and $3t_2$ (I.P. = 22.1eV)

orbitals. The MD of the 1e orbital reported in the present work (figure 10.8) indicates the presence of an appreciable symmetric component (i.e. non-zero intensity at p=0). This would also give rise to finite intensity at p=0 for the MD composed of an almost equal mixture of 1e and $3t_2$ orbitals whereas the earlier reported MD at 20.0eV [CC&82] shows little intensity at p=0. In fact, the reported MD is in better agreement with the MD corresponding to the $3t_2$ orbital alone obtained in the present work (figure 10.9). The MDs of the valence orbitals of CF_4 obtained in the present work are discussed below.

(i) The outermost valence orbitals: $1t_1$, $4t_2$ and 1e.

The MDs of the $1t_1$, $4t_2$ and 1e orbitals are shown in figures 10.6, 10.7 and 10.8 respectively. It should be noted that only the MD measured at 17.4eV (figure 10.7) of necessity contains contributions from all three orbitals, with that from the $4t_2$ orbital being the most dominant (see figures 10.2 and 10.3). The theoretical MD (figure 10.7) corresponds to the sum of calculated MDs of the three contributing orbitals, appropriately weighted according to the Gaussian deconvolution shown for the binding energy spectrum at ϕ=8° (figures 10.2 and 10.3). The summed theoretical curves are normalized to the experimental MD at $p=0.74a_0^{-1}$, corresponding to ϕ=8°. The absence of density at the carbon centre of both the $1t_1$ and 1e orbitals, as shown

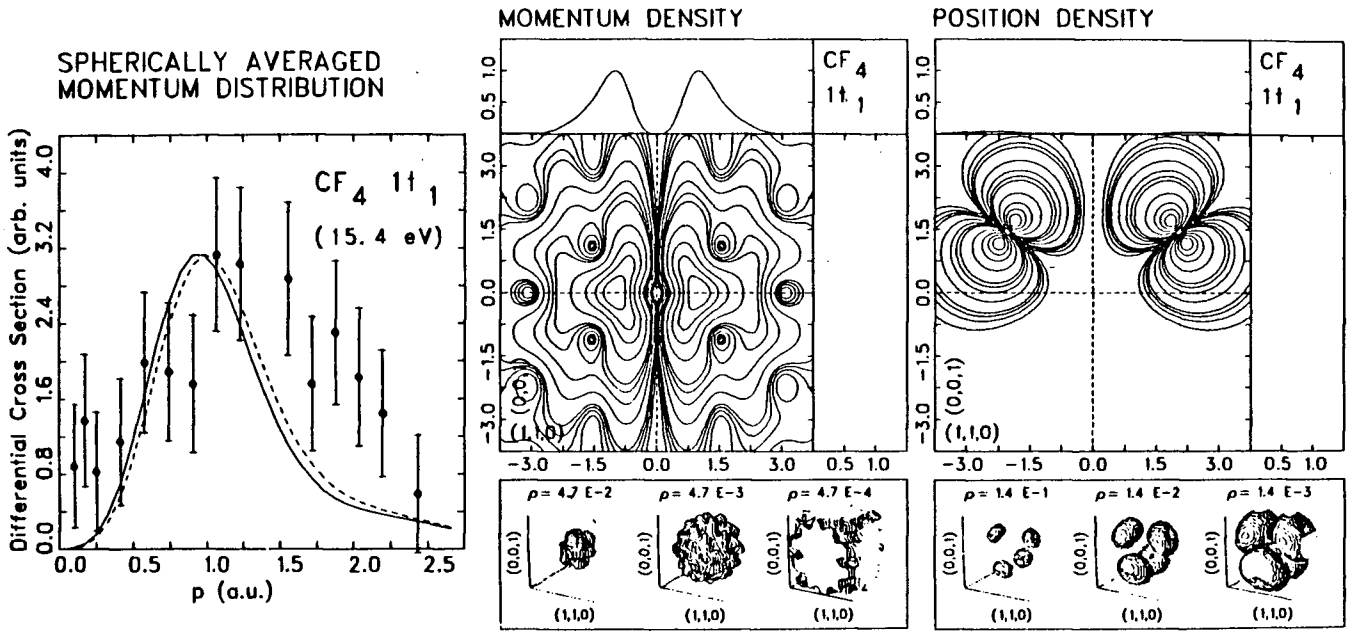

Figure 10.6 - Molecular momentum distributions (left) and density visualization in momentum (centre) and position (right) space for the CF_4 $1t_1$ orbital. Theoretical momentum distributions are evaluated using the Snyder and Basch wavefunction [SB72] (solid line) and the GAUSS76 431G wavefunction [HL&80] (dashed line).

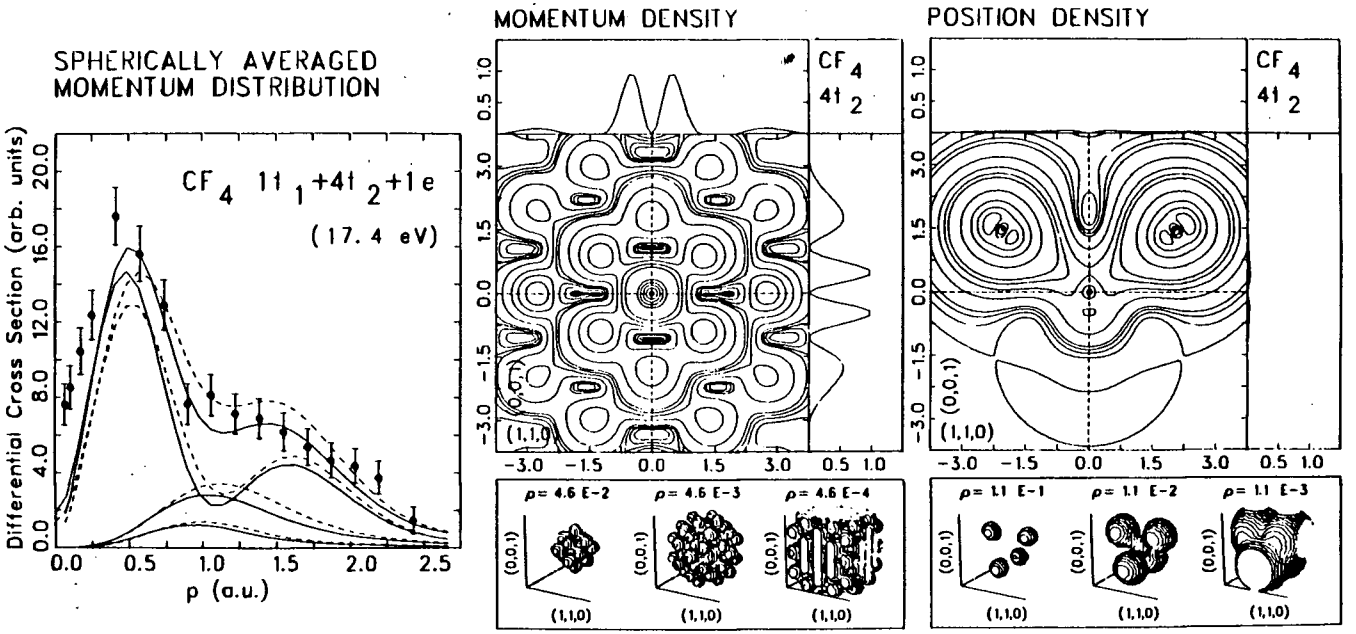

Figure 10.7 - Momentum distribution measured at 17.4eV (left) and density visualization in momentum (centre) and position (right) space for the CF_4 $4t_2$ orbital. Individual theoretical momentum distributions of the three contributing orbitals ($1t_1$, $4t_2$ and $1e$) are evaluated using the Snyder and Basch wavefunction [SB72] (solid lines) and the GAUSS76 431G wavefunction [HL&80] (dashed lines).

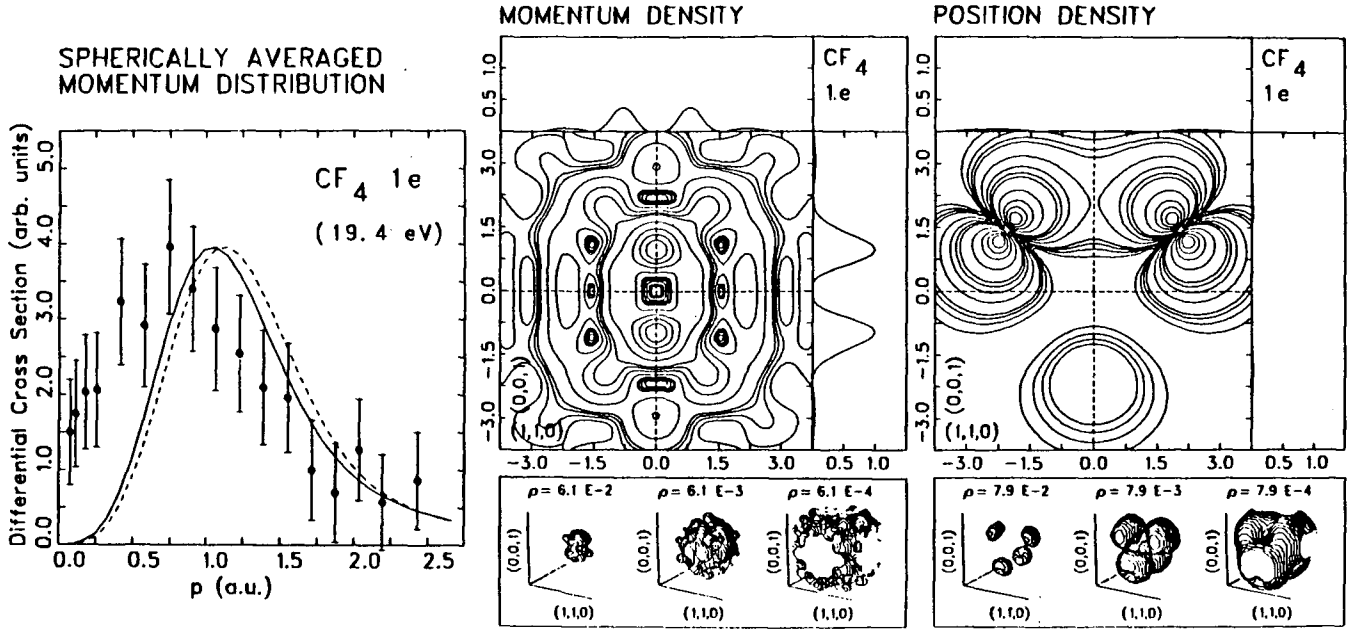

Figure 10.8 - Molecular momentum distributions (left) and density visualization in momentum (centre) and position (right) space for the CF_4 1e orbital. Theoretical momentum distributions are evaluated using the Snyder and Basch wavefunction [SB72] (solid line) and the GAUSS76 431G wavefunction [HL&80] (dashed line).

by the r-space density contour maps and surface plots (figures 10.6 and 10.8 respectively) clearly illustrates the nonbonding nature of these orbitals. The major atomic components of the $1t_1$, $4t_2$ and 1e orbitals are due to fluorine 2p orbitals.

In general, there is poor agreement between the experimental MDs for the $1t_1$ and 1e orbitals (figures 10.6 and 10.8) and their corresponding theoretical MDs computed using the two SCF double-zeta quality wavefunctions [SB72, HL&80]. Such a discrepancy in the MDs of the nonbonding orbitals between experiment and theory is not uncommon. In the SCF variational procedure, these outermost orbitals contribute the least to the total energy and are likely to be less well modelled by the method. In particular, the experimental MD of the outermost orbital ($1t_1$) is significantly broader and has its maximum at higher p ($p_{max} \simeq 1.2 a_0^{-1}$) than either of the theoretical MDs ($p_{max} \simeq 1.0 a_0^{-1}$). This orbital provides one of the broadest MDs, with the largest p_{max}, observed to date in binary (e,2e) experiments. The only other MD with comparable width and p_{max} is that of the Cd 4d atomic orbital reported by Frost *et al.* [FWM83]. Although the MD of the $4t_2$ orbital cannot be measured directly with the present energy resolution, it is possible to get a qualitative idea of its shape since Gaussian deconvolution of the ϕ=8° binding energy spectrum (figures 10.2 and 10.3) suggests that over 80% of the

intensity at 17.4eV comes from the $4t_2$ orbital. The theoretical r-space density map (figure 10.7) indicates that the $4t_2$ orbital is "weakly" antibonding and is composed of a small negative overlap between the C 2p and the F 2p atomic orbitals. The maximum at $p\simeq0.4a_0^{-1}$ and the well-defined shoulder at $p\simeq1.3a_0^{-1}$ of the MD at 17.4 eV (figure 10.7) indicate the presence of p-space molecular density oscillations (see later). The $4t_2$ orbital therefore provides the first experimental observation of density (bond) oscillations. Density oscillations are more easily observable experimentally in the case of CF_4 for two reasons. Firstly the large F-F separation results in the first density oscillation being within the normal (e,2e) experimental momentum range ($<2.5a_0^{-1}$). Shorter internuclear separations conversely cause the first oscillation to occur at a much larger momentum as for example in H_2 [LB83b] (chapter 5) or CO_2 [CB82a, LB84b] (chapter 7). Secondly the intensity of the spherically averaged momentum density in the region of the first oscillation is large because of the well defined high (cubic) symmetry of the CF_4 $4t_2$ orbital in momentum-space (figure 10.7). It should be noted that there is excellent agreement between the experimental MD at 17.4eV and the theoretical MDs particularly in the $p>0.5a_0^{-1}$ region. The non-zero intensity near p=0 in the experimental MD

indicates the presence of a symmetric component due to C 2s.[3] Part of the intensity at p=0 of the MD measured at 17.4eV may also come from the MD of the 1e orbital (figure 10.8), which also has a strong symmetric component. The theoretical MDs of the 1e orbital (figure 10.8) are shifted towards high momentum, in contrast to the opposite shift in the theoretical MDs of the $1t_1$ orbital (figure 10.6), each with respect to the corresponding experimental MDs. The 1e orbital may have overlap between C 2s and F 2p, in contrast to the totally nonbonding nature shown by the theoretical r-space density map (figure 10.8).

It is also of interest to note that the good agreement found between the experimental MD at 17.4eV and its summed theoretical MDs removes any ambiguity associated with the energy ordering of the $1t_1$, $4t_2$ and 1e orbitals. Previous CNDO/2 calculation [D68] and XPS studies [S&69] gave the wrong order in the orbital energies of the $1t_1$ and $4t_2$ orbitals of CF_4. The correct ordering is as shown in figure 10.1.

(ii) The bonding $3t_2$ and antibonding $4a_1$ orbitals.

Figures 10.9 and 10.10 show the MDs of the outer valence $3t_2$ and $4a_1$ orbitals respectively. In contrast to the poor

---

[3] Due to the T_d symmetry of the molecule, only C 2s can give rise to a symmetric component (i.e. non-zero intensity at p=0) in the MD.

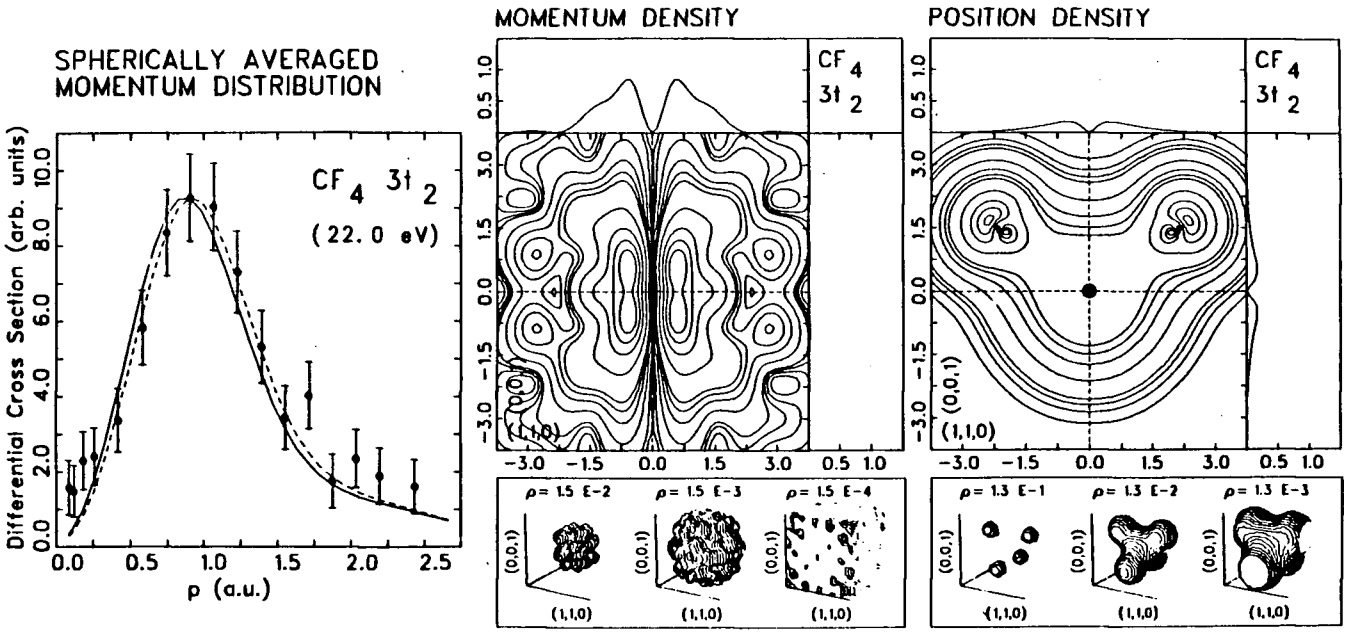

Figure 10.9 - Molecular momentum distributions (left) and density visualization in momentum (centre) and position (right) space for the CF_4 $3t_2$ orbital. Theoretical momentum distributions are evaluated using the Snyder and Basch wavefunction [SB72] (solid line) and the GAUSS76 431G wavefunction [HL&80] (dashed line).

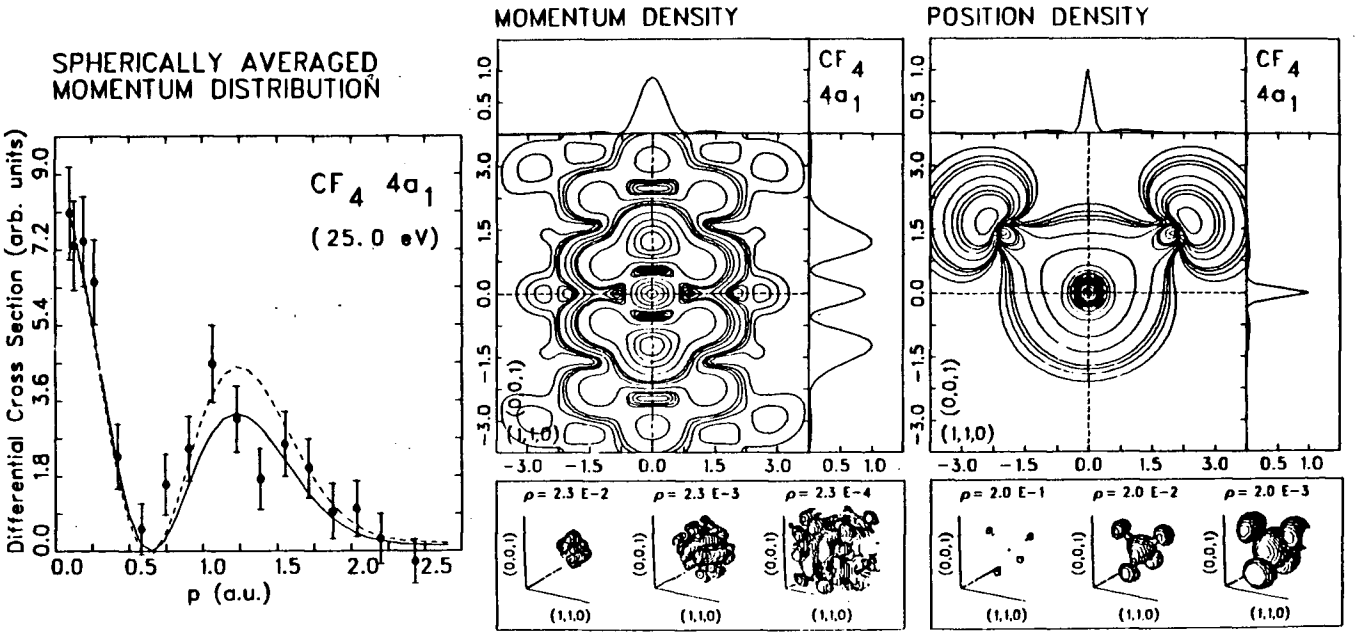

Figure 10.10 - Molecular momentum distributions (left) and density visualization in momentum (centre) and position (right) space for the CF_4 $4a_1$ orbital. Theoretical momentum distributions are evaluated using the Snyder and Basch wavefunction [SB72] (solid line) and the GAUSS76 431G wavefunction [HL&80] (dashed line).

agreement between the experimental and calculated MDs found in the case of the three outermost orbitals, excellent agreement is observed for both the $3t_2$ and $4a_1$ orbitals. The $3t_2$ orbital is made up essentially of strong positive overlap between C 2p and F 2p atomic orbitals. There is a slow fall-off in the MD of the $3t_2$ orbital in the $p>1.5a_0^{-1}$ region. Comparison of the r-space density map of the $4t_2$ orbital (figure 10.7) with that of the $3t_2$ orbital (figure 10.9) shows the "rapid" variations of the r-space density in the region between the F atoms in the former ($4t_2$ —— antibonding character) and the "smooth" variations of density in the F-F internuclear region in the latter ($3t_2$ —— bonding character). This difference in bonding nature causes more well defined r-space density lobes in an antibonding orbital (figure 10.7) than in a bonding orbital (figure 10.9). Secondary density oscillations are therefore more severe in the antibonding orbital than those in the bonding orbital, as shown by the respective p-space density maps (figures 10.7 and 10.9).

Unlike the $3t_2$ orbital, the $4a_1$ orbital is essentially composed of negative overlaps (i.e. antibonding) between C 2s and F 2p atomic orbitals. The near-zero minimum observed at $p\simeq0.6a_0^{-1}$ in the experimental MD (figure 10.10) clearly reflects the antisymmetric overlap between the C 2s and F 2p atomic orbitals, which together with the high symmetry of the molecule results in the formation of a near-spherical "nodal"

surface in p-space. A similar nodal surface also occurs in the r-space density map at $\simeq 0.4a_0$ (figure 10.10). It should be noted that the MD of the $4a_1$ orbital represents the most clear-cut example observed to date of a composite s-p type MD. This effect can also be seen in the results of Cambi *et al*. [CC&82]. Other experimental MDs of s-p composite nature include the MDs of all the outermost a_1 orbitals of the CH_3X (where X = Cl [MG&82], Br, I [MC&84], OH [MBW81] and CN [MB&83]) series as well as the outermost antibonding σ orbitals of CO_2 [LB84b] (chapter 7), CS_2 [LB84c] (chapter 8) and OCS [LB84d] (chapter 9). All of these MDs have much less well defined minima than that observed for the $4a_1$ orbital in CF_4.

(iii) The inner valence orbitals: $2t_2$ and $3a_1$.

Figures 10.11 and 10.12 show the MDs of the $2t_2$ and $3a_1$ orbitals respectively. The r-space density plots of the $2t_2$ orbital indicates antibonding overlaps between C 2p and F 2s atomic orbitals. It is important to note that the tetrahedrally arranged F 2s orbitals can only give rise to a pseudo p-type MD. (See earlier footnote). The presence of C 2s in the $3a_1$ orbital, on the other hand, gives rise to pseudo s-type MD. The $3a_1$ orbital can be considered as composed of bonding overlaps between C 2s and F 2s atomic orbitals. The theoretical MDs of the $2t_2$ orbital are shifted towards high p with respect to the experimental MD.

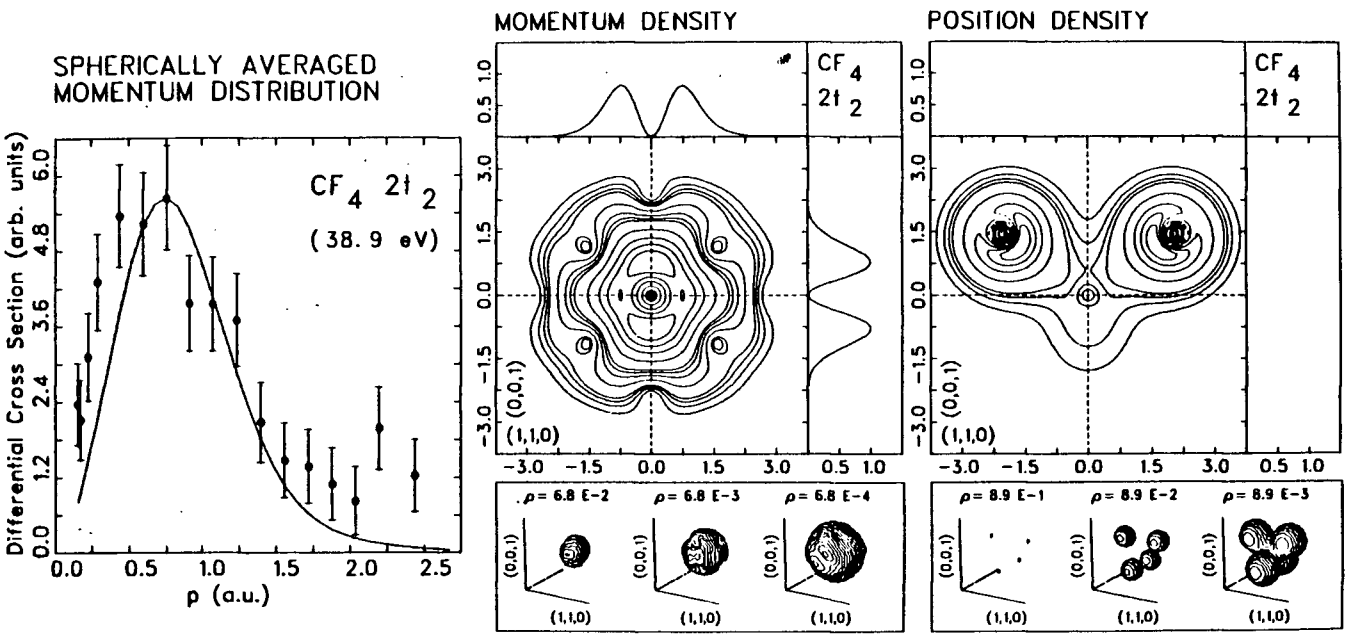

Figure 10.11 - Molecular momentum distributions (left) and density visualization in momentum (centre) and position (right) space for the CF_4 $2t_2$ orbital. Theoretical momentum distributions are evaluated using the Snyder and Basch wavefunction [SB72] (solid line) and the GAUSS76 431G wavefunction [HL&80] (dashed line).

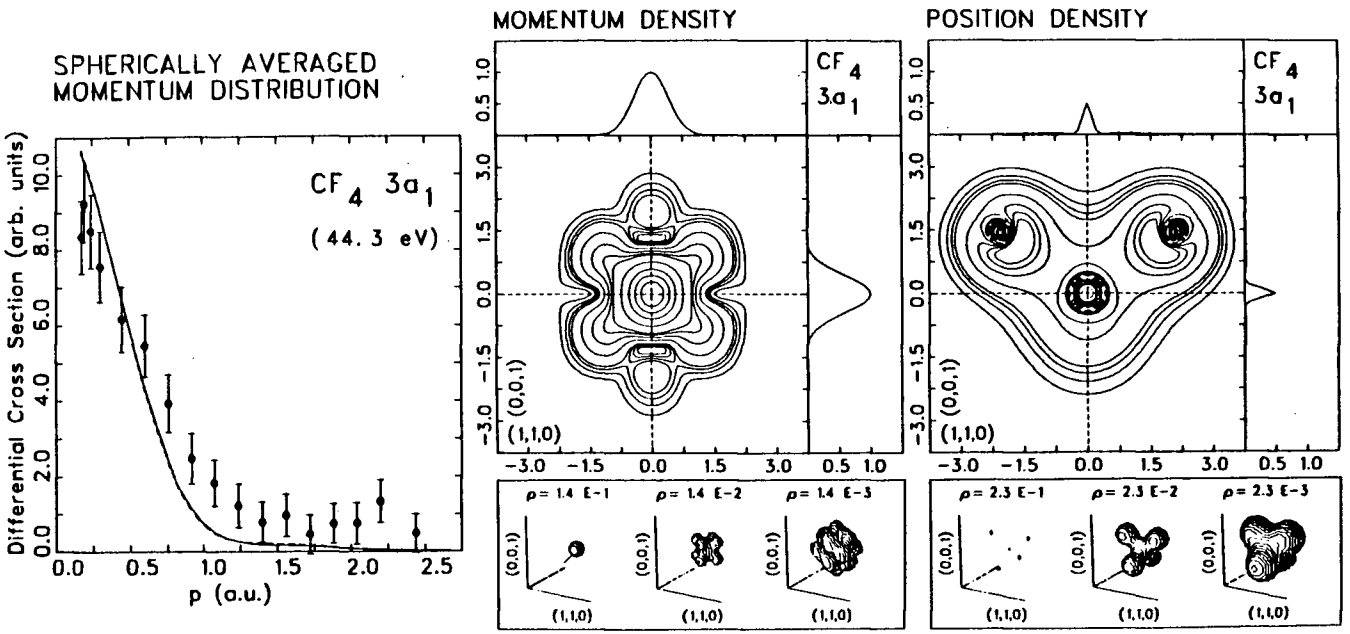

Figure 10.12 - Molecular momentum distributions (left) and density visualization in momentum (centre) and position (right) space for the CF_4 $3a_1$ orbital. Theoretical momentum distributions are evaluated using the Snyder and Basch wavefunction [SB72] (solid line) and the GAUSS76 431G wavefunction [HL&80] (dashed line).

Discrepancy between experiment and theory is also observed in the MD of the $3a_1$ orbital, where the theoretical MDs are sharper (i.e. with smaller half-width) than the experimental one. The small mixing between the $2t_2$ and $3a_1$ poles predicted in the Green's function calculation will certainly be responsible for part of the observed discrepancies. The major contributing factor, however, lies in the quality of the employed SCF wavefunctions.

It is of interest to note that there are only small differences between the MDs generated by the two wavefunctions [SB72, HL&80] for the outer valence orbitals (figures 10.6-10.10), i.e. where atomic p components are involved. In particular, the use of the additional polarization functions in the GAUSS76 431G* wavefunction [HL&80] appears to shift the MD towards a slightly higher momentum. The half-widths of the theoretical MDs calculated by the two wavefunctions are very similar. In the case of the inner valence orbitals (figures 10.11 and 10.12), which are mainly composed of atomic s orbitals, MDs generated by the two wavefunctions are in fact almost indistinguishable from each other.

10.3.2 Directional Momentum-Space Density Topography In Two- And Three-Dimensions

Before discussing some of the more novel features of the theoretical momentum-space orbital densities of a nonlinear molecule, it is important to realize that the momentum-space wavefunction at any point in p-space involves integration of sums of powers of the gradient of the r-space wavefunction over the whole r-space (the Fourier transform —— see chapter 2). Therefore any contour cut of the p-space density cannot in general be related to the corresponding cut in the r-space density. However, since it is reasonable to anticipate that some of the more abrupt variations in the r-space density function occur along the C-F bond, density topographical changes in the F-C-F plane in r-space may therefore represent the more important features contributing to the changes observed in the p-space density in the same plane. The (3-dimensional) constant density surface plots at the three selected density values are therefore intended to supplement the contour maps by providing more comprehensive views of the density functions. It should be noted that since symmetry orbitals (i.e. sums of degenerate orbitals of the same

orbital symmetry)[4] are used to generate the corresponding density functions, it is therefore not surprising to see that the r-space density surfaces of individual symmetry orbitals have the same point group symmetry as that of the molecule (T_d). Several interesting features of the p-space density plots will now be discussed.

In contrast to the "local" nuclear oriented variation in the r-space density contour maps (of the F-C-F plane), the corresponding p-space density contour maps reveal complex oscillatory structures spanning over the whole plane. This density oscillation behaviour in p-space is most vividly shown in the density contour maps of the antibonding $4t_2$ (figure 10.7) and $4a_1$ orbitals (figure 10.10). Moreover, as is perhaps best illustrated by the p-space contour maps of the (strongly bonding) $3t_2$ orbital (figure 10.9), the longitudinal direction of p-space density lobes is oriented in a p-space direction essentially perpendicular to that in the r-space counterpart.

The symmetry properties of the wavefunction are invariant under the Fourier transform. It follows that the

---

[4] It should be noted that the degenerate orbitals (e.g. the three components of the $1t_1$ orbital in CF_4 or the five components of atomic d orbitals) contributing to a symmetry orbital may have different individual momentum profiles even though they have identical orbital energies. In this connection, it is also of importance to note that in binary (e,2e) spectroscopy it is the MDs of *symmetry orbitals* which are measured since orbital selection is obtained by choosing appropriate (binding) energies.

p-space symmetry orbital density should have T_d symmetry. This, together with the automatic inversion centre at the p-space origin, results in cubic symmetry in p-space, as is evident from the surface plots (figures 10.6-10.12) and the enlarged examples in figure 10.13 below. The inversion symmetry, coupled with the immense oscillatory secondary lobal structures, results in a complex surface as can be seen from the 3D visualizations (figures 10.6-10.12). Examples of the symmetry invariance and the resultant cubic symmetry in momentum space arising from the inversion centre are more clearly shown in the 20% momentum density surface plots of the $4t_2$ and $3a_1$ orbitals in figure 10.13. It is also evident that some of the nodal structures are retained in p-space. For instance, the r-space density surface plots of the $1t_1$ orbital (figure 10.6) have "(curved) nodal surfaces" originating from the r-space origin and separating the F atoms. In p-space, these are manifested as "nodal lines", which are clearly shown in the p-space density contour map (figure 10.6). The nodal point at the origin is also preserved in both r-space and p-space as shown in the respective density maps of the 1e orbital (figure 10.8).

The (pseudo) s-type and (pseudo) p-type designation of the momentum distributions is governed by the presence or absence of density at the p-space origin. In the case of the valence orbitals of CF_4, pseudo s-type structure can only be due to the presence of the C 2s atomic orbital. This is

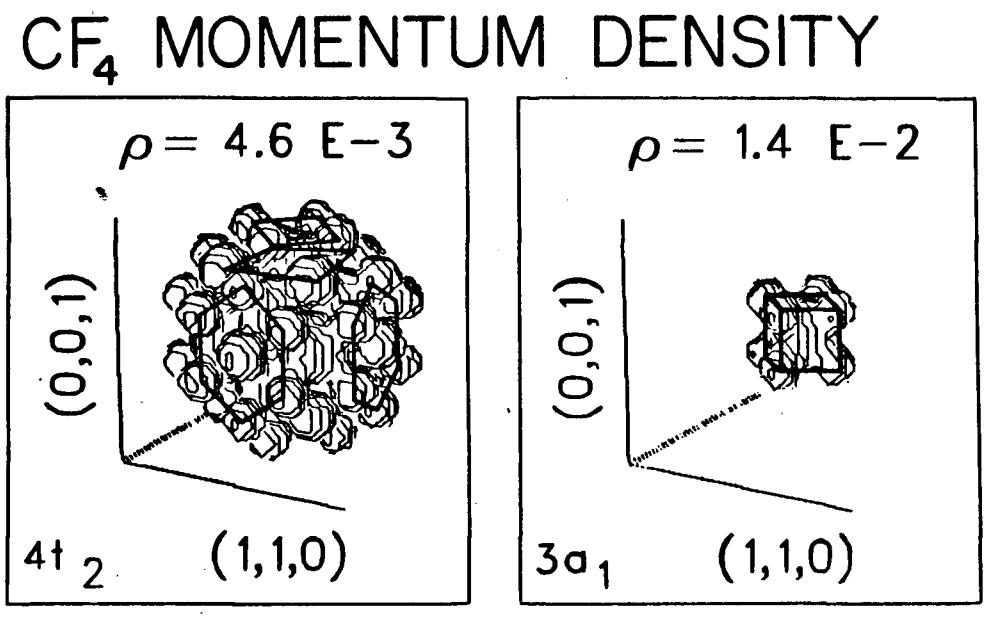

Figure 10.13 - Three-dimensional 2% density surface plots of the $4t_2$ (left) and $3a_1$ (right) orbitals in momentum-space. The densities are generated using the Snyder and Basch wavefunction [SB72]. Guide-lines have been drawn to emphasize the "cubic" symmetry of the molecular orbitals in momentum space.

clearly illustrated by the p-space density contour maps and the associated projection plots of the $4a_1$ (figure 10.10) and $3a_1$ (figure 10.12) orbitals. All the other pseudo p-type orbitals do not have major contributions from C 2s. The p-space densities of the inner valence orbitals (i.e. $2t_2$ in figure 10.11 and $3a_1$ in figure 10.12) are generally more spherical with less oscillatory structure and exhibit a faster fall-off in p-space than those of the outer valence orbitals (figures 10.6-10.10). As shown by the r-space surface plots, the inner valence orbitals are essentially made up of "nonbonding" atomic s orbitals, which are considerably more localized on the atomic centres. The outer valence orbitals, on the other hand, are made up essentially of the more spatially extended atomic p orbitals (see figure 10.1). Overlaps of these extended functions cause more abrupt changes in the r-space density, which are responsible for the p-space density in the high momentum region. An excellent example is the antibonding $4a_1$ orbital, which has rapid fluctuations in r-space density between F centres (see figure 10.10) so that the corresponding p-space density has a more extended high momentum part.

Chapter XI

CONCLUDING REMARKS

This thesis reports new and definitive measurements of binding energy spectra and momentum distributions of the valence orbitals of a number of atoms and molecules obtained using a high momentum resolution binary (e,2e) spectrometer. Details of the construction and operation of the spectrometer are reported (chapter 3). The high momentum resolution of the spectrometer is achieved by incorporating a new pair of three-element asymmetric immersion lenses, capable of high angular selection, in the secondary electron optical systems for momentum analysis of the outgoing electrons after the (e,2e) collisions. Computer control of the spectrometer has extended the viability and accuracy of the real-time data acquisition process. The high impact energy presently employed has helped to ensure the validity of the (e,2e) reaction model as well as to upgrade the signal-to-noise performance of the spectrometer. All these modifications of the original design [HHB77] have significantly improved the angular resolution and the overall performance of the spectrometer (chapter 3) as well as the obtainable data quality.

The spectroscopic results of the atoms and molecules reported in this thesis have further demonstrated the

usefulness of binary (e,2e) spectroscopy. In particular, electron correlation effects have been found to be extremely important and quite common in the inner valence region of atoms (for instance, the noble gases —— chapter 4) and molecules (CO_2, CS_2 and OCS —— chapters 7-9 respectively). The understanding and characterization of the observed many-body states can be substantiated by the corresponding momentum distributions. Moreover, momentum distributions measured at carefully selected energies are related to the spherically averaged momentum densities of individual (valence) orbitals. With the presently available momentum resolution, these experimental momentum distributions are instrumental in assessing the quality of *ab-initio* SCF LCAO-MO wavefunctions. As demonstrated in the studies reported in this thesis, double-zeta quality wavefunctions have been found to provide reasonably good agreement in the molecular momentum distributions of most outer valence orbitals except the lone pair (nonbonding) orbitals (see chapters 7-10). Similarly the excellent agreement in the atomic momentum distributions of the noble gases (chapter 4) between experiment and the Hartree-Fock theory has confirmed the accuracy of Hartree-Fock wavefunctions in the case of closed-shell atoms. Attempts have been made where possible in this thesis to compare momentum distributions of similar orbitals of valence isoelectronic species (for instance, in the case of the noble gas group —— chapter 4, and of the linear

triatomic group: CO_2, CS_2 and OCS —— chapter 9). Such comparative or correlation studies have proven to be useful in understanding the nature of the involved orbitals. For instance the relative extents of the s-p compositions in the outermost bonding σ orbitals of CO_2 and OCS can be understood in terms of the amounts of C-O bonding overlap involved. Another notable example is that the trend observed in the shape of experimental momentum distributions of the np orbitals of the noble gases (chapter 4) can be related to the trend of the spatial extent of these orbitals in position-space (the inverse spatial reversal property).

The utility of experimental momentum distributions can be further extended in the special case of molecular hydrogen to provide the first experimental estimation of the spherically averaged bond density in the molecule (chapter 6). The nature of the covalent bond in molecular hydrogen is shown to be quite different in momentum-space and in position-space. The dynamics of the bond formation in momentum-space is also investigated phenomenologically using density difference maps calculated by theoretical wavefunctions at different internuclear separations (chapters 5 and 6).

This thesis has also attempted to provide an exploration of momentum-space Fourier transform and Virial properties (originally discussed by Coulson and Duncanson [CD41]) using significantly improved 2-dimensional and 3-dimensional

computer graphic visualization techniques to exhibit the many interesting features in the orbital densities in momentum-space and position-space. This density topographical approach is also helpful in interpreting the many features observed in the experimental spherically averaged momentum distributions. An example of the usefulness of such an approach is in the case of the CF_4 $4t_2$ orbital (chapter 10). The observed secondary peak in the experimental momentum distribution is found to be the first experimental evidence of molecular momentum-space density oscillations (chapter 10) as illustrated by the density maps and surface plots. Other momentum-space properties such as symmetry properties, inverse spatial reversal and molecular density directional reversal properties have also been amply discussed and examplified.

The end of the present work as reported in this thesis marks the fifteen anniversary of binary (e,2e) spectroscopy. It is perhaps not just a coincidence that the closing of the present work should signal a new phase in the development of the field in view of the recent advances in vacuum, computer and fast electronic technology. These technological developments should help to resolve two of the present experimental limitations, i.e. energy resolution and data collection efficiency, and should help to extend the binary (e,2e) method to the study of more corrosive, reactive and unstable species. The next generation of binary (e,2e)

spectrometers will undoubtedly be differentially pumped and have incorporated a multichannel angle-sensitive detection method [MJ&81] as well as more sophisticated electron optics which allow energy monochromation without great loss in transmission [Z82]. These improvements will eventually extend the binary (e,2e) method to the study of radical and transient species, of which many theoretical works are available in the literature. It will also open up the possibility of studying more readily corrosive and reactive species such as the halogens. Of perhaps more importance is that the improvements will allow one of the very first (e,2e) experiments for gases absorbed on thin films [AE&69] to be repeated with much better data quality. The application of (e,2e) on thin films [WD&82] and solids [FW82b] has the potential of providing the three-dimensional momentum density information. Recent developments in this direction [WD&82, FW82b] have already triggered new developments in reaction models which involve relativistic effects [FMS82] because of the high impact energy involved. The development of the relativistic (e,2e) reaction theory [FMS82] has also provided a basis and posted a challenge to the experimentalists to obtain the first orbital momentum distribution of a core orbital.

The bulk of the (e,2e) data in the literature (present work included) has called for improved theoretical modelling for the ionization process. The many-body Green's function

method and the symmetry adapted cluster expansion configuration interaction method have both shown promise in predicting, in qualitative agreement with experiment, features of the inner valence region in the binding energy spectrum. Refinements of such techniques should now be possible with the advances in computer technology. As numerous (e,2e) experiments have suggested the insensitivity of the variational method in correctly modelling the large r part of the valence orbitals of the overall wavefunction, a new challenge to theoretical quantum chemists is perhaps to devise a whole new approach in modelling the valence orbitals. There is also the question of the validity of the target Hartree-Fock approximation of which most of the (e,2e) data have been interpreted. A binary (e,2e) theory beyond the target Hartree-Fock approach with the consideration of relaxation and configurational interaction will be of interest. In this case, the simplistic orbital picture will no longer be applicable. In retrospect experimental (and theoretical) quantum chemistry using binary (e,2e) spectroscopy has just begun.

REFERENCES

Convention: Refenences are enclosed in squared brackets in the text. Each reference is labelled by a code of maximum five (or six) characters. Each code is composed of the first characters of the last names of the first two (or three) contributing authors and the year of the publication. In cases where identical codes occur, a sixth letter (in lower case) is used to differentiate the different publications. Individual items of a publication are listed in the following order:

Authors, Journal, Volume-Number (Year) Page-Number.

The year is in round brackets and is used to separate the volume-number and the page-number.

A70 L. Asbrink, Chem. Phys. Lett. 7 (1970) 549.

A71 S. Aksela, Rev. Sci. Instrum. 42 (1971) 810.

A72 S. Aksela, Rev. Sci. Instrum. 43 (1972) 1350.

A83 P.W. Atkins, "Molecular Quantum Mechanics", Oxford University Press, New York (1983).

AE&69 U. Amaldi, A. Egidi, R. Marconero and G. Pizzella, Rev. Sci. Instrum. 40 (1969) 1001.

AG&72 C.J. Allan, U. Gelius, D.A. Allison, G. Johansson, H. Siegbahn and K. Siegbahn, J. Electron Spectrosc. Relat. Phenom. 1 (1972) 131.

AR72a A. Adams and F.H. Read, J. Phys. E 5 (1972) 150.

AR72b A. Adams and F.H. Read, J. Phys. E 5 (1972) 156.

AW&78a M.Y. Adam, F. Wuilleumier, S. Krummacher, V. Schmidt and W. Mehlhorn, J. Phys. B 11 (1978) L413.

AW&78b M.Y. Adam, F. Wuilleumier, N. Sandner, V. Schmidt and G. Wendin, J. Physique 39 (1978) 129.

AY78 V.P. Afanas'ev and S. Ya. Yavor, Sov. Phys. Tech. Phys. 23 (1978) 622.

B51 T.J. Berlin, Chem. Phys. 19 (1951) 208.

B75 R.F.W. Bader, in "Theoretical Chemistry", Physical Chemistry Series Two, Int. Rev. Sci, A.D. Buckingham and C.A. Coulson (eds.), Butterworths, London (1975) p.79.

B79 J. Berkowitz, "Photoabsorption, Photoionization, and Photoelectron Spectroscopy", Academic, New York (1979).

B80 J.K. Burdett, "Molecular Shapes: Theoretical Models of Inorganic Stereochemistry", Wiley-Interscience, New York (1980).

B82 C.E. Brion, in "Physics of Electronic and Atomic Collisions", S. Datz (ed.), North-Holland, Amsterdam, (1982) p.579.

BC68 R.F.W. Bader and A.K. Chandra, Can. J. Chem. 46 (1968) 953.

BC&82 C.E. Brion, J.P.D. Cook, I.G. Fuss and E. Weigold, Chem. Phys. 64 (1982) 287.

BD&60 S. Bratoz, R. Daudel, M. Roux and M. Allavena, Rev. Mod. Phys. 32 (1960) 412.

BF74 R.A. Bonham and M. Fink, "High Energy Electron Scattering", van Nostrand Reinhold, New York (1974).

BF80 R.A. Bonham and M. Fink, in "Electron and Magnetization Densities in Molecules and Crystals", P. Becker (ed.), Plenum, New York (1980).

BH67 R.F.W. Bader and W.H. Henneker, J. Chem. Phys. 46 (1967) 3341.

BH81 C.E. Brion and A. Hammett, in "The Excited State in Chemical Physics, Part 2", J.W. McGowan (ed.), Adv. Chem. Phys. 45, Wiley, New York (1981) p.1.

BH&80 C.E. Brion, S.T. Hood, I.H. Suzuki, E. Weigold and G.R.J. Williams, J. Electron Spectrosc. Relat. Phenom. 21 (1980) 71.

BL&84 A.O. Bawagan, L. Lee, C.E. Brion and K.T. Leung, to be published.

BM&74 M.S. Banna, B.E. Mills, D.W. Davies ad D.A. Shirley, J. Chem. Phys. 61 (1974) 4780.

BM&82 C.E. Brion, I.E. McCarthy, I.H. Suzuki, E. Weigold, G.R.J. Williams, K.L. Bedford, A.B. Kunz and R. Weidman, J. Electron Spectrosc. Relat. Phenom. 27 (1982) 83.

BP69 R.F.W. Bader and H.J.T. Preston, Int. J. Quant. Chem. 3 (1969) 327.

BRB70 C.R. Brundle, M.B. Robin and H. Basch, J. Chem. Phys. 53 (1970) 2196.

BS72 R.E. Brown and V.H. Smith, Jr., Phys. Rev. A 5 (1972) 140.

BS&74 P.S. Bagus, M. Schrenk, D.W. Davis and D.A. Shirley, Phys. Rev. A 9 (1974) 1090.

BS&81 C.E. Brion, W.B. Stewart, D.S.C. Yee and P. Crowley, J. Electron Spectrosc. Relat. Phenom. 23 (1981) 399.

BT78 C.E. Brion and K.H. Tan, Chem. Phys. 34 (1978) 141.

BW73 R.A. Bonham and H.F. Wellenstein, Int. J. Quant. Chem. Symp. 7 (1973) 377.

BY77 C.E. Brion and D.S.C. Yee, J. Electron Spectrosc. Relat. Phenom. 12 (1977) 77.

C22 A.H. Compton, Phys. Rev. A 19 (1922) 267.

C62 E. Clementi, J. Chem. Phys. 36 (1962) 750.

C71 M. Cooper, Adv. in Phys. 20 (1971) 453.

C72 C.F. Coombs (ed.), "Basics Electronic Instrument Handbook", McGraw-Hill, New York (1972).

C75 J.A. Coekin, "High Speed Pulse Techniques", Pergamon, New York, (1975).

C80 J.P.D. Cook, Ph.D. Thesis, The University of British Columbia (1980).

C82 R. Carbi (ed.), "Current Aspects of Quantum Chemistry-1981", Elsevier Scientific, New York (1982).

CA71 T.A. Carlson and C.P. Anderson, Chem. Phys. Lett. 10 (1971) 561.

CB82a J.P.D. Cook and C.E. Brion, Chem. Phys. 69 (1982) 339.

CB82b J.P.D. Cook and C.E. Brion, in "Momentum Wave Function-1982", E. Weigold (ed.) AIP Conf. Proc. No. 86, New York (1982) p.278.

CBH80 J.P.D. Cook, C.E. Brion and A. Hamnett, Chem. Phys. 45 (1980) 1.

CC&81 R. Cambi, G. Ciullo, A. Sgamellotti, F. Tarantelli, R. Fantoni, A. Giardini-Guidoni and A. Sergio, Chem. Phys. Lett. 80 (1981) 295.

CC&82 R. Cambi, G. Ciullo, A. Sgamellotti, F. Tarantelli, R. Fantoni, A. Giardini-Guidoni, M. Rosi and R. Tiribelli, Chem. Phys. Lett. 90 (1982) 445.

CD41 C.A. Coulson and W.E. Duncanson, Proc. Cambridge Phil. Soc. 37 (1941) 55, 67, 74, 397, 406; 38 (1942) 100; 39 (1943) 180.

CD77 L.S. Cederbaum and W. Domcke, Adv. Chem. Phys. 36 (1977) 205.

CG&72 R. Camilloni, A. Giardini-Guidoni, R. Tiribelli and G. Stefani, Phys. Rev. Lett. 29 (1972) 618.

CG&78 R. Camilloni, A. Giardini-Guidoni, I.E. McCarthy and G. Stefani, Phys. Rev. A 17 (1978) 1634.

CG&80 R. Camilloni, A. Giardini-Guidoni, I.E. McCarthy and G. Stefani, J. Phys. B 13 (1980) 397.

CKM71 T.A. Carlson, M.O. Krause and W.E. Moddeman, J. Physique Colloque C4 32 (1971) 76.

CKG82 T.A. Carlson, M.O. Krause and F.A. Grimm, J. Chem. Phys. 77 (1982) 1701.

CMT78 M.A. Coplan, J.H. Moore and J.A. Tossell, J. Chem. Phys. 68 (1978) 329.

CMW84 J.P.D. Cook, J. Mitroy and E. Weigold, Phys. Rev. Lett. 52 (1984) 1116.

CM&79 M.A. Coplan, J.H. Moore, J.A. Tossell and A. Gupta, J. Chem. Phys. 71 (1979) 4005.

CM&84 J.D.P. Cook, I.E. McCarthy, A.T. Stelbovics and E. Weigold, to be published.

CR74 E. Clementi and R. Roetti, At. Data & Nucl. Data Tables 14 (1974) 177.

CS&76 R. Camilloni, G. Stefani, A. Giardini-Guidoni, R. Tiribelli and D. Vinciguerra, Chem. Phys. Lett. 41 (1976) 17.

CS&79 R. Camilloni, G. Stefani, R. Fantoni and A. Giardini-Guidoni, J. Electron Spectrosc. Relat. Phenom. 17 (1979) 209.

CTY71 G. Csanak, H.S. Taylor and R. Yaris, Adv. At. Mol. Phys. 7 (1971) 287.

CWB81 F. Carnovale, M.G. White and C.E. Brion, J. Electron Spectrosc. Relat. Phenom. 24 (1981) 63.

CW&81 J.P.D. Cook, M.G. White, C.E. Brion, W. Domcke, J. Schirmer, L.S. Cederbaum and W. von Niesson, J. Electron Spectrosc. Relat. Phenom. 22 (1981) 261.

D55 J.A. Darbyshire, Electronic Engineering (1955) 523.

D62 E.R. Davidson, J. Chem. Phys. 37 (1962) 577.

D68 D.W. Davies, Chem. Phys. Lett. 2 (1968) 173.

D69 M.J.S. Dewar, "The Molecular Orbital Theory of Organic

Chemistry", McGraw-Hill, New York (1969).

D73 B.M. Deb, Rev. Mod. Phys. 45 (1973) 22.

Di78 Digital Equipment Corporation, "Microcomputer handbook series - memories and peripherals", (1978).

DC&79 W. Domcke, L.S. Cederbaum, J. Schirmer, W. von Niessen, C.E. Brion and K.H. Tan, Chem. Phys. 40 (1979) 171.

DD&77a A.J. Dixon, S. Dey, I.E. McCarthy, E. Weigold and G.R.J. Williams, Chem. Phys. 21 (1977) 81.

DD&77b S. Dey, A.J. Dixon, K.R. Lassey, I.E. McCarthy, P.J.O. Teubner, E. Weigold, P.S. Bagus and E.K. Viinikka, Phys. Rev. A 15 (1977) 102.

DHW78 A.J. Dixon, S.T. Hood and E. Weigold, Phys. Rev. Lett. 40 (1978) 1262.

DH&80 J. Delwiche, M.J. Hubin-Franskin, G. Caprace, P. Natalis and D. Roy, J. Electron Spectrosc. Relat. Phenom. 21 (1980) 205

DL77 J.E. Draper and C.Y. Lee, Rev. Sci. Instrum. 48 (1977) 852.

DL79 K.G. Dyall and F.P. Larkins, J. Electron Spectrosc. Relat. Phenom. 15 (1979) 165.

DL82a K.G. Dyall and F.P. Larkins, J. Phys. B 15 (1982) 203.

DL82b K.G. Dyall and F.P. Larkins, J. Phys. B 15 (1982) 219.

DMW76 A.J. Dixon, I.E. McCarthy and E. Weigold, J. Phys. B 9 (1976) L195.

DM&75 S. Dey, I.E. McCarthy, P.J.O. Teubner and E. Weigold, Phys. Rev. Lett. 34 (1975) 782.

DM&77 A.J. Dixon, I.E. McCarthy, E. Weigold and G.R.J. Williams, J. Electron Spectrosc. Relat. Phenom. 12 (1977) 239.

DM&78 A.J. Dixon, I.E. McCarthy, C.J. Noble and E. Weigold, Phys. Rev. A 17 (1978) 597.

DW66 G. Das and A.C. Wahl, J. Chem. Phys. 44 (1966) 87.

E70 P. Eisenberger, Phys. Rev. A 2 (1970) 1678.

E71 I.R. Epstein, Chem. Phys. Lett. 9 (1971) 9.

E73 I.R. Epstein, Acc. Chem. Research 6 (1973) 145.

E75 I.R. Epstein, in "Theoretical Chemistry", Physical Chemistry Series Two, Int. Rev. Sci, A.D. Buckingham and C.A. Coulson (eds.), Butterworths, London (1975) p.107.

E82 R.G. Egdell, in "Specialist Periodical Reports: Electronic Structure and Magnetism of Inorganic Compounds", The Royal Society of Chemistry, Vol 7 London (1982) p.1.

EE70 A.B. El-Kareh and J.C.J. El-Kareh, "Electron Beams, Lenses and Optics" Vol 1 and 2, Academic, New York (1970).

EJS80 H. Ehrhardt, K. Jung and E. Schubert, in "Coherence and Correlation in Atomic Collisions", H. Kleinpoppen and J.F. Williams (eds.), Plenum, New York (1980) p.41.

ES&69 H. Ehrhardt, M. Schulz, T. Tekaat and K. Willmann, Phys. Rev. Lett. 22 (1969) 89.

ET77 I.R. Epstein and A.C. Tanner, in "Compton scattering", B.G. Williams (ed.), McGraw-Hill, New York (1977) p.209.

F35 V. Fock, Z. Phys. 98 (1935) 98.

FG&81 I. Fuss, R. Glass, I.E. McCarthy, A. Minchinton and E. Weigold, J. Phys. B 14 (1981) 3277.

FH14 J. Franck and G. Hertz, Verh. Deutsch Phys. Ges. 16 (1914) 10.

FH72 T. Fukamachi and S. Hosoya, Phys. Lett. 38A (1972) 341.

FM73 J.B. Furness and I.E. McCarthy, J. Phys. B 6 (1973) L205.

FMS82 I. Fuss, J. Mitroy and B.M. Spicer, J. Phys. B 15 (1982) 3321.

FM&78 I. Fuss, I.E. McCarthy, C.J. Noble and E. Weigold, Phys. Rev. A 17 (1978) 604.

FR61 S. Fraga and B.J. Ransil, J. Chem. Phys. 35 (1961) 1967.

FR71 M.J. Feinberg and K. Ruedenberg, J. Chem. Phys. 54 (1971) 1495.

FRM70 M.J. Feinberg, K. Ruedenberg and E.L. Mehler, Adv. Quant. Chem. 5 (1970) 28.

FW82a L. Frost and E. Weigold, J. Phys. B 15 (1982) 2531.

FW82b L. Frost and E. Weigold, in "Momentum Wave Functions 1982", E. Weigold (ed.), AIP Conference Proceedings No. 86, New York (1982) p.314.

FWM83 L. Frost, E. Weigold and J. Mitroy, J. Phys. B 16 (1983) 223-31.

G72 P. Grivet, "Electron Optics", Pergamon, New York (1972).

G74 U. Gelius, J. Electron Spectrosc. Relat. Phenom. 5 (1974) 985.

GFT80 A. Giardini-Guidoni, R. Fantoni and R. Tiribelli, Phys. Lett. 77A (1980) 19.

GF&79 A. Giardini-Guidoni, R. Fantoni, R. Marconero, R. Camilloni and G. Stefani, XIth Int. Conf. on Phys. of Electron and Atomic Collision, Kyoto (1979) Abstracts of Papers, p.212.

GF&80 A. Giardini-Guidoni, R. Fantoni, R. Tiribelli, R. Marconero, R. Camilloni and G. Stefani, Phys. Lett. 77 A (1980) 19.

GF&81 A. Giardini-Guidoni, R. Fantoni, R. Camilloni and G. Stefani, Comments Atom. Molec. Phys. 10 (1981) 107.

GT&77 A. Giardini-Guidoni, R. Tiribelli, D. Vinciguera, R. Camilloni and G. Stefani, J. Electron Spectrosc. Relat. Phenom. 12 (1977) 405.

H28 F. Hund, Z. Physik 51 (1928) 759.

H69 D.W.O. Heddle, J. Phys. E 2 (1969) 1046.

HC68 W.H. Henneker and P.E. Cade, Chem. Phys. Lett. 2 (1968) 575.

HD&80 M.J. Hubin-Franskin, J. Delwiche, P. Natalis, G. Caprace and D. Roy, J. Electron Spectrosc. Relat. Phenom. 18 (1980) 295.

HHB76a S.T. Hood, A. Hamnett and C.E. Brion, Chem. Phys. Lett. 39 (1976) 252.

HHB76b S.T. Hood, A. Hamnett and C.E. Brion, Chem. Phys. Lett. 41 (1976) 428.

HHB77 S.T. Hood, A. Hamnett and C.E. Brion, J. Electron Spectrosc. Relat. Phenom. 11 (1977) 205.

HK70 D.W.O. Heddle and M.V. Kurepa, J. Phys. E 3 (1970) 552.

HL&80 W.J. Hehre, W.A. Lathan, R. Ditchfield, M.D. Newton and J.A. Pople, Nat. Resource Comput. Software Cat. Vol. 1, GAUSS76 (1980).

HM&73 S.T. Hood, I.E. McCarthy, P.J.O. Teubner and E. Weigold, Phys. Rev. A 8 (1973) 2494.

HM&74 S.T. Hood, I.E. McCarthy, P.J.O. Teubner and E. Weigold, Phys. Rev. A 9 (1974) 260.

HP78 J.E. Hansen and W. Persson, Phys. Rev. A 18 (1978) 1459.

HR76 E. Harting and F.H. Read, "Electrostatic Lenses", Elsevier, Amsterdam (1976).

HS&76 A. Hamnett, W. Stoll, G. Branton, M.J. van der Wiel and C.E. Brion, J. Phys. B 9 (1976) 945.

HS&83 A. Harmalkar, A.M. Simas, V.H. Smith Jr. and W.M. Westgate, Int. J. Quant. Chem., Vol XXIII (1983) 811.

HW&73 S.T. Hood, E. Weigold, I.E. McCarthy and P.J.O. Teubner, Nature 245 (1973) 65.

I71 M. Inokuti, Rev. Mod. Phys. 43 (1971) 297.

JS73 W.L. Jorgensen and L. Salem, "The Organic Chemists' Book of Orbitals", Academic Press, New York (1973).

K33 T. Koopmans, Physica 1 (1933) 104.

K74 G. Klopman (ed.), "Chemical Reactivity and Reaction Paths", Wiley, New York (1974).

K79 C. Kunz (ed.), "Synchrotron Radiation - Techniques and Applications", Topics in Current Physics, Vol 10, Springer-Verlag, Berlin (1979).

K83 B. Kovac, J. Chem. Phys. 78 (1983) 1684.

KK&81 K. Kimura, S. Kalsumata, T Achiba and S. Iwata, "Handbook of Helium (He I) Photoelectron Spectra of Fundamental Organic Molecules. Ionization energies, ab-

initio assignments and valence electronic structure for 200 molecules", Japan Scientific Societies Press, Tokoyo (1981).

KPH81 J. Kimman, G.Y. Pan and F.J. de Heer, XIIth Int. Conf. on Phys. of Electron & Atomic Collision, Tennessee (1981), Abstracts of Papers, p.255.

KR60 W. Kolos and C.C.J. Roothaan, Rev. Mod. Phys. 32 (1960) 205-210 and 219-232.

KS77 P. Kaijer and V.H. Smith, Jr, Adv. Quant. Chem., 10 (1977) 37.

KT76 F.F. Komarov and M.M. Temkin, J. Phys. B 9 (1976) L255.

KW72 M.O. Krause and F. Wuilleumier, J. Phys. B 5 (1972) L143.

L50 M. Levy, Proc. Roy. Soc. A204 (1950) 145.

L72a W.N. Lipscomb, "Theoretical Chemistry", Physical Chemistry Series One, Vol 1, A.D. Buckingham (ed.), Butterworth, London (1972) p167.

L72b V.G. Levin, Phys. Lett. 39A (1972) 125.

L72c F. Lootsma, "Numerical Methods for Non-Linear Optimization", Academic Press, New York (1972).

L77 J.S. Lee, J. Chem. Phys. 66 (1977) 4906.

L79 M. Levy, Proc. Natl. Acad. Sci. 76 (1979) 6062.

L81 F.P. Larkins, J. Phys. B 14 (1981) 1477.

L82 J.R. Lombardi, J. Phys. Chem. 86 (1982) 3513.

L84a P.W. Langhoff, private communication.

L84b P.W. Langhoff, private communication.

LB83a K.T. Leung and C.E. Brion, Chem. Phys. 82 (1983) 87.

LB83b K.T. Leung and C.E. Brion, Chem. Phys. 82 (1983) 113.

LB84a K.T. Leung and C.E. Brion, J. Am. Chem. Soc. (1984), in press.

LB84b K.T. Leung and C.E. Brion, submitted to Chem. Phys. (1984).

LB84c K.T. Leung and C.E. Brion, submitted to Chem. Phys. (1984).

LB84d K.T. Leung and C.E. Brion, submitted to Chem. Phys. (1984).

LB84e K.T. Leung and C.E. Brion, Chem. Phys. (1984) in press.

LCG77 P.O. Lowdin, J.L. Calais and O. Goscinski (eds.), "Quantum Chemistry - A scientific Melting Pot", Int. J. Quant. Chem., Vol XII, Supp. 1, Wiley- Interscience (1977).

LH67 W.D. Lyon and J.O. Hircshfelder, J. Chem. Phys. 46 (1967) 1788.

LN&75 V.G. Levin, V.G. Neudatchin, A.V. Pavlitchenkov and Yu F. Smirnov, J. Chem. Phys. 63 (1975) 1541.

LP64 P.O. Lowdin and B Pullman (eds.), "Molecular orbitals in Chemistry, Physics and Biology", Academic, New York (1964).

LP83 P.O. Lowdin and B. Pullman (eds.), "New Horizons of Quantum Chemistry", D. Reidel, Boston (1983).

LS78 J.W. Liu and V.H. Smith, Jr., Mol. Phys. 35 (1978) 145.

LW81 B. Lohmann and E. Weigold, Phys. Lett. 86A (1981) 139.

M28 R.S. Mulliken, Phys. Rev. 32 (1928) 186.

M67 L. Marton (ed.), "Atomic and Electron Physics", Methods of Experimental Physics, Vol 4, Academic, New York (1967) p.1-149.

M73 I.E. McCarthy, J. Phys. B 6 (1973) 2358.

M75 I.E. McCarthy, J. Phys. B 8 (1975) 2133.

M79 H.S.W. Massey, "Atomic and Molecular Collisons", (3rd ed.) Taylor and Francis, London (1979).

M80 I E McCarthy, in "Coherence and Correlation in Atomic Collisons", H Kleinpoppen and J F Williams (eds), Plenum, New York (1980) p.1.

M81 C. Moore, "Curve Fitting Routines", UBC CURVE, UBC Computing Centre, (September 1981).

M83 J. Mitroy, Ph.D. Thesis, University of Melbourne (1983).

Mu75 "Single channel electron multipliers", Technical Information 16, TP1504, Mullard Limited (1975).

Mu76 "Microchannel plates", Technical Information 31, TP1561, Mullard Limited (1975).

MB52 H.S.W. Massey and E.H.S. Burhop, "Electronic and Ionic Impact Phenomena", Clarendon Press, Oxford (1952).

MB69 H.S.W. Massey and E.H.S. Burhop, "Electronic Impact Phenomena", Vols 1 and 2, Clarendon, Oxford (1969).

MBW81 A. Minchinton, C.E. Brion and E. Weigold, Chem. Phys. 62 (1981) 369.

MB&83 A. Minchinton, C.E. Brion, J.P.D. Cook and E. Weigold, Chem. Phys. 76 (1983) 89.

MC77 D.H. Madison, R.V. Calhoun, Phys. Rev. A 16 (1977) 552.

MC&81 J.N. Migdall, M.A. Coplan, D.S. Hench, J.H. Moore, J.A. Tossell, V.H. Smith Jr. and J.W. Liu, Chem. Phys. 57 (1981) 141.

MC&84 A. Minchinton, J.P.D. Cook, E. Weigold and W. von Niessen, to be published.

MFW82 A. Minchinton, I. Fuss and E. Weigold, J. Electron Spectrosc. Relat. Phenom. 27 (1982) 1.

MG&82 A. Minchinton, A. Giardini-Guidoni, E. Weigold, F.P. Larkins and R.M. Wilson, J. Electron Spectrosc. Relat. Phenom. 27 (1982) 191.

MJK59 I.E. McCarthy, E.V. Jezak and A.J. Kromminga, Nucl. Phys. 12 (1959) 274.

MJ&81 C. Martin, P. Jelinsky, M. Lampton, R.F. Malina and H.O. Anger, Rev. Sci. Instrum. 52 (1981) 1067.

MKS78 R.L. Martin, S.P. Kowalczyk and D.A. Shirley, J. Chem. Phys. 68 (1978) 3829.

ML81 D.H. Madison and R. Lang, J. Phys. B 14 (1981) 4137.

MM65 N.F. Mott and H.S.W. Massey, "The Theory of Atomic Collisions", Clarendon, Oxford (1965).

MN63 Z. Mathies and V.G. Neudatchin, Soviet Phys. JETP 45 (1963) 131.

MS76 R.L. Martin and D.A. Shirley, J. Chem. Phys. 64 (1976) 3685.

MS80 I.E. McCarthy and A.T. Stelbovics, in "Atomic and Molecular Processes in Controlled Thermonuclear Fussion", NATO Adv. Study Institutes Series B, V53, M R C McDowell and A M Ferendeci (eds), Plenum, New York (1980) p.207.

MTC82 J.H. Moore, J.A. Tossell and M.A. Coplan, Acc. Chem. Res. 15 (1982) 192.

MUP78 I.E. McCarthy, P. Uylings and R. Poppe, J. Phys. B 11 (1978) 3299.

MU&74 I.E. McCarthy, A. Ugbabe, E. Weigold and P. Teubner, Phys. Rev. Lett. 33 (1974) 459.

MW73 T. Mulvey and M.J. Wallington, Rep. Prog. Phys. 36 (1973) 347.

MW76a I.E. McCarthy and E. Weigold, Phys. Rep. 27C (1976) 275.

MW76b I.E. McCarthy and E. Weigold, Adv. in Phys. 25 (1976) 489.

MW83 I.E. McCarthy and E. Weigold, Comtemp. Phys. 24 (1983) 163.

MWY60 A.D. McLean, A. Weiss, and M. Yoshimine, Rev. Mod. Phys. 32 (1960) 211.

MY67 A.D. McLean and M. Yoshimine, Supp. to I.B.M. J. Res. Dev. (1967).

N73 G. Norlen, Physica. Scripta. 8 (1973) 249.

N83 H. Nakatsuji, Chem. Phys. 76 (1983) 283.

NH78 H. Nakatsuji and K. Hirao, J. Chem. Phys. 68 (1978) 2053.

NY82 H. Nakatsuji and T. Yonezawa, Chem. Phys. Lett. 87 (1982) 426.

Or80 EG&G ORTEC Instruments for Research and Applied Sciences, 1980/81 Catalog.

P68 F.L. Pilar, "Elementary Quantum Chemistry", McGraw-Hill, New York (1968).

P71 W. Persson, Physica. Scripta. 3 (1971) 133.

PB70 J.A. Pople and D.L. Beveridge, "Approximate Molecular Orbital Theory", McGraw-Hill, New York (1970).

PCR73 W.C. Price, S.S. Chissick and T. Ravensdale (eds.), "Wave Mechanics - the first fifty years", Butterworths, London (1973).

PP29 G. Podolsky and L Pauling, Phys. Rev. 34 (1929) 109.

PPG82 R.K. Pathak, P.V. Panat, and S.R. Gadre, Phys. Rev. A 26 (1982) 3073.

PW35 L. Pauling and E.B. Wilson, "Introduction to Quantum Mechanics", McGraw-Hill, New York (1935).

PW74 A.W. Potts and T.A. Williams, J. Electron Spectrosc. Relat. Phenom. 3 (1974) 3.

R51 C.C.J. Roothaan, Rev. Mod. Phys. 23 (1951) 69.

R72 J.S. Risley, Rev. Sci. Instrum. 43 (1972) 95.

R77 J.W. Rabalais, "Principles of Ultraviolet Photoelectron Spectroscopy", Wiley-Interscience, New York (1977).

R78 F.H. Read, Inst. Phys. Conf. 38 (1978) 249.

R83 B.I. Ramirez, Chem. Phys. Lett. 94 (1983) 180.

RC62 M. Roux and M.J. Cornille, Chem. Phys. 37 (1962) 933.

RC83 W.G. Richards and D.L. Cooper, "Ab-initio Molecular Orbital Calculations for Chemists", Clarendon Press, Oxford (1983).

S67 J.A.R. Samson, "Techniques of Vacuum Ultraviolet Spectroscopy", Wiley, New York (1967).

S72 H.F. Schaefer III., "The Electronic Structure of Atoms and Molecules", Addison-Wesley, Reading, Massachusetts (1972).

S73 W. Steckelmacher, J. Phys. E 6 (1973) 1061.

S75 R.M. Singru, Phys. Stat. Sol. (a) 30 (1975) 11.

S&69 K. Siegbahm et al., "ESCA Applied to Free Molecules", North-Holland, Amsterdam (1969).

SB72 L.C. Snyder and H. Basch, "Molecular Wavefunctions and

Properties", Wiley, New York (1972).

SCG78 G. Stefani, R. Camilloni and A. Giardini-Guidoni, Phys. Lett. 64A (1978) 364.

SCG79 G. Stefani, R. Camilloni and A. Giardini-Guidoni, J. Phys. B 12 (1979) 2583.

SD&79 J. Schirmer, W. Domcke, L.S. Cederbaum, W. von Niessen and L. Asbrink, Chem. Phys. Lett. 61 (1979) 30.

SFC74 D.P. Spears, H.J. Fischbeck and T.A. Carlson, Phys. Rev. A 9 (1974) 1603.

SH77 S. Suzer and N.S. Hush, J. Phys. B 10 (1977) L705.

SH81 H. Smid and J.E. Hansen, J. Phys. B 14 (1981) L811.

SM72 D.W. Smith and W.B. McRae, "Energy, Structure and Reactivity", Proc. 1972 Boulder Summer Research Conf. on Theoretical Chemistry, Wiley, New York (1972).

SO73 A. Streitwiesser Jr and P.H. Owens, "Orbital and Electron Density Diagrams", Macmillan, New York (1973).

SWS84 A.M. Simas, W.M. Westgate and V.H. Smith Jr., J. Chem. Phys. 80 (1984) 2636.

TB&70 D.W. Turner, C. Baker, A.D. Baker and C.R. Brundle, "Handbook of Molecular Photoelectron Spectroscopy", Wiley-Interscience, New York (1970).

TL&84 J.A. Tossell, S.M. Lederman, J.H. Moore, M.A. Coplan and D.J. Chornay, J. Am. Chem. Soc. 106 (1984) 976-9.

TM66 D.W. Turner and D.P. May, J. Chem. Phys. 45 (1966) 471.

TM&82 J.A. Tossell, J.H. Moore, M.A. Coplan, G. Stefani and R. Camilloni, J. Am. Chem. Soc. 104 (1982) 7416.

TRK70 S. Trajmar, J.K. Rice and A. Kuppermann, Adv. Chem. Phys. 18 (1970) 15.

UWM75 A. Ugbabe, E. Weigold and I.E. McCarthy, Phys. Rev. A 11 (1975) 576.

V80 H.A. van Hoof, J. Phys. E 13 (1980) 1081.

VA75 J.R. van Wazer and I. Absar, "Electron Densities in Molecules and Molecular Orbitals", Academic Press, New York (1975).

VB74 M.J. van der Wiel and C.E. Brion, J. Electron Spectrosc. Relat. Phenom. 1 (1974) 439.

W33 S. Weinbaum, J. Chem. Phys. 1 (1933) 593.

W74 T. Wright, Comm. ACM 17 (1974) 152.

W76 G.H. Wagniere, "Introduction to Elementary Molecular Orbital Theory and to Semi-empirial Methods", Lecture Notes in Chemistry, Vol 1, Springer-Verlag, New York (1976).

W77a B.G. Williams, Physica. Scripta. 15 (1977) 92.

W77b B. Williams (ed.), "Compton Scattering", McGraw-Hill, New York (1977).

W77c G. Wendin, Physica Scripta 16 (1977) 296.

W78 J.F. Williams, J. Phys. B 11 (1978) 2015.

W79 J.L. Wiza, Nucl. Inst. Meth. 162 (1979) 587.

WA&80 F. Wuilleumier, M.Y. Adam, N. Sandner and V. Schmidt, J. Physique Letters 41 (1980) L373.

WD80 H. Winick and S. Doniach, "Synchrotron Radiation Research", Plenum, New York (1980).

WD&77 E. Weigold, S. Dey, A.J. Dixon, I.E. McCarthy, K.R. Lassey and P.J.O. Teubner, J. Electron Spectrosc. Relat. Phenom. 10 (1977) 177.

WD&82 J.F. Williams, S. Dey, D. Sampson and D. McBrinn, in "Momentum Wave Functions 1982", E. Weigold (ed.), AIP Conference Proceedings No. 86, New York (1982) p.314.

WHM75 E. Weigold, S.T. Hood and I.E. McCarthy, Phys. Rev. A 11 (1975) 566.

WHT73 E. Weigold, S.T. Hood and P.J.O. Teubner, Phys. Rev. Lett. 30 (1973) 475.

WH&73 E. Weigold, S.T. Hood, I.E. McCarthy and P.J.O. Teubner, Phys. Lett. 44 A (1973) 531.

WK72 F. Wuilleumier and M.O. Krause, in "Electron Spectroscopy" D.A. Shirley (ed.), North-Holland, Amsterdam (1972) p.259.

WK74 F. Wuilleumier and M.O. Krause, Phys. Rev. A 10 (1974) 242.

WK&81 B. van Wingerden, J.T.N. Kimman, M. van Tilburg and F.J. de Heer, J. Phys. B 14 (1981) 2475.

WLB81 M.G. White, K.T. Leung and C.E. Brion, J. Electron Spectrosc. Relat. Phenom. 23 (1981) 127.

WM77 K. Wittel and S.P. McGlynn, Chem. Rev. 77 (1977) 745.

WM&77 E. Weigold, I.E. McCarthy, A.J. Dixon and S. Dey, Chem. Phys. Lett. 47 (1977) 209.

WS80 P.R. Woodruff and J.A.R. Samson, Phys. Rev. Lett. 45 (1980) 110.

Z82 H. Zscheile, J. Phys. E 15 (1982) 749.

ZKK66 V.V. Zashkvara, M.I. Korsunskii and O.S. Kosmacher, Sov. Phys. Tech. Phys. 11 (1966) 96.

Appendix A

BIBLIOGRAPHY OF BINARY (e,2e) SPECTROSCOPIC STUDIES

The development of binary (e,2e) spectroscopy over the last fifteen years has firmly established itself as an important, powerful probe for electronic structure and orbital densities. Numerous studies using binary (e,2e) spectroscopy have provided data for testing various collision approximations and models for the reaction mechanism in the (e,2e) ionization process. Specific informations concerning the binding energy spectra and spherically averaged momentum distributions of atoms, molecules and solids (thin-film) have been accumulated. These data have provided complementary information to those obtained using photoelectron spectroscopy and the Compton scattering method. The experimental binding energy spectra have generated tremendous theoretical interest in the calculation of the ionization spectral distribution using the many-body Green's function and the symmetry adapted cluster expansion techniques. The measurement of momentum distributions at selective ionization energies (of individual orbitals) has provided a direct and unique evaluation of the quality of *ab-initio* self-consistent-field wavefunctions. Theoretical works using the generalized overlap technique have attempted to go beyond the Hartree-Fock level. Recent developments in orbital density topographical studies using contour mapping and

three-dimensional graphic visualization techniques have provided a renewed interest in the investigation of momentum-space chemical properties. This approach, together with the recently developed auto-correlation functional analysis of the momentum density, have helped to improve the present understanding of experimental momentum distributions and momentum-space properties in general.

The growing number of publications has called for a summary of the present status of the field. An up-to-date bibliography of all the published works in binary (e,2e) spectroscopy is therefore given below. The following compilation includes all the experimental and theoretical studies based upon high energy symmetric (e,2e) reactions in both the coplanar and noncoplanar scattering kinematics. It should be noted that two data banks on photoabsorption and photoionization cross section measurements using the high energy asymmetric (e,2e) reaction (the dipole (e,2e) spectroscopy) have recently been published.[1] Future compilations should include the low energy (e,2e) works.

The chemical reference table gives an annotated reference listing of all the chemicals that have been investigated by binary (e,2e) spectroscopy. The chemicals are listed in ascending order of the number of electrons in the system. Each entry has the following items:

---

[1] See C.E. Brion and J.P. Thomson, J. Electron Spectrosc. Relat. Phenom. 33 (1984) 287; 301.

(1) SPECIES: This gives the number of electrons of the system of chemicals and is followed by the names of the chemicals usually in ascending order of atomic centres.

(2) REF: References of the works done on the species are listed in ascending order by the year of the publication. In cases when more than one work has been published in the same year, the references are listed alphabetically. Each reference is coded normally by five characters with the last two indicating the year of the publication. The remaining characters are the first characters of the last names of the lead authors. In cases where the same five characters are used for more than one reference, a sixth character (in lower case) is used.

(3) CODE: An approximate classification of the nature of the work is indicated using the following coding system:

C = Coplanar (experimental)
N = Noncoplanar (experimental)
T = Theory or calculation
R = Review

For the experimental work (i.e. C or N), the employed base incident energy (in units of 100eV) is enclosed in round brackets. The character "v" (for variable) is used to denote cases where several incident energies have been used.

(4) BES: The range of the binding energy spectrum (BES) is given in units of eV. In cases where the given spectrum is a

sum of the binding energy spectra measured at several angles, the word "sum" is used.

(5) MD: The momentum distribution (MD) of the orbital is labelled by its orbital name whenever possible. When no single orbital can be assigned, the energy (in eV) at which the momentum distribution is sampled is given. It should be noted that capitol letters "S" and "P" are used to denote "σ" and "π" respectively.

(6) COMMENTS: Some brief comments of the content of the published work are given.. Various short-hand notations are used:

AEA = Average Eikonal Approximation
CI = Configuration Interaction
CWIA = Coulomb Wave Impulse Approximation
DF = Dirac-Fock
DWIA = Distorted Wave Impulse Approximation
EA = Eikonal Approximation
FA = Factorization Approximation
GF = Green's Function
HF = Hartree-Fock
MO = Molecular Orbital
PWBA = Plane Wave Born Approximation
PWIA = Plane Wave Impulse Approximation
S(n=2) = σ(n=2)

Figure A.1 gives a diagrammatic summary of all the chemicals investigated by binary (e,2e) spectroscopy. Although the grouping of the chemicals in the diagram is somewhat arbitrary, the diagram attempts to emphasize chemically related groups of atoms and molecules. For instance,

isoelectronic species are bound by horizontal rectangles with heavy solid lines. Systems of chemicals such as the noble gases, hydrogen halides, methyl halides, etc. are listed vertically.

The second table gives a listing of all the theoretical works (T) and review articles (R) of binary (e,2e) spectroscopy. The titles of these articles are also given. Finally, the references are listed alphabetically by the reference codes (see item 2 above). The items in each reference are given in the following manner:

Authors, Journal Volume (Year) Page. >Title

Note that the title is given at the end of each reference and is prefixed by the character ">".

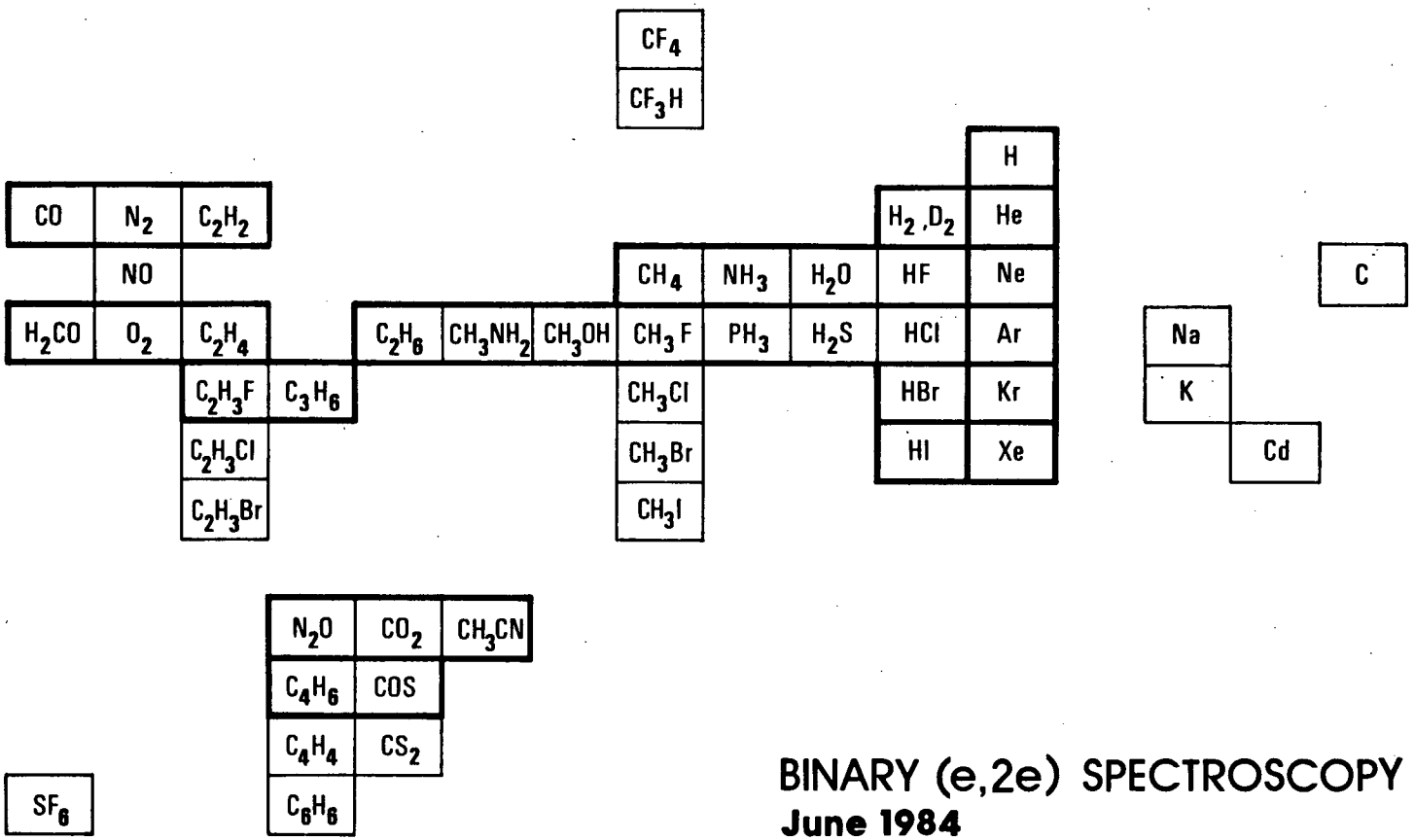

Figure A.1 - Chemical Reference Diagram.

>>> C H E M I C A L R E F E R E N C E T A B L E <<<

August, 1984

SPECIES	REF	CODE	BES	MO	COMMENTS
1					
H	WH&77	C(2,5)	8-25	1s	double-theta plot
	WN&79a	C(v)	-	-	double-theta plot, DWIA, PWIA, PWBA
	WN&79b	C(v)	-	-	double-theta plot, DWIA, PWIA, PWBA
	LW81	N(4,8,12)	11-20	1s	cf exact solution
	MW83a	N(4,8,12)	-	1s	cf exact solution
2					
He	HM&73	N(v)	-	1s	
	MU&74	C(8)	10-75	-	n=2 transition
	DMW76	N(?)	-	-	S(n=2)/S(n=1) vs momentum, CI effect
	GT&77b	C(v)	-	1s	PWIA, DWIA
	MCS77	T			
	CG&78	C(4)	-	1s	constant p plots
	FM&78	C(v)	-	1s	FA, DWIA, EA
	SCG78	C(v)	-	1s	absolute to a factor of 2, PWIA, CWIA
	WK&79	C(-)	-	-	absolute to 20%, various reaction models
	LB1	T			S(n=2)/S(n=1) vs momentum
	WK&81	C(-)	-	-	absolute to 20%, PWBA, DWIA, AEA
	LB83a	N(12)	18-30	1s	density maps, comparison study
	LB83b	N(12)	18-30	1s	cf Compton scattering data, density difference maps
	LR83	T			S(n=2)/S(n=1) vs momentum, CI effects
H2	M73	T			
	WH&73	N(4,10)	14-20	1Sg	
	DM&75	N(v)	-	1Sg	
	WM&77	N(12)	10-55	1Sg,1Su,37,10.5	correlation
	MC&81	N(4)	-	1Sg	absolute wrt WK&81
	WK&81	C(-)	-	-	absolute to 20%
	LB83b	N(12)	11-23	1Sg	density maps and density difference maps
D2	DM&75	N(v)	-	1Sg	
6					
C	AE&69	C(140)	0-600	-	thin film
	CG&72a	C(90)	0-400	K,L shells	thin film
	CG&72b	C(93)	-	K,L shells	thin film
10					
Ne	BC&74	C(25)	0-65	-	
	UWM75	C(v)	10-65	2p,2s	optical model, DWIA
	WHM75	N(2,4)	10-80	-	
	GT&77b	C(v)	-	2p,2s	PWIA,DWIA
	DM&78	N(12)	15-65	2p,2s	PWIA,DWIA
	FM&78	C(v)	-	2p,2s	FA,DWIA,EA
	SCG79	C(v)	-	2p,2s	
	CG&80	C(v)	-	2p,2s	
	LB83a	N(12)	6-64	2p,2s	density maps
HF	BM&79	N(4)	12-50	1P,3S,2S	
	BH&80	N(12)	5-55	1P,3S,2S	GF
H20	DD&77a	N(4,12)	10-50	1b1,3a1,1b2,2a1	
	HHB77a	N(4)	10-45	1b1,3a1,1b2,2a1	

cont'd

SPECIES	REF	CODE	BES	MD	COMMENTS
NH3	CS&76	C(v)	-	3a1,1e,2a1	DWIA
	HHB76a	N(4)	8-42	3a1,1e,2a1	
	WMW77	T			
	TL&84	N(-)	-	3a1	autocorrelation
CH4	HW&73	N(4)	0-70	1t2,2a1,32.5,47.5	
	M73	T			
	WD&76	N(6,12)	10-55	1t2,3a1,31	
	HHB77a	N(4)	20-38	-	
	CC&81	N(16)	10-40	1t2,2a1	GF
11					
Na	LW82	N(12)	-	3s,2p	
14					
CO	M75	T			
	DD&77b	N(4,12)	10-70	5S,1P,4S,3S,28,32, 38,43,55,60	CI
	TM&82	N(4)	-	5S,1P,4S,3S	autocorrelation
N2	CS&76	N(v)	-	2Sg	DWIA
	WD&77	N(4,6,12)	10-75	3Sg,1Pu,2Su,2Sg, 28,32.5	
C2H2	DM&77	N(4,12)	7-47	1Pu,3Sg,2Su,2Sg,29	GF
	CMT78	N(4)	10-26sum	1Pu,3Sg,2Su,2Sg	
	CM&79	N(4)	-	1Pu	
15					
NO	BC&82	N(12)	5-55	2P,4S,3S	density maps
	FGT82	N(26)	5-52	2P,17,22,41	density maps
	TM&82	N(4)	-	2P,5S,4S	autocorrelation
16					
O2	SWB80	N(4,12)	10-65	1Pg,1Pu,18.1,20.3,24.5, 2Su,32.5,2Sg,47	
	TM&82	N(4)	-	1Pg,1Pu,3Sg,2Su,2Sg	autocorrelation
H2CO	HHB76b	N(4)	10-40	-	
C2H4	CM&78	N(4)	10-36sum	1b1u,1b1g,3ag,1b2u,2b3u, 2ag,27.4	
	DH&78	N(10)	5-50	1b1u,1b1g,3ag,1b2u,2b3u, 2ag,27.4,31.2	
	CM&79	N(4)	-	1b1u	
18					
Ar	FW73a	T			
	FW73b	T			
	HM&73	N(v)	-	3p,3s	
	WHT73	N(4)	5-50	3p,3s	
	BC&74	C(25)	10-45	-	
	HM&74	N(v)	5-50	3s,40	
	UWM75	C(v)	10-50	3p,3s	optical model DWIA
	WHM75	N(2,4)	10-50	-	
	FM&78	C(v)	-	3p,3s	FA,DWIA,EA
	MUP78	T			
	W78	C(1.5)	15-44	3p,3s	high resolution

>>> C H E M I C A L R E F E R E N C E T A B L E <<<

cont'd

SPECIES	REF	CODE	BES	MO	COMMENTS
	ML81	T			
	LB83a	N(12)	10-50	3p,3s	density maps
	LW&83	C(80)	0-40	3p	asymmetric
	MAM84	T			CI
HCl	BH&8O	N(12)	8-50	2P,5S,4S	GF
	SB&8O	N(12)	8-50	-	
H2S	CB79	N(4)	6-40	2b1,5a1,2b2,4a1	
	CBH8O	N(4)	6-40	2b1,5a1,2b2,4a1	GF
PH3	HHB77b	N(4)	8-32	5a1,2e,19.5,22.6,25.5	
C2H6	DD&7G	N(4,12)	10-55	1eg,3a1g,1eu,2a2u, 2a1g,33,38,42.5,48	
CH3F	CC&81	N(16)	10-45	2e,4a1,3a1	GF
CH3OH	MBW81	N(12)	8-46	2a",7a',15.1,5a', 4a',3a',36'	GF
CH3NH2	TL&84	-	-	3a1	autocorrelation
19					
K	LW82	N(12)	-	4s,3p	
22					
CO2	GT&77a	C(16)	10-52	1Pg,19,20.5,33,39	
	CB82	N(4)	10-48	1Pg,1Pu,3Su,4Sg, 33,38	GF,density maps
N2O	FG&8O	N(26)	0-55	2P,7S,1P,6S,5S,4S	absolute wrt WK&81
	MFW82	N(12)	5-55	2P,7S,1P,6S,5S,4S	GF
CH3CN	MB&83	N(12)	8-40	2e,7a1,1e,6a1,5a1,4a1	
24					
C3H6	CM&79	N(4)	-	3e	
	TMC79	N(4)	-	3e	Jahn-Teller effect
C2H3F	FG&82	N(16)	10-45	2a",10a',15,15.5, 17.5,19,21.5,5a',4a'	GF
	CC&83a	N(16)	10-45	10.5,13,15,15.5,	GF
26					
CH3Cl	MG&82	N(12)	8-44	2e,3a1,1e,2a1,1a1, 31.5	MO
	MC&84	N(12)	8-44	2e,3a1,1e,2a1,1a1	GF,comparison study of MeX group
30					
OCS	CW&81	N(4)	10-45		GF
C4H6	CM&79	N(4)	-	1bg,1au	

>>> CHEMICAL REFERENCE TABLE <<< cont'd

SPECIES	REF	CODE	BES	MD	COMMENTS
32					
C2H3Cl	CC&83b	N(16)	5-45	-	GF
34					
CHF3	CC&82	N(16)	10-50	-	GF
	CC&83a	N(16)	10-50	-	GF
36					
Kr	BC&74	C(25)	10-40	4p,4s	-
	WHM75	N(2,4)	0-50	4p,4s,37	-
	GT&77b	C(v)	-	4p,4s	PWIA,DWIA
	FG&81	N(12)	10-52	4p,4s	CI,correlation effect
	LB83a	N(12)	10-48	4p,4s	density maps
HBr	BM&82	N(12)	7-50	4P,8S,7S	GF
42					
CF4	CC&82	N(16)	15-50	17,20,4a1,2t2,3a1	GF
C6H6	FM&81	N(12)	6-50	-	MO,GF
44					
CH3Br	MC&84	N(12)	5-45	2e,3a1,1e,2a1,1a1	GF
47					
Ag	SN82	C(5000)	-	-	K-shell ionization,thin film,asymmetric
48					
Cd	LWM83	N(12)	-	5s,4d	CI effects
50					
C2H3Br	CC&83b	N(16)	7-45	9.2,10.2,12.4,13.2, 15.4	GF
54					
Xe	UWM75	C(v)	5-40	5p,5s	optical model,DWIA
	GT&77b	C(v)	-	5s	PWIA,DWIA
	HHB77a	N(4)	10-36	-	
	DM&78	N(12)	5-85	5p,5s	PWIA,DWIA
	GF&80c	C(v)	-	5p,5s	absolute to a factor of 2,DWIA,AEA
	LB83a	N(12)	8-44	5p,5s	density maps
	CMW84	N(12)	-	5p3/2,5p1/2	relativistic effects
HI	BM&82	N(12)	5-35	6P,11S,10S	GF
62					
CH3I	MC&84	N(12)	7-48	2e,3a1,1e,2a1,1a1	GF
70					
SF6	GF&79	C(26)	10-55	15,17,19,22,2a1g, 1eg,1t1u,1a1g	

>>> CHEMICAL REFERENCE TABLE <<< cont'd

SPECIES	REF	CODE	BES	MD	COMMENTS
79 Au	FMS82	T		1s	relativistic
80 Hg	MF82	T		6s1/2,5d5/2,5d3/2	HF,DF,relativistic
90 Th	FMS82	T		1s	relativistic

REF	CODE	TITLE
FM73a	T	Optical model wave functions for atomic scattering.
FM73b	T	The (e,2e) experiment as a probe for atomic structure.
M73	T	Theory of the (e,2e) reaction on molecules.
M75	T	Theory of the (e,2e) reaction on molecules II.
MCS77	T	Triple-differential cross sections for electron-impact ionization of helium.
WMW77	T	Investigation of generalized overlap via (e,2e) spectroscopy.
MUP78	T	Comparison of (e,2e), photoelectron and conventional spectroscopies for the Ar II ion.
M80	T	Theory of (e,2e) experiments.
MS80	T	Theoretical methods for ionization.
L81	T	The (e,2e) satellite spectrum of helium.
ML81	T	Theoretical (e,2e) cross sections for ionization of the 3s state of argon.
FMS82	T	A theory for relativistic (e,2e) reactions.
MF82	T	Momentum distributions for mercury.
LR83	T	The helium (e,2e) satellite spectrum.
MAM84	T	The (e,2e) spectrum of argon.
GI68	R	Angular distribution of the outgoing electrons in electronic ionization.
NNS69	R	Quasielastic knockout of an electron by a fast electron from atoms, molecules and very thin crystalline films.
AC70	R	Value and limitations of quasi-free electron scattering experiments on atoms.
L72	R	On the (e,2e) reactions in solids.
GM&74	R	Study of atomic structure by means of (e,2e) impulsive reactions.
LN&75	R	Structure of wavefunctions of atoms in the (e,2e) reaction.
MW76a	R	(e,2e) spectroscopy.
MW76b	R	The determination of the dynamic structures of atoms and molecules using the (e,2e) reaction.
A77	R	On the display of basic properties of the molecular electronic wavefunctions in the (e,2e) quasielastic knockout experiments.
W77a	R	The determination of electronic momentum distributions and molecular structure using the (e,2e) reaction.
W77b	R	The experimental determination of electron momentum densities.
W77c	R	Investigation of (e,2e) knockout reaction via molecular electronic structure calculations.
GM&78	R	Studies of ionic states in atoms and molecules by (e,2e) coincidence measurements of direct ionization processes.
MW78	R	Electron coincidence spectroscopy: a new way of looking into matter.
WM78	R	(e,2e) collisions.
CS&79	R	Study of molecular orbitals by means of (e,2e) spectroscopy on oriented molecules.
GCS80	R	Impulsive (e,2e) experiments: A tool to test different ionization theories and electronic structures of atoms and molecules.
GF&80a	R	Measurement of ionization potentials of molecules by (e,2e) spectroscopy.
GF&80b	R	(e,2e) spectroscopy.
W80a	R	Electron coincidence experiments in atomic physics.
W80b	R	(e,2e) spectroscopy.
GF&81	R	(e,2e) experiments.
W81	R	(e,2e) theory and experiment.
CTM82	R	Momentum densities in chemistry.
FH&82	R	Relativistic (e,2e).
FW82	R	(e,2e) on solids - a progress report.
L82	R	Electron correlation and molecular effects in (e,2e) spectroscopy.
M82a	R	Theory of the (e,2e) reaction.
M82b	R	Binary (e,2e) spectroscopy of molecules - electronic momentum distributions and molecular structure.
MTC82	R	Electronic structure of molecules by (e,2e) spectroscopy.
W82	R	Electron coincidence spectroscopy - momentum space wavefunction of electrons in atoms annd molecules.
WD&82	R	Progress report on (e,2e) collisons in thin films.
MW83b	R	Observing the motion of electrons in atoms and molecules.

List of References

A77 N R Avery; in "Momentum Wave-Functions-1976", AIP Conf. Proc. V36, AIP Press, New York, (1977) 195-203. >On the (e,2e) reactions in solids.

AC70 U Amaldi Jr and C Ciofi Degli Atti; Il Nuovo Cimento, Vol LXVIA, (1970) 129-38. >Value and limitations of quasi-free electron scatttering experiments on atoms.

AE&69 U Amaldi, A Egidi, R Marconero and G Pizzella; Rev. Sci. Instrum. 40 (1969) 1001-4. >Use of a two channeltron coincidence in a new line of research in atomic physics.

BC&74 A Botticelli, R Camilloni, A Giardini-Guidoni, G Missoni, G Stefani, R Tiribelli and D Vinciguerra; Annali di Chimica 64 (1974) 189-97. >(e,2e) reactions on noble gases. Configuration interaction peaks in the energy spectrum of valence electrons.

BC&82 C E Brion, J P D Cook, I G Fuss and E Weigold; Chem. Phys. 64 (1982) 287-97. >Molecular orbital momentum distributions and binding energies for nitric oxide.

BH&80 C E Brion, S T Hood, I H Suzuki, E Weigold, G R J Williams; J. Electron Spectrosc. Relat. Phenom. 21 (1980) 71-91. >Momentum distributions and ionization potentials for the valence orbitals of hydrogen fluoride and hydrogen chloride.

BM&79 C E Brion, I E McCarthy, I H Suzuki and E Weigold; Chem. Phys. Lett. 67 (1979) 115-8. >Momentum distributions for the valence orbitals of hydrogen fluoride.

BM&82 C E Brion, I E McCarthy, I H Suzuki, E Weigold, G R J Williams, K L Bedford, A B Kunz and E Weidman; Electron Spectrosc. Relat. Phenom. 27 (1982) 83-107. >Electron momentum distributions and binding energies for the valence orbitals of hydrogen bromide and hydrogen iodide.

CB79 J P D Cook and C E Brion; J. Electron Spectrosc. Relat. Phenom. 15 (1979) 233-6. >Valence shell momentum distributions, binding energies and calculated wavefunction evaluation for H2S by binary (e,2e) spectroscopy.

CB82 J P D Cook and C E Brion; Chem. Phys. 69 (1982) 339-56. >Binary (e,2e) spectroscopy and momentum-space chemistry of CO2.

CBH80 J P D Cook, C E Brion and A Hamnett; Chem. Phys. 45 (1980) 1-13. >On the ionization and momentum distributions of the valence electrons of H2S.

CC&81 R Cambi, G Ciullo, A Sgamellotti, F Tarantelli, R Fantoni, A Giardini-Guidoni and A Sergio; Chem. Phys. Lett. 80 (1981) 295-300. >Ionization of CH4 and some fluromethanes: A Green's function study and an (e,2e) spectroscopic investigation.

CC&82 R Cambi, G Ciullo, A Sgamellotti, F Tarantelli, R Fantoni, A Giardini-Guidoni, M Rosi and R Tiribelli; Chem. Phys. Lett. 90 (1982) 445-52. >Ionization of fluoromethanes: CHF3 and CF4. A Green's function study and an (e,2e) spectroscopic investigation.

CC&83a R Cambi, G Ciullo, M Rosi, A Sgamellotti, F Tarantelli, R Fantoni and A Giardini-Guidoni; Int. J. Mass Spect. Ion Phys. 46 (1983) 261-4. >Ionization of fluorinated methanes and ethylenes through (e,2e) process and Green's function approach to predict ionization potentials.

CC&83b R Cambi, G Ciullo, A Sgamellotti, F Tarantelli, R Fantoni, A Giardini-Guidoni, I E McCarthy and V Di Martino; Chem. Phys. Lett. 101 (1983) 477-84. >An (e,2e) spectroscopic investigation and a Green's function study of the ionization of chloro- and bromo-ethylene.

CG&72a R Camilloni, A Giardini-Guidoni, G Stefani and R Tiribelli; Frascati Report No. LNF72/53, Rome (1972). >Quasi-free electron scattering on bound electron coincidence measurements of scattered and emitted electrons in carbons.

CG&72b R Camilloni, A Giardini-Guidoni, R Tiribelli and G Stefani; Phys. Rev. Lett. 29 (1972) 618-21. >Coincidence measurement of quasifree scattering of 9keV electrons on K and L shells of carbon.

CG&78 R Camilloni, A Giardini Guidoni, I E McCarthy and G Stefani; Phys. Rev. A 17 (1978) 1634-41. >Mechanism of the (e,2e) reaction with atoms.

CG&80 R Camilloni, A Giardini Guidoni, I E McCarthy and G Stefani; J. Phys. B 13 (1980) 397-409. >The eikonal approximation for the (e,2e) reaction.

CM&78 M A Coplan, A L Migdall, J H Moore and J A Tossell; J. Am. Chem. Soc. 100 (1978) 5008-11. >Valence electron momentum distributions of ethylene from the (e,2e) experiment.

CM&79 M A Coplan, J H Moore, J A Tossell and A Gupta; J.

Chem. Phys. 71 (1979) 4005-9. >Electron momentum distributions in the pi orbitals of small hydrocarbons from the (e,2e) experiment.

CMT78 M A Coplan, J H Moore and J A Tossell; J. Chem. Phys. 68 (1978) 329-30. >Valence electron momentum distributions for acetylene.

CMW84 J P D Cook, J Mitroy and E Weigold; Phys. Rev. Lett. 52 (1984) 1116-8. >Direct observations of relativistic effects in single-electron momentum distributions in xenon outer shells.

CS&76 R Camilloni, G Stefani, A Giardini-Guidoni, R Tiribelli and D Vinciguerra; Chem. Phys. Lett. 41 (1976) 17- 20. >Electron momentum distributions of valence states of NH3 and the 2Sg of N2 as measured by (e,2e) experiments.

CS&79 R Camilloni, G Stefani, R Fantoni and A Giardini-Guidoni; J. Electron Spectrosc. Relat. Phenom. 17 (1979) 209-28. >Study of molecular orbitals by means of (e,2e) spectroscopy on oriented molecules.

CTM82 M A Coplan, J A Tossell and J H Moore; in "Momentum Wave-Functions-1982", AIP Conf. Proc. V86, AIP Press, New York, 1982, 82-9. >Momentum densities in chemistry.

CW&81 J P D Cook, M G White, C E Brion, W Domcke, J Schirmer, L S Cederbaum and W von Niessen; J. Electron Spectrosc. Relat. Phenom. 22 (1981) 261-70. >On the valence shell binding energy spectrum of carbonyl sulphide.

DD&76 S Dey, A J Dixon, I E McCarthy and E Weigold; J. Electron Spectrosc. Relat. Phenom. 9 (1976) 397-412. >(e,2e) spectroscopy of ethane.

DD&77a A J Dixon, S Dey, I E McCarthy, E Weigold and G R J Williams; Chem. Phys. 21 (1977) 81-8. >(e,2e) spectroscopy of H2O -- separation energy spectra and valence orbital electron momentum distributions.

DD&77b S Dey, A J Dixon, K R Lassey, I E McCarthy, P J O Teubner, E Weigold, P S Bagus and E K Viinikka; Phys. Rev. A15 (1977) 102-11. >(e,2e) spectroscopy of the CO molecule.

DH&78 A J Dixon, S T Hood, E Weigold and G R J Williams; J. Electron Spectrosc. Relat. Phenom. 14 (1978) 267-75. >Correlation effects and electron momentum distributions in the valence orbitals of ethylene.

DMW76 A J Dixon, I E McCarthy and E Weigold; J. Phys. B9 (1976) L195-8. >Excitation of the n=2 states of He+ in the ionization of helium.

DM&75 S Dey, I E McCarthy, P J O Teubner and E Weigold; Phys. Rev. Lett. 34 (1975) 782-5. >(e,2e) probe for hydrogen molecule wave functions.

DM&77 A J Dixon, I E McCarthy, E Weigold and G R J Williams; J. Electron Spectrosc. Relat. Phenom. 12 (1977) 239-48. >Electron ionization spectroscopy of acetylene: momentum distributions of valence orbitals and correlation effects.

DM&78 A J Dixon, I E McCarthy, C J Noble and E Weigold; Phys. Rev. A17 (1978) 597-603. >Factorized distorted-wave approximation for the (e,2e) reaction on atoms: Noncoplanar symmetric.

FGT82 R Fantoni, A Giardini-Guidoni and R Tiribelli; J. Electron Spectrosc. Relat. Phenom. 26 (1982) 99-105. >(e,2e) spectroscopy of valence states of the NO molecule.

FG&80 R Fantoni, A Giardini-Guidoni, R Tiribelli, R Camilloni and G Stefani; Chem. Phys. Lett. 71 (1980) 335-8. >Satellite structures and momentum distributions in binary (e,2e) spectroscopy of N2O.

FG&81 I Fuss, R Glass,. I E McCarthy, A Minchinton and E Weigold; J. Phys. B14 (1981) 3277-87. >Electron correlation effects in the (e,2e) valence separtion energy spectra of krypton.

FG&82 R Fantoni, A Giardini-Guidoni, R Tiribelli, R Cambi, G Ciullo and A Sgamellotti; Mol. Phys. 45 (1982) 839- 52. >An (e,2e) spectroscopic investigation and a Green's function study of the ionization of fluoroethylene.

FH&82 I Fuss, R Helstrom, R Henderson and J Mitroy; in "Momentum Wave-Functions-1982", AIP Conf. Proc. V86, AIP Press, New York, 1982, 297-313. >Relativistic (e,2e).

FM73a J B Furness and I E McCarthy; FUPH-R-95; Oct. 73. >Optical model wave functions for atomic scattering.

FM73b J B Furness and I E McCarthy; J. Phys. B 6 (1973) L205-7. >The (e,2e) experiment as a probe for atomic structure.

FMS82 I Fuss, J Mitroy and B M Spicer; J. Phys. B 15 (1982) 3321-31. >A theory for relativistic (e,2e) reactions.

FM&78 I Fuss, I E McCarthy, C J Noble and E Weigold; Phys. Rev. A 17 (1978) 604-13. >Factorized distorted wave approximation for the (e,2e) reaction on atoms:

Coplanar symmetric.

FM&81 I Fuss, I E McCarthy, A Minchinton, E Weigold and F P Larkins; Chem. Phys. 63 (1981) 19-30. >Momentum distributions and binding energies for the valence orbitals of methanol.

FW82 L Frost and E Weigold; in "Momentum Wave-Functions-1982", AIP Conf. Proc. V86, AIP Press, New York, 1982, 326-32. >(e,2e) on solids - a progress report.

FW82 L Frost and E Weigold; J. Phys. B 15 (1982) 2531-8. >Electron coincidence spectroscopy of sodium and potassium.

FWM83 L Frost, E Weigold and J Mitroy; J. Phys. B 16 (1983) 223-31. >Valence electron momentum distributions in cadmium.

GCS80 A Giardini-Guidoni, R Camilloni and G Stefani; in "Coherence and Correlation in Atomic Collisons", H Kleinpoppen and J F Williams (eds), Plenum, New York, (1980) 13-39. >Impulsive (e,2e) experiments: A tool to test different ionization theories and electronic structure of atoms and molecules.

GF&79 A Giardini-Guidoni, R Fantoni, R Tiribelli, D Vinciguerra, R Camilloni and G Stefani; J. Chem. Phys. 71 (1979) 3182-8. >Study of electronic properties of the SF6 molecule by (e,2e) spectroscopy.

GF&80a A Giardini-Guidoni, R Fantoni, R Camilloni and G Stefani; Adv. in Mass Spect., V8A, A Quayle (ed.), Heyden & Son, (1980) 71-8. >Measurement of ionization potentials of molecules by (e,2e) spectroscopy.

GF&80b A Giardini-Guidoni, R Fantoni, R Camilloni and G Stefani; in NATO Advanced Study Inst. for "Emission and Scattering Techniques", Series C, Vol 73, P Day (ed.), D Reidel, London, (1980) 293-317. >(e,2e) spectroscopy.

GF&80c A Giardini Guidoni, R Fantoni, R Tiribelli, R Marconero, R Camilloni and G Stefani; Phys. Lett. 77 A (1980) 19-22. >Absolute (e,2e) cross section measured for the valence orbital of Xe.

GF&81 A Giardini-Guidoni, R Fantoni, R Camilloni and G Stefani; Comments Atom. Mol. Phys. 10 (1981) 107-20. >(e,2e) experiments.

GI68 A E Glassgold and G Ialongo; Phys. Rev. 175 (1968) 151-9. >Angular distribution of the outgoing electrons in electronic ionization.

GM&74 A Giardini-Guidoni, G Missoni, R Camilloni and G Stefani; in "Electrons and Photons Interactions with Atoms", H. Kleinpoppen and M R C McDowell (eds), Plenum, New York, (1974) 149-60. >Study of Atomic Structure by means of (e,2e) impulsive reactions.

GM&76 A Giardini-Guidoni, G Missoni, R Camilloni and G Stefani; Adv. in Mass Spectr., V7A, N.R. Daly (ed.), Heyden & Son, (1978), 175-81. >Studies of ionic states in atoms and molecules by (e,2e) coincidence measurements of direct ionization processes.

GT&77a A Giardini-Guidoni, R Tiribelli, D Vinciguerra, D Camilloni and G Stefani; J. Electron Spectrosc. Relat. Phenom. 12 (1977) 405-14. >Study of valence states of the CO2 molecule by (e,2e) momentum spectroscopy.

GT&77b A Giardini-Guidoni, R Tiribelli, D Vinciguerra, R Camilloni, G Stefani and G Missoni; in "Momentum Wave-Functions-1976", AIP Conf. Proc. V36, AIP Press, New York, 1977, 205-26. >Validity of the (e,2e) reactions as a probe of the atomic and molecular structure.

HHB76a S T Hood, A Hamnett and C E Brion; Chem. Phys. Lett. 39 (1976) 252-6. >An (e,2e) study of ammonia: binding energies and momentum distributions of valence electrons.

HHB76b S T Hood, A Hamnett and C E Brion; Chem. Phys. Lett. 41 (1976) 428-30. >The assignment of the ionization potentials of formaldehyde by an (e,2e) experiment.

HHB77a S T Hood, A Hamnett and C E Brion; J. Electron Spectrosc. Relat. Phenom. 11 (1977) 205-24. >Molecular orbital momentum distributions and binding energies for H2O using an electron impact coincidence spectrometer.

HHB77b A Hamnett, S T Hood and C E Brion; J. Electron Spectrosc. Relat. Phenom. 11 (1977) 263-74. >A study of the bonding in phosphine by an electron impact coincidence experiment.

HM&73 S T Hood, I E McCarthy, P J O Teubner and E Weigold; Phys. Rev. A8 (1973) 2494-500. >Angular correlation for (e,2e) reactions on atoms.

HM&74 S T Hood, I E McCarthy, P J O Teubner and E Weigold; Phys. Rev. A9 (1974) 260-6. >Structure of atoms from the (e,2e) reaction.

HW&73 S T Hood, E Weigold, I E McCarthy and P J O Teubner; Nature Phys. Sci. 245 (1973) 65-8. >Momentum space wavefunctions and binding energies of the valence electrons in methane by the (e,2e) technique.

L72 V G Levin; Phys. Lett. 39A (1972) 125-6. >Structure of wavefunctions of atoms in the (e,2e) reaction.

L81 F P Larkins; J. Phys. B 14 (1981) 1477-84. >The (e,2e) satellite spectrum of helium.

L82 F P Larkins; in "Momentum Wave-Functions-1982", AIP Conf. Proc. V86, AIP Press, New York, 1982, 144-66. >Electron correlation and molecular effects in (e,2e) spectroscopy.

LB83a K T Leung and C E Brion; Chem. Phys. 82 (1983) 87- 111. >Experimental investigation of the valence orbital momentum distributions and ionization energies of the noble gases by binary (e,2e) spectroscopy.

LB83b K T Leung and C E Brion; Chem. Phys. 82 (1983) 113- 37. >Binary (e,2e) spectroscopic study and momentum space chemistry of the two-electron systems: He and H2.

LN&75 V G Levin, V G Neudatchin, A V Pavlitchenkov and Yu F Smirnov; J. Chem. Phys. 63 (1975) 1541-6. >On the display of basic properties of the molecular electronic wavefunctions in the (e,2e) quasielastic knockout experiments.

LR83 F P Larkins and J A Richards; Chem. Phys. 81 (1983) 329-33. >The helium (e,2e) satellite spectrum.

LW81 B Lohmann and E Weigold; Phys. Lett. 86A (1981) 139-41. >Direct measurement of the electron momentum probability distribution in atomic hydrogen.

LW&83 A Lahmam-Bennani, H F Wellenstein, A Duguet and M Rouault; J. Phys. B 16 (1983) 121-30. >Absolute triple differential cross sections for the 3p ionization of argon by electron impact.

M73 I E McCarthy; J. Phys. B 6 (1973) 2358-67. >Theory of the (e,2e) reaction on molecules.

M75 I E McCarthy; J. Phys. B 8 (1975) 2133-39. >Theory of the (e,2e) reaction on molecules II.

M80 I E McCarthy; in "Coherence and Correlation in Atomic Collisons", H Kleinpoppen and J F Williams (eds), Plenum, New York, (1980) 1-11. >Theory of (e,2e) experiments.

M82a I E McCarthy; in "Momentum Wave-Functions-1982", AIP Conf. Proc. V86, AIP Press, New York, 1982, 5-18. >Theory of the (e,2e) reaction.

M82b A Minchinton; in "Momentum Wave-Functions-1982", AIP Conf. Proc. V86, AIP Press, New York, 1982, 115-43. >Binary (e,2e) spectroscopy of molecules - electronic momentum distributions and molecular structure.

MAM84 J Mitroy, K Amos and I Morrison; J. Phys. B 17 (1984) 1659-74. >The (e,2e) spectrum of argon.

MBW81 A Minchinton, C E Brion and E Weigold; Chem. Phys. 62 (1981) 369-75. >Momentum distributions and ionization potentials for the valence orbitals of benzene.

MB&83 A Minchinton, C E Brion, J P D Cook and E Weigold; Chem. Phys. 76 (1983) 89-101. >Molecular orbital electron momentum distributions and separation energies of CH3CN.

MCS77 D H Madison, R V Calhoun and W N Shelton Phys. Rev. A 16 (1977) 552-62. >Triple-differential cross sections for electron-impact ionization of helium.

MC&78 J H Moore, M A Coplan, T L Skillman and E D Brooks; Rev. Sci. Instr. 49 (1978) 463-8. >Multichannel (e,2e) apparatus.

MC&81 J N Migdall, M A Coplan, D S Hench, J H Moore, J A Tossell, V H Smith and J W Liu; Chem. Phys. 57 (1981) 141-6. >The electron momentum distribution of molecular hydrogen.

MF82 J Mitroy and I Fuss; J. Phys. B 15 (1982) L367-70. >Momentum distributions for mercury.

MFW82 A Minchinton, I Fuss and E Weigold; J. Electron Spectrosc. Relat. Phenom. 27 (1982) 1-14. >Valence electron separation energies and momentum distributions for N2O.

MG&82 A Minchinton, A Giardini-Guidoni, E Weigold, F P Larkins and R M Wilson; J. Electron Spectrosc. Relat. Phenom. 27 (1982) 191-203. >Momentum distributions and separation energies for the valence orbitals of chloromethane.

ML81 D H Madison and R Lang; J. Phys. B 14 (1981) 4137-47. >Theoretical (e,2e) cross sections for ionization of the 3s state of argon.

MS80 I E McCarthy and A T Stelbovics; in "Atomic and Molecular Processes in Controlled Thermonuclear Fussion", NATO Adv. Study Institutes Series B, V53, M R C McDowell and A M Ferendeci (eds), Plenum, New York, (1980) 207-44. >Theoretical methods for ionization.

MTC82 J H Moore, J A Tossell and M A Coplan; Acc. Chem. Res. 15 (1982) 195-8. >Electronic structure of molecules

by (e,2e) spectroscopy.

MUP78 I E McCarthy, P Uylings and R Poppe; J. Phys. B 11 (1978) 3299-308. >Comparison of (e,2e), photoelectron and conventional spectroscopies for the Ar II ion.

MU&74 I E McCarthy, A Ugbabe, E Weigold and P J O Teubner; Phys. Rev. Lett. 33 (1974) 459-62. >(e,2e) reaction as a probe for details of the helium wavefunction.

MW76a I E McCarthy and E Weigold; Phys. Rep 27C (1976) 275-371. >(e,2e) spectroscopy.

MW76b I E McCarthy and E Weigold; Adv. in Phys. 25 (1976) 489-515. >The determination of the dynamic structures of atoms and molecules using the (e,2e) reaction.

MW78 I E McCarthy and E Weigold; Endeavour 2 (1978) 72-9. (Pergamon Press) >Electron coincidence spectroscopy: a new way of looking into matter.

MW83a I E McCarthy and E Weigold; Am. J. Phys. 51 (1983) 152-5. >A real "thought" experiment for the hydrogen atom.

MW83b I E McCarthy and E Weigold; Contemp. Phys. 24 (1983) 163-84. >Observing the motion of electrons in atoms and molecules.

NNS69 V G Neudachin, G A Novoskol'tseva and Yu F Smirnov; Soviet Physics JETP 28 (1969) 540-3. >Quasielastic knockout of an electron by a fast electron from atoms, molecules and very thin crystalline films.

SB&78 T L Skillman, E D Brooks, M A Coplan and J H Moore; Nucl. Instr. and Meth. 155 (1978) 267-72. >A microcomputer based multiple detector data acquisition system.

SB&80 I H Suzuki, C E Brion, E Weigold and G R J Williams; Int. J. Quan. Chem. XVIII (1980) 275-80. >Binding energies at different momenta for the valence orbitals of HCl by the binary (e,2e) method.

SCG78 G Stefani, R Camilloni and A Giardini Guidoni; Phys. Lett. 64 A (1978) 364-6. >Asolute (e,2e) differential cross section measured in coplanar conditions: He.

SCG79 G Stefani, R Camilloni and A Giardini Guidoni; J. Phys. B 12 (1979) 2583-94. >Absolute (e,2e) coplanar symmetric cross sections measured for valence orbitals of Ne.

SN82 E Schule and W Nakel; J. Phys. B 15 (1982) L639-41. >Triply-differential cross section for K-shell ionization of silver by relativistic electron impact.

SWB80 I H Suzuki, E Weigold and C E Brion; J. Electron Spectrosc. Relat. Phenom. 20 (1980) 289-303. >Electron coincidence spectroscopy of O2: Valence electron momentum distributions and binding energies.

TL&84 J A Tossell, S M Lederman, J H Moore, M A Coplan and D J Chornay; J. Am. Chem. Soc. 106 (1984) 976-9. >Experimental evidence for delocalization of the lone- pair orbital in CH3NH2 from (e,2e) spectroscopy.

TM&82 J A Tossell, J H Moore, M A Coplan, G Stefani and R Camilloni; J. Am. Chem. Soc. 104 (1982) 7416-. >Fourier analysis of the orbital momentum densities of CO, NO and O2.

TMC79 J A Tossell, J H Moore and M A Coplan; Chem. Phys. Lett. 67 (1979) 356-8. >Molecular distortions and electron momentum distributions.

UWM75 A Ugbabe, E Weigold and I E McCarthy; Phys. Rev. A 11 (1975) 576-85. >(e,2e) reaction in inert gases: Coplanar symmetry geometry.

W77a E Weigold; in "Momentum Wave-Functions-1976", AIP Conf. Proc. V36, AIP Press, New York, (1977) 84-110. >The determination of electronic momentum distributions and molecular structure using the (e,2e) reaction.

W77b B G Williams; Physcia Scripta 15 (1977) 92-111. >The experimental determination of electron momentum densities.

W77c G R J Williams; in "Momentum Wave-Functions-1976", AIP Conf. Proc. V36, AIP Press, New York, (1977) 151-67. >Investigation of (e,2e) knockout reactions via molecular electronic structure calculations.

W78 J F Williams; J. Phys. B11 (1978) 2015-21. >High resolution energy and angular correlation of the scattered and ejected electrons in electron impact ionization of argon atoms.

W80a E Weigold; FIAS-R-61, March 80. >Electron coincidence experiments in atomic physics.

W80b E Weigold; Proceedings, XI ICPEAC, Kyoto (1980) 81-93. >(e,2e) spectroscopy.

W81 E Weigold; Nucl. Phys. A 353 (1981) 327c-40c. >(e,2e) theory and experiment.

W82 E Weigold; Aust. J. Phys. 35 (1982) 571-91. >Electron coincidence spectroscopy - momentum space wavefunction

of electrons in atoms and molecules.

WD&76 E Weigold, S Dey, A J Dixon, I E McCarthy and P J O Teubner; Chem Phys. Lett. 41 (1976) 21-4. >(e,2e) spectroscopy of methane.

WD&77 E Weigold, S Dey, A J Dixon, I E McCarthy, K R Lassey and P J O Teubner; J. Electron Spectrosc. Relat. Phenom. 10 (1977) 177-91. >(e,2e) spectroscopy of N2 -- Valence momentum distributions and configuration interaction.

WD&82 J F Williams, S Dey, D Sampson and D McBrinn; in "Momentum Wave-Functions-1982", AIP Conf. Proc. V86, AIP Press, New York, 1982, 315-25. >Progress report on (e,2e) collisions in thin films.

WHM75 E Weigold, S T Hood and I E McCarthy; Phys. Rev. A11 (1975) 566-75. >Structure of inert gases from the (e,2e) reaction.

WHT73 E Weigold, S T Hood and P J O Teubner; Phys. Rev. Lett. 30 (1973) 475-8. >Energy and angular correlations of the scattered and ejected electrons in the electron-impact ionization of argon.

WH&73 E Weigold, S T Hood, I E McCarthy and P J O Teubner; Phys. Lett. 44A (1973) 531-2. >The (e,2e) reaction in molecules: Momentum space wave function of H2.

WH&77 E Weigold, S T Hood, I Fuss and A J Dixon; J. Phys. B 10 (1977) L623-7. >Ionization of atomic hydrogen: Angular correlations of the outgoing electrons.

WK&79 B van Wingerden, J T N Kimman, M van Tilburg, E Weigold, C J Joachain, B Piraux and F J de Heer; J. Phys. B 12 (1979) L627-31. >Absolute triple- and double- differential cross sections for ionization of helium by electron impact.

WK&81 B van Wingerden, J T N Kimman, M van Tilburg and F J de Heer; J. Phys. B 14 (1981) 2475-98. >Triple and double differential cross sections for electron impact ionization of helium and molecular hydrogen.

WM78 E Weigold and I E McCarthy; Adv. Atom. Mol. Phys. 14 (1978) 127-79. >(e,2e) collisions.

WMW77 G R J Williams, I E McCarthy and E Weigold; Chem. Phys. 22 (1977) 281-7. >Investigation of generalized overlap via (e,2e) spectroscopy.

WM&77 E Weigold, I E McCarthy, A J Dixon and S Dey; Chem. Phys. Lett. 47 (1977) 209-12. >Ground state correlations in H2 measured by the (e,2e) technique.

WN&79a E Weigold, C J Noble, S T Hood and I Fuss; J. Phys. B 12 (1979) 291-313. >(e,2e) experiments on atomic hydrogen: Comparison with the distorted and plane wave impulse approximations.

WN&79b E Weigold, C J Noble, S T Hood and I Fuss; J. Electron Spectrosc. Relat. Phenom. 15 (1979) 253-6. >Electron impact ionization of atomic hydrogen: Experimental and theoretical (e,2e) differential cross sections.

PUBLICATIONS

1) K.T. Leung and C.E. Brion, Chem. Phys. 82 (1983) 87-111. "Experimental investigation of the valence orbital momentum distributions and ionization energies of the noble gases by binary (e,2e) spectroscopy".

2) K.T. Leung and C.E. Brion, Chem. Phys. 82 (1983) 113-137. "Binary (e,2e) spectroscopic study and momentum-space chemistry of the two-electron systems He and H_2".

3) K.T. Leung and C.E. Brion, Lecture Notes in Chemistry, F.A. Gianturco and G. Stefani (eds.), Vol. 35, Springer-Verlag, New York, (1984), 151-155. "(e,2e) Chemistry".

4) K.T. Leung and C.E. Brion, J. Am. Chem. Soc., (1984), in press. "The bond density of molecular hydrogen in momentum-space".

5) K.T. Leung and C.E. Brion, Chem. Phys., (1984), in press. "Valence orbital momentum-space densities of carbon tetrafluoride".

6) K.T. Leung and C.E. Brion, Chem. Phys. (1984), submitted. "Outer valence orbital momentum distributions of carbon dioxide".

7) K.T. Leung, C.E. Brion and P.W. Langhoff, Chem. Phys., (1984), submitted. "Valence orbital momentum distributions and ionization energies of carbon disulfide".

8) K.T. Leung and C.E. Brion, Chem. Phys., (1984), submitted. "Binary (e,2e) spectroscopic study of carbonyl sulfide and the momentum-space chemistry of CO_2, CS_2 and OCS".

9) M.G. White, K.T. Leung and C.E. Brion, J. Electron Spectrosc. Relat. Phenom. 23 (1981) 127-145. "Absolute dipole oscillator strengths for photoabsorption and photoionisation of COS".